A COMPUTATIONAL STUDY INTO THE MECHANISM OF PEROXIDASE AND HALOPEROXIDASE IN ENZYMES AND BIOMIMETIC MODEL COMPLEXES

A thesis submitted to the University of Manchester for the degree of Doctor of Philosophy in the Faculty of Science and Engineering.

2019

MUHAMMAD QADRI EFFENDY BIN MUBARAK

Department of Chemical Engineering and Analytical Science

Table of Contents

Word Count : 68’ 399

List of Figure

List of Scheme

List of Table

Abstract

Herein, I present a computational study approach to gain insight of the various chemical and physical properties of peroxidases and haloperoxidases activity in enzymes and biomimetic model complexes.

Heme enzymes are one of versatile enzyme existing in nature. In Chapter 3 and Chapter 4, we did a detailed study on two types of heme enzymes namely Chloroperoxidase and Cytochrome P450, respectively. Chloroperoxidase is a unique enzyme that are able to neutralize hydrogen peroxide into water and at same time convert halides into hypohalide. While, Cytochrome P450 utilizes O2 and NO on the active site of the enzyme and converts L-tryptophan to 4-nitrotryptophan. Even, both enzymes have similar structure of heme arrangement, however, the arrangement of amino acid residue in their active site is a key factor to determine their type of reaction and capability to react with various substrate. Thus, the understanding of their respective processes by environmentally utilize oxidants might lead for future applications in various fields.

The attempt to mimic the structural features of the coordination environment of the natural enzyme always give good result for us to remodel desired reaction. Hence, in Chapter 5, Chapter 6 and Chapter 7 we did a detailed study on biomimetic complexes containing vanadium and iron. Overall, vanadium-oxo form is sluggish oxidants and reacts slowly with their respective substrate. However, the conversion of vanadium-oxo to vanadium-peroxo intermediate by using any peroxide is an important step to make it as better oxidant. In Chapter 7, we did collaboration work with the experimentalist group to demonstrate the incorporation of a dialkylamine group into the second coordination sphere of a Fe^{II} complex allows the formation of Fe^{IV}-oxo intermediate which is unusual phenomena. In this work, we are able to prevent the formation of Fe^{III} species and hydroxyl radicals where this species prone to engage in uncontrolled radical chemistry. In the biomimetic model complexes study, several factors had been studied that give a significant effect to the rate reaction such as ligand architecture, type of equatorial ligand and second-coordination effect.

In Chapter 8 and Chapter 9, we did work to identify how the metal substituent affects the chemical reactivity of biomimetic complexes. We did replaced iron by ruthenium and manganese, and performed a detailed computational study for their respective systems and observe the reactivity of the system. Then we did thermochemical cycles and valence bond patterns analysis to explain the differences in chemical properties and identify how the metal substituent affect the chemical reactivity of complexes with substrates.

Declaration

That no portion of the work referred to in the thesis has ben submitted in support of an application for another degree or qualification of this or any other university or other institute of learning.

Copyright Statement

The author of this thesis (including any appendices and/or schedules to this thesis) owns certain copyright or related rights in it (the "Copyright") and s/he has given The University of Manchester certain rights to use such Copyright, including for administrative purposes.

ii. Copies of this thesis, either in full or in extracts and whether in hard or electronic copy, may be made **only** in accordance with the Copyright, Designs and Patents Act 1988 (as amended) and regulations issued under it or, where appropriate, in accordance with licensing agreements which the University has from time to time. This page must form part of any such copies made.

iii. The ownership of certain Copyright, patents, designs, trademarks and other intellectual property (the "Intellectual Property") and any reproductions of copyright works in the thesis, for example graphs and tables ("Reproductions"), which may be described in this thesis, may not be owned by the author and may be owned by third parties. Such Intellectual Property and Reproductions cannot and must not be made available for use without the prior written permission of the owner(s) of the relevant Intellectual Property and/or Reproductions.

iv. Further information on the conditions under which disclosure, publication and commercialisation of this thesis, the Copyright and any Intellectual Property and/or Reproductions described in it may take place is available in the University IP Policy (see http://documents.manchester.ac.uk/DocuInfo.aspx?DocID=24420), in any relevant Thesis restriction declarations deposited in the University Library, The University Library's regulations (see http://www.library.manchester.ac.uk/about/regulations/) and in The University's policy on Presentation of Theses.

List of Abbreviations

- BDE Bond dissociation energy
- BS Basis set
- Cl Chloride
- CPCM Continuum polarized conductor model
- Cpd 0 Compound 0
- Cpd I Compound I
- Cpd II Compoound II
- CPO Chloroperoxidase
- CYP450 Cytochrome P450
- Cys Cysteinate
- DFT Density functional theory
- EA Electron affinity
- EPR Electron paramagnetic resonance
- Eq Equation
- Fe Iron
- GGA Generalised gradient approximation
- Glu Glutamic
- GTO Gaussian type orbitals
- H_2O_2 Hydrogen peroxide
- HAT hydrogen atom transfer
- HCO_4^- Peroxymonocarbonate
- HF Hartree Fock
- His Histidine
- I Intermediate
- IE Ionization energy
- KIE Kinetic isotope effect
- LDA Local density approximation
- MD Molecular dynamics
- Me Methyl
- MM Molecular mechanics
- Mn Manganese
- N4Py N,N-bis(2-pyridylmethyl)-N-bis(2-pyridyl)methylamine
- OH Hydroxyl
- P Product
- pdb Protein data bank
- PES Potential energy surface
- PT Proton transfer
- Q Charge density
- QM Quantum mechanics
- Re Reactant

- Ser Serine
- SP Stationary point
- STO Slater type orbitals
- Sub Substrate
- TAML Tetra-amido macrocyclic ligand
- $TPPCl_8$ 2,3,7,8,12,13,17,18-octachloro-*meso*-tetraphenylporphyrinato
- TS Transition state
- V Vanadium
- VBrPO Vanadium bromoperoxidase
- VClPO Vanadium chloroperoxidase
- VHPO Vanadium haloperoxidase
- VIPO Vanadium iodoperoxidase
- ZPE Zero point energy

List of Publication

- M Qadri E Mubarak, Sam P De Visser. Computational Study on the Catalytic Reaction Mechanism of Heme Haloperoxidase Enzymes**.** *Israel Journal of Chemistry*. 2019.
- M Qadri E Mubarak, Sam P De Visser. Reactivity Patterns of Vanadium(IV/V)-Oxo Complexes with Olefins in the Presence of Peroxides: A Computational Study. *Dalton Transactions.* 2019, 48**:** 16899-16910.
- M Qadri E Mubarak, Sam P De Visser. Second-Coordination Sphere Effect on the reactivity of vanadium-peroxo complexes: A computational study. *Inorganic Chemistry*. 2019, 58, 23 15741-15750. https://doi.org/10.1021/acs.inorgchem.9b01778.
- M Qadri E Mubarak, Alexander B Sorokin, Sam P De Visser. Properties and Reactivity of u-Nitrido Bridged Dimetal Porphyrin Complexes. How Does Ruthenium Compare to Iron? *Journal of Biological Inorganic Chemistry*. 2019, 1-8. https://doi.org/10.1007/s00775-019-01725-7.
- Khaled Cheaib, M Qadri E Mubarak, Katell Sénéchal-David, Christian Herrero, Régis Guillot, Martin Clémancey, Jean-Marc Latour, Sam P De Visser, Jean-Pierre Mahy, Frédéric Banse, Frédéric Avenier. Selective Formation of an $Fe^{IV}O$ or an $Fe^{III}OOH$ Intermediate From Iron(II) and H_2O_2: Controlled Heterolytic versus Homolytic Oxygen–Oxygen Bond Cleavage by the Second Coordination Sphere. *Angewandte Chemie.* 2019, 131(3): 864-868.
- Jan Paulo T. Zaragoza, Daniel C. Cummins, M. Qadri E. Mubarak, Maxime A. Siegler, Sam P. De Visser, and David P. Goldberg.Hydrogen Atom Abstraction by High-Valent Fe(OH) versus Mn(OH) Porphyrinoid Complexes: Mechanistic Insights from Experimental and Computational Studies. *Inorganic Chemistry.* 2019.
- Neelam Zeb, Muhammad H Rashid, M. Qadri E. Mubarak, Sidra Ghafoor, Sam P De Visser. Flavonol Biosynthesis by Nonheme Iron Dioxygenases: A Computational Study into the Structure and Mechanism. *Journal of Inorganic Biochemistry*. 2019, 198:110728. https://doi.org/10.1016/j.jinorgbio.2019.10728.

Acknowledgement

First of all, I give thanks to Almighty God for His Grace, His Merciful and Lovingkindness for seeing me through the challenging years of my PhD programme at the University of Manchester. Without His strength, peace, reassurance, encouragement, boldness, courage and so much more this would not be possible.

I would like to thank to my supervisor Dr Samuel P. De Visser, for his kindness, support, wisdom and patience in guiding me all these year. His experience has been invaluable to me, I have learnt a lot from him and that will be with me for many years to come.

Beside, I would like to thank to my mother, Siti Darhajah Aziz who always give her best advice and without her I would not be where I am today. Not to forget, my late father, Mubarak Yusof whom I cherish the most. Then, I am grateful to my wife, Ainul Basyirah Ishak, for her support in many thing. Not to forget, my beautiful daughter, Maryam for giving enjoyable moment all these years. In fact, all of you gave me strength to soar higher.

I am also thankful to my collegues which have continuously helped me during all these years, providing friendship, great conversation and encouragement; Fabian, Amy, Nick, Hafez, Neelam, Emily and Yen Ting. Thank you.

Note to forget, I would also like to thank to my family, friends and my colleagues in ISMA who have been with me during this process. Thank you to all your support, prayers and encouragement.

Lastly I would like to thank the Government of Malaysia and Islamic Science University of Malaysia (USIM) for providing the studentship which has allowed me to do the research recorded in this PhD and more.

"MALAYSIA TANAH TUMPAH DARAHKU"

Preface

There is so much we can learn from nature which human have been doing for decades. A lot of invention to date were inspired by nature ranging from mathematical formula until great machine. This including the mechanism of chemical transformations occur in nature which then can be used for our own benefit in various fields. The conversion of hydrogen peroxide and halide to water and hypohalous acid is one of the Holy Grails reaction in nature. To date, haloperoxidase group enzymes is the only enzymes known to perform this simultaneous reaction which can lead to future application in various fields. Thus, the aim of this studies to gain insights of peroxidase and haloperoxidase activity in enzymes and biomimetic model complexes by using computational approaches which will further our understanding into the future development.

My thesis consists of nine chapters. The first chapter is a general overview of the topics covered in the thesis. Second chapter is a section devoted to computational methods which fundamental topics of theoretical chemical calculations are discussed. The other seven chapters are selected projects undertaken, during the course of the postgraduate research training. Each reference to the published article is given on first page of each project chapter. All of the projects presented form a coherent and continuous part of the thesis with the subjects relating to one another. I hope the findings contained in this thesis will further expand the understanding of the chemistry and applications of peroxidase and haloperoxidase activity in enzymes and biomemitic model complexes.

M. Qadri E. Mubarak

Manchester, United Kingdom

Chapter 1

INTRODUCTION

1.1 Introduction

Humans have try to understand nature for decades and learned a lot from it. Many inventions have been inspired by nature ranging from mathematical formula to sophisticated machines. This includes the mechanism of chemical transformations which then can be utilized and improved to suit human needs in various fields. Metalloenzymes exist naturally and contain at least one metal element in its active site where the conversion of substrates takes place (Zampella *et al.*, 2006; Khaled Cheaib *et al.*, 2019). The enzymes play a vital role by catalyzing a variety of chemical transformations in biological systems. Enzymes are selective as to what reaction they catalyze and which chemical compounds they accept as substrates. Hence, there is a great interest in understanding the reaction mechanisms of enzymatic reactions to be used as biocatalysts for a variety applications (McKenna, Benemann and Traylor, 1970; Hoffman *et al.*, 2013; Timmins and De Visser, 2015; Eady, Antonyuk and Hasnain, 2016). Thus, in biocatalysis we aim to gain important insights into chemical reaction mechanisms in order for us to understand better how enzymes work in nature but also try to find applications for commercial exploitation of these system. As experimental work is often challenging to reveal the information of intermediate and transition state structure of enzymes due to the fact they are short-lived, computational studies seems to be one of the most suitable approaches.

Haloperoxidase enzymes efficiently catalyze the oxidation of higher halides X^- (Cl^-, Br^-) to the corresponding hypohalous acids (HOX) by using hydrogen peroxide (H_2O_2) as the oxygen source. The controlled partial oxidation of such substrates to well-defined products is potentially very useful for humankind. Halogenated compounds (organohalogens) display various functions and applications, including growth reproduction and defence (Weichold, Milbredt and van Pée, 2016). Additionally, organohalogens have been showns to have many biological properties; for example,

antibacterial, antifungal, antiviral, anti-inflammatory, anti-proliferative, anti-fouling, anti-feedant, cytotoxic and insecticidal activity (Blunt *et al.*, 2011). As a result, many of the current bestselling herbicides, pesticides and insecticides contain a halogen atom (Jeschke, 2010).

Vanadium is one of the most abundant transition metal elements on Earth, but despite this, there are only few examples of natural systems known that utilize vanadium ions, which is surprising (Vilter, 1984). Vanadium Haloperoxidas (VHPO) abundantly exists in the marine environment and is thought to be responsible for the biosynthesis of halogenated natural products. In addition, vanadium can be found as vanadium-porphyrin complexes especially in crude oil. Recent work characterized vanadium-porphyrin complexes by using various spectroscopy technique, although their function and origin remain unknown (Gupta *et al.*, 2015). Finally, the natural product amavidin is a vanadium(IV) containing compound found in fungi that showed catalase and peroxidase type activity (Wever and Van Der Horst, 2013; Rehder, 2015).

Furthermore, evidence has emerged of useful pharmaceutical properties of vanadium containing compounds, for instance, vanadium-porphyrins are used as anti-HIV agents, and diaminotris(phenolato) vanadium(V) complexes as anticancer drugs (Thompson, 2001). In biomimetic chemistry, many reports have appeared in the literature that discuss the coordination environment and reactivity of vanadium complexes (Ligtenbarg, Hage and Feringa, 2003; Wever and Van Der Horst, 2013; Rehder, 2015). For instance, vanadium(IV) and vanadium(V) complexes have been shown to react with olefins through epoxidation, (Conte *et al.*, 2011) but also react with aliphatic groups such as cyclohexane by hydroxylation and desaturation reactions. Previous report observed that vanadium complexes able to react with olefins through substitution of a C–H bond with C–X (X = Cl, Br, I) (Ten Brink *et al.*, 2000). Therefore, vanadium based enzymes are highly versatile as oxidation catalysts.

Despite the remarkable importance of oxidation reaction of haloperoxidase, a detailed study on vanadium haloperoxidase and choloroperoxidase to the best of our knowledge has never been reported. In this thesis, a detailed series of work had done to gain insight into the mechanism of peroxidase and haloproxidase in enzymes and biomemitic model complexes.

1.2 Classification of Haloperoxidase

Over the past 60 years, three different types of haloperoxidases have been discovered. These are grouped according to the nature of their active halogenating agent, nature of their mechanism, co-factor and substrate. We can classify haloperodise enzymes to three group consists of vanadium-containing haloperoxidases (Lowell P. Hager *et al.*, 1966; Rehder, 2015), heme-containing haloperoxidases (Lowell P Hager *et al.*, 1966; Lowell P. Hager *et al.*, 1966; Morris and Hager, 1966) and flavin adenine dinucleotide dependant haloperoxidse enzymes (Nakano *et al.*, 1995). All of these enzymes mentioned have important role in their respective biosystem. In the next few sections, I will give a brief overview of VHPO and heme haloperoxidase as the focus of this study.

1.3 Vanadium Haloperoxidase

Vanadium is one of the most abundant transition metal elements that exist in the ocean (Martinez *et al.*, 2001; Wever, 2012) and is commonly found in the form of a vanadate oxyanion at pH 7 (Rehder, 1999; Martinez *et al.*, 2001; Crans *et al.*, 2004). VHPO was first discovered in seaweed about 35 years ago (Vilter, 1984) in seawater with the concentration around 30 to 35nM (Everett, Soedjak and Butler, 1990) and responsible for the biosynthesis of halogenated natural products. However there are only few examples of natural systems known that utilize a vanadium ion, which is surprising. Two types of enzymes that use vanadium are known so far, namely nitrogenases (Burns, Fuchsman and Hardy, 1971; Schweitzer *et al.*, 2008; Butler and Sandy, 2009; Hu and Ribbe, 2011; Hoffman *et al.*, 2013) and haloperoxidases (Winter and Moore, 2009). The latter being the

focus of this section. VHPO enzymes can be found seaweed (Wever, 2012) , fungi (Vollenbroek *et al.*, 1995) and lichen (Plat, Krenn and Wever, 1987).

All currently characterized VHPOs are eukaryotic in origin and have been isolated as either vanadium bromoperoxidase or chloroperoxidase (Weyand *et al.*, 1999; Amadio *et al.*, 2015). The haloperoxidases are named after the most electronegative halide they are able to oxidize, and thus a vanadium chloroperoxidase (VClPO) is able to oxidize chloride, bromide, and iodide, whereas, vanadium bromoperoxidases (VBrPO) reacts with bromide and iodide and iodioperoxidases (VIPO) react with iodide alone (De Boer, Boon and Wever, 1988; Schijndel *et al.*, 1994; A Messerschmidt, Prade and Wever, 1997).

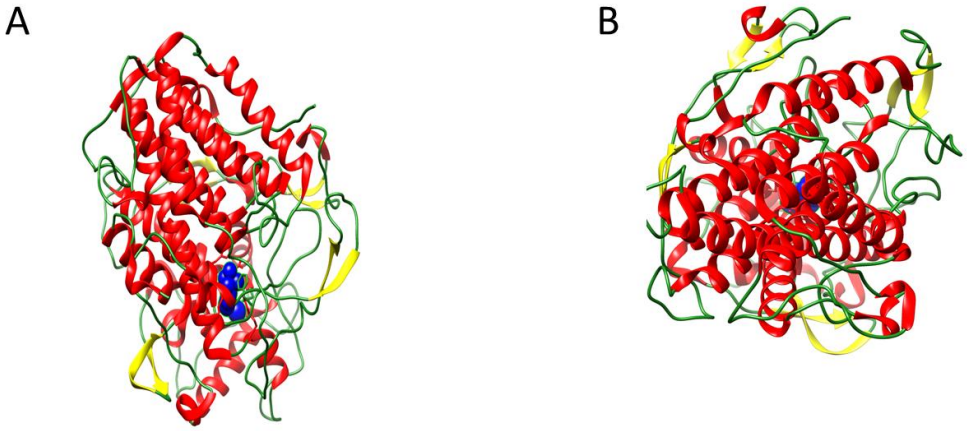

Figure 1.1. Crystal structure of the vanadium chloroperoxidase from *C. inaequalis* (1IDQ.pdb) (Albrecht Messerschmidt, Prade, and Wever 1997) highlighting the side-by-side four α-helix loops common to all vanadium haloperoxidases enzymes, with the vanadium cofactor (blue ball) anchored at the bottom of this channel. The structure is shown in the cartoon representation with the secondary structure highlighted; red are α-helixs, green are loops, and yellow are β-sheets.

1.3.1 Structure of VHPO and it's Active Site

In VHPO, the vanadium centre acts as a Lewis acid and does not change its oxidation state (+5) throughout the catalytic cycle; therefore, it is a stable compound (Ten Brink *et al.*, 2000; Crans *et al.*, 2004; Vaillancourt *et al.*, 2006; Butler and Sandy, 2009). According to various sources, only three VHPO's have had their crystal structure resolved so far. VClPO from the fungus *C. inaequalis* (Albrecht Messerschmidt and Wever 1996; Albrecht Messerschmidt, Prade, and Wever 1997; Macedo-Ribeiro et al. 1999; McLauchlan et al. 2018b), VBrPO from the brown alga *A. nodosum* (Weyand *et al.*, 1999) and VBrPO from the red alga *C. officinalis* (Isupov *et al.*, 2000). All these VHPO structures less than a 30% sequence similarity. However, they each share a common active site structure consisting of two side-by-side four-α-helix bundles with the vanadium active site located at the bottom, as shown in Figure 1.1 (Albrecht Messerschmidt and Wever 1996; Albrecht Messerschmidt, Prade, and Wever 1997; Weyand et al. 1999; Isupov et al. 2000).

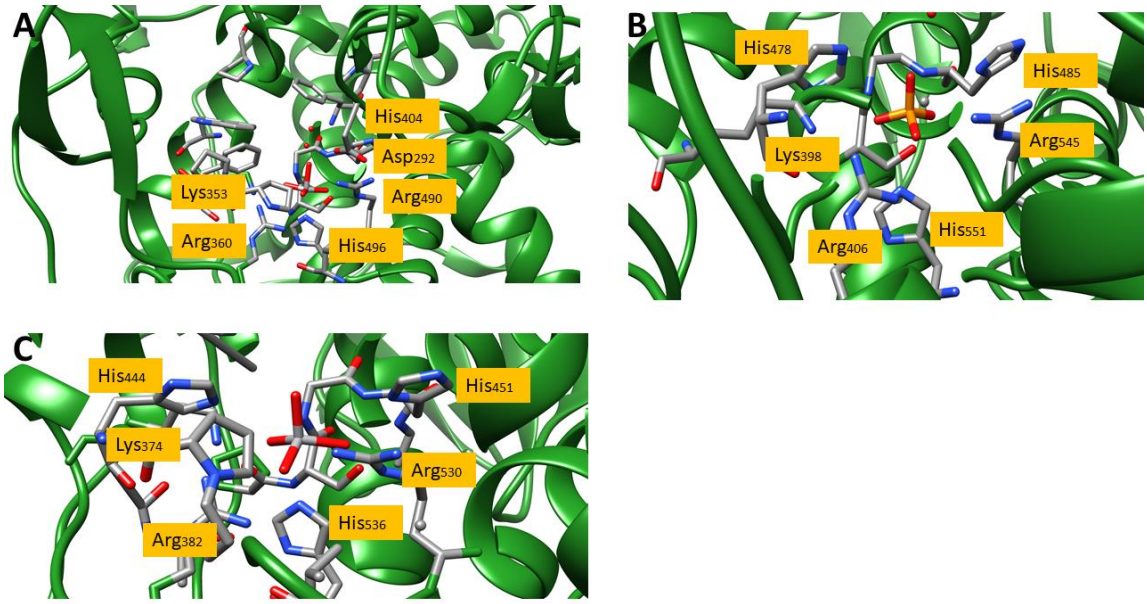

Figure 1.2. Active site structure of VHPO as taken from the A) VClPO (1IDQ.pdb) from the fungus *C. inaequalis* (Albrecht Messerschmidt, Prade, and Wever 1997) B) VBrPO (1QHB.pdb) from the brown alga *A. nodosum* (Weyand *et al.*, 1999) C) VBrPO(5AA6.pdb) from the red alga C. officinalis (Isupov *et al.*, 2000). All structure taken protein databank file with key polar residues highlighted.

Among all the VHPO ezymes mentioned, we can see they all have a similar arrangement of amino acid residues in the active site as shown in Figure 1.2. Figure 1.2 reveals that all VHPO structures are bound in a trigonal bipyramidal form linked to the protein via one histidine ligand, whereas the other four ligands are oxygen-based (Hemrika *et al.*, 1997) (Wever and Hemrika, 2006). The vanadate oxyanion cofactor is ligated to a histidine residue for all VHPOs at the bottom of a four-α-helix bundle, serving as its anchor (Albrecht Messerschmidt, Prade, and Wever 1997; Weyand et al. 1999; Isupov et al. 2000). Meanwhile, the negative charge of the oxygen of vanadate group is compensated by hydrogen bonds to three positively charged residue around the centre which are Arg_{360}, Arg_{490} and Lys_{353}. While, the Arg_{490} forms a salt bridge with residue of Asp_{292} (Wever and Hemrika, 2006). Furthermore, mutational studies that replaced histidine with an alanine prevented the cofactor from binding, thus solidifying its role as an "anchor" (Renirie, Hemrika & Wever, 2000).

If we look closely to the structure, the vanadate binding pocket seems to form a very rigid frame stabilising oxyanion. Due to large number of hydrogen bonding interactions around the active site the protein environment is important stabilizing the enzyme. The vanadate binding pocket is at the end of a channel that supplies access and release to the small substrate and products of the reaction (Wever and Hemrika, 2006). One half of the surface of the channel is mainly hydrophobic and lined with Pro_{47}, Pro_{221}, Tyr_{350}, Phe_{393} and Pro_{395} as contribution side chain. The other half of the channel is predominantly polar with several carbonyl oxygens and the ion pair Arg_{490}-Asp_{292} (Wever and Hemrika, 2006). In addition, the vanadate oxyanion contains several negative charges which the VHPO active site has to compensate for to facilitate binding. It compensates for these negative charges by providing an extensive hydrogen bonding network with several protonated amino acid residues in the conserved active site such as Lys_{355}, Arg_{360} and Arg_{490} as shown in Figure 1.2(A). Furthermore, computational studies identified a key role of a Lys_{353} residue in

the substrate-binding pocket that polarizes the peroxo cofactor and assists with charge redistribution in the reaction with substrates.

Clearly, the VHPO structure is bound to one nitrogen atom of a histidine linkage and the other four ligands are oxygen-based. However, experimental studies unable to establish whether the oxygen ligands are either oxo, hydroxo, or water as monodentate ligands or peroxo as bidentate ligand. Numerous sources suggested the apical oxygen ligand to form hydroxyl bond due to the bond length approximately around 1.93 Å in the crystal structure while the other three oxygen atoms form a plane. Computational work reveal possible isomers of resting state of VHPO (Zampella *et al.*, 2005, 2006; Schneider *et al.*, 2007; Sanna *et al.*, 2012). It was concluded that the most stable resting-state structure of VHPO is vanadium (V)-dioxo-dihydroxo structure with one oxo group equatorial and one hydroxo group axial which hydrogen bonds to a protonated His_{404} (Zampella *et al.*, 2005, 2006; Schneider *et al.*, 2007; Sanna *et al.*, 2012).

More recent QM/MM studies (Waller *et al.*, 2007) focused on characterizing intermediates of the catalytic cycle of VHPO and compared the work with experimental ^{51}V nuclear magnetic resonance (NMR) studies. The resting-state and peroxo-bound structures were investigated specstroscopically by using ^{51}V-NMR methods and established isotropic chemical shifts of 931 ppm and 1135 ppm, respectively (Časný and Rehder, 2001). Based on both studies, it was established that most likely the peroxo form of VHPO is unprotonated or can alternatively contain a hydroxo group in the equatorial position which is similar for VClPO and VBrPO (Hemrika *et al.*, 1997; Pacios and Gálvez, 2010).

1.3.2 Advantages of VHPO

Vanadium is special in many aspects such as the tetrahedral anion vanadate(V) is structrurally and chemically similar to the phosphate anion. Comparative analysis of the sequences and active site of amino acids of VHPOs show high structural conservation and an overlap with several classes of acid phosphatases. The structure similarity between both reported having the volume of the circumscribing spheres of 125 Å and 102 Å, respectively (Hemrika *et al.*, 1997; Rehder, 2015). Thus, vanadate can be one of the alternative elements for substitution of phosphate in enzymes (Hemrika *et al.*, 1997; Rehder, 2015).

Furthermore, vanadium does not change its redox state through catalytic cycle (Arber *et al.*, 1989) compared to iron and therefore it is not possible for VHPO to suffer from oxidative inactivation (Vilter, 1984; Vaillancourt *et al.*, 2006; Butler and Sandy, 2009). Thus, makes VHPO possess a high stability in extreme environments (Schijndel *et al.*, 1994; Vollenbroek *et al.*, 1995). As a result, VHPOs are receiving attention from the pharmaceutical industry as potential sources of halogenating enzymes due to their resistant in high concentration of hydrogen peroxide substrate, hypohalous acid (Liu *et al.*, 1987; Schijndel *et al.*, 1994) and various organic solvents such as methanol, ethanol, 1-propanol, acetone, dioxane and sodium dodecyl sulphate (de Boer *et al.*, 1986; Tromp, Van and Wever, 1991). In addition, VHPO also has tolerance with high temperature (de Boer *et al.*, 1986; Coupe *et al.*, 2007) and has the ability to oxidise organic sulphides in the absence of halides (Ten Brink *et al.*, 2000). Furthermore, VHPO was thought to be similar to chloroperoxidase with regards to their low regioselectivity and stereoselectiviy.

In marine algae, VHPO enzymes could be involved in anti-oxidant protection and in chemical defence and are likely to have a key role in the biochemical part of the iodine and bromine recycling in marine environments (Tromp, Van and Wever, 1991). Some of

VBrPOs found predominantly in marine algae have demonstrated a preference for indole derivatives even in the presence of other substrates (Martinez *et al.*, 2001) which implicates that they have a certain degree of substrate specificity and may have a function related to marine natural products biosynthesis (Carter-Franklin and Butler, 2004). In addition, VBrPO were involved in natural defence mechanisms of biosystems by reducing the colonization of bacteria at the surface of algae through the disruption of quorum sensing (Borchardt *et al.*, 2001). While, VClPO are found predominantly in terrestrial fungi and, they have been associated with the degradation of plant cell walls, thereby facilitating the penetration of fungal hyphae into the host (Wever and Hemrika, 2006; Rehder, 2013, 2015).

As the catalytic turnover of VHPO far exceeds any synthetic catalyst for halide oxidation known to date, this family of proteins has attracted interest for bio-inspired catalyst design (Butler, 1999; Ligtenbarg, Hage and Feringa, 2003). Pharmaceutical applications have emerged based upon structural analogues of the active site of VHPO and has prompted further research into the structure and function of the VHPO (Martinez *et al.*, 2001; Thompson, 2001; Carter-Franklin and Butler, 2004).

1.3.3 Mechanism of VHPO

The catalytic cycle of VHPO is currently still under debate although more information is being obtained from ongoing studied that have led to increased mechanistic understanding of halogenase biochemistry. Until now, there is limited knowledge of the nature of the resting state, its possible intermediates and how the co-factor is regenerated. Little is known on the oxygen-bound intermediates as none have been trapped and characterized experimentally. Figure 1.3 shows the general mechanistic cycle proposed by several studies of computational and experimental method, e.g., mutational and steady state kinetics, on the VClPO from *C. inaequalis* (Macedo-Ribeiro & Hemrika *et al.*, 1999; Isupov & Dalby *et al.*, 2000; Renirie, Hemrika & Wever, 2000; Hemrika & Renirie *et al.*, 1999; Zampella & Fantucci *et al.*, 2005; Zampella & Fantucci *et al.*, 2006; Schneider &

Zampella *et al.*, 2008; Waller & Buhl *et al.*, 2007; Waller & Geethalakshmi *et al.*, 2008; Geethalakshmi & Waller *et al.*, 2009; Rehder & Casney *et al.*, 2004; Pacios & Gálvez, 2010; Conte & Coletti *et al.*, 2011; Butler, 1999; Conte & Coletti *et al.*, 2011).

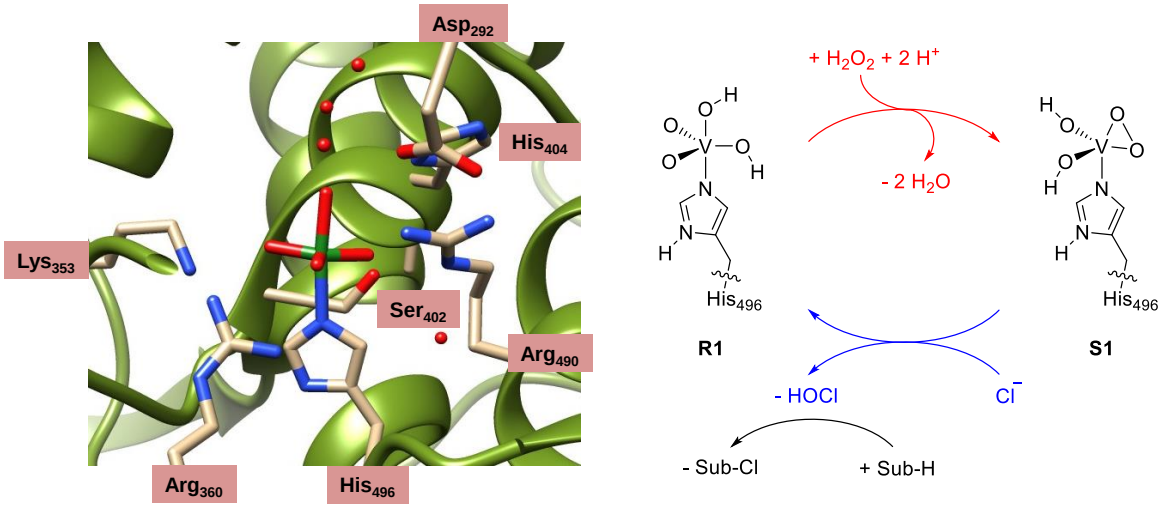

Figure 1.3. Active site structure of VHPO as taken from the 1IDQ protein databank file with key polar residues highlighted. The right-hand-side depicts the proposed catalytic cycle of VHPO enzymes from the literature with Sub-H representing a substrate.

However, VHPO still poorly understood in the context of biosynthesis mechanism (Winter and Moore, 2009). Thus there is urgency to reveal and understand the mechanistic cycle of the VHPO. From all the information we gathered so far, all studies agree that the VHPO enzymes utilizes hydrogen peroxide and a covalently bound vanadate cofactor to oxidize halides, X^- (Cl^-,Br^-, and I^-) into hypohalous acid, HOX. Colpas (Colpas *et al.*, 1996), suggested the first stage of the catalytic cycle is proton transfer to one of the oxygen atoms directly bound to the vanadium. Previous studies suggest, that as hydrogen peroxide binds, a series of proton transfers occur involving histidine residue, resulting in the release of water and the generation of vanadium(V)-peroxo(oxo)-hydroxo intermediate (van Schijndel, Vollenbroek & Wever, 1993). Once the peroxide binds

side-on, the vanadium site is distorted from a trigonal bipyramidal to a tetragonal bipyramidal structure (Macedo-Ribeiro & Hemrika *et al.*, 1999), and His_{404} no longer make hydrogen bonds to any of the oxygen atoms of the cofactor, instead Lys_{153} makes direct contact with one of the peroxide oxygen atoms, activating the bound peroxide further through charge separation. The vanadium(V)-peroxo(oxo)-hydroxo intermediate then reacts with a halide to form a vanadium(V)-hypohalide-dioxo(hydroxo) complex which reacts with substrates containing functional groups such as hydrocarbons, sulphides and olefins. Finally, restoration of the cofactor to its initial resting state is thought to occur again after a series of protonation steps, enabling the hypohalide to leave the active site as hypohalous acid (Hemrika *et al.*, 1999).

Scheme 1.1 shows the catalytic cycle as proposed by Butler *et al.* and Conte *et al.* (Butler, 1999; Conte *et al.*, 2011). The mechanism starts from a vanadium (V)-dioxo-dihydroxo with all three oxo groups in the equatorial positions. The axial oxo group of vanadium is the imidazole group of His_{404} that links it to the protein. Thereafter, the H_2O_2 attacks the vanadium centre and reduces reduces the hydroxo group to an oxo group with the assistance of the distal His_{404} group. Proton relay has occurred at this stage. After the formation of a vanadium(V)-peroxo group a reaction with halide (X^-) to form hypohalide takes place which then reacts with substrates to form halogenated products. The peroxo-bound vanadium (V)-oxo intermediate has been shown to react with aliphatic hydrocarbons, sulfides, and olefins to generate alcohols, sulfoxides, and epoxides as the product, respectively (Conte *et al.*, 2011). However, the mechanism proposed does not take the protein into consideration. For instance, many possibilities of protein relays can be happen inside the active site area as VHPO itself surrounded by various polar amino acid residues. From this study, the protein relay seem to be one of important factor that needs to be considered.

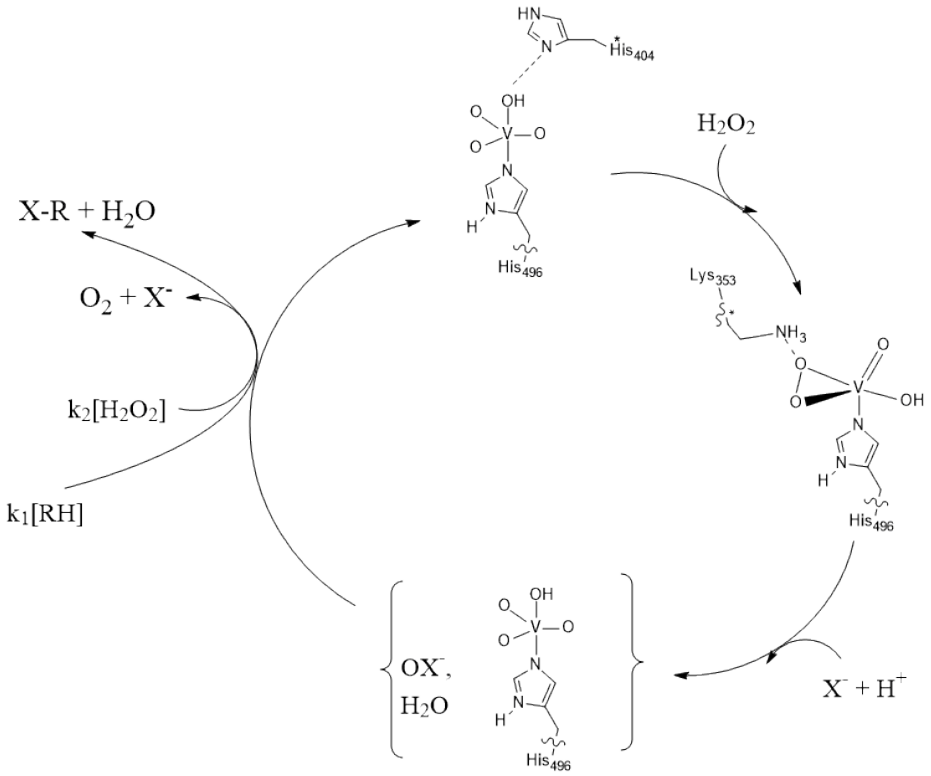

Scheme 1.1. Mechanistic consideration for studying haloperoxidase enzymes proposed (Butler, 1999; Conte *et al.*, 2011).

Scheme 1.2 shows a mechanistic cycle of VHPO enzymes proposed by Hemrika *et. al,* (Hemrika *et al.*, 1999). This study divided the mechanism into two individual steps approach, namely the formation of vanadium-peroxo intermediate and the synthesis of hypohalide. The first reaction cycle, involves the formation of the vanadium peroxo intermediate illustrated by species A, B and C (Scheme 1.2). While for the second cycle involving involving the reaction of halide with the vanadium-peroxo intermediate is illustrated by species D, E and F (Scheme 1.2), respectively. The mechanism show the formation of the peroxo intermediate in which His_{404} activates the apical hydroxide to deprotonate the peroxide and lead to formation of the side-on bound peroxo group. Here, the vanadium acts as Lewis acid withdrawing electron density from the bound peroxide.

The two arginine residues present in the active site namely Arg_{490} and Arg_{360} assist with electron withdrawal and Lys_{353} by forming hydrogen bond to one of the peroxide oxygen atoms. The finding suggested the protonation of the bound peroxide might occur and make it more reactive. The next step is nucleophilic attack by halide as shown in D that will breaking the oxygen-oxygen bond and formation of the nucleophilic OX-group. Later, this group will take up a proton from water molecule to form HOCl as shown in E and completed the mechanism cycle.

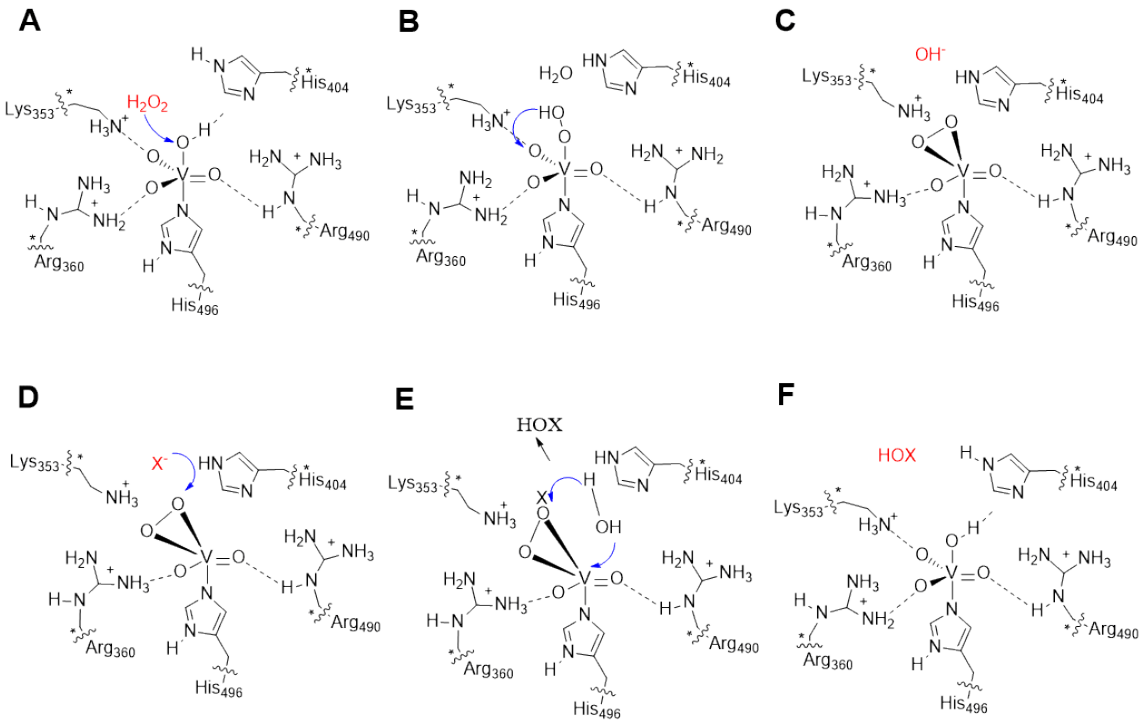

Scheme 1.2. Reaction scheme for VHPO mechanism (Hemrika *et al.*, 1999).

Scheme 1.3 illustrated the mechanism involved in the catalytic cycle of VHPOs proposed by the Pecoraro group (Zampella *et al.*, 2005; Schneider *et al.*, 2007; Sanna *et al.*, 2012). They had proposed that the mechanism of VHPOs involving the oxidation of halide by two electrons, and not with a one-electron or radical mechanism of oxidation (Amadio *et al.*, 2015). Initially, the H_2O_2 will attack to form a stable peroxovanadate intermediate, which then reacts with halide. After halide oxidation takes place, the electron oxidized halogen intermediate "X^+'', which is a mixture of different halogen species such as OX^-, X^{3-} or X_2, and then rapidly halogenates organic substrates in a non-enzymatic reaction. In the absence of organic substrate, a second equivalent of H_2O_2 is oxidized to form a single oxygen and X^- is produced which can further react with electron-rich substrates to form halogenated organic compounds. Their group suggested vanadium remains in the +5 oxidation state throughout the entire catalytic cycle and will become totally inactive when the oxidation state of vanadium reduced to +4.

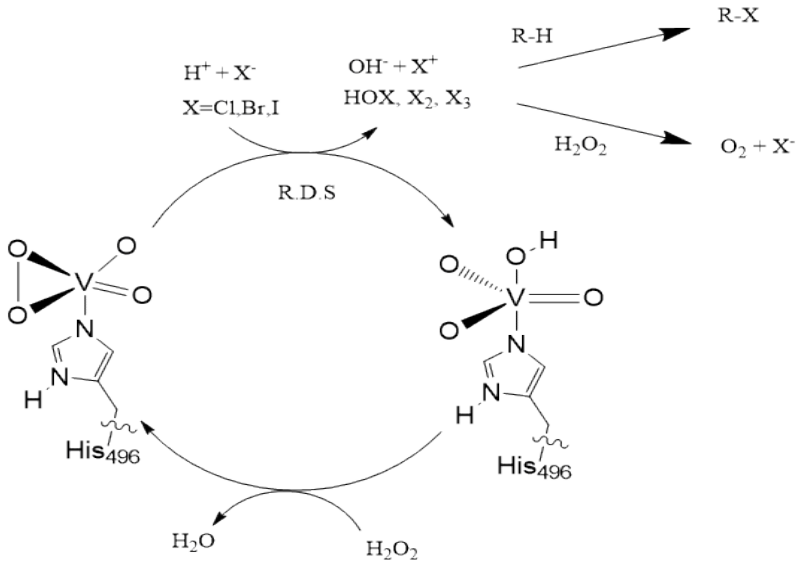

Scheme 1.3. Proposed mechanism of VHPOs by Pecoraro's group.

Furthermore, recent studies on biomemitic complexes containing vanadium show that conversion of vanadium-oxo species to vanadium-peroxo species is important step to improve the rate of reaction of the enzymes (Kumar *et al.*, 2015; Dar *et al.*, 2019; Mubarak and De Visser, 2019a, 2019b). Thus, understanding the factors that determine the substrate selectivity for the cycle will be a key factor to any further application of VHPO.

1.4 Heme Haloperoxidase

The class of heme enzymes in chemical biology is very large and take part in important functions in biosystems related to oxygen transport, electron transfer, substrate detoxification and biosynthesis processes (Sono *et al.*, 1996; Solomon *et al.*, 2000; Costas *et al.*, 2004; Meunier, De Visser and Shaik, 2004; Abu-Omar, Loaiza and Hontzeas, 2005; Denisov *et al.*, 2005; Kryatov, Rybak-Akimova and Schindler, 2005; van Eldik, 2007; Bruijnincx, Van Koten and Gebbink, 2008; Ortiz De Montellano, 2010; SP De Visser, 2011; McDonald and Que, 2013; Nam, Lee and Fukuzumi, 2014; Huang and Groves, 2017). Many of heme enzymes utilize molecular oxygen and react as monoxygenases or dioxygenases with substrates (Kadish, Smith and Guilard, 2013). The monoxygenases are

widespread among all forms of life and are highly versatile in their substrate scope and function. In particular, the cytochromes P450 are common in human physiology and are found in the liver. They initiate the metabolism and detoxification of xenobiotics such as drug molecules (Sono *et al.*, 1996; Meunier, De Visser and Shaik, 2004; De Montellano, 2005; Denisov *et al.*, 2005; Huang and Groves, 2018).

Among the heme enzymes that exist in nature, the heme haloperoxidases are a unique set of heme enzymes. The first heme-dependent haloperoxidase was discovered in 1966 from *Caldariomyce fumago*, the producer of caldariomycin (Lowell P Hager *et al.*, 1966; Morris and Hager, 1966). Since its discovery, it has been shown to function as a catalase, peroxidase and perform P450-like oxygen insertion reactions. Despite its have varying catalytic ability at its actives site, this enzyme oxidises halide ions in the presence of hydrogen giving it the name chloroperoxidase (CPO). Furthermore, the porphyrin structure of CPO is similar to peroxidase and cytochromes P450 (Nicholls, Fita and Loewen, 2000; Njuma, Ndontsa and Goodwin, 2014) (Veitch and Smith, 2000; Raven, 2003; Smulevich, Feis and Howes, 2005; Zederbauer *et al.*, 2007; Poulos, 2014).

1.4.1 The Structure of Heme Haloperoxidase

Figure 1.4 shows the comparison of various heme enzymes found in nature. Structurally, CPO shares many of its features with P450 enzymes and peroxidases. If we look closely at the structure of P450 enzymes, it contains a cysteinate axial ligand bound to the heme group and a polar distal pocket. However, the distal residue of CPO is not a histidine but a glutamic acid and the arginine that is highly conserved in peroxidases is not present in CPO. Although monoxygenases, catalases and peroxidases all have a central heme co-factor with a bound to iron(III) in the resting state, they all have a unique secondary structure. In all structure, the heme binds the protein through different type of amino acid side chain linkage with the metal in the axial ligand position. Furthermor, the type of bonding varies between the various heme enzymes.

Figure 1.4 shows the cytochromes P450 bind the heme to the protein via a cysteinate axial ligand, while the catalases use a tyrosinate and the peroxidases use a neutral histidine ligand instead. These differences in axial ligand have been correlated with a "push"-effect of electron density from the axial ligand to the iron and are believed to give the enzyme their specific activity and function (Dawson *et al.*, 1976; Poulos, 1996; Ogliaro, De Visser and Shaik, 2002) as well as the redox potential of the heme. Interestingly, even all of these enzymes mention differ in secondary structure but these enzymes form a high-valent iron(IV)-oxo heme cation radical active species, called Compound I (Cpd I), in their catalytic cycle as the active species (Nam, 2007; Watanabe, Nakajima and Ueno, 2007; Davydov *et al.*, 2008; Rittle and Green, 2010).

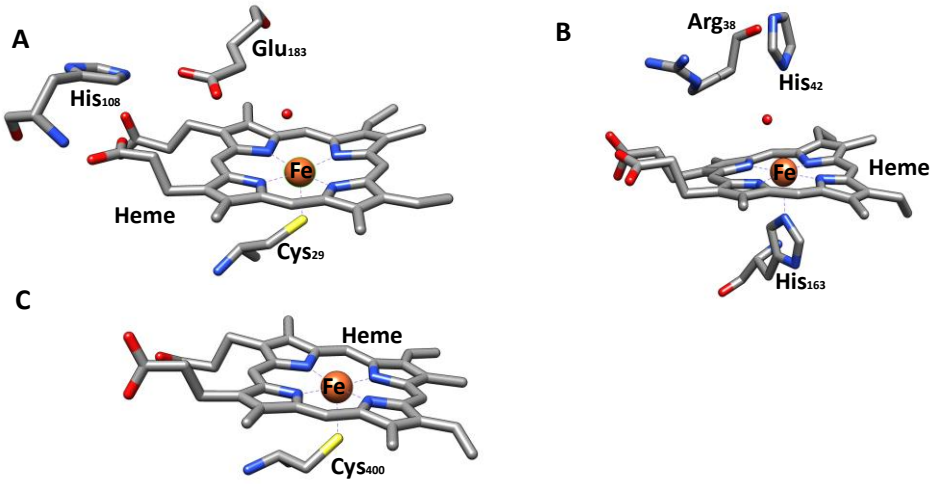

Figure 1.4. Comparison of the active sites in (A) chloroperoxidase (PDB 2J18) (Dawson *et al.*, 1976), (B) peroxidase (PDB 2GHC) (Badyal & Joyce et al., 2006) and (C) cytochrome P450 (PDB 1FAG) enzymes (Li & Poulos, 1997).

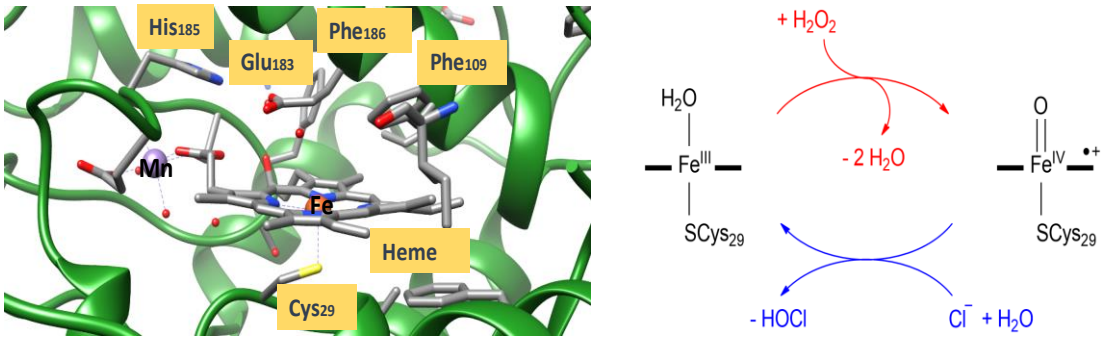

Figure 1.5. Active site structure of Heme Haloperoxidase as taken from the 1CPO protein databank file with key polar residues highlighted. The right-hand-side depicts the proposed catalytic cycle of Heme Haloperoxidase enzymes from the literature.

The active site of a typical chloroperoxidase (CPO), namely from *Leptoxyphium fumago*, is given in Figure 1.5 as taken from the 2J18 protein databank file (pdb) (Dawson *et al.*, 1976). The central heme cofactor is linked to the protein through a cysteinate axial ligand in analogy to the P450s. Based on Figure 1.5, CPO has a distinctly different active site structure from peroxidases that contain a histidine axial ligand. On the distal site of the heme is a hydrogen-bonding network of polar amino acid residues that includes the side chain of Glu_{183} and the nearby His_{105} and Ser_{176} residues. Our studies showed this intricate network to be involved in the conversion of hydrogen peroxide into Cpd I through proton relay mechanisms and in agreement with previous works (Bathelt, Mulholland and Harvey, 2005; Derat *et al.*, 2005; Derat and Shaik, 2006a, 2006b; Harvey, Bathelt and Mulholland, 2006; Hersleth *et al.*, 2006; Vidossich *et al.*, 2010; Vidossich, Alfonso-Prieto and Rovira, 2012). Furthermore, the distal site of CPO also has a number of polar residues that stabilize hydrogen bonding interactions and have the ability to relay protons in the active site of CPO, namely the His_{105} and Glu_{183} residues. As we can see from Figure 1.5, there is a manganese(II) ion located in close proximity to the heme propionate groups that hold it into position together with the Glu_{183} and His_{108} amino acid residues. However, its function remains unclear.

1.4.2 The Mechanism of Heme Haloperoxidase

The heme haloperoxidase enzyme utilizes hydrogen peroxide on a heme active site and converts it into hypohalide (Geigert *et al.*, 1986; Dawson and Sono, 1987; Sono *et al.*, 1996; Pan *et al.*, 2007; Manoj and Hager, 2008). Scheme 1.4 is the summary of mechanism of heme haloperoxidase reveal in Chapter 3. Heme haloperoxidase enzymes can be found in fungi and their functions focus on the biosynthesis of natural products and antibiotics (Vaillancourt *et al.*, 2006; van Pe *et al.*, 2006; Butler and Sandy, 2009; Shepherd *et al.*, 2015; Timmins and De Visser, 2018).

Furthermore, Compound I (Cpd I) in CPO is the only complex that has been characterised through various spectroscopic techniques such as absorption (Palcic *et al.*, 1980), resonance Raman (Egawa *et al.*, 2001), electron paramagnetic resonance (EPR) (Schulz *et al.*, 1984), and Mössbauer (Schulz *et al.*, 1984) spectroscopic measurements (Hoffman, 2003). Additionally, computational studies using density functional theory (DFT) (Green, 1999) gained insight into the unusual electronic coupling found in CPO's Compound I (Cpd I), suggesting that the thiolate acquires radical character during Cpd I formation. Furthermore, CPO is a crucial model for studying the reaction intermediates of P450 enzymes and many of the short lived intermediates of CPO have been characterised by a wide range of spectroscopic methods. One of these intermediates is Cpd I, which has been both spectroscopically characterised and studied by computational modelling (Green, Dawson and Gray, 2004; Shaik *et al.*, 2005; Stone, Behan and Green, 2005; Kim *et al.*, 2006; Vardhaman *et al.*, 2011). Overall, due to the broad specificity of these enzymes (Latham *et al.*, 2018), the hypohalous acid is thought to freely diffuse into solution, attacking the substrate with little selectivity.

During the catalytic cycle of CPO, H_2O_2 binds to the iron (III)-heme and is converted into water and an iron (IV)-oxo heme cation radical species called Cpd I. UV/Vis, electron paramagnetic resonance and Mössbauer spectroscopic studies characterized Cpd I as a triradical species with a heme radical coupled to two unpaired electrons on the metal-oxo

group (Dawson and Sono, 1987; Stone, Behan and Green, 2005; Hirao *et al.*, 2006; Kim *et al.*, 2006). This was in agreement with our DFT study and previous study as well on CPO and P450 Cpd I models (Green, 1999; Ogliaro *et al.*, 2001; Schöneboom *et al.*, 2002; Bathelt *et al.*, 2005; Radoń, Broclawik and Pierloot, 2011). Then, Glu_{183} participates in the heterolytic cleavage of the peroxide O-O bond to form the reactive intermediate, Cpd I by protonation of peroxyanion intermediate, Fe-OOH (Silaghi-Dumitrescu, 2008).

Then, after the formation of Cpd I, we introduce two type of reaction by introducing different protonation state. This lead to two different pathway and further information can be obtained in Chapter 3. Overall, Cpd I is react with chloride ion to form hypochloric acid product, which drifts out of the heme active site. Later, the hypochloric acid products can then reacts with a substrate through halogenation. After that, with the addition of water the iron(III) resting state is regenerated (Wagenknecht and Woggon, 1997).

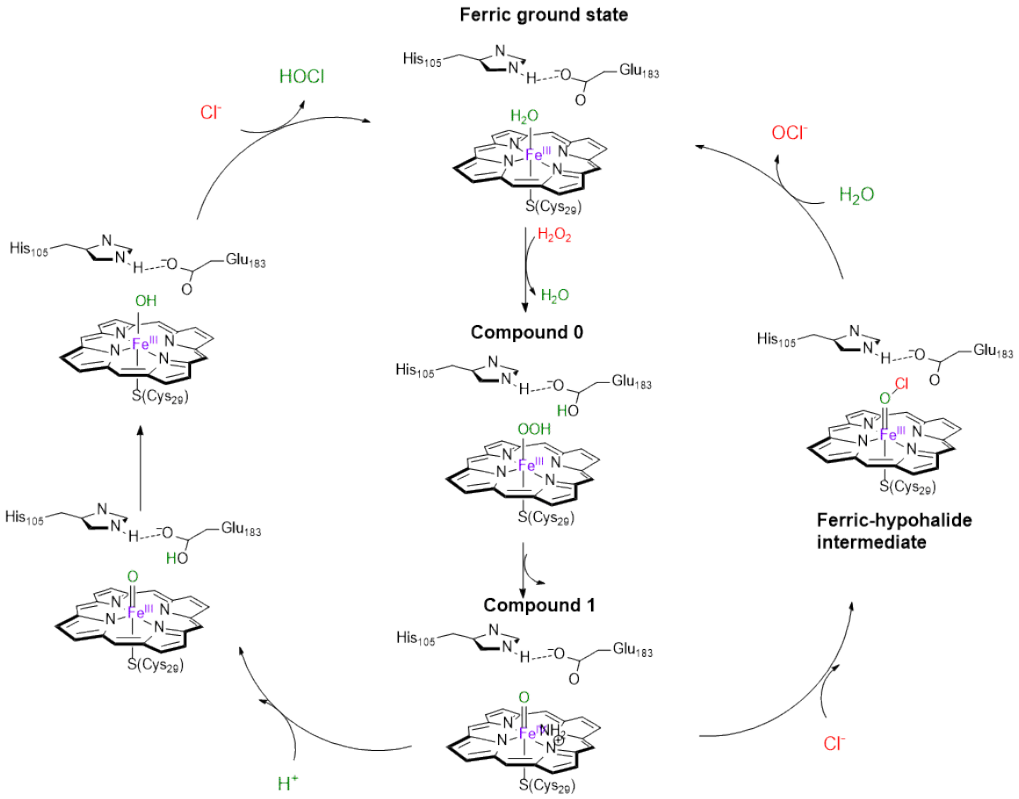

Scheme 1.4. Catalytic cycle of the heme haloperoxidase from CPO. For clarity the side chains of the heme have been removed. The figure adopted from Chapter 6, Project 2.

In Chapter 3, we will present a computational study on the conversion of hydrogen peroxide and halide into hypohalide products at heme active site centre. As far as we are aware, a detailed study into the mechanism of H_2O_2 activation on an iron(III)-heme resting state model and its subsequent reaction with Cl^- to form hypohalide has never been reported and is the focus of the study and will further discussed in Chapter 3.

Despite the remarkable importance of oxidation reaction shown by haloperoxidase, a detailed study on reaction mechanism of the enzymes to the best of our knowledge has never been reported. To gain insight into the properties and reactivity of enzymes activated by hydrogen peroxide, we decided to investigate several peroxidase and halogenase enzymes containing vanadium and iron as focus of this study.

1.5 Summary of Research Objectives

This thesis consist of seven project that was conducted during this PhD programme. The objective of the studies are to further enrich the understanding of the chemistry of peroxidase and haloperoxidase activity in natural enzymes and biomemitic model complexes. In hopes to contribute to the respective field so that the design of related enzymes is benifitted by a broader theoretical understanding of mechanism of reaction, regio- and enantio-selectivity, sites of activation, biosynthesis, coordination chemistry while also exploring the potential and limitation of the computational approaches.

Chapter 2, Methods: In this chapter, the computational methodology and approach of the calculations used in this thesis are presented. A brief introduction to density functional theory, transition state theory and enzyme kinetics is given, together with the basics of energy graphs and the concepts used for relating the calculated energies to experiments.

Chapter 3, Project 1: Heme haloperoxidases are unique enzymes in nature where it able converting the H_2O_2 and halides on a heme center to generate water and hypohalide. In this project, we studied cluster model of the active site of heme haloperoxidase and using computational approach to understand how the enzyme work.

Hence, the objective for this study are:

I. To investigate the active site of heme haloperoxidase that contribute to whole reaction mechanism.
II. To investigate the effect of different density functional theory methods on the active site model of heme haloperoxidase.
III. To investigate the effect of different protonation state of heme haloperoxidase towards the mechanistic cycle of enzyme.

Chapter 4, Project 2: Cytochrome P450(CYP450) enzymes were proved to catalyze various reaction in nature. A recently discovered CYP450 isozyme TxtE utilizes O2 and NO on a heme center and able to convert L-tryptophan to 4-nitrotryptophan which is unusual reaction.

Hence, the objective for this study is

I. To investigate possible nitration pathways leading to products using computational approach of active site of models of CYP450 isozyme TxtE.
II. To investigate the the differences between CYP450 monoxygenases and CYP450 TxtE.
III. To investigate the effect of the addition of electric field towards the energy of cluster model.

Chapter 5, Project 3: Vanadium-oxo and vanadium-peroxo complexes are intermediate that can be found in the catalytic cycle of vanadium haloperoxidases. Recently two novel vanadium-oxo complexes were trapped and characterized with a trigonal bipyramidal ligand design either as solvent exposed vanadium center or the vanadium inside.

Hence, the objective for this study are:

I. To study how the ligand architecture affecting the reaction of conversion of vanadium-oxo to vanadium-peroxo species.
II. To investigate how the ligands framework affect the differences in chemical properties and reactivity.

Chapter 6, Project 4: Vanadium porphyrin complexes can be found in crude oil however their function in nature still poorly understood. Therefore, we decided to perform a detailed density functional theory study into the properties and reactivities of vanadium(IV)- and vanadium(V)-oxo complexes with different substituent on heme framework. In particular, we investigated the reactivity of various model of

$[V^{V}(O)(TPPCl_8)]^{+}$ and $[V^{IV}(O)(TPPCl_8)]$ with cyclohexene in the presence of H_2O_2 and HCO_4^{-}.

Hence, the objective for this study are:

I. To identifiy the effect of ligand architecture on porphyrin ring towards the enzyme.
II. To enhance the rate of reaction by introducing different ligand framework on porphyrin ring.
III. To investigate the effect of equatorial ligand, the local environment and the presence of anionic axial ligands towards the reactivity of system.

Chapter 7, Project 5: In this chapter we did collaboration work with experimental group (Banse's group) focusing on biomimetic model containing nonheme Fe^{II} complexes. I did the DFT calculations that give all the computional results. Direct formation of Fe^{IV}-oxo species from reaction of nonheme Fe^{II} complexes with H_2O_2 is highly attractive for the development of selective oxidation reactions however there is no report yet able to produce Fe^{IV}-oxo yet. Nonetheless, when using this oxidant, most of the Fe^{II} species known to date undergo a single electron oxidation generating Fe^{III} and hydroxyl radicals prone to engaging in uncontrolled radical chemistry. Here, we demonstrate that by introducing dialkylamine group into the second coordination sphere of a Fe^{II} complex allows to switch the reactivity from the usual formation of Fe^{III} species towards the selective generation of a Fe^{IV}-oxo intermediate.

Hence, the objective for this study are:

I. To characterize the Fe^{IV}-oxo complex by spectroscopy method.
II. To establish the mechanistic cycle of the biomemitic complexes by DFT approach.
III. To understand the second coordination effects towards the development of Fe^{IV}-oxo species.

Chapter 8, Project 6: This is a collaboration project with Goldberg's group. The aim of this project is to gain insight into the analogous structure of high-valent metal-hydroxide containing iron and manganese which have been implicated as key intermediates in hydroxylation chemistry. The Goldberg's group did the chemical synthesis, characterization, and kinetic studies of the biomemitic complexes. While, I am responsible to conduct all DFT work present in this project.

Hence, the objective for this study are:

I. To examine the hydrogen atom transfer (HAT) reactivity of a Cpd-II model complex Fe^{IV}(OH)(ttppc)(1),tppcc=5,10,15-tris(2,4,6-triphenyl)-phenyl corrole, towards substituted phenol derivatives.
II. To identify the rate constant of the biomemitc model complexes.
III. To compare the HAT reactivity of Fe^{IV}(OH)(ttppc) complexes to the analogous Mn^{IV}(OH)(ttppc) complex,

Chapter 9, Project 7: Methane hydroxylation by metal-oxo oxidants is one of the Holy Grails in biomimetic and biotechnological applications. There is only few enzymes known to date that perform this reaction in Nature which are iron-containing soluble methane monooxygenase and copper-containing particulate methane monooxygenase. Recent studies reported that μ-nitrido bridged diiron(IV)-oxo porphyrin and phthalocyanine complexes hydroxylate methane to methanol efficiently. In this study, we are trying to remodel analogous structure of μ-nitrido bridged diiron(IV)-oxo porphyrin by replacing the iron with ruthenium.

Hence, the objective for this study are:

I. To investigate whether the reaction rates are enhanced by replacing iron by ruthenium.

II. To analysis the differences of the electronic structure of diiron(IV)-oxo and diruthenium(IV)-oxo complexes

III. To investigate the strength of the O–H bond formation during the reaction.

Chapter 2

METHODS

2.1 QM Modelling: Applications in Enzymatic and Bioinorganic Reactions

Computational chemistry techniques is one of the fruitful approach to solve chemical problems. In computational chemistry, we will try to imitate a model of a chemical system close to its nature and run the simulation by using various software package to meet the objective of research. Nowadays, computational chemistry is becoming an important subdiscipline of chemistry and has been proven in many cases to reveal the bioinformation and mechanistic cycle of enzyme (Ligtenbarg, Hage and Feringa, 2003; Siegbahn and Himo, 2009; Quesne, Borowski and De Visser, 2016). Even, there is Nobel Laureate winner among computational chemistry.

In general, we can divided the computational approaches to three groups which are classical mechanics, molecular dynamics (MD) and quantum mechanics (QM) methods. These three techniques using different mathematical method to tackle their respective problem. The differences between each technique are in term of calculation speed and accuracy. Classical mechanics is the least computationally demanding among all of the methods. One of the advantages of the classical mechanic approach, we can investigate large chemical systems model with more than 100,000 atoms as stationary method by conductiong QM/MM calculation to find optimal reaction paths and stationary points on potential energy surface. To conduct QM/MM calculation, several programs packages are available. For example, for MM calculations, AMBER and CHARMM. While, a widely used software package for QM calculation such as Gaussian. An effective approach to carry out QM/MM calculation that our group used is to connect existing QM (Gaussian) and MM (CHARMM) software packages by an interface program like ChemShell. In addition, classical mechanics can be coupled to MD hence a time-dependent calculation can be performed.

Where, the computational techniques within QM scope are *ab initio*, semi-empirical, and density functional theory (DFT) (Lewars, 2016). QM methods are computationally more

demanding therefore not recommended to be used to calculate chemical systems with a large number of atoms such as an enzymes active site (Lewars, 2016). However with the advancement of current algorithms and technology, modelling of an enzymes active site within 400 atom is doable (Siegbahn and Himo, 2009; Santoro *et al.*, 2016).

Molecular mechanics (MM) describes atoms and bonds in molecules as balls joined together by springs. The energy of each bond, angle and dihedral is then calculated using classical mechanics and summed up to give the overall energy of the system. In MD, Newton's laws of motion describe atoms in molecules in the same way as MM. However, each atom has a directional force applied to it. These techniques is fast and can help us to understand the stability of systems over time, or how two systems interact with one another through non-covalent interactions. As this method do not consider the arrangement or influence of electrons in atoms or chemical bonds hence, the reaction pathway of a chemical system cannot be revealed by this method. Thus make this as one of the limitation. Alternatively, techniques based on the Schrödinger equation is used (Schrödinger, 1926), which better describes electrons (Lewars, 2016).

The Schrödinger equation as shown in Equation 2.1 (Schrödinger, 1926) forms the basis foundation of *ab initio* techniques. *Ab initio* quantum chemistry methods attempt to solve the electronic Schrödinger equation given the positions of the nuclei and the number of electrons in order to reveal useful information of calculated system such as electron densities, energies and other properties of the system (Lewars, 2016). The Eq. 2.1 describes the electrons movement in a system by calculating the energy and wavefunction of each electron present in an atom. However, to solve the Schrödinger equation for multi-electron systems is not an easy task. Therefore, approximations based on QM are applied. Even *ab initio* techniques are accurate approach, however computationally demanding. Thus, the method with less computationally demand were favorable.

The semi-empirical method is faster than the *ab initio* method but slower than molecular mechanics. The semi-empirical is one of method that lies on the Schrödinger equation

(Schrödinger, 1926) and it is parameterised by experimental data. Compared to the *ab initio* method, the semi-empirical method uses more approximations and experimental data to help to calculate the wavefunction and energy of a system. Thus, using semi-empirical methods in systems which have not been experimentally parameterised is discouraged, as it may yield unreliable data (Lewars, 2016).

The final quantum chemical method based on the Schrödinger equation (Schrödinger, 1926) is DFT (Gross & Dreizler, 2013). Even *ab initio* methods are appealing due to their rigorous and systematic treatment of electron correlation effects. However, the *ab initio* is expensive approach with increasing system size. The real distinction between *ab-inito* and DFT is that *ab-initio* methods are wave-function based, while DFT is electronic-function base (Lewars, 2016). The DFT uses electron density function to obtain the quantum chemical properties of the respective system. As the electron density function is less complex than the wavefunction, the computational time for a calculation reduces greatly compared to semi-empirical and *ab initio* methods. In addition, the accuracy of DFT calculation is better to semi-empirical methods led to successful application to a variety of quantum chemistry problems (K. Cheaib *et al.*, 2019; Zeb *et al.*, 2019).

2.2 Fundamentals of Computational Methods

2.2.1 The Schrödinger Equation

French physicist Louis de Broglie in 1923 described electron as both of a particle and a wave known as the wave-particle duality (De Broglie, 1923). The wave-particle duality presents a challenge for physicists trying to understand the nature of electrons. Therefore, a mathematical model describing not only the particle nature but also the wave nature of an electron, led to the invention of the Schrödinger equation (Schrödinger, 1926). The Equation 2.1a shows the time-Independent Schrödinger equation for a one-dimensional motion along the spatial coordinate of x.

$$\frac{d^2\psi}{dx^2} + \frac{2m}{h^2}(\hat{E} - \hat{V})\psi = 0 \quad \text{Eq. 2.1a}$$

Where, the wavefunction (Ψ), represents the amplitude of the particle/wave, the mass of the particle (m), the total energy of the system (E), the potential energy of a particle as a function of its position (V) and Plank's constant (h).

The time-independent Schrödinger equation is widely use in quantum base calculation by describing through the wavefunction. However, the Schrödinger equation does not directly define the wavefunction. Interpretations of quantum mechanics address questions such as what the relation is between the wavefunction, the underlying reality, and the results of experimental measurements (Schrödinger, 1926).

Thus, to extract information from the wavefunction, a mathematical operation need to be applied by squaring the wavefunction (Ψ^2) to generate a probability distribution which is proportional to find an electron near a particular point.

Eq. 2.1a only consider one spatial dimension, despite the real chemical system consists of more than one spatial dimension. Thus, we introduce Eq. 2.1b for system contain N-electrons and M-nuclei of charge Z.

$$H = -\frac{1}{2}\sum_{i=2}^{N} V_i^2 - \frac{1}{2}\sum_{A=1}^{M}\frac{1}{M_A}V_A^2 - \sum_{i=1}^{N}\sum_{A=1}^{M}\frac{Z_A}{r_{iA}} + \sum_{i=1}^{N}\sum_{j>1=1}^{N}\frac{1}{r_{ij}} + \sum_{A=1}^{M}\sum_{B>1}^{M}\frac{Z_A Z_B}{R_{AB}} \quad \text{Eq 2.1b}$$

Then, we need to expand the Eq. 2.1a to three spatial dimension. In order to do So, Laplacian (∇_2) is introduce as shown in Eq. 2.2 which replaces $\frac{d^2}{dx^2}$ in the one-dimensional Schrödinger equation.

$$\nabla^2 = \frac{\partial^2}{\partial x^2} + \frac{\partial^2}{\partial y^2} + \frac{\partial^2}{\partial z^2} \text{ Eq. 2.2}$$

Then, insertion of the Laplacian into Eq. 2.1a will produce Eq. 2.3. Now, the wavefunction is describe by three spatial dimensions:

$$\nabla^2\psi + \frac{2m}{h^2}\left(\hat{E} - \hat{V}\right)\psi = 0 \text{ Eq. 2.3}$$

Then, Eq. 2.3 can be simplify to derive Eq. 2.4,

$$\hat{H}\psi = \hat{E}\psi \text{ Eq. 2.4}$$

Whereby:

$$\hat{H} = -\frac{h^2}{2m}\nabla^2 + \hat{V} \text{ Eq. 2.5}$$

$$\hat{V} = \frac{e^2}{4\pi\varepsilon_o r} \text{ Eq. 2.6}$$

Eq. 2.5 shows the simplified three-dimensional Schrödinger equation, the Hamiltonian $(\hat{H})$ specifies that a mathematical operation is to be performed to the wavefunction (Ψ) which will result in the total energy $(\hat{E})$ of the system being produced. The Hamiltonian ($\hat{H}$) contains the potential energy term of Coulomb interactions ($\hat{V}$) and the kinetic energy

of an electron and a proton. However, the definition of the Hamiltonian ($\hat{H}$) depends on the physical system being described by the Schrödinger equation and as the system increases in variability, the Hamiltonian becomes more complex. Due to the complexity of Schrödinger equation, it is only can be use to solve system that containing of only one-electron such as hydrogen atom ($H^{\cdot}$), helium monocation ($He^{\cdot}$) and hydrogen molecule ion ($H^{2+\cdot}$). However, for systems with more than one electron, the assignment of electrons to particular orbitals is an approximation based on the solution for the hydrogen atom.

As the size of a system increase, the Schrödinger equation becomes more complex. This problem namely as Many-Body-Problem. It states that, for systems consist of more than one atom and one electron, the solution to the Schrödinger equation is dependent on both the atomic nuclei ($R_1 \ldots R_N$) and the electrons ($r_1 \ldots r_N$) as shown in Eq. 2.7 (Gross and Dreizler, 2013; Lewars, 2016).

$$\hat{H}(R_1 \ldots R_N; r_1 \ldots r_N)\psi(R_1 \ldots R_N; r_1 \ldots r_N) = \hat{E}\psi(R_1 \ldots R_N; r_1 \ldots r_N) \quad \text{Eq. 2.7}$$

Whereby R is the spatial coordinate of each nuclei and r is the spatial coordinate of each electron. Therefore, the complexity of Hamiltonian function increase for larger systems, as it need to sum of all possible interactions between electrons and nuclei in a system. Then to simplify this equation, the Born-Oppenheimer approximation (Born and Oppenheimer, 1927, 2000) were introduced.

2.2.2 Born-Oppenheimer Approximation

As solving Many-Body-Problem by using Schrödinger equation is not an easy task, indeed approximations are necessary. The Born-Oppenheimer approximation are needed to calculate an approximate wavefunction (Born and Oppenheimer, 1927, 2000). In computational work, wavefunction or known as molecular orbital is a mathematical function describing the wave-like behaviour of an electron in a system. This function can

be used to calculate chemical and physical properties such as the probability of finding an electron in any specific region. The term *orbital* was introduced by Robert S. Mulliken in 1932 as an abbreviation for *one-electron orbital wave function* (Mulliken, 1932) which is used to describe the region of space in which the function has a significant amplitude. Molecular orbitals are constructed by combining atomic orbitals or hybrid orbitals from each atom of the molecule, or other molecular orbitals from groups of atoms. It can be quantitatively calculated using the Hartree-Fock or self-consistent field (SCF) methods (Lewars, 2016).

In Born-Oppenheimer approximation, it separates the motion of atomic nuclei from the motion of electrons. The reason for doing so because an atomic nucleus is over 1000 times heavier and moves slower than an electron. Where the mass of nucleus is 1.673×10^{-27} kg and the mass for electron is 9.109×10^{-31} kg, respectively. As acceleration is inversely proportional to mass, the acceleration of an electron is much greater than the atomic nuclei thus the nuclei can be assume as stationary (Born and Oppenheimer, 1927, 2000).

The Born-Oppenheimer approximation separates the Schrödinger equation into nuclear and electronic components.

Eq. 2.8 shows the nuclear Schrödinger equation:

$$\hat{H}_{nuc}(\boldsymbol{R})\Psi_{nuc}(\boldsymbol{R}) = \hat{E}_{nuc}(\boldsymbol{R})\Psi_{nuc}(\boldsymbol{R}) \qquad \text{Eq. 2.8}$$

Where, **R** is the variable positions of the atomic nuclei.

Eq. 2.9 shows the electronic Schrödinger equation which is the foundation of many quantum mechanical methods such as the Hartree-Fock approximation (Hartree, 1928) and DFT (Gross and Dreizler, 2013):

$$\hat{H}_{ele}(\boldsymbol{r},\boldsymbol{R})\Psi_{ele}(\boldsymbol{r},\boldsymbol{R}) = \hat{E}_{ele}(\boldsymbol{R})\Psi_{ele}(\boldsymbol{r},\boldsymbol{R}) \qquad \text{Eq. 2.9}$$

Where **R**, represents atomic nuclei with fixed parameters and **r** represents the variable positions of the electrons. Thus, the electronic wavefunction depends on the nuclei position and is a function of each set of spatial variables for each electron in a system.

Then, the Hamiltonian is simplified to Eq. 2.10 comprimising nuclei (*N*) and electrons (*n*).

$$\widehat{H} = -\frac{h^2}{2m}\sum_{i=1}^{n}\nabla_i^2 - \sum_{I=1}^{N}\sum_{i=1}^{n}\frac{Ze^2}{r_{i,I}} + \sum_{i=1}^{n}\sum_{j=1}^{n'}\frac{e^2}{r_{i,j}} \quad \text{Eq 2.10}$$

Where Z is the nuclear charge, r is the electron position and R is the nuclei (Lewars, 2016). In Equation 2.10, the first term is the kinetic energy of the electron, the second term is the electron nuclear attraction, and the third term is the interaction of the electrons present in a system (Lewars, 2016). Later, Hartree-Fock Approximation is introduce to simplify the Eq. 2.10.

2.2.3 Hartree-Fock Approximation

To solve Schrödinger equation for larger systems is not an easy task as it describes the electronic wavefunction of all electrons. However, the Hartree Approximation simplifies the electronic wavefunction by giving each electron a separate wavefunction (Hartree, 1928). The individual wavefunctions are then multiplied together to produce the total wavefunction namely the Hartree product (Hartree, 1928). By using Hartree Approximation, it will produces a set of Schrödinger equations for each electron whose wavefunction is dependent on the position of every other electron in the system.

Therefore, to solve the wavefunction for one electron, a self-consistent approach has to be used. First, the self-consistent approach uses an initial guess for the wavefunction to solve the equation. Once the equation is solved using the initial guess, the output of wavefunction is compared to the input wavefunction. If they differ, the output wavefunction becomes the new initial wavefunction, and the cycle repeats. However,

when the output wavefunction is the same as the input wavefunction, the electron consider to be close to its ground state (Gross and Dreizler, 2013; Lewars, 2016).

Later, Fock in the 1930's improvise upon the Hartree Approximation (Fock, 1930) producing the Hartree-Fock Approximation (HF). The HF introduced elements of spin and symmetry into the equation by including an exchange energy term ensuring that no two electrons with the same spin could be in the same space following Pauli Exclusion Principle (Duck, Pauli and Sudarshan, 1997) where the electron-electron repulsion make the total energy of a system become lower (Duck, Pauli and Sudarshan, 1997; Gross and Dreizler, 2013; Lewars, 2016).

The HF is categorised as a wavefunction based approach, however the computational cost associated with these calculations increases significantly with the size of the system. Hence, it makes the calculation of systems that have just tens of electrons become sluggish. Alternatively, DFT do not suffer this problem (Gross and Dreizler, 2013; Lewars, 2016) and become one of favourable choice. DFT have capability to handle of calculations of thousands electrons. In addition, most DFT methods do include some element of the HF particularly in the exchange-correlation functional.

2.3 Density Functional Theory

As previously discussed in Section 2.2, the Many-Body Problem creates difficulty for solving the Schrödinger equation. To overcome the Many-Body Problem, approximations either the wave-function base or the density-function base will be chose. Despite, the wave-function based methods are more accurate compared to density-function based methods. However, the computational cost of running large chemical system increases exponentially with increasing system size (Lewars, 2016).

In wavefunction base methods, it separate the total electronic wavefunction into individual electron wavefunctions. Thus make the total wavefunction base methods is a function of 3N variables, with N defined as the number of total electrons in the system. To understand better, let's take oxygen molecules as example which consist of 16 electrons.

Therefore the total wavefunction consists of 48 dimensions. Even the density functional base methods are less complex compared to wave-function base methods but the DFT is still accurate where the deviation is only within few kcalmol^{-1} off with the actual value led to its implementation to a broad range of QM procedure.

The density functional methods is based on the summation of total electron density ($n(\boldsymbol{r})$) as shown in Eq. 2.11. The total electron density is directly related to the sum of the square of each individual electronic wavefunction (Ψ^2).

$$n(\boldsymbol{r}) = 2\sum_i \psi_i^2 \quad \text{Eq. 2.11}$$

In DFT, finding the ground state electron density is the main focus to solve Schrödinger equation (Hohenberg and Kohn, 1964). DFT consider that from the ground state electron density, the ground state energy of a system can be found. The self-consistent method are use to find the ground state electron density akin to that used in the HF. In general, the self-consistent method can be simplified to four steps as described as below (Sholl and Steckel, 2011; Lewars, 2016):

A – First, an initial trial of total electron density ($n_{ini}(r)$) is defined.
B – Second, using $n_{ini}(r)$, a set of individual electronic wavefunctions ($\psi_{ini}(r)$) are calculated using the Kohn-Sham equations.
C – Third, using, $\psi_{ini}(r)$ a new total electron density is calculated ($n_{new}(r)$).
D – Fourth, $n_{new}(r)$ is compared with $n_{ini}(r)$, if they are the same then the ground state electron density has been found and the ground state energy can be computed. If not, then $n_{ini}(r)$ needs to be updated and the cycle starts again from step B.

Even the DFT are computationally less demanding compared to other method mention, however its still have its own limitation. To date, DFT only able to handle chemical

systems within the limit of 1000 atoms. It is not recommended to analyse systems with more than 1000's of atom compared with MM and MD (Lewars, 2016) as not computational-wise method. Thus, the objective of calculation need to align with the method chosen.

2.3.1 The Foundation of Modern DFT

The foundation of modern DFT methods are involving two theorems proposed by Hohenberg and Kohn (Hohenberg and Kohn, 1964) and the Kohn-Sham (Kohn and Sham, 1965). According to the Hohenberg-Kohn theorems as shown in Eq. 2.12, the ground-state of electronic energy of a system is uniquely defined by its electron density ($\rho(\mathbf{r})$), and there exists a variational principle that any trial density ($\rho'(\mathbf{r})$) will result in an energy higher than or equal to the exact ground-state energy.

$$E[\rho'(\boldsymbol{r})] \geq E[\rho(\boldsymbol{r})] \qquad \text{Eq. 2.12}$$

The electronic energy as shown in Eq. 2.13 is expressed as the sum of three different terms, which are the kinetic energy of the electrons ($\boldsymbol{T}$), the nuclear-electron attraction ($\boldsymbol{V}_{ne}$) and the electron-electron repulsion ($\boldsymbol{V}_{ee}$).

$$E[\rho(\boldsymbol{r})] = T[\rho(\boldsymbol{r})] + V_{ne}[\rho(\boldsymbol{r})] + V_{ee}[\rho(\boldsymbol{r})] \quad \text{Eq. 2.13}$$

While, $\boldsymbol{V}_{ee}$ contains two components which are the classical Coulomb repulsion ($\boldsymbol{J}$) and all non-classical contributions to the electron-electron repulsion ($\boldsymbol{V}_{\boldsymbol{ee}}$).

The Kohn–Sham equation is the one electron Schrödinger equation of a fictitious system of non-interacting particles that generate the same density as any given system of interacting particles (Kohn and Sham, 1965). The Kohn–Sham equation is defined by a local effective (fictitious) external potential in which the non-interacting particles move, denoted as $v_s(\mathbf{r})$ or $v_{\text{eff}}(\mathbf{r})$, called the Kohn–Sham potential (Kohn and Sham, 1965). As the particles in the Kohn–Sham system are non-interacting fermions, the Kohn–Sham

wavefunction is a single Slater determinant constructed from a set of orbitals that are the lowest energy solutions.

While, within the Kohn-Sham formalism as shown in Eq. 2.14, the density is expressed in terms of orbitals (φ_i), while the kinetic energy of the electrons ($\boldsymbol{T}$) is divided into two parts (Kohn and Sham, 1965).

$$p(\boldsymbol{r}) = \sum_{i=1}^{N} |\emptyset_i(\boldsymbol{r})|^2 \qquad \text{Eq. 2.14}$$

$$E[\rho(\boldsymbol{r})] = T_{ni}[\rho(\boldsymbol{r})] + V_{ne}[\rho(\boldsymbol{r})] + J[\rho(\boldsymbol{r})] + E_{XC}[\rho(\boldsymbol{r})] \quad \text{Eq. 2.15}$$

One part represents the kinetic energy of a fictitious system of non-interacting electrons ($\boldsymbol{T}_{ni}$) and another part represents the difference in kinetic energy between the fictitious non-interacting system and the real system. The latter is a correction term which grouped together with all non-classical contributions to the electron-electron repulsion into an exchange correlation energy term ($\boldsymbol{E}_{xc}$).

Eventhough DFT is an exact theory, only approximate solutions to the electronic energy can be obtained. Due the exact expression of the exchange-correlation functional, $E_{XC}[\rho(\mathbf{r})]$ is unknown. Later, various DFT methods have been developed and proposed by theoretician chemist in order to describe this exchange-correlation energy.

2.3.2 The Kohn-Sham Equation

The Kohn-Sham equation as shown in Equation 2.16 is one of a breakthrough solution to determine the ground state electron density and ground state energy of a system. The

Kohn- Sham equation is responsible for calculating the individual electronic wavefunction using the initial trial of total electron density.

$$\left[-\frac{h^2}{2m}\nabla^2 + V(r) + V_H(r) + V_{XC}(r)\right]\psi_i(r) = \varepsilon_i\psi_i(r) \quad \text{Eq. 2.16}$$

Where the term $\Psi(r)$, represents the individual electronic wavefunction as a function of three spatial coordinates in x,y and z dimension, and εi represents the orbital energy of the corresponding Kohn–Sham energy levels.

On the left hand side of the equation is the kinetic energy of an individual electron and few potential energy terms. The first potential energy term, V(r) is the interaction between an electron and the atomic nuclei. The second potential energy term, $V_H(r)$ is the electronic repulsion between the individual electron and the total electron density, also known as the Hartree potential. The third potential energy term, $V_{XC}(r)$, is the exchange-correlation energy term (Sholl and Steckel, 2011; Lewars, 2016).

In order to calculate the $V_H(r)$, it is important to get the information of total electron density as it show coulomb interaction between the individual electron and the total electron density. However, requiring a total electron density creates a problem when calculating the ground state electron density. To solve the problem, the calculation of trial electron required at the beginning of the self-consistent calculation. The default method of defining the initial trial electron density is by superimposing the electron densities for each atom in its isolated state. However, the speed of a calculation can be increased by using a better initial approximation from a previous calculation (Sholl and Steckel, 2011; Lewars, 2016).

While, the exchange-correlation potential, $V_{XC}(r)$, and its exact definition are known for systems with a uniform electron gas. Therefore, in the majority of scenario the exchange-correlation potential is an approximation value. Neverthless in DFT, it is important to choose correct exchange-correlation function because the solution of the

Schrödinger equation is depend on it. Therefore as precautionwhere, it is necessary to benchmark any computational results from DFT with experimental data (Sholl and Steckel, 2011; Lewars, 2016).

2.3.3 The Exchange-Correlation Potential

The exchange energy is the interaction between electrons with parallel spins and prevents two parallel-spin electrons from being found at the same point in in accordance with the Pauli Exclusion Principle (Sholl and Steckel, 2011; Lewars, 2016). While, the correlation energy is a measure of how much the movement of one electron influenced by the presence of all other electrons in the system. In any calculation, it is important to show a good exchange-correlation functional that relates the electron density of a system to the exchange-correlation energy for one electron.

The exchange-correlation functional is an approximated value and it only contributes small fraction of energy to the total energy of a system. However, the exchange-correlation term is necessary for the accurate description of binding between atoms. Despite its lack of contribution in terms of total energy, yet it is important to still try and get the most accurate description of the exchange-correlation energy found in the exchange-correlation functional. Typically, the exchange-correlation functional is separated into two part which are exchange and correlation parts which are then summed together. As example, in the B3LYP functional as described in Eq 2.18, the B3 denotes the use of the Becke 88 exchange function (Becke, 1993), and the LYP, the Lee, Yang, and Parr correlation function (Lee, Yang and Parr, 1988).

Figure 2.1 show Jacob's ladder scheme several different functionals varying in complexity illustrated using Jacob's ladder (Perdew *et al.*, 2005). The Jacobs ladder scheme groups the DFT functions according to their complexity. Beginning from the Hartree Approximation to exact exchange-correlation function. Ascending from the Hartree Approximation, is the local density approximation (LDA), the generalised

gradient approximation (GGA), the meta-GGA, the hybrid-GGA, and the hybrid-meta-GGA. The exchange-correlation functionals can be further classified as either empirical or non-empirical. Empirical functionals are formulated by fitting to the known experimental results. While, non-empirical functionals are formulated only by satisfying some physical rules (Sholl and Steckel, 2011; Lewars, 2016). While, the meta-GGA functional is an improvement over the GGA by allowing the exchange and correlation functionals to be derived from the second derivatives of Kohn-Sham orbitals.

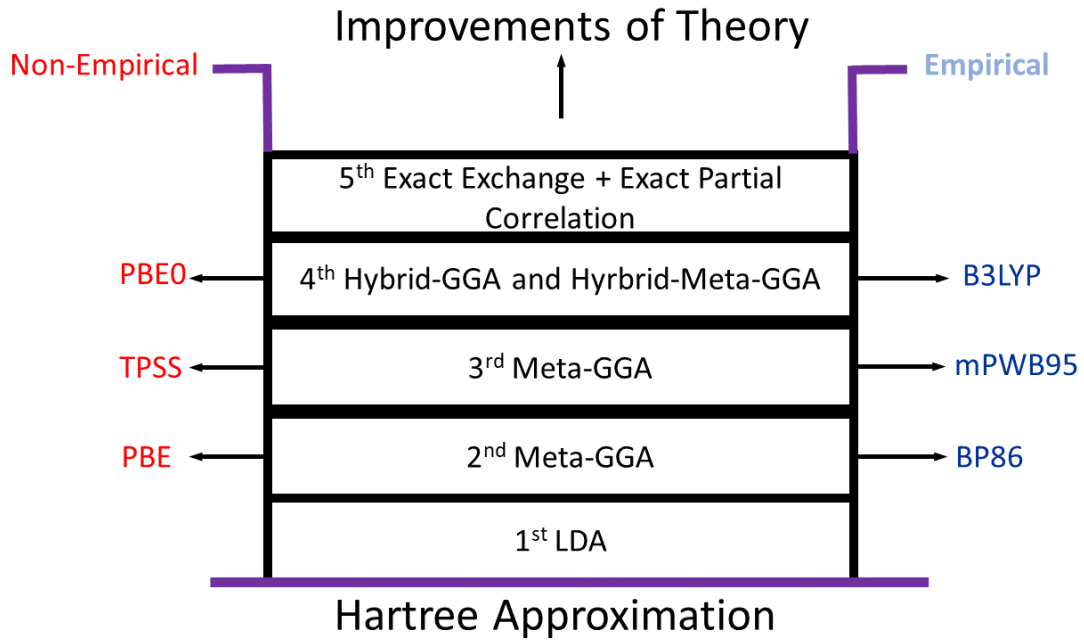

Figure 2.1. The Jacob's ladder categorisation of the various exchange-correlation terms by Perdew (Perdew *et al.*, 2005), with the least complex on bottom and the exact exchange-correlation on top.

The overall of exchange correlation energy, $E_{xc,}$ is the summation of DFT exchange energies, energy from HF theory and DFT correlation energies. Eq. 2.17 and Eq. 2.18 shows the ratios of the different exchange and correlation functions mixed together in PBE0 (Adamo and Barone, 1999) and B3LYP (Becke, 1988, 1993; Lee, Yang and Parr, 1988) hybrid functionals, respectively.

$$E_{xc}^{PBE0} = 0.25E_x^{HF} + 0.75\Delta E_x^{PBE} + E_c^{mPW91} \qquad \text{Eq. 2.17}$$

$$\mathrm{E_{xc}^{B3LYP} = 0.8E_x^{Slater} + 0.2E_x^{HF} + 0.72\Delta E_x^{Becke} + 0.19E_c^{VWN} + 0.81E_c^{LYP}} \qquad \text{Eq. 2.18}$$

The difference between each of the DFT functionals exist so far, is how many variable describing the electron of a system like BP86 (Perdew, 1986; Becke, 1988). However, by including more variables into the exchange-correlation functional will increase computational cost.

2.3.4 The B3LYP Functional

One of mostly used exchange-correlation functionals in this thesis is the B3LYP (Lee, Yang and Parr, 1988; Becke, 1993; Stephens *et al.*, 1994) as per Eq. 2.19.

$$E_{xc}^{B3LYP} = (1-a)E_x^{LSDA} + aE_x^{HF} + b\Delta E_x^{B88} + cE_c^{LYP} + (1-c)E_c^{VWN} \qquad \text{Eq. 2.19}$$

The functional is composed of different terms. $E_{\mathrm{x}}^{\mathrm{LSDA}}$ is the exchange functional according to the local spin density approximation (LSDA) derived for the uniform electron gas, and $\Delta E_{\mathrm{x}}^{\mathrm{B88}}$ is the gradient correction to the LSDA exchange, as proposed by Becke (Becke, 1988). E_{c}^{VWN} and cE_{c}^{LYP} are two correlation functionals, developed by

Vosko, Wilk, and Nusair (Vosko, Wilk and Nusair, 1980), and Lee, Yang and Parr (Lee, Yang and Parr, 1988), respectively. The E_x^{HF} is the exact HF exchange energy. The parameters *a*, *b* and *c* were determined to 0.20, 0.72 and 0.81, respectively, by fitting to experimental data.

2.4 Basis Set

In DFT calculation, atomic orbitals are described by basis functions. The basis functions are mathematical descriptions of space in order to solve Schrödinger equation. Then, the basis functions are then grouped to form a basis set. The chosen of good basis set is one of factor lead to accuracy of energy thus will reflect the final result as it gives a better description of atomic orbitals and molecular orbitals (Sholl and Steckel, 2011; Lewars, 2016).

To date, most of the basis sets exist developed by Slater Type Orbital (STO) (Slater, 1930) or Gaussian Type Orbital (GTO) (Boys, 1950) calculation per Eq. 2.20 and Eq. 2.21 respectively. Both method rely on Linear Combination of Atomic Orbitals (LCAO) method. Each STO and GTO can be describes as the "basis set" in any computational software packages. Although STOs are more accurate functions to describe the electron wave function however the computational cost is higher of using these funtions over equal accuracy achievable with a higher number of Gaussian Function at less computation cost. Thus GTOs is one of the alternative in modern calculation (Cramer, 2013).

$$R(r) = r^{n-1}e^{-\frac{(Z-s)}{n*}r} \qquad \text{Eq. 2.20}$$

$$R(r) = r^{n-1}e^{-\frac{(Z-s)}{n*}r^2} \qquad \text{Eq. 2.21}$$

where *s* is a shielding constant, *n* is natural number that varies with the principal quantum number *n*, and $\zeta = (Z\text{-}s)/n^*$ is the effective nuclear charge of the nucleus. While the values for *s* and *n** are determined by the Slater's rule (Slater, 1930; Mueller, 2007).

In LCAO method, the molecular wave functions is represented by the summation of linear combination of atomic orbitals.

To understand further, let have a look at the Eq. 2.23:

$$\psi_i = C_{\mu i}\phi_\mu \quad \text{Eq. 2.23}$$

One would like to take the mentioned basis sets φ_μ with specific pre-exponential and exponential factors depending on the elemen and atomic orbital. Then only linear coeffiecent of $C_{\mu i}$ would need to be optimized to describe each molecular orbital ψ_i as presented in Eq. 2.23, where φ consist the atomic orbital basis set, ψ_i is the i^{th} molecular wave function.

However, the STO functions are centred on each nucleus, it is computationally demanding to integrate those functions. Instead, GTO and a linear combination of Gaussian functions (Mueller, 2007) more favourable option. The computation time for latter method greatly reduced than in STO due to the fact that two Gaussian functions centred at two different nuclei is equal to a single Gaussian centred at a third point (Mueller, 2007).

2.5 Effective Core Potential

In a chemical reaction, only valence electron will interact to make a reaction. While, the core electrons of an atom or molecules do not take part in chemical reactions. However, the core electron are needed to expand the wavefunctions into the valence orbitals. Their absence would remove the inter-electronic repulsions required for better valence orbital description. Especially in heavy metals, the core electrons contribute to relativistic effects. Therefore, rather than including all electrons in the wavefunctions, they are treated simultaneously at two different levels. The first is to represent the core electrons with a

suitable function and second, to treat the valence electrons explicitly (Jensen, 2007). As example, Vanadium atom consist of 23 electron with the arrangement of $1s^2 2s^2 2p^6 3s^2 3p^6 \mathbf{3d^3 4s^2}$. Thus, 5 electrons (in bold) will considered explicitly while others are represented as a core potential. This approach will good results even at low computational cost and also relativistic effects are accounted (Lewars, 2016).

2.6 Geometry Optimization using DFT

In order to reveal mechanistic cycle of a chemical system, the characterisation of reactants, intermediates, products and the various transition states is a must. In most cases, solving chemical problems involves optimizing all molecular structures of the minimum energy points on the potential energy surface (PES). The stationary points are the points where the gradients of the first derivatives of the energy with respect to the nuclear coordinates are equal to zero. When the gradient is zero at the time the eigenvalues are all positive, then the corresponding structure is already at a local minimum.

Contrary, when the gradient of curvature is negative but positive in all the other directions, then it is a first order saddle point. At this point, we can identify the TS structure (Atkins and Friedman, 2011). For a linear molecule, it is sufficient to illustrate PES in two-dimensional plot as the energy of molecule structure varies by only changing inter-nuclear distances instead the PES for large system would be multi-dimensional based on the degrees of freedom within the molecule (Foresman and Frisch, 1996; Lewars, 2016). Therefore, there is more than one minima structure possible exist in large system however the optimization algorithms would only consider global minimum as stationary points.

Figure 2.2 represents a three-dimensional of a PES of the reaction landscape for a system. Clearly, the reactants and intermediates are always in local minima and connected through transition state. The stationary points are the points where the gradients of the first derivatives of the energy with respect to the nuclear coordinates are equal to zero.

The goal of doing a geometry optimisation is to characterise a SP on the PES which could be either a local minimum, or a transition state. To perform this calculation, an input structure is chosen that resembles the desired points of coordinates. Later, the input file submitted to any QM software packages such as Gaussian 09. DFT calculates the energy of the complex and moves forward on the PES however this may not correspond to the local minimum energy structure. Its energy and gradients are computed at that point and they determine the extent and direction of the calculation. Usually the gradients point to the rapidly decreasing energy from the current coordinates and steepness of its slope.

An optimisation algorithm systematically changes the geometry until it has found a SP corresponding to the minimum or transition state structure (Lewars, 2016). Therefore, the overall process consists of a self-consistent calculation in DFT to identify the ground state electron density and energy with regard to the input geometry. The geometry is then altered and the process is repeated until the system has reached a state of convergence. Some optimization algorithms involve calculating the second derivatives and storing the Hessian (force constant matrix) which may determine the next step of minimization (Lewars, 2016).

These optimisation algorithms are complex associated with their efficiency. During the optimisation, the algorithm uses the first and second derivatives of the energy with respect to the geometric parameters. To understand this more clearly, at the end of each SCF cycle during a DFT calculation an electron density is generated which is related to the sum of the individual electronic wavefunctions associated with three spatial variables. From the individual electronic wavefunctions the energy can also be calculated, therefore, the energy with respect to each geometric parameter is able to be calculated. However, this is no small task and results in a multitude of linear equations that need processing. One way to process a collection of linear equations is by using a mathematical matrix, which is a tool to easily manipulate and extract valuable information from a collection of linear equations (Lewars, 2016).

Furthermore, for an efficient geometry optimisation, the algorithm uses the first and second derivatives of the energy with respect to the geometric parameters, represented in matrices. The first derivative matrix is called the gradient matrix. The second derivative matrix is generated from the first and is called the force-constant matrix, also known as the Hessian (Lewars, 2016). The gradient matrix is a guess calculated using the molecular orbitals which are generated from the basis sets. The geometric variables are then altered, and for the new geometry, a new gradient and Hessian are calculated. This process continues until the geometry, energy, and gradient have ceased to change appreciably. At this point, the system is said to be converged (Lewars, 2016). In addition, during a geometry optimisation, it is standard protocol to perform an optimisation with a lower level basis set and then follow this up with an additional optimisation or single point using a higher level basis set reading in the previously generated gradient and Hessian as a starting point which widely been used in this thesis (Lewars, 2016).

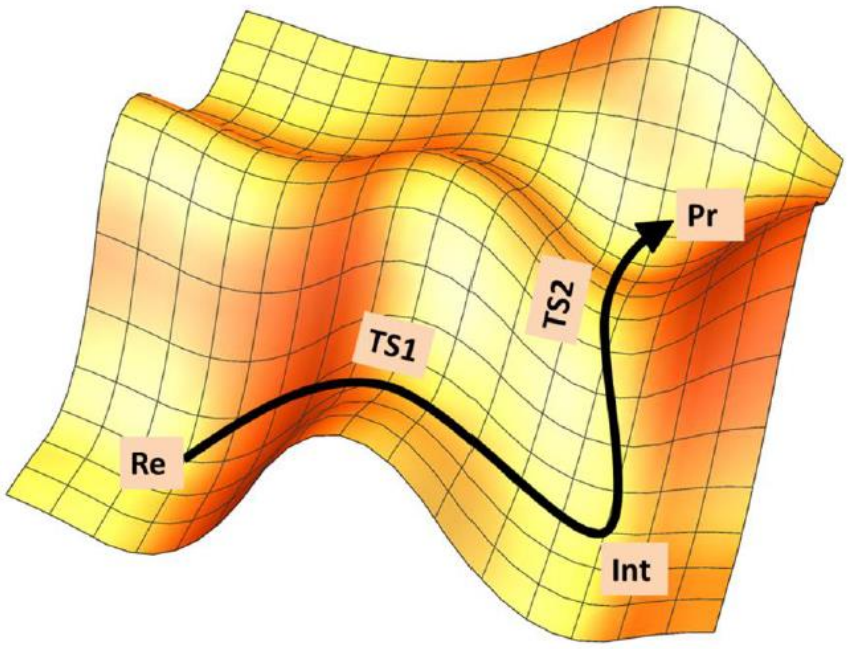

Figure 2.2. A three-dimensional representation of a potential energy surface of the reaction landscape for a system where labelled as reactant (Re), transition states (TS), intermediate (Int), product (Pr). There are many pathways lead to product from reactant however, the lowest is shown here.

2.7 Transition State Theory-Reaction Mechanism from PES

There are many different methods to identifying a possible transition state of reaction. One of the technique is to perform a relaxed PES scan involves fixing a degree of freedom of either bond length, angle or dihedral in stepwise steps between two intermediate. Then, the results of a PES scan consist of two minima connected with the highest energy called as transition state (TS) or activated complex (Lewars, 2016).

Figure 2.3 represents a relaxed PES of the O-O bond cleavage for one of reaction occur in heme haloperoxidase mechanism (Chapter 3). In order to confirm the structure of the local minima and TS, the respective coordinate taken from PES and an optimisation of structure is performed. During a transition state optimisation, the Hessian is calculated as for a normal optimisation. Instead of the atoms moving in a direction which decreases the overall energy but, the atoms will move to a direction which increases the energy along one degree of freedom. Further, a frequency calculation or vibrational analysis need to be perform to identify imaginary frequency to validate the TS structure (Lewars, 2016).

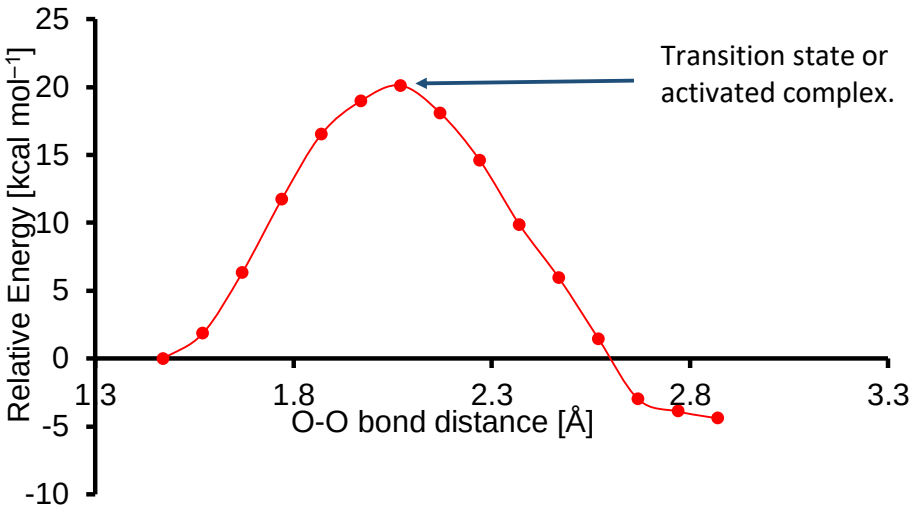

Figure 2.3. A relaxed PES scan of O-O bond breaking for the heme haloperodise.

Transition state theory (TST) is mathematical relationship that relates the rate constant (k) of a chemical reaction to the free energy of activation $\Delta G^{\ddagger}$ for the reaction as per Eq. 2.24.

$$k = \left(\frac{k_B T}{H}\right) e^{(-\Delta G\ddagger/RT)} \quad Eq.\ 2.24$$

Where

T = temperature,

R = gas constant,

H = Planck constant and

k_B = Boltzmann constant.

In the energy graph of a reaction, $\Delta G^{\ddagger}$ corresponds to the barrier from the lowest energy point to the highest transition state along a specic reaction pathway defined as the rate-limiting step (RDS). Thus, different pathways of a chemical reaction can be compared on the basis of their calculated barriers, and most favourable mechanisms can be confirm.

2.8 Zero Point Correction

The minimum total energy of optimized geometry is not the actual absolute value but only an electronic energy (E_e). Thus, it needs to be corrected by including zero-point energy (ZPE) to give the 0 K enthalpy of the chemical system. In reality, the nuclei or electrons are constantly in motions even at absolute temperature. Thus, there are entropy contributions from translational, rotational, and vibrational motion of electron. However, translational and rotational motions of nuclei can be ignore as it contribute insignificant values of energy (Lewars, 2016).

While, vibrational motions considered to be the most significant entropy contribution and can be obtained through frequency calculations. Later, this value is added to the E_e to give the actual total energy (*E*) as per Eq. 2.25 at 0 K (Foresman and Frisch, 1996; Leach, 2001).

$$E = E_e + ZPE \qquad \text{Eq. 2.25}$$

Further, under standard conditions temperature and pressure (298.15 *K* and 1 atm), other thermodynamic quantities like enthalpy, entropic contributions, and Gibbs free energy can be estimated by frequency calculations and added to the electronic energy (Frisch, Hratchian and Nielsen, 2009; Lewars, 2016).

2.9 Dispersion Correction Effect

In fact, the DFT struggles to describe the weak van der Waals (VdW) interactions exist between molecules in a calculated system. The VdW interactions are a direct result of long range electron correlations due to temporary fluctuations of the electron density of molecule (Grimme, 2011; Grimme *et al.*, 2016). Since, the London dispersion effects exist on all chemical system but the effects is more significant for larger system. One way to to describe VdW interactions is by using high-level wavefunction based methods which treat the electron correlation in a more appropriate way. However, this approach is not recommended as it will increase the computational resource.

Over the years, few methods have been developed incorporate dispersion interactions into DFT calculation. One of popular dispersion corrections (E_{disp}) method is by using DFT-D3 method as shown in Eq. 2.27 (Grimme, 2011; Grimme *et al.*, 2016). The E_{dis} works by adding a dispersion energy contribution to the energy obtained from previous calculation as shown in Eq. 2.26 (Grimme, 2011; Grimme *et al.*, 2016).

$$E_{DFT-D3} = E_{DFT} + E_{disp} \qquad \text{Eq. 2.26}$$

In this thesis, E_{disp} were calculated using DFT-D3 methods, which are based on an atom-pairwise additive treatment of the dispersion energy.

$$E_{disp}^{DFT-D3} = -\sum_{AB}\sum_{n=6,8,10,\ldots} S_n \frac{C_n^{AB}}{R_{AB}^n} f_{damp}(R_{AB}) \quad \text{Eq. 2.27}$$

The dispersion correction obtained as a sum over all atom pairs in the system, where R_{AB} is the interatomic distance, and C_n^{AB} are dispersion coefficients for the atom pair *AB*. S_n is scaling factors that are chosen for each density functional, while f_{damp} are damping functions that determine the behaviour at short interatomic distances. The addition of dispersion corrections to B3LYP calculated energies showed to provide improvement of the accuracy for various types of energies as well as being able to reproduce experimental data (Minenkov, Occhipinti and Jensen, 2009).

2.10 Computational Strategy: Level of Theory

The size and chemical nature of a chemical system will determine the selection of methods and basis sets need to be used. The selection of appropriate method and basis set leads to good results in any calculation. One of recommended approach is by explore the PES of a system with a small basis set. Later, larger basis set is introduce to estimate energy and describe various molecular properties. This approach leads to computational savings and research-quality results and have been implemented in many study of ours (Mueller, 2007; Khaled Cheaib *et al.*, 2019; Mubarak and De Visser, 2019a, 2019b).

2.11 Energy Graphs

One of a must part in quantum chemical is to suggest mechanistic cycle of a system studied. Thus, the construction of energy graphs is one of helpful way to visualize and understand the different reaction pathways revealed in the chemical reaction. In energy

graphs, we are able to show the energy barriers associated with each pathways. Figure 2.4 is a simplification of the multidimensional energy describes the energy of a methane hyroxylation by ruthenium complex. Detailed information of methane hydroxylation by ruthenium complexes will be further discussed in Chapter 9.

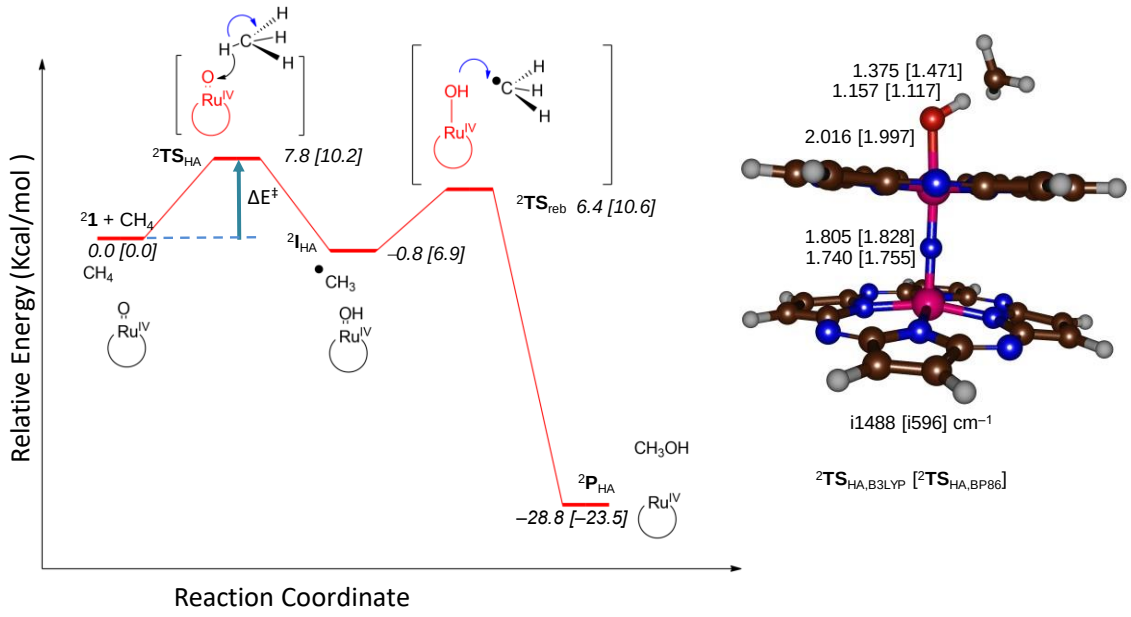

Figure 2.4. Hypothetical energy profile of methane hydroxylation by Ruthenium complex in two-dimensional.

In Figure 2.4, the path from reactant to product with the lowest energy involved is indicated in red. In this two-dimensional energy profile, the stationary points, intermiediate and transistion state reveal in the calculation are indicated with horizontal lines. While, the highest energy is always associated to transition state structure. The energy barrier between reactant and first transition state denoted as $\Delta E^{\ddagger}$ is the rate determining step for this calculation. By creating this energy landscpae, a chemical

reaction can be visualized as a series of geometrical changes resulting in the transformation of reactants into products and the changing of energy between reactant to product can be well described.

2.12 Enzyme Catalysis and Kinetics

Enzymes are able to enhance the rate of reaction of chemical reactions by lowering the free energy of activation ($\Delta G^{\ddagger}$). Even the origin of the catalytic power of an enzymes remain unknown, but it was suggested, the amino acid residues around the active site will pre-organized to stabilize the transition state by electrostatic effects (Warshel, 1998). The catalytic power of an enzyme ca be defined as per Eq. 2.27.

$$\Delta G^{\ddagger} = \Delta G^{\ddagger}_{uncat} - G^{\ddagger}_{cat} \quad \text{Eq. 2.27}$$

Where the uncatalyzed reaction is in solution.

Then, to have better understanding about the enzymes, let's have look at Eq. 2.28 which describes how the enzyme work in real environment.

$$E + S \leftrightarrows E.S \rightarrow E + P \quad \text{Eq. 2.28}$$

First, a substrate (S) will binds to an enzyme (E) to form an enzyme-substrate complex (E·S). Then, E·S is converted to product (P), regenerating the free enzyme. The efficiently of enzyme is dependent on the concentration of each component.

The Michaelis-Menten equation as show in Eq. 2.29 describe the kinetics of enzyme-catalyzed reactions. Where, the rate of product formation is defined by the Michaelis-Menten as shown in Eq. 2.29, where K_M is Michaelis constant and $[E]_T$ is the total concentration of enzyme.

$$v = \frac{d[P]}{dt} = k_{cat}\,[E.S] = \frac{k_{cat}\,[E]_t[S]}{K_M + [S]} \quad \text{Eq. 2.29}$$

$$K_M = \frac{k_{-1} + k_{cat}}{K_1} \quad \text{Eq. 2.30}$$

For situation when the substrate concentration is low, $[S] << K_M$, we are using Eq. 2.30 to solve the problem. Under these conditions, assumption of $[E]_T \approx [E]$ been made. It is because most enzymes molecule are free and do not have a substrate to bind in the active site. Then, k_{cat}/K_M is used to measure the enzyme's preference for different substrates. Besides, k_{cat}/K_M indicates the catalytic efficiency of enzyme under non-saturating condition.

$$v = \frac{k_{cat}}{k_M} = [E]_T[S] = \frac{k_{cat}}{K_M}[E][S] \quad \text{Eq. 2.31}$$

While, if the concentration of substrate is high in solution, another assumption been made, where the $[S] >> K_M$. Thus, modify the Michaelis-Menten equation as per Eq. 2.31.

$$v = V_{max} = k_{cat}[E.S] = k_{cat}[E]_T \quad \text{Eq. 2.32}$$

Here, we assume that $[E{\cdot}S] = [E]_T$ as all enzymes have a substrate thus the enzyme become saturated. It's made the reaction rate is equal to the maximum rate, where k_{cat} is the overall rate constant. Then, by using transition state theory, a theoretically-determined energy barrier for a particular enzymatic reaction can be compared with an experimentally determined k_{cat}, if the data is available.

Chapter 3

PROJECT 1

Computational Study on the Catalytic Reaction Mechanism of Heme Haloperoxidase Enzymes

M. Qadri E. Mubarak[§] and Sam P. De Visser[§]

[§] The Manchester Institute of Biotechnology and Department of Chemical Engineering and Analytical Science, The University of Manchester, 131 Princess Street, Manchester M1 7DN, United Kingdom.

Abstract

Heme haloperoxidases are unique enzymes in biology that react with H_2O_2 and halides on a heme center to generate hypohalide, which reacts with a substrate by halide transfer. We studied model complexes of the active site of heme haloperoxidase and investigated the reaction mechanism starting from an iron(III)-hydrogen peroxide-heme complex. We find two stepwise proton transfers by active site Glu and His residues to form Compound I and water, whereby the second proton transfer step is rate-determining. In a subsequent reaction with chloride the oxygen atom transfer is studied to form hypohalide. Overall, the free energy of activation of the second proton transfer and oxygen atom transfer to halide are similar in energy with free energies of activation around 20 kcal mol^{-1}. The calculations show that during oxygen atom transfer from Compound I to halide, significant charge-transfer happens prior to the transition state. This implies that the reaction may be enhanced in polar environments and through second-coordination sphere effects. The studies show that the conversion of H_2O_2 and halide on a heme center is fast and few intermediates along the reaction mechanism will have a lifetime that is long enough to enable trapping and characterization with experimental methods. A range of active site models and density functional theory methods were tested, but little effect is seen on the mechanism and optimized geometries.

Published Reference

Mubarak, M. Qadri E. and Sam P. De Visser. "Computational Study on the Catalytic Reaction Mechanism of Heme Haloperoxidase Enzymes" Israel Journal of Chemistry (2019).

3.1 Introduction

The class of heme enzymes in chemical biology is very large and take part in vital functions in biosystems related to oxygen transport, electron transfer, but are also responsible for substrate detoxification and biosynthesis processes. Many heme enzymes utilize molecular oxygen and, for instance, react as monoxygenases or dioxygenases with substrates, whereby one or two oxygen atoms are incorporated into the substrate structure (Kadish, Smith and Guilard, 2013). These monoxygenases are widespread among all forms of life and are highly versatile in their substrate scope and function. In particular, the cytochromes P450 are common in human physiology and are found in the liver where they initiate the metabolism and detoxification of xenobiotics such as drug molecules (Sono *et al.*, 1996; Meunier, De Visser and Shaik, 2004; De Montellano, 2005; Denisov *et al.*, 2005; Huang and Groves, 2018). As such there is great interest in their biochemical function and activity. Other heme enzymes convert dioxygen into water and react as catalases (Nicholls, Fita and Loewen, 2000; Njuma, Ndontsa and Goodwin, 2014), while the structurally similar peroxidases bind H_2O_2 instead (Veitch and Smith, 2000; Raven, 2003; Smulevich, Feis and Howes, 2005; Zederbauer *et al.*, 2007; Poulos, 2014).

Although monoxygenases, catalases and peroxidases all have a central heme co-factor with a bound iron (III) in the resting state, they all have a unique secondary structure and particularly show variations in how the metal links to the protein. Thus, the heme binds the protein through an amino acid side chain linkage with the metal in the axial ligand position and the type of bonding varies between the various heme enzymes. In particular, the cytochromes P450 bind the heme to the protein via a cysteinate axial ligand, while the catalases typically use a tyrosinate and the peroxidases a neutral histidine ligand instead. These differences in axial ligand have been correlated with a "push"-effect of electron density from the axial ligand to the iron and are believed to give the enzyme their specific activity and function (Dawson *et al.*, 1976; Poulos, 1996; Ogliaro, De Visser and Shaik, 2002). Specifically, the axial ligand affects the redox potential of the heme and hence its catalytic properties. Interestingly, all of these enzymes form a high-valent iron(IV)-oxo

heme cation radical active species, called Compound I (Cpd I), in their catalytic cycle as the active species (Nam, 2007; Watanabe, Nakajima and Ueno, 2007; Davydov *et al.*, 2008; Rittle and Green, 2010).

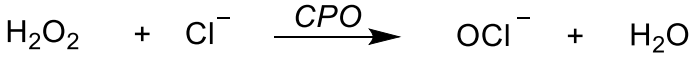

Scheme 3.1. General reaction catalysed by chloroperoxidase (CPO) enzymes.

A unique set of heme enzymes in Nature are the heme haloperoxidases, which bind hydrogen peroxide on a heme active site and convert it into hypohalide as a means to halogenate a substrate (Scheme 3.1) (Geigert *et al.*, 1986; Dawson and Sono, 1987; Sono *et al.*, 1996; Pan *et al.*, 2007; Manoj and Hager, 2008). These enzymes are found in fungi and their functions focus on the biosynthesis of natural products and antibiotics (Vaillancourt *et al.*, 2006; van Pe *et al.*, 2006; Butler and Sandy, 2009; Shepherd *et al.*, 2015; Timmins and De Visser, 2018). The active site of a typical chloroperoxidase (CPO), namely from *Leptoxyphium fumago*, is given in Figure 3.1 as taken from the 2J18 protein databank file (pdb) (Dawson *et al.*, 1976). The central heme cofactor is linked to the protein through a cysteinate axial ligand (Cys_{29}) in analogy to the P450s. As such, chloroperoxidase has a distinctly different structure from other peroxidases that contain a histidine axial ligand. On the distal site of the heme is a hydrogen-bonding network of polar amino acid residues that includes the side chain of Glu_{183} and the nearby His_{105} and Ser_{176} residues. Detailed computational studies on, e.g., heme peroxidases showed this intricate network to be involved in the conversion of hydrogen peroxide into Cpd I through proton relay mechanisms (Bathelt, Mulholland and Harvey, 2005; Derat *et al.*, 2005; Derat and Shaik, 2006a, 2006b; Harvey, Bathelt and Mulholland, 2006; Hersleth *et al.*, 2006; Vidossich *et al.*, 2010; Vidossich, Alfonso-Prieto and Rovira, 2012). The distal site of CPO also has a number of polar residues that stabilize hydrogen bonding interactions and can relay protons, namely the His_{105}, Ser_{176} and Glu_{183} residues. In addition, there is a manganese(II) ion located in close proximity to the heme propionate groups that hold it into position together with the Glu_{104} and Ser_{108} amino acid residues.

This manganese ion is lacking in other heme peroxidases and monoxygenases, but its function remains unclear.

During the catalytic cycle of CPO, H_2O_2 binds to the iron (III)-heme and is converted into water and an iron (IV)-oxo heme cation radical species called Compound I (Cpd I). UV/Vis, electron paramagnetic resonance and Mössbauer spectroscopic studies characterized Cpd I as a triradical species with a heme radical coupled to two unpaired electrons on the metal-oxo group (Dawson and Sono, 1987; Stone, Behan and Green, 2005; Hirao *et al.*, 2006; Kim *et al.*, 2006). This was confirmed with detailed density functional theory and QM/MM studies on CPO and P450 Cpd I models (Green, 1999; Ogliaro *et al.*, 2001; Schöneboom *et al.*, 2002; Bathelt *et al.*, 2005; Radoń, Broclawik and Pierloot, 2011). Cpd I is expected to react with halides (X^- = Cl^-/Br^-/I^-) to form hypohalide products, which drifts out of the heme active site and reacts with a substrate through halogenation. In this work we will present a computational study on the conversion of hydrogen peroxide and halide on a heme center into hypohalide products and the structural and electronic features of the reaction mechanism.

Previous studies on CPO (Green, Dawson and Gray, 2004; Stone *et al.*, 2006; Stone, Behan and Green, 2006; Silaghi-Dumitrescu, 2008; Lai *et al.*, 2009; Lai, Chen and Shaik, 2009; Chen *et al.*, 2010; Morozov and Chatfield, 2016; Chatfield and Morozov, 2018) mainly focused on the electronic configuration of Cpd I and its one-electron reduced form, i.e. Compound II (Cpd II). The studies highlighted the effect of environmental effects on the stability and electronic configuration and spectroscopic, e.g. Mössbauer parameters, of Cpd I due to hydrogen bonding interactions of water molecules and active site residues. As far as we are aware, a detailed study into the mechanism of H_2O_2 activation on an iron(III)-heme resting state model and its subsequent reaction with Cl^- to form hypohalide has never been reported and is the focus of this paper.

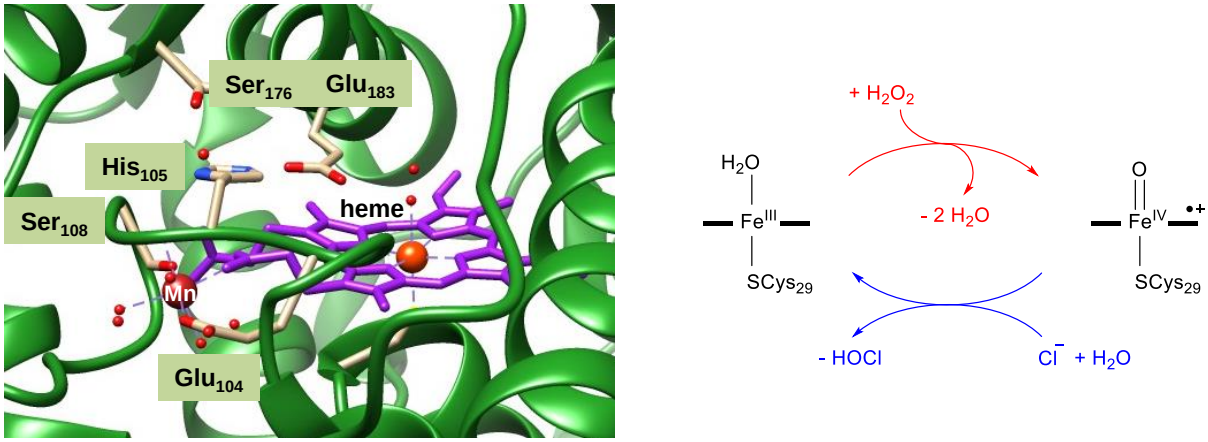

Figure 3.1. Crystal structure coordinates (left-hand-side) as taken from the 2J18 pdb file of the heme haloperoxidase enzyme. Right-hand-side depicts the catalytic cycle of hypohalide formation investigated and reported in this work.

3.2.1 Methods

3.2.1 Model Set-up.

We initially ran a series of density functional theory calculations on cluster models that were based on the crystal structure coordinates of the 2J18 pdb file (Seitlich *et al.*, 2007), see Scheme 3.2. The set-up uses previously reported procedures that start from a pdb file (Quesne, Borowski and De Visser, 2016; Timmins, Saint-André and De Visser, 2017). We took the pdb file and added hydrogen atoms using pH = 7 conditions and subsequently solvated the protein. Thereafter, an active site model was selected that included the heme with all its substituents abbreviated to methyl groups and the cysteinate axial ligand by methylmercaptate. Hydrogen peroxide was inserted into the distal position of the heme. The distal hydrogen bonding network was mimicked by propionate for Glu_{183} and ethyl-imidazole for His_{105} as our minimal model **A** (Scheme 3.2). The terminal carbon atom of these two amino acid side-chains was fixed in position with respect to the iron atom during the geometry optimizations. We also tested an enlarged model, namely model **B** that in addition to model **A** contained two water molecules. Finally, we investigated the models with protonated Glu_{183} group: Models **A'** and **B'**.

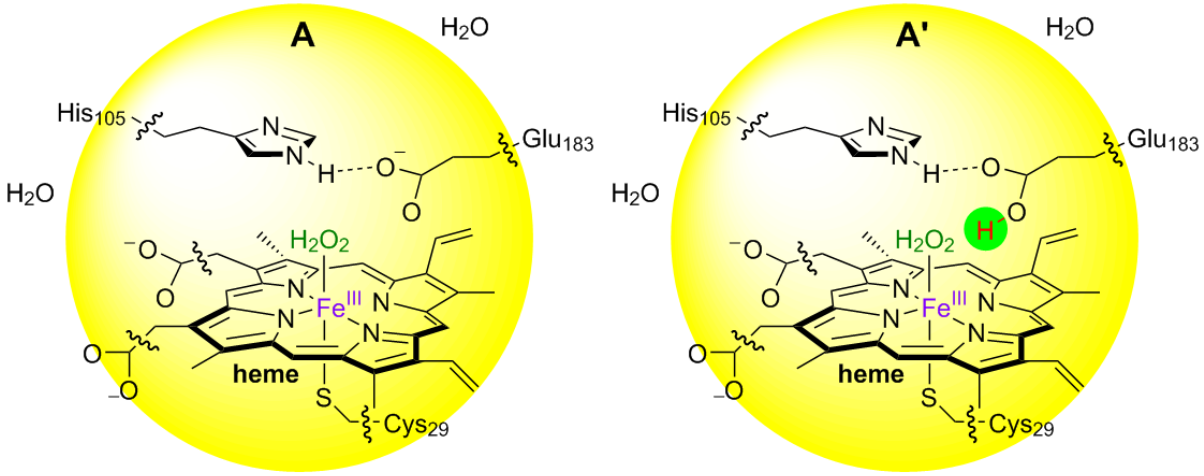

A = $Fe^{III}(H_2O_2)$(heme)Cys_{29}--$His_{105}Glu_{183}$

B = **A** + 2 H_2O

A' = $Fe^{III}(H_2O_2)$(heme)Cys_{29}--$His_{105}Glu_{183}$

B' = **A** + 2 H_2O

Scheme 3.2. Cluster models studied in this work.

3.2.2 DFT Methods and Procedures

Density functional theory methods as implemented in the *Gaussian*-09 software package were used (Frisch, Hratchian and Nielsen, 2009). We tested several density functional methods for consistency including B3LYP (Becke, 1993) and PBE0 (Perdew, Burke and Ernzerhof, 1996; Adamo and Barone, 1999). However, little differences in spin state ordering and relative energies were obtained, see Supporting Information for details. Geometry optimizations, constraint geometry scans and frequencies were done with a LANL2DZ basis set on iron (with core potential) and 6-31G* on the rest of the atoms: basis set BS1 (Hay and Wadt, 1985). To improve the energies, single point calculations were done with an LACV3P+ basis set on iron (with core potential) and 6-311+G* on the rest of the atoms: basis set BS2. Solvent was included in all calculations through the

conductor polarized continuum model (CPCM) with a dielectric constant of ε = 5.7 mimicking chlorobenzene. To test the effect of dispersion on the energetics of the reaction a series of single point calculations at UB3LYP-D3/BS2 level of theory were performed for the reaction mechanisms for Model A and Model B with dispersion corrections implemented through the D3 model of Grimme et al (Grimme *et al.*, 2010). In general, no dramatic changes are seen between the B3LYP and B3LYP-D3 results, see Supporting Information for details. These methods were used previously for calculations on heme and porphyrin systems and reproduced experimental spectroscopic properties and rate constants well (Sainna, Kumar, *et al.*, 2015; Cantú Reinhard *et al.*, 2016). Indeed, an overlay of the optimized geometries of model **A** and **B** with the crystal structure coordinates (Figure S1, Supporting Information) gives good overlap between the three structures. All local minima described in this work had real frequencies only, while the transition states were characterized with a single imaginary frequency for the correct mode.

3.3 Results and Discussion

In order to gain insight into the catalytic mechanism of CPO enzymes we modelled the catalytic cycle of CPO. In particular, our DFT studies focused on the steps for H_2O_2 conversion into Cpd I and water (reaction in red in Figure 3.1) and the subsequent reaction of Cpd I with Cl^- to form OCl^- products (reaction in blue in Figure 3.2). Let us start with discussing the first step on the formation of Cpd I using DFT cluster models.

We started with calculating two isomeric iron(III)-hydrogen peroxide bound models (**IA** and **IB**), whereby the active site Glu_{183} either forms a direct hydrogen bond with the proximal oxygen atom of H_2O_2 (in **IA**) or with the distal oxygen atom (in **IB**). Figure 3.2 displays optimized geometries of ^{2}**IA** and ^{2}**IB** as calculated for model **A**, while the obtained structures for model **B** are very similar (see Supporting Information). We identify the model-type with a subscript **A** or **B** after the label of the structure. For all models and methods tested, the doublet spin state is the ground state for both configurations. Moreover, structure $^2\mathbf{IB_A}$ is well lower in free energy than $^2\mathbf{IA_A}$ by ΔG = 9.5 (1.8) kcal mol^{-1} for model **A** and **B**; as such the two models predict the same ground

state structure. The lower stability of ^{2}**IB$_A$** over ^{2}**IA$_A$** probably stems from an additional hydrogen bond of the proximal OH group with one of the heme nitrogen atoms. In addition, there appears to be a stereochemical clash in **IA** between the protonated His group and the H_2O_2 moiety. Optimized geometries give a short Fe–S distance of 2.239 (2.253) Å and a long Fe–O bond of 2.318 (2.148) Å for ^{2}**IA$_A$** (^{2}**IB$_A$**). Hydrogen bonding interactions between the Glu and His residues stabilize and position the H_2O_2 molecule. The optimized geometries for model **B** are similar to those found for model **A** and confirm the spin-state ordering. The electronic configuration is typical for resting state structures (Green, 2000; Rydberg, Sigfridsson and Ryde, 2004; Groenhof *et al.*, 2005; Shaik *et al.*, 2005; Balding *et al.*, 2008), with a singly occupied metal-type orbital and configuration $\delta_{x2-y2}^2\ \pi^*_{xz}^2\ \pi^*_{yz}^1$ in the doublet spin state. The quartet and sextet spin state structures were also calculated and found to be close in free energy to ^{2}**IB$_A$**; however, their mechanism for proton transfer was substantially higher in energy, therefore, we will focus on the doublet spin mechanisms only.

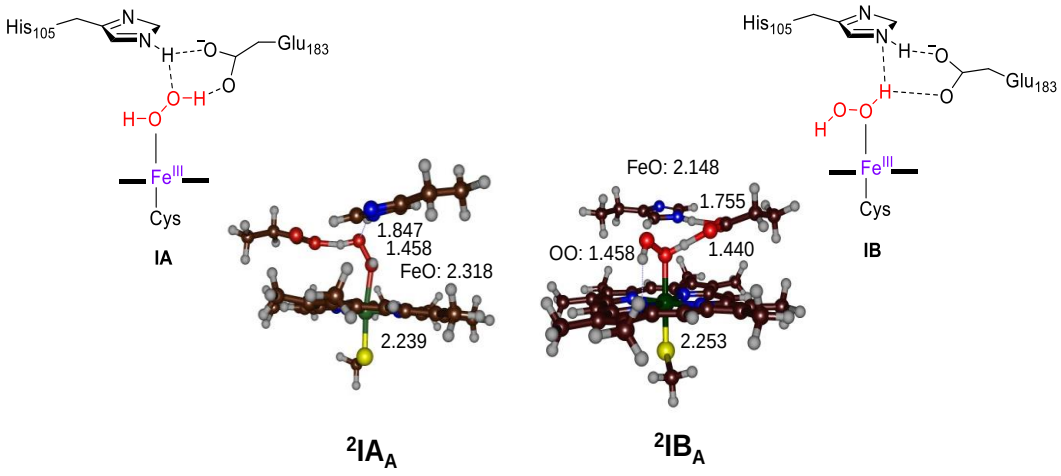

Figure 3.2. B3LYP/BS1 optimized geometries of ^{2}**IA** and ^{2}**IB** as calculated with model A. Bond lengths are in angstroms.

Subsequently, we explored H_2O_2 activation by ^{2}**IA** and ^{2}**IB** for models A and B and the mechanism with relative free energies is given in Figure 3.3. Starting from ^{2}**IB** there are two possible proton transfer reactions to form the iron(III)-hydroperoxo complex, namely from His_{105} (via transition state ^{2}**TS$_{PT,11}$**) or from Glu_{183} (via transition state ^{2}**TS$_{PT,12}$**). We located both transition states and find ^{2}**TS$_{PT,12}$** the lowest in energy of the two for both model A and B, namely 0.4 and 1.7 kcal mol^{-1} above the free energy of ^{2}**IB**$_A$ and ^{2}**IB**$_B$, respectively. As such the first proton transfer will be extremely fast and it will be difficult to trap and characterize a hydrogen peroxide bound heme structure. By contrast to ^{2}**TS$_{PT,12}$**, the alternative proton-transfer barrier $^2TS_{PT,11}$ has a free energy of activation of 17.0 (16.3) kcal mol–1 for models A (B). Therefore, addition of two hydrogen bonded water molecules has little effect on the energetics and feasibility of the proton transfer reactions. Furthermore, changing the density functional method from B3LYP to PBE0 only has a minor effect on the calculated energetics and no dramatic changes in structure are seen (Supporting Information). Previously, particularly for Mn complexes (Ghosh *et al.*, 2003; Yang *et al.*, 2016) major shifts in the relative energies were obtained and sometimes even a spin-state ordering reversal was observed.

We then optimized the local minima that are formed after these proton transfer barriers with either deprotonated His_{105} or deprotonated Glu_{183}, structures ^{2}**IB1** and ^{2}**IB2**. The ^{2}**IB2**$_A$/^{2}**IB2**$_B$ structures are slightly lower in energy than the reactant complexes by –4.0/–1.9 kcal mol^{-1}, respectively. Although, the transition state ^{2}**TS**$_{PT,11,B}$ relaxes to the local minimum ^{2}**IB1**$_B$, on the other hand the pathway for model A did not relax to ^{2}**IB1**$_A$, but instead converged to a rotated OOH structure, namely ^{2}**IC**$_A$. The latter is ΔG = 1.8 kcal mol^{-1} more stable than the reactant complex. For Model **B**, after proton abstraction from the distal oxygen atom of H_2O_2, the iron(III)-hydroperoxo group quickly reorients towards the His_{105} and Glu_{183} residues with the proximal OH group to form ^{2}**IC**$_A$. Thus, both ^{2}**TS**$_{PT,B1}$ and ^{2}**TS**$_{PT,B2}$ relax to form the same intermediate ^{2}**IC**. Clearly, the basicity of a His residue is too large and cannot exist in its deprotonated form in the vicinity of a protonated Glu residue, so that His_{105} remains in its singly protonated state.

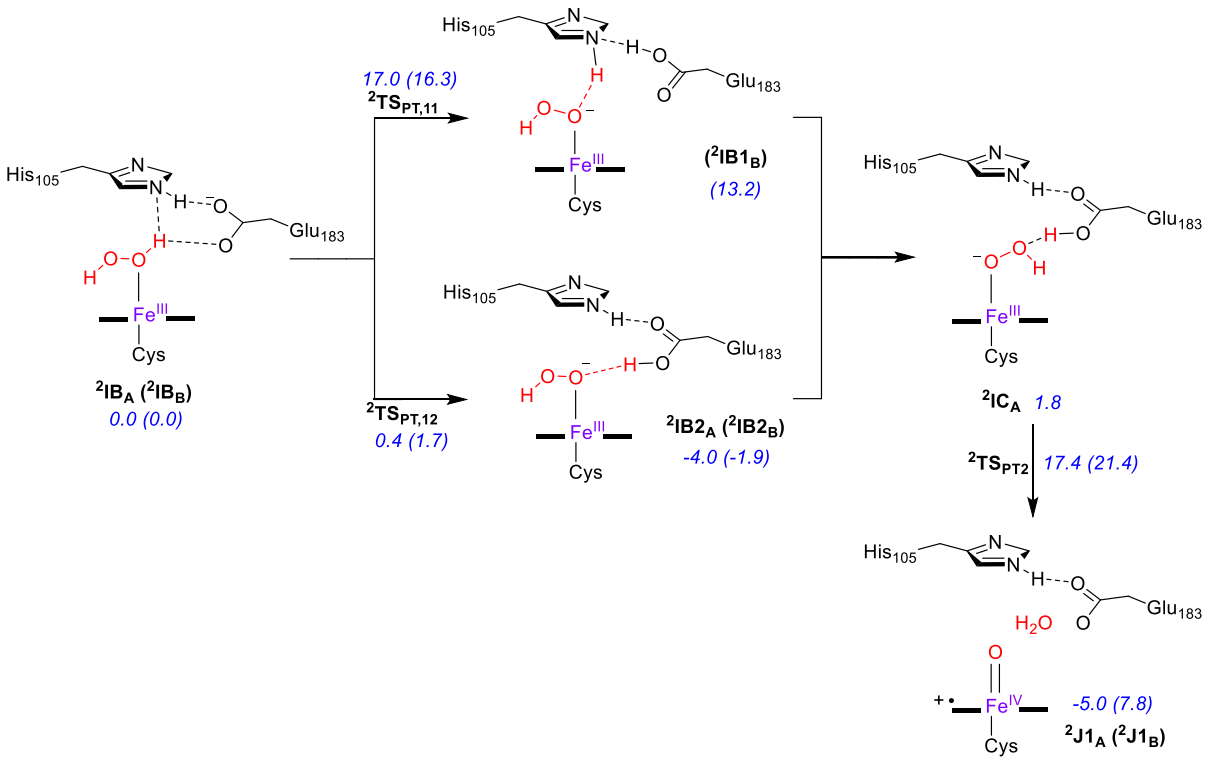

Figure 3.3. Reaction mechanism of conversion of an iron(III)-H_2O_2 complex into Cpd I for model structures A (B). Free energies contain ZPE, thermal (at 298K) and entropic corrections and are calculated at UB3LYP/BS2//UB3LYP/BS1 (UPBE0/BS2//UPBE0/BS1) with values in kcal mol^{-1}.

The most stable iron(III)-hydroperoxo complexes have the OH group in hydrogen bonding orientation with the protonated Glu_{183} residue in **IC**. A second proton transfer from protonated Glu_{183} via ^{2}**TS**$_{PT2}$ gives Cpd I and a water molecule (**J1**) via barriers of $\Delta G^{\ddagger}$ = 17.4 and 21.4 kcal mol^{-1} for models **A** and **B**. Again, the energies calculated at B3LYP and PBE0 level of theory are close and the density functional method appears to have no significant effect on the kinetics. The transition state via ^{2}**TS**$_{PT2}$ represents a proton-coupled-electron-transfer for heterolytic O–O bond cleavage, where a proton migrates from Glu_{183} to the terminal oxygen atom of the iron(III)-hydroperoxo group,

while simultaneously an electron transfer takes place from the iron to the oxygen. Indeed, large spin density changes are seen during the pathway from ^{2}**IC**$_A$ to ^{2}**J1**$_A$. Thus, ^{2}**IC**$_A$ has a single unpaired electron in a metal-type 3d orbital and gives spin density of 1.11 on iron and –0.20 on the porphyrin ring, while little (less than 0.1) is found on the OOH unit. In the transition state (^{2}**TS**$_{PT2}$) the spin on iron increases to 1.57 as well as on the newly formed water molecule (–0.26) but little on the oxo group. Further electronic changes happen en route to the iron(IV)-oxo heme cation radical species, whereby a full radical develops on the oxo and porphyrin units (with opposite spin) and an overall doublet spin state with three unpaired electrons is formed. At B3LYP level of theory the overall reaction from the H_2O_2 bound reactant to form Cpd I is slightly exergonic (by 5.0 kcal mol^{-1}), while it is slightly endergonic at PBE0 level of theory (by 7.8 kcal mol^{-1}).

Optimized geometries of the transition states from Figure 3.3 are given in Figure 3.4 as obtained for models **A** and **B**. Structurally, the two models give only minor differences in optimized structures. As discussed above in Figure 3.2, the reactant H_2O_2 bound complexes have short Fe–S distances of 2.239/2.253Å and long Fe–O distances of 2.318/2.148Å. Upon the first proton transfer to H_2O_2, little changes in the Fe–S distances are seen in the transition states, but the Fe–O bonds shorten to 2.018 – 2.064Å. Hence, the Fe–O bond strengthens; moreover, it shortens further to 1.889Å in ^{2}**IC**$_A$. This value is typical for iron(III)-hydroperoxo(heme) complexes, where the Fe–O bond can be considered as a single bond (Ogliaro *et al.*, 2002; Kamachi *et al.*, 2003; Hirao, Kumar and Shaik, 2006; Porro, Sutcliffe and De Visser, 2009). The imaginary frequencies found for the proton transfer steps are rather low (i201 to i684 cm^{-1}), while typical hydrogen atom abstraction barriers have much larger imaginary frequencies of well over i1500 cm^{-1}. This implies that the potential energy surface is rather flat and may lead to limited amount of tunnelling. Geometrically, the first proton transfer via ^{2}**TS**$_{PT,12}$ has the transferring proton almost midway in between the donor and acceptor groups, while the structures are more product-like for ^{2}**TS**$_{PT,11}$. The latter is typical for low-energy barriers and seen before in a

systematic study of substrate hydroxylation by iron(IV)-oxo oxidants (Shaik, Kumar and De Visser, 2008; Visser, 2010).

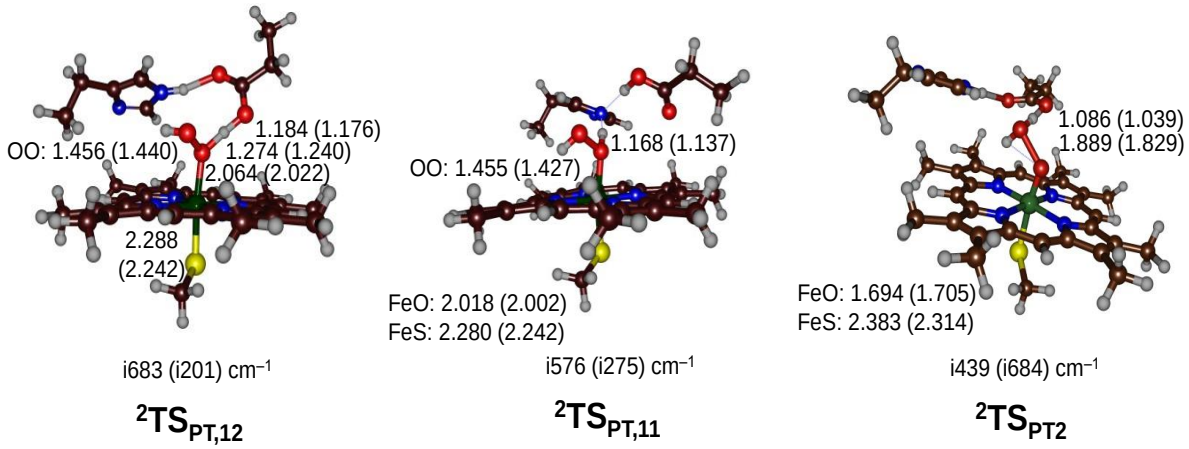

Figure 3.4. Optimized geometries of doublet spin proton-transfer transition states ^{2}**TS**$_{PT,11}$, ^{2}**TS**$_{PT,12}$ and ^{2}**TS**$_{PT2}$ as obtained at UB3LYP/BS1 (UPBE0/BS1) in Gaussian-09. Bond lengths are in angstroms and the imaginary frequency in cm^{-1}.

The second proton transfer via ^{2}**TS**$_{PT2}$ sees the Fe–O bond shorten further to 1.694/1.705Å for ^{2}**TS**$_{PT2,A}$/^{2}**TS**$_{PT2,B}$. At the same time, the O–O bond elongates to 1.889/1.829Å, respectively. The imaginary mode, therefore, reflects simultaneous proton transfer from GluH to the terminal oxygen atom of the hydroperoxo group and O–O bond rupture to form Cpd I and a water molecule.

Subsequently, we added a Cl^{-} anion to structures **A** and **B** to create a halide bound Cpd I structure (**J1'**) and calculated the oxygen atom transfer reaction to form hypochloride products (**J2**) via a transition state (**TS**$_{OCl}$). Optimized geometries and electronic configurations of ^{2,4}**J1'**$_{A}$ are given in Figure 3.5. The Cpd I structures have close-lying doublet and quartet spin state structures with electronic configuration $\delta_{x2\text{-}y2}^{2}$ $\pi^{*}_{xz}{}^{1}$ $\pi^{*}_{yz}{}^{1}$ $a_{2u}{}^{1}$. This matches previous computational studies as well as the experimental assignment of CPO Cpd I.[11,12,25] The $\delta_{x2\text{-}y2}$ orbital is a nonbonding orbital in the plane of the heme,

while the π^*_{xz}/π^*_{yz} represent the antibonding interactions of the 3d-metal orbital with a 2p orbital on oxygen. In the structures without halide, i.e. ^{2,4}**J1**, this orbital occupation results in a spin density of about 2 on the FeO group and 1 or –1 on the porphyrin in either quartet or doublet spin. Interestingly, with halide bound, as in ^{2,4}**J1'**, a partial electron transfer has occurred and spin density of –0.43/0.42 is observed in ^{2}**J1'**$_A$/^{4}**J1'**$_A$, respectively. At the same time, spin density is reduced on the porphyrin manifold. These structures and spin density distributions are similar to those found for the reaction of biomimetic iron(IV)-oxo species with halides that were found to proceed with a similar reaction mechanism and rates (Draksharapu *et al.*, 2015; Barman *et al.*, 2016; Colomban *et al.*, 2019). As seen in nonheme iron halogenase calculations, halide transfer is easier when the halide is neutral rather than anionic (Timmins, Fowler, *et al.*, 2018). It may very well be that haloperoxidases operate by a similar mechanism, whereby the halide loses electron density prior to a covalent bond formation step. Moreover, the oxygen atom transfer to halide may be sensitive to environmental factors and the polarity of the protein pocket. To find out if that is indeed the case we calculated the oxygen atom transfer to halide using several models.

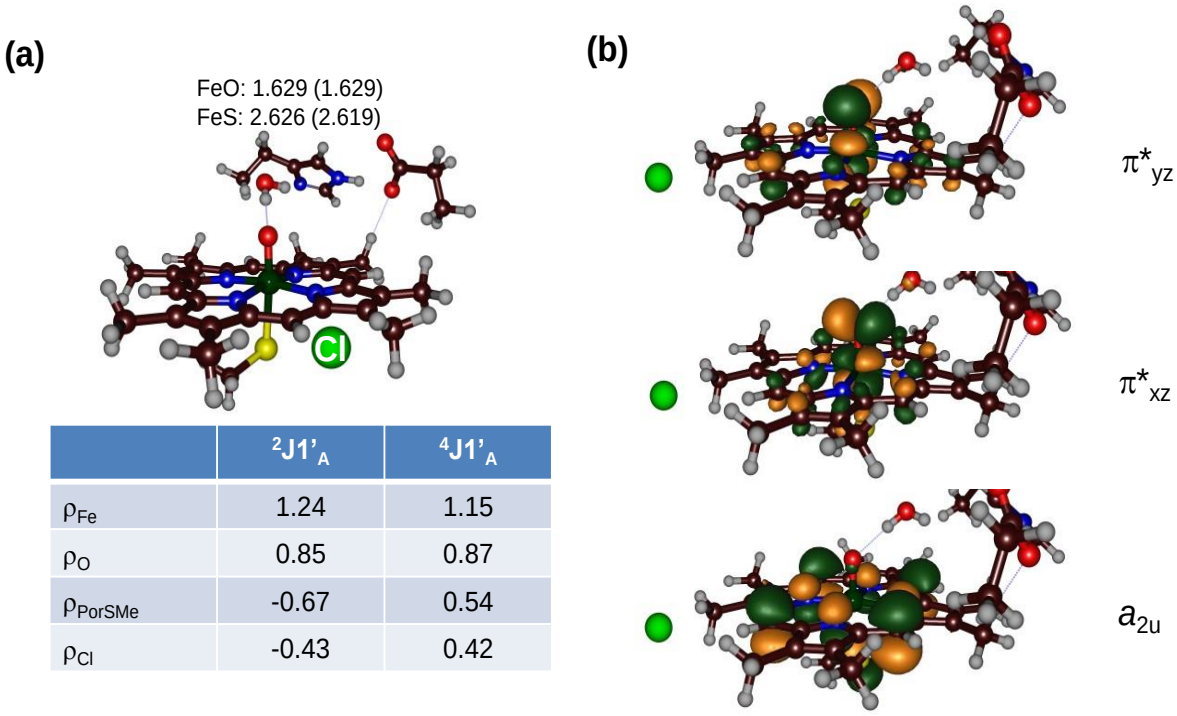

	$^{2}J1'_{A}$	$^{4}J1'_{A}$
ρ_{Fe}	1.24	1.15
ρ_{O}	0.85	0.87
ρ_{PorSMe}	-0.67	0.54
ρ_{Cl}	-0.43	0.42

Figure 3.5. (a) Optimized geometries of $^{4,2}J1'_{A}$ as obtained in Gaussian-09. Bond lengths for $^{2}J1'_{A}$ ($^{4}J1'_{A}$) are given in angstroms and group spin densities in atomic units. (b) Singly occupied molecular orbitals of $^{2}J1'_{A}$.

The oxygen atom transfer from Cpd I to halide was calculated on the doublet and quartet spin state surface and details are given in Figure 3.6. Even though Cpd I has degenerate doublet and quartet spin state surfaces, as a matter of fact only on the doublet spin state surface a low energy pathway was found. Thus, the doublet spin barrier ($^{2}\mathbf{TS}_{OCl,A}$) is 16.2 kcal mol^{-1} higher in energy than Cpd I and leads to a hypochloride bound iron(III) complex **J2A**. The transition state is characterized with a long O–Cl bond of 2.749Å and an imaginary frequency of i92 cm^{-1} for the O–Cl stretch vibration. The oxygen atom transfers to second row atoms, such as Cl^{-} or sulphides typically has transition state structures with small imaginary frequencies. In our case, the vectors for the displacement in the transition state clearly show a stretch vibration for the C–Cl/O–S motion (Kumar, De Visser, *et al.*, 2005; Kumar, Sastry and De Visser, 2011). We were unable to find a

quartet spin transition state; however constraint geometry scans implicate it to be well higher than 30 kcal mol^{-1}. The reaction is slightly endothermic overall by 11.2 kcal mol^{-1}.

As the protonation state in the active site pocket can vary due to accessible proton relay channels, we decided to also explore the oxygen atom transfer by Cpd I to halide with a model where the active site is protonated, i.e. containing either a neutral histidine or a protonated Glu_{183} or alternatively have a doubly protonated His_{105} and a deprotonated Glu_{183}. Interestingly, both configurations are found to be within 1 kcal mol^{-1}, which implies that the protons in the active site must be highly labile and free to move around. The mechanism of hypochloride formation from Cpd I and Cl^- was, therefore, studied with an initial proton transfer from the distal site proton-relay groups to form iron(IV)-hydroxide, i.e. protonated Compound II, via transition state $^{2,4}\mathbf{TS}_{PT3}$. The mechanism with relative energies is shown in Figure 3.7. Thus, the proton transfer has small barriers on the doublet and quartet spin state surface with values of $\Delta G^{\ddagger}$ = 3.6 (4.5) kcal mol^{-1}. Electronically, these transition states give a little amount of spin density on the halide (ρ = 0.20) and hence partial charge transfer has occurred. The transition states are characterized by a Grotthuss-type proton relay mechanism, whereby simultaneous a proton from protonated Glu_{183} to a water molecule is transferred and a proton from that water molecule to Cpd I. The imaginary frequency indeed shows the motions of those two protons, while the heavy atoms are almost stationary. The value of the imaginary frequency is large as expected for a proton transfer. Both doublet and quartet spin transition states are relatively central and have the transferring proton midway between the donor and acceptor groups.

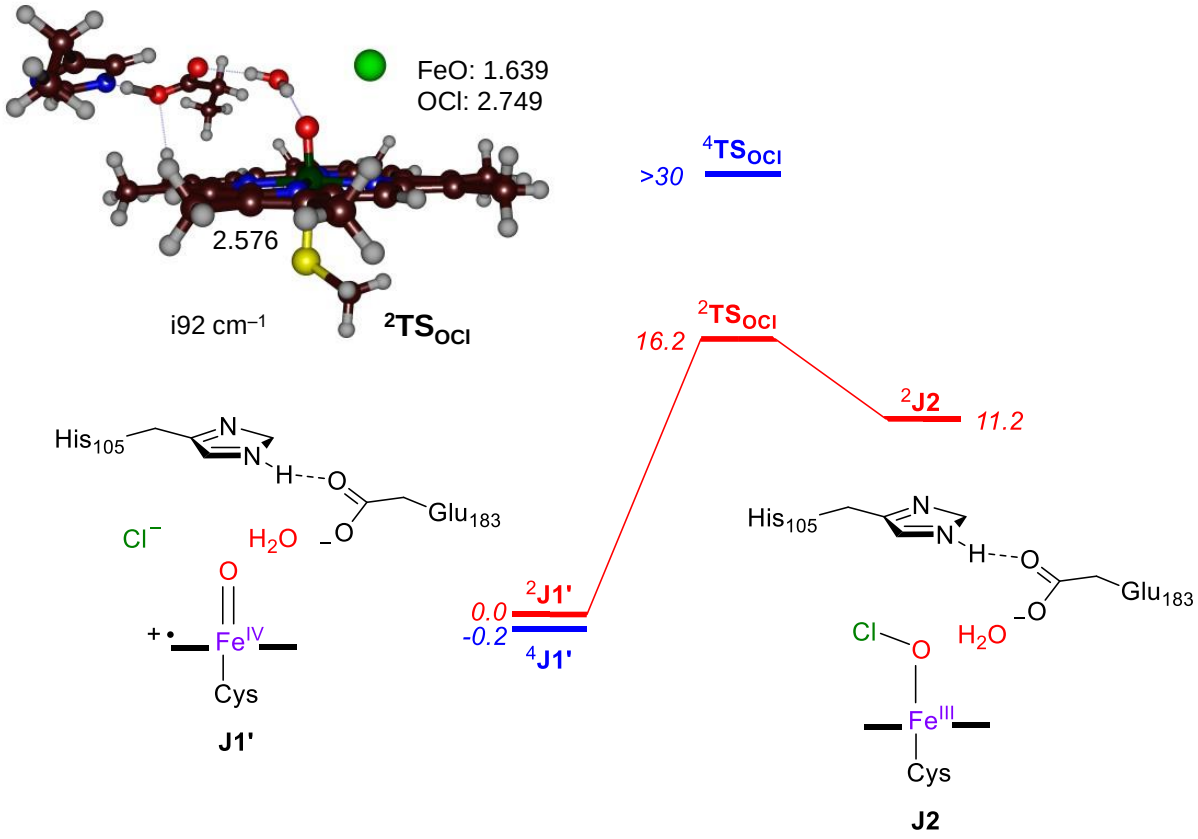

Figure 3.6. Reaction mechanism of oxygen atom transfer to chloride by Cpd I as calculated at UB3LYP/BS1 on model **A**. Free energies (in kcal mol^{-1}) contain zero-point, solvent, thermal (at 298 K) and entropic corrections, while the optimized geometry of ^{2}**TS**$_{OCl}$ gives bond lengths in angstroms and the imaginary frequency in cm^{-1}.

After the proton transfer, the system relaxes to protonated Compound II (structure **J2**) that reacts via a hydroxo transfer to halide via transition state $\mathbf{TS}_{\mathrm{HOCl}}$ to form hypohalide products (**P3**). On the doublet spin state surface the transition state was determined at $\Delta G^{\ddagger}$ = 25.8 kcal mol^{-1}, while at the quartet it is well higher lying. Although this would implicate a slow process a barrier of this magnitude would be able to proceed under room temperature conditions. The transition state is early with a long O–Cl distance of 2.155Å. Previous studies on halide transfer to nonheme iron(IV)-oxo and iron(III)-hydroperoxo complexes showed similar O–Cl distances and imaginary frequencies (Vardhaman *et al.*, 2011; Vardhaman, Barman, Kumar, C. V Sastri, *et al.*, 2013). The higher reaction barriers for Compound II or protonated Compound II versus Cpd I match previous DFT studies on their reactivity differences well (Li *et al.*, 2017; Postils *et al.*, 2018).

We also calculated the full reaction mechanisms on the quartet and sextet spin state surfaces. Particularly on the sextet spin state high barriers are found; however, in the product state (**P3**) the sextet spin state becomes the ground state and is below the quartet spin state by 2.6 kcal mol^{-1}, while the doublet spin product is 6.3 kcal mol^{-1} higher. This spin state ordering matches experimentally obtained spins with electron paramagnetic resonance studies that characterized the product as a sextet spin state (Kobayashi *et al.*, 1980).

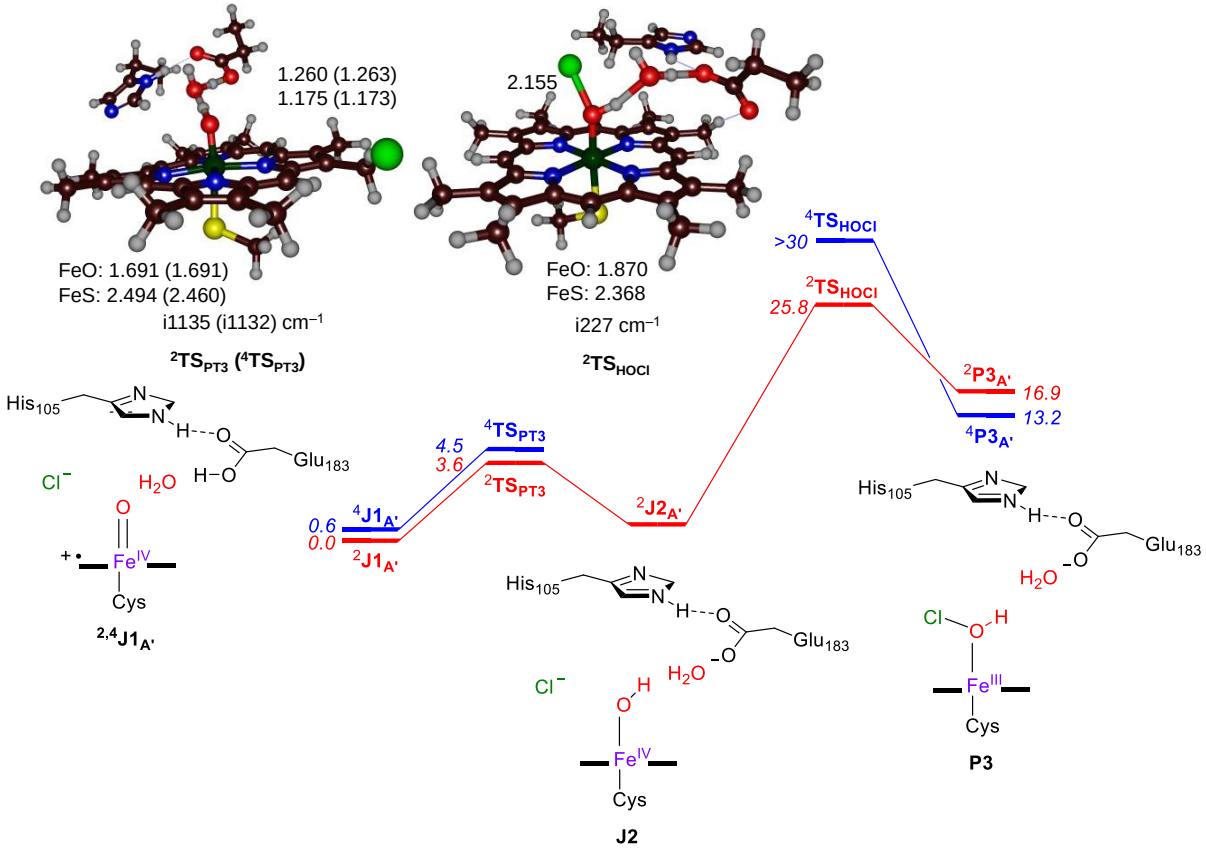

Figure 3.7. Reaction mechanism of oxygen atom transfer to chloride by Cpd I as calculated at UB3LYP/BS1 on protonated model **A'**. Free energies (in kcal mol^{-1}) contain zero-point, solvent, thermal (at 298 K) and entropic corrections, while the optimized geometry of $^{2}\mathbf{TS}_{OCl}$ gives bond lengths in angstroms and the imaginary frequency in cm^{-1}.

3.4 Summary and Conclusion

In this work a density functional theory study is reported on the catalytic cycle of the heme chloroperoxidase enzymes. Several models with different active site protonation states were explored and several density functional theory methods tested. Overall, the density functional theory method has little effect on the mechanism and optimized geometries and has only a small effect on the calculated kinetics. Firstly, we investigated the conversion of H_2O_2 on an iron(III)-heme active site into Cpd I through sequential protonations. It is shown that active site residues in their pH 7 protonation states can perform the reaction easily. Initially, a proton is abstracted from the distal oxygen atom of H_2O_2 to form an iron(III)-hydroperoxo group. The proton is then reshuttled by the active site amino acids (His_{105} and Glu_{183}) to the terminal oxygen atom to form water and Cpd I. Upon addition of chloride a long-range electron transfer is seen, whereby considerable spin density is generated on the halide. Two possible mechanisms for hypochloride were investigated, namely direct oxygen atom transfer from Cpd I and initial protonation of Cpd I followed by OH transfer. Both pathways should be feasible in the protein and may be competitive. Although the former pathway gives the lowest overall barrier, actually the second pathway cannot be ruled out either as it starts with a low barrier proton transfer step and hence may drive the reaction to protonated Compound II.

Chapter 4

PROJECT 2

Mechanism of Tryptophan Nitration by a Cytochrome P450 Enzyme

Qadri E. Mubarak,[§] Savvas Louka,[§] Gregory L. Challis[‡] and Sam P. De Visser[§]

[§] The Manchester Institute of Biotechnology and Department of Chemical Engineering and Analytical Science, The University of Manchester, 131 Princess Street, Manchester M1 7DN, United Kingdom.

[‡] Department of Chemistry, University of Warwick, Coventry, United Kingdom.

Abstract

Cytochrome P450 enzymes catalyze many vital reaction processes in the human body related to biodegradation and biosynthesis particularly in the liver. Usually, the CYP450s act as monoxygenases, where they bind molecular oxygen and transfer one of its oxygen atoms to substrate, while the other one leaves the process as water. A recently discovered CYP450 subfamily TxtE utilizes O_2 and NO on a heme center and converts L-tryptophan selectively to 4-nitrotryptophan. The aromatic nitration process by environmentally benign oxidants is important from a biotechnological perspective and as such understanding the details of the reaction mechanism might lead to future applications. Therefore, to gain insight into the mechanism of L-Trp nitration by CYP450 enzymes, we performed a computational study using active site models of CYP450 TxtE and studied possible pathways leading to products. Our work proposes a reaction mechanism that starts from an iron(III)-superoxo complex and proceeds to form peroxynitrite in a reaction with NO. This is followed by homolytic N-O bond cleavage to form an NO_2 radical and Compound II via small free energy of activation. Free NO_2 then activates one of aromatic C-atoms of substrate and Compound II picks up a proton via the rate-determining step to form nitrated tryptophan. We explored L-Trp nitration on the C^4-, C^5-, C^6- and C^7-positions and find preferential C^4-activation although small changes to the shape and size of the substrate binding pocket may give additional products. Our study highlights the differences between CYP450 monoxygenases and CYP450 TxtE and particularly how proton relay channels have been blocked to avoid hydroxylation of substrate. Moreover, our work shows that the polarity of the protein stabilizes the NO_2 addition reaction and enables a regio- and chemoselective tryptophan nitration pathway.

Draft paper submitted for publication

4.1 Introduction

Aromatic nitration is an important reaction in industry where an NO_2 group is installed on an arene scaffold; however, typically these reactions are performed in organic solvents with heavy metal ions as catalysts (Kochi, 1992; Esteves *et al.*, 2003; Yan and Yang, 2013; Sun, 2014; Wang *et al.*, 2018). Obviously, an environmentally benign catalyst that uses first-row transition metals in water would be preferential and as such research is conducted into exploring enzymatic and biomimetic pathways to nitrate arene-type substrates. Interestingly, in recent years several proteins have been discovered that react through arene nitration (Bourassa *et al.*, 2001; Schopfer, Baker and Freeman, 2003; Toader *et al.*, 2003; Chaki *et al.*, 2009; Su and Groves, 2009; Kong *et al.*, 2015). These enzymes often utilize peroxynitrite as a nitrating agent that is formed from a reaction of dioxygen with NO (Ramezanian, Padmaja and Koppenol, 1996). Furthermore, several biotechnological studies have indicated enzyme mutants and bioengineered proteins, e.g., of nonheme iron halogenases, that are able to perform substrate nitration reactions (Matthews *et al.*, 2014; Timmins, Quesne, *et al.*, 2018). In particular, Bollinger et al engineered the nonheme iron halogenase SyrB2 to enable nitration of aliphatic groups efficiently (Matthews *et al.*, 2014). Alongside these enzymatic systems also a biomimetic model of SyrB2 was identified that was shown to react with substrates through aliphatic nitration in water, although hydroxylation pathways were predicted to proceed in parallel (Timmins, Quesne, *et al.*, 2018).

Recently, a novel cytochrome P450 (CYP450) subfamily was discovered that is able to nitrate either a tryptophan or tyrosine residue (Barry *et al.*, 2012; Yu *et al.*, 2013; Dodani *et al.*, 2014, 2016; Girvan and Munro, 2016; Tomita *et al.*, 2017; Zuo *et al.*, 2017; Jiang *et al.*, 2018; Zuo and Ding, 2019). This is an unusual CYP450-type reaction as these enzymes normally operate as monoxygenases and typically convert aliphatic and aromatic groups into alcohols or C=C double bonds into epoxides. In the human body, the CYP450s catalyze key reactions for human health that vary from biodegradation of xenobiotics to biosynthesis of hormones (Sono *et al.*, 1996; De Montellano, 2005; Denisov *et al.*, 2005;

Kadish, Smith and Guilard, 2013; Huang and Groves, 2018). Thus, liver CYP450 isozymes, e.g. CYP450 2D6 and CYP450 3A4 (Das, Grinkova and Sligar, 2007; Sevrioukova and Poulos, 2013; Poulos, 2014; Guengerich and Yoshimoto, 2018), are known to initiate the metabolism of drug and xenobiotic molecules, while the CYP450 aromatase isozymes are involved in the biosynthesis of estrogen (Krámos and Oláh, 2014; Manna, Molehin and Ahmed, 2016; Guengerich, 2017). In general, the CYP450s utilize molecular oxygen on a heme center and react as monoxygenases, whereby one oxygen atom is transferred to a substrate, while the other oxygen atom is reduced to a water molecule (Meunier, De Visser, and Shaik 2004; Ortiz De Montellano 2010; Huang and Groves 2017). The CYP450s are known to activate relatively inert C–H bonds as strong as the ones in propane, but also react with arenes through aromatic hydroxylation.

Thaxtomin phytotoxins are biosynthesized in plant-pathogenic *Streptomyces* species from L-4-nitrotryptophan and L-phenylalanine. The L-Phe residue in the resulting N,N-dimethyl-diketopiperazine is hydroxylated at the C_α and aromatic ring positions by the bifunctional CYP450 TxtC (Barry *et al.*, 2012; Yu *et al.*, 2013; Dodani *et al.*, 2014; Greule *et al.*, 2018; Alkhalaf *et al.*, 2019). The CYP450 TxtE class of enzymes bind L-tryptophan, O_2 and NO in the active site and convert it to L-4-nitrotryptophan selectively. Little is known about the mechanism of this chemical reaction, but it is believed that an initial reaction of NO with O_2 gives peroxinitrite that then splits into either NO_2^+ or $NO_2^\bullet$ (Barry *et al.*, 2012). Similar to the CYP450s, another heme enzyme, namely nitric oxide synthase was shown to activate peroxynitrite (Lang *et al.*, 2016). Furthermore, CYP450 3A4 under addition of peroxynitrite was found to transfer NO_2 to tyrosine residues in the protein (Lin *et al.*, 2012) . The studies implicate that most likely free $NO_2^\bullet$ or NO_2^+ is generated that migrated through the protein and reacted with these aromatic residues.

As little is known on the catalytic reaction mechanism of L-Trp nitration by CYP450 TxtE, we decided to embark on a computational study. In particular, the works focuses on understanding the selectivity of nitration of substrate. Our work shows that an initial

precursor iron(III)-peroxynitrite complex homolytically cleaves into an iron(IV)-oxo heme and NO_2. As substrate L-tryptophan is located close to the formed NO_2 it is activated rapidly to form nitrated products. Clearly, substrate binding must be a precursor to NO addition to an iron(III)-superoxo intermediate in the catalytic cycle. Our work rationalizes substrate nitration by CYP450 isozymes and gives suggestions to further engineer them for more efficient biotechnological applications.

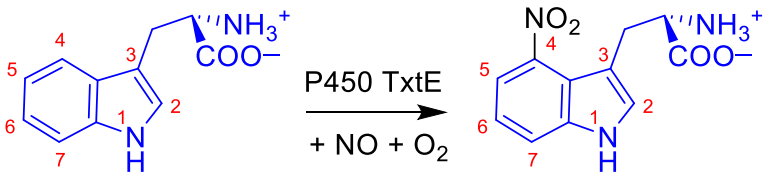

Scheme 4.1. Reaction catalyzed by P450 TxtE.

4.2 Methods

Density functional theory calculations were performed on active site model complexes of TxtE based on the crystal structure coordinates of the 4TPO protein databank (pdb) file (Dodani *et al.*, 2014). Our initial calculations used a minimal active site model (model **A**) that included an iron(III)-peroxynitrite-heme (with side chains replaced by hydrogen atoms) and thiolate for the axial cysteinate ligand. A complete tryptophan amino acid was included as substrate, where the carboxylic acid group was protonated and the amide group deprotonated, Scheme 4.2. Hence, the overall charge of model A was –1 and the system was calculated in the individual doublet and quartet spin states. No constraints were put on this model.

A second and more elaborate model (model **B**) was subsequently studied that included the substrate binding pocket as obtained from the 4TPO pdb file (Dodani *et al.*, 2014). Thus, model **B** contained model **A** with one propionate side chain of the heme included and expanded with part of the substrate binding pocket, namely the Arg_{59} and Tyr_{89} side chains, the small peptide chain Asn_{293}-Gln_{294}-Phe_{295}-Thr_{296}-Trp_{297}-Arg_{298}, and

Glu_{394}-Phe_{395}, whereby the Gln_{294} residue was abbreviated to Gly. The Trp substrate in Model **B** had a zwitterionic state with the carboxylate group deprotonated and in a salt bridge with Arg_{59} and the amide group protonated. This model has 250 atoms and overall charge –1. To make sure that the structure did not deviate too much from the crystal structure coordinates some geometric constraints were placed on several α-carbon atoms of the protein backbone in the model as identified with a star in Scheme 4.2. A comparison of starting and final structures of the geometry optimizations showed little changes of the protein part of the model and hence kept the features of the protein structure intact.

For Model A a range of possible reaction pathways for substrate nitration were explored using Gaussian-09 (Frisch, Hratchian and Nielsen, 2009), see Supporting Information. Using the obtained insight, we then investigated the low energy pathways with the expanded cluster model B. Based on our previous experience with heme systems we used well-tested and validated approaches (Cantú Reinhard et al. 2016; Yang et al. 2016; Cantú Reinhard and De Visser 2017). All geometries were fully optimized without constraints and transition states were characterized with a single imaginary frequency for the correct mode. For a number of transition state geometries also intrinsic reaction coordinate scans were performed that connected to the two local minima adjacent to the transition state (see Supporting Information).

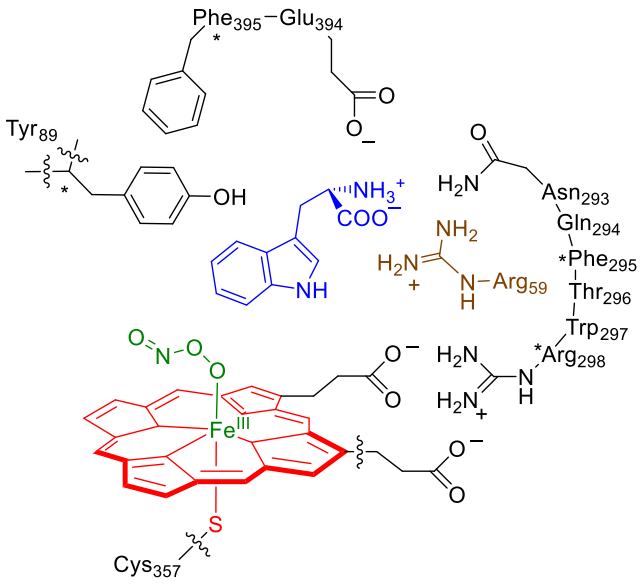

Scheme 4.2. Active site model of TxtE investigated in this work. Atoms labeled with a star were fixed.

The hybrid density functional method UB3LYP (Lee, Yang and Parr, 1988; Becke, 1993) was used for all calculations in combination with an LACVP basis set on iron with core potential and 6-31G* on the rest of the atoms (C, N, O, H, S), basis set BS1 (Francl *et al.*, 1982; Hay and Wadt, 1985). All optimizations, frequencies and geometry scans included a continuum polarized conductor model (CPCM) with a dielectric constant mimicking chlorobenzene (Tomasi, Mennucci and Cammi, 2005). To obtain more accurate energies, we did single point calculations with an LACV3P+ basis set on iron with electron core potential and 6-311+G* on the rest of the atoms: basis set BS2. These methods and approaches were used previously and shown to predict the correct regio- and chemoselectivities of reaction mechanisms and give free energies of activation to within 3 kcal mol^{-1} of experiment (Cantú Reinhard, Faponle, and De Visser 2016; Timmins, Saint-André, and De Visser 2017; Cantú Reinhard et al. 2017).

4.3 Results

The P450 catalytic cycle for a monoxygenation reaction mechanism starts with substrate binding to the iron(III)-heme resting state, release of water from the sixth ligand position of the heme followed by a reduction by a redox partner and molecular oxygen binding. Subsequently, a reduction and two protonation steps leads to Compound I, i.e. an iron(IV)-oxo heme cation radical species that is the active oxidant in oxygen atom transfer reactions. Trp nitration by P450 TxtE is believed to deviate from this mechanism and upon forming of the iron(II)-superoxo species reacts with NO to form an iron(III)-peroxynitrite intermediate. Indeed, in many Biosystems the P450 nitration enzyme is linked to a nitric oxide synthase that provides the NO by reacting L-Arg on a heme center (Barry *et al.*, 2012; Dodani *et al.*, 2014).

To understand the catalytic reaction mechanism of Trp nitration by P450 TxtE, we set up several cluster model complexes that include the substrate binding pocket and heme groups as shown in Scheme 4.2. Details of the small cluster model results are given in the Supporting Information, while we focus on the large active site data in the main paper only. We explored several reaction pathways for substrate nitration as displayed in Scheme 4.3.

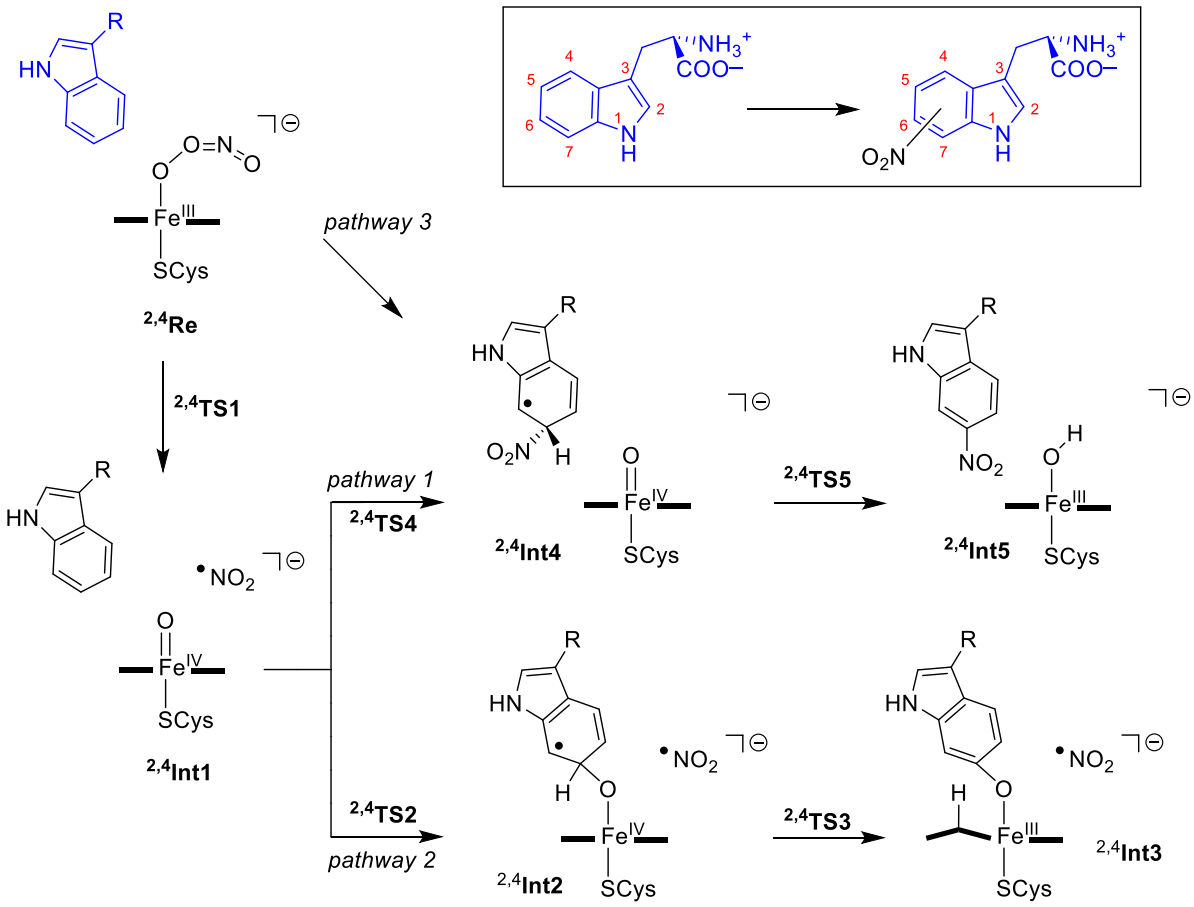

Scheme 4.3. Reaction mechanisms and labeling of Trp nitration by a peroxynitrite bound P450 model as explored by DFT with activation of the C^6-position as an example.

The full mechanism was calculated for nitration at the C^4-, C^5-, C^6- and C^7-positions. Furthermore, as substrate is latched in the substrate binding pocket with different residues on both sides, we considered attack on either side of the aromatic ring, designated endo- and exo-pathways.

We started our work from the iron(III)-peroxynitrite complexes in the doublet and quartet spin states and investigated three major reaction pathways. Pathway 1 and 2 start with a homolytic O-O bond cleavage in the peroxynitrite group to form Compound II, i.e. an

iron(IV)-oxo heme, and NO_2 (complex **Int1**) via a transition state **TS1**. Thereafter, pathways 1 and 2 diverge and substrate attack of either NO_2 or iron(IV)-oxo were investigated. In pathway 1, the free NO_2 radical attacks the substrate directly to form intermediate **Int4** via transition state **TS4**, which after proton transfer to Compound II via transition state **TS5** leads to nitrated Trp and protonated Compound II (**Int5**). In pathway 2, by contrast, an electrophilic addition of the oxo to a carbon atom of the Trp substrate takes place to form a radical intermediate **Int2** via a transition state **TS2**. This is then followed by abstraction of the *ipso*-proton from the Trp carbon atom by the heme to form the protonated heme structure **Int3** via transition state **TS3**. A proton reshuttle leads to phenol products or alternatively the NO_2 radical attacks the *ipso*-position to form nitrated Trp products. In addition, to these two pathways, we also tested a direct attack of peroxynitrite on these carbon-positions of L-Trp to form intermediate **Int4** using model **A**. However, this pathway (Supporting Information Figure S11) is high in energy and did not lead to NO_2 transfer to substrate; instead the peroxynitrite structure stayed intact. As such peroxynitrite will need to be activated first and split into NO_2 and an iron(IV)-oxo species in order to be reactive. Hence, pathway 3 was ruled out for further studies.

The potential energy landscape for the reaction of the iron(III)-peroxynitrite complex with L-Trp on the lowest energy doublet and quartet spin states for pathway 1 is given in Figure 4.1. The reactant states (**Re**$_B$) are in a doublet spin ground state as expected for iron(III) complexes and give a small barrier of $\Delta G^{‡}$ = 3.8 kcal mol^{-1} via ^{2}**TS1**$_B$ for homolytic O**–**O cleavage to form iron(IV)-oxo and an NO_2 radical. The quartet spin barrier is well higher in energy, i.e. $\Delta G^{‡}$ = 15.6 kcal mol^{-1}, and, therefore the reaction will take place on a dominant doublet spin state surface.

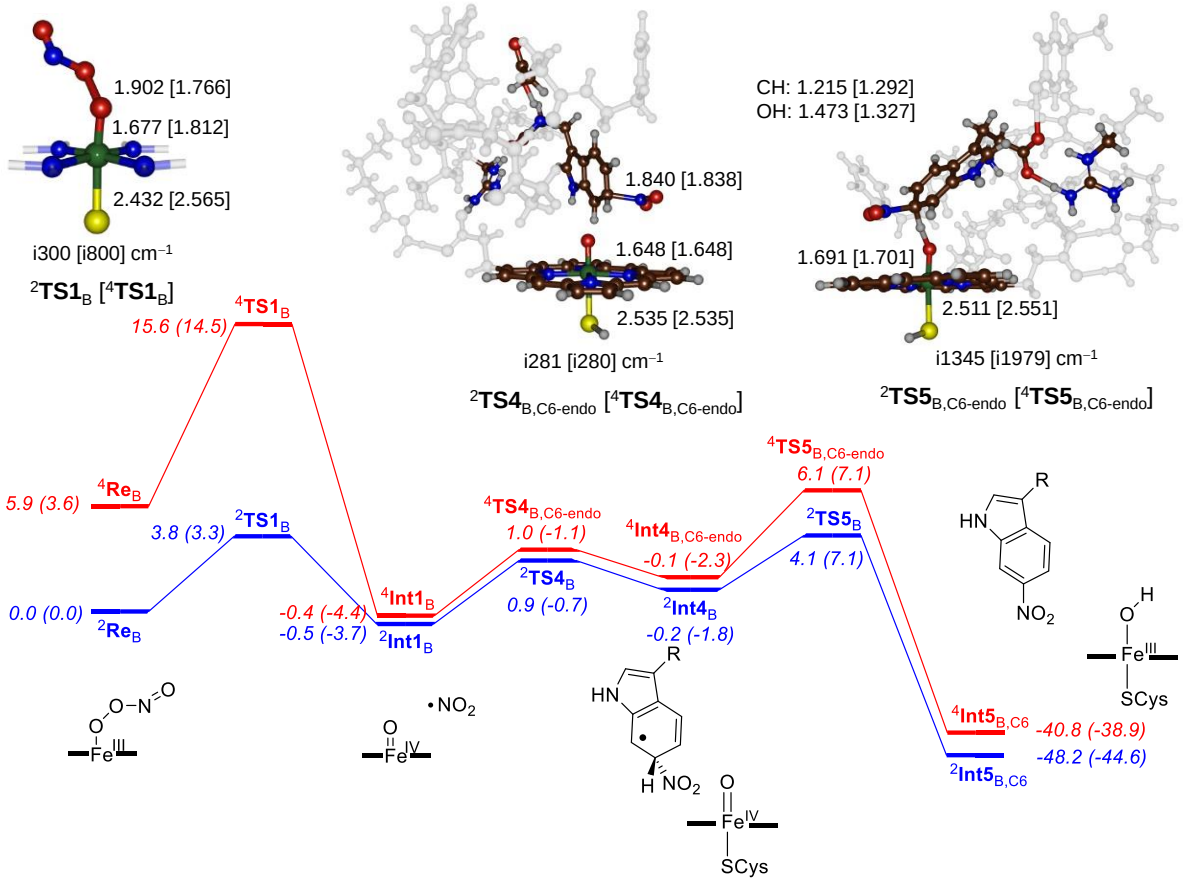

Figure 4.1. Potential energy landscape (with values in kcal mol^{-1}) of L-Trp nitration at the C^6-position via endo-attack in active site model complex **B**. All geometries optimized in Gaussian at UB3LYP/BS1. The two energetic values represent ΔE+ZPE (ΔG) data with energies obtained using basis set BS2 and with ZPE and solvent corrections; free energies are given in parenthesis at 298K and contain, ZPE, thermal, solvent and entropic corrections. Optimized geometries of transition states give bond lengths in angstroms and the imaginary frequency in cm^{-1}.

The peroxynitrite-cleaving transition state geometries have strongly elongated O–O distances of 1.902 (1.766) Å for ^{2}**TS1**$_{B}$ (^{4}**TS1**$_{B}$) and visualization of the imaginary frequency shows an O–O bond cleavage mode. The first reaction step is virtually thermoneutral on the doublet spin state and brings the quartet spin state to within a fraction of a kcal mol^{-1}. Electronically, ^{4,2}**Int1**$_{B}$ can be characterized as an iron(IV)-oxo heme complex, i.e. Compound II (CpdII), with an NO_2 radical in close proximity. Indeed the group spin densities (Supporting Information) of ^{4,2}**Int1**$_{B}$ show a full spin on the NO_2 group.

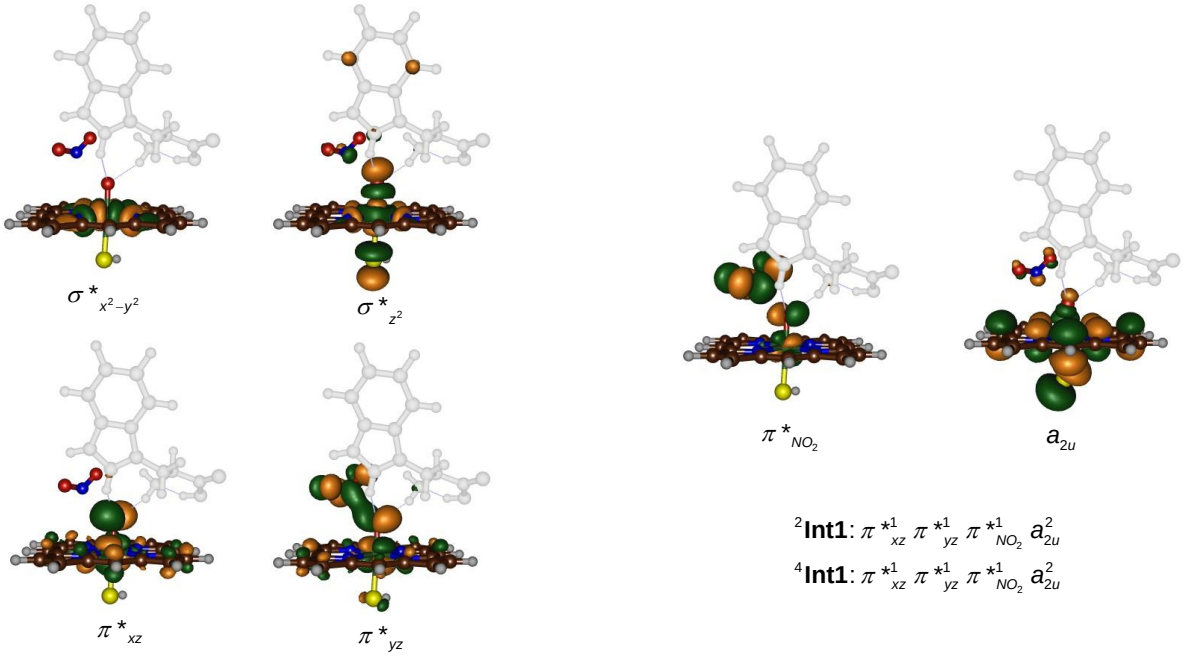

Figure 4.2. High-lying occupied and low-lying virtual orbitals of ^{2,4}**Int1**.

The molecular valence orbitals of ^{4,2}**Int1** are depicted in Figure 4.2. Thus, CpdII has an electronic configuration with two unpaired electrons in π* orbitals (π^*_{xz} and π^*_{yz}) for the

antibonding interaction of a 3d iron orbital with a 2p on the oxo group. The π^*_{yz} orbital mixes somewhat with a π^*_{NO2} orbital and hence there is a small but weak long-range interaction between CpdII and NO_2. Two virtual orbitals for the σ*-antibonding interactions of the metal with the first-coordination sphere atoms are labelled σ^*_{z2} and σ^*_{x2-y2}. These two virtual orbitals are low in energy, but may get occupied during the reaction mechanism. The heme-based a_{2u} orbital is doubly occupied in CpdII. Finally, a π^* orbital on the NO_2 group complements the set of orbitals in Figure 4.2.

Thus, the two unpaired electrons in π^*_{xz} and π^*_{yz} can be ferromagnetically coupled to the NO_2 radical (in orbital π^*_{NO2}) into an overall quartet spin state or antiferromagnetically coupled into an overall doublet spin state. As such there are two different spin-configurations for the CpdII structure with overall doublet and quartet spin. These two configurations are close in energy and indeed we find them within 1 kcal mol^{-1}. In previous work on P450 reactivity by Compound I (CpdI), i.e., the iron(IV)-heme cation radical species, which is the one electron oxidized form of Cpd II, it was found to also have close lying doublet and quartet spin state structures, but with $\pi^*_{xz}{}^1$ $\pi^*_{yz}{}^1$ $a_{2u}{}^1$ configuration (Shaik *et al.*, 2002, 2005). Thus, reaction mechanisms with substrates were shown to proceed on competing spin-state surfaces with competing rate-constants. Moreover, examples have been highlighted in the past, where product distributions were different on each of the spin-state surfaces (Ji *et al.*, 2015; Pickl *et al.*, 2019). Therefore, we calculated the full mechanism of L-Trp nitration on the doublet and quartet spin states for all reactions.

We attempted to optimize the geometry of the product from heterolytic cleavage of peroxynitrite to give ^{4,2}CpdI + NO_2^-. However, when we swapped molecular orbitals in ^{4,2}**Int1**, the SCF converged back to the original conformation. Therefore, the heterolytic cleavage pathway is high in energy and is inaccessible for the enzyme and will not take place here.

Subsequently, we investigated the electrophilic addition of NO_2 to L-Trp substrate from the ^{2,4}**Int1**$_B$ structures and, as an example, we show the calculated mechanism for activation of the C^6_{endo}-position of L-Trp by CpdII in Figure 4.1. The C–N bond formation transition states takes place via barriers ^{2,4}**TS4**$_{B,C6\text{-}endo}$. On both the doublet and quartet spin state surfaces small barriers of $\Delta G^{‡}$ = 3.0 and 3.3 kcal mol^{-1} are found. Nevertheless, both transition states were characterized as shown in Figure 4.1 with a single imaginary frequency of i280 cm^{-1} representing a C–NO_2 stretch vibration. As the transition states represents NO_2 transfer to L-Trp and no electron is transferred to CpdII, there are little changes to the geometry of the CpdII part as compared between ^{2,4}**Int1**$_B$ and ^{2,4}**TS4**$_{B,C6\text{-}endo}$ and geometrically those parts of the structure are the same. The transition state is a pure NO_2 attack on the aromatic ring of L-Trp and no electron transfer to the heme takes place. The shallow intermediate (^{2,4}**Int4**$_{B,C6\text{-}endo}$) is followed by another low-energy barrier, namely the proton transfer from L-Trp to CpdII with barriers of $\Delta G^{‡}$ = 8.9 and 9.4 kcal mol^{-1} , respectively, above ^{2}**Int4**$_{B,C6\text{-}endo}$ and ^{4}**Int4**$_{B,C6\text{-}endo}$. These structures are characterized with a large imaginary frequency (i1345 and i1979 cm^{-1}), which is typical for the transfer of a light atom such as a proton to an iron(IV)-oxo species.[58] Both transition states are relatively central with similar O–H and C–H distances.

Therefore, the overall reaction mechanism of L-Trp nitration by an iron(III)-peroxynitrite heme reactant gives barriers with free energy of activation below 10 kcal mol^{-1} on the doublet and quartet spin states. Clearly, these reactions will be fast and efficient and it is unlikely that NO_2 will drift out of the substrate binding pocket if substrate is present. Obviously, it is important that NO_2 does not drift out of the protein pocket as it is known to activate aromatic protein residues and could react with enzymatic residues if the substrate is not positioned well (Lang *et al.*, 2016)

In particular, the substrate binding pocket of the 4TPO pdb file[21] is lined with several aromatic residues, e.g., Phe$_{79}$, Trp$_{82}$, Tyr$_{89}$, Trp$_{297}$ and Phe$_{395}$. Clearly, peroxynitrite activation and the synthesis of NO_2 should not lead to nitration of any of these active site

residues. Therefore, NO_2 should be used as soon as it is found and based on the low barrier will activate bound substrate rapidly.

As our proposed mechanism of L-Trp nitration by P450 enzymes suggests the formation of a free NO_2 radical after homolytic cleavage of peroxynitrite, we decided to explore pathways leading to C^4-, C^5-, C^6- and C^7-nitration for model **B**. Of course, these mechanisms have two stereochemical isomers, which are designated as the exo- and endo-pathways. Optimized geometries of all ^{2,4}**TS4**$_B$ transition states are given in Figure 4.3, while the one for C^6_{endo} is above in Figure 4.1. As this reaction step proceeds away from the heme center and no electron transfer takes place, it means that the heme CpdII distances are the same in all structures. Indeed, the Fe–O and Fe–S distances shown in Figure 4.3 show very little variation. A little bit more variation is seen in the C–N bond that is being formed in the transition state. The shortest distances are found for C^5-activation whereby the endo-pathway gives the shortest distances of 1.714 Å, while those for the exo-pathway are 1.721 Å. By contrast, much longer C–N distances are found for the C^7-activation with values of 1.830/1.831 Å for ^{2}**TS4**$_{B,C7\text{-}endo}$/^{4}**TS4**$_{B,C7\text{-}endo}$ and 1.827/1.842 Å for ^{2}**TS4**$_{B,C7\text{-}exo}$ / ^{4}**TS4**$_{B,C7\text{-}exo}$.

Next, we looked at the energetics for NO_2 transfer to the C^4-, C^5-, C^6- and C^7-positions of L-Trp substrate through attack from the exo and endo directions. We located C–N bond formation transition states (^{2,4}**TS4**$_B$) and the subsequent local minima (^{2,4}**Int4**$_B$) as well as the *ipso*-proton abstraction transition state (^{2,4}**TS5**$_B$) by CpdII leading to the nitrated product complexes ^{2,4}**Int5**$_B$ and the energies with respect to ^{2}**Re**$_B$ for all pathways are given in Table 4.1. Several barriers for C–N bond formation via **TS4**$_B$ are very low in energy and could not be located precisely, but geometry scans find them to be less than 1 kcal mol^{-1} above the **Int1**$_B$ intermediate. These pathways should lead to addition of NO_2 to L-Trp to C^4-exo, C^4-endo, C^5-endo, C^6-exo and C^7-endo positions.

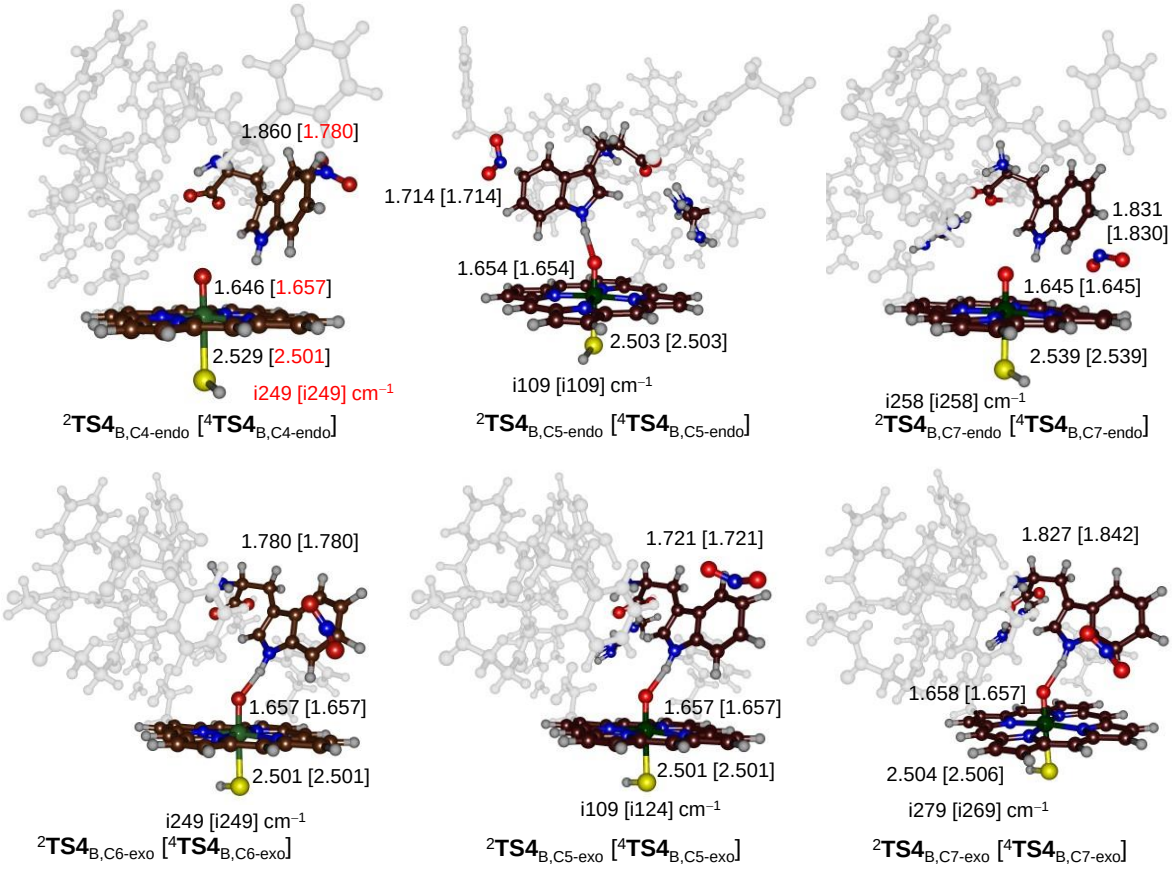

Figure 4.3. UB3LYP/BS1 optimized transition state geometries for NO_2 attack on L-Trp substrate via ^{2,4}**TS4**$_B$. N–C bond formation barriers calculated for attack on the C^4, C^5, C^6 and C^7-positions. Bond lengths are in angstroms and the imaginary frequency in the transition state in cm^{-1}.

As a matter of fact most **TS4**$_B$ barriers are found within a small window of 4 kcal mol^{-1} and only doublet spin C^4-endo is higher in energy, i.e. its transition state is about 7 kcal mol^{-1} above ^{2}**Int1**$_B$. The NO_2 addition local minimum (^{2,4}**Int4**$_B$) is followed by proton abstraction from the ipso-position by CpdII to form nitrated Trp and protonated CpdII. Due to the position of the substrate in the binding pocket in several cases substantial proton abstraction barriers are found. Thus, the C^6- and C^7-positions of L-Trp are pointing toward the iron(IV)-oxo group of the heme and hence are in the right position for proton

transfer. Indeed, most **TS5**$_B$ barriers for C^6- and C^7-nitration barriers of less than 7 kcal mol^{-1} with respect to isolated reactants are found. By contrast, the C^5-exo position points away from the heme and consequently proton transfer is difficult and high barriers are obtained as a result of major structural orientations.

Overall, the work shows that the aromatic nitration by P450 TxtE is triggered by a reaction of NO with an iron(III)-superoxo species that releases NO2 radicals rapidly. These NO2 radicals react with aromatic rings through nucleophilic addition and the nearby CpdII species abstracts a proton to form nitrated products. However, as a free NO_2 radical is formed, this means substrate selectivity will be determined by the tightness and orientation of Trp in the substrate binding pocket. How and why this selectivity is determined, we discuss further in the paper.

4.4 Discussion

In this work a computational study on the P450 aromatic nitration enzyme TxtE is performed that focuses on the catalytic reaction mechanism and the nature of the selectivity of the reaction. Overall, our studies show that the mechanism is distinctly different from P450 monoxygenases, where initially an active species (Compound I, CpdI) is formed that subsequently reacts with substrates (Sono *et al.*, 1996; Kadish, Smith and Guilard, 2013; Sevrioukova and Poulos, 2013; Poulos, 2014; Guengerich and Yoshimoto, 2018; Huang and Groves, 2018). To explain the differences in catalytic reaction cycle of P450 TxtE and P450 monoxygenases we display the two side-by-side in Scheme 4.4. Both catalytic cycles start from an iron(III)-heme complex that is linked to the protein through a thiolate bridge with a cysteinate residue. The sixth coordination site of the iron(III) is occupied by a water molecule in the resting state (structure **A** in Scheme 4.4). Upon substrate binding the water molecule is released and the metal complex undergoes a spin-state change from low-spin to high-spin. DFT calculations showed that the high-spin is preferential over the low-spin in the 5-coordination iron(III) complex,

whereas the spin-state ordering is reversed in 6-coordinate environments (De Visser and Shaik, 2003).

Table 4.1. Relative energies of NO2 transfer to various positions of L-Trp substrate.[a]

Pathway	^{2}**TS4**$_{B}$ (^{4}**TS4**$_{B}$)	^{2}Int4$_{B}$ (^{4}Int4$_{B}$)	^{2}**TS5**$_{B}$ (^{4}**TS5**$_{B}$)	^{2}Int5$_{B}$ (^{4}Int5$_{B}$)
C^{4}-exo	>-3.0 (>-3.0)	-3.5 (-3.5)	>6.6	-58.0 (-22.2)
C^{4}-endo	6.6 (>0.0)	6.4 (-1.4)	11.0 (15.0)	-49.2(-14.9)
C^{5}-exo	0.9 (0.9)	-0.6 (0.0)	16.9 (17.9)	-49.6(-15.8)
C^{5}-endo	>3.0 (>0.0)	2.7 (-4.2)	8.3 (10.3)	-57.7 (-23.6)
C^{6}-exo	0.6 (-0.1)	0.3 (-0.4)	6.1 (6.6)	-40.8 (-46.9)
C^{6}-endo	3.2 (2.2)	0.2 (1.1)	6.4 (6.1)	-45.9 (-40.8)
C^{7}-exo	2.4 (2.4)	0.2 (0.2)	2.7 (4.5)	-60.9(-56.1)
C^{7}-endo	-1.0 (-1.0)	-1.6 (0.2)	1.8 (3.8)	-56.9 (-27.2)

*a*Values in kcal mol^{-1} represent ΔE+ZPE data with energies obtained at UB3LYP/BS1//UB3LYP/BS2 relative to ^{2}**Re**$_{B}$.

Thereafter, the complex is reduced by the reduction partner and binds molecular oxygen (complex **B** in Scheme 4.4). Beyond complex **B**, the catalytic cycles of P450 monoxygenase and P450 nitration diverge. Thus, the monoxygenases reduce structure **B** and after two proton transfer steps generate a high-valent iron(IV)-oxo heme cation radical species called CpdI. The latter reacts with substrates through oxygen atom transfer and converts aliphatic C–H bonds into alcohols, C=C double bonds into olefins and arenes into phenols (Sono *et al.*, 1996; Meunier, de Visser and Shaik, 2004; De Montellano,

2005; Ortiz De Montellano, 2010; Kadish, Smith and Guilard, 2013; Huang and Groves, 2017, 2018; Greule *et al.*, 2018).

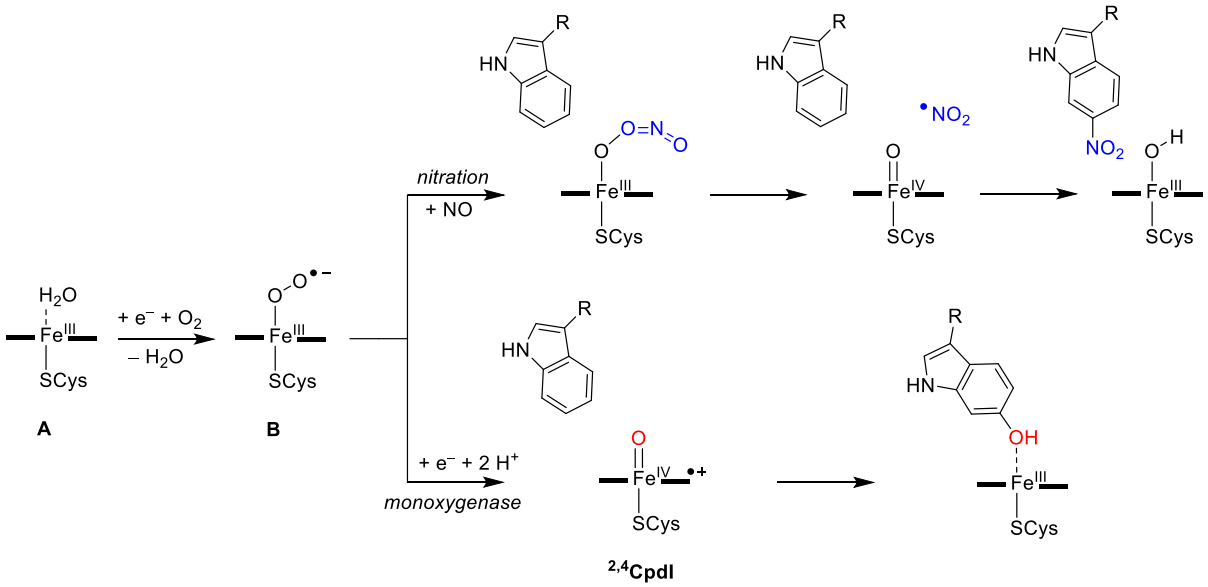

Scheme 4.4. Comparative catalytic cycles of P450 nitration and P450 monoxygenases.

The P450 TxtE isozymes, by contrast, bind a molecule of NO that reacts with the iron(III)-superoxo intermediate (**B**) to form an iron(III)-peroxynitrite intermediate. As discussed above, several pathways for NO_2 transfer to L-Trp substrate were calculated here and our lowest energy mechanism involves a reaction that starts with the iron(III)-peroxynitrite splitting into Compound II (CpdII), i.e. iron(IV)-oxo heme, and NO_2 radical. The latter then attacks substrate at the C^4-position and the *ipso*-proton at C^4 moves to Cpd II to generate an iron(III)-hydroxo complex. A proton transfer from the protein then brings the catalytic cycle back into the resting state. At this stage it is not clear whether this proton transfer step happens prior or after product release.

The catalytic cycles of P450 nitration and monoxygenation in Scheme 4.4 show dramatic differences. Thus, P450 TxtE would require only a single electron from a reduction partner and no proton transfer to generate an iron(III)-peroxynitrite as active species, whereas P450 monoxygenases need two electrons and two external protons to form CpdI. However, one proton transfer is needed in P450 TxtE to convert protonated Compound II back into the resting state.

To understand these differences in proton relay mechanisms during the catalytic cycle of P450 TxtE and P450 mooxygenases, we analyzed structures of two representative nitration and monoxygenase enzymes, and extracts of two pdb structures are shown in Figure 4.4. In particular, Figure 4.4 displays an extract of the active site structures of P450 TxtE (4TPO pdb as a representative of a nitration P450)[21] and $P450_{cam}$ (3WRH pdb as a monoxygenase P450 structure) (De Visser, 2006; Shaik *et al.*, 2011). Thus, $P450_{cam}$ hydroxylates camphor regio- and stereoselectively at the C^4-position and its mechanism has been extensively studied with experimental and computational methods (Berman *et al.*, 2000; Davydov *et al.*, 2001; Balding *et al.*, 2008). An analysis of the 4TPO pdb file as compared to that of $P450_{cam}$ is given in Figure 4.4.

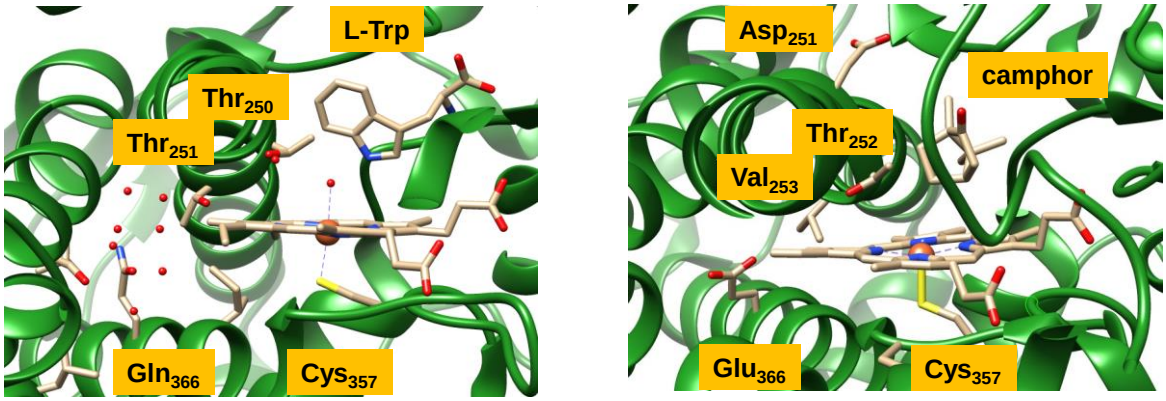

Figure 4.4. Extracts of the crystal structure coordinates of P450 TxtE (left) and $P450_{cam}$ (right) as taken from the 4TPO and 3WRH prdb files. Amino acids are labeled as in the pdb files.

As rationalized and discussed previously (Kamachi and Yoshizawa, 2003; Shaik *et al.*, 2005), $P450_{cam}$ has a number of active site residues involved in proton-relay during the catalytic cycle. Firstly, a buried Glu_{366} residue is connected via a chain of water molecules to the alcohol group of Thr_{252} that is located just above the heme. The Glu_{366} residue is believed to deliver the first proton in the catalytic cycle of P450 monoxygenases (Kamachi and Yoshizawa, 2003), while Asp_{251} delivers the second one. The Asp_{251} residue points out of the active site, but computational modelling showed that a rotation of the side chain brings the carboxylate group close to the Thr_{251} alcohol group and hence can deliver a second proton into the substrate binding pocket to complete the formation of CpdI.

An analysis of the TxtE pdb file 4TPO shows that the Glu_{366} residue is missing and is replaced by a Gln residue. Nevertheless, the Gln environment is similar to that of Glu_{366} in $P450_{cam}$, namely at the end of a cavity surrounded by apolar residues, such as Leu and Ile. Interestingly, also Val_{253} is not seen in P450 TxtE and in its position another Thr residue is located (Thr_{251}). Nevertheless, it is clear from the TxtE pdb file that one proton source is lacking in the active site. Therefore, proton transfer in P450 TxtE will be considerably

slower than in $P450_{cam}$, where one proton may already be stored on Glu_{366} prior to the start of the catalytic cycle, which should lead to efficient conversion of the iron(III)-superoxo to an iron(III)-hydroperoxo complex. As such, we predict that mutation of Gln_{366} in P450 TxtE to Glu (or Asp) may enable monoxygenase activity of substrates. On the other hand, the mutation of Glu_{366} to Gln in $P450_{cam}$ should reduce or slow the protonation steps during the catalytic cycle and in the presence of NO might lead to aromatic nitration of substrates.

In $P450_{cam}$ the second proton in the catalytic cycle is proposed to be delivered through the rotation of Asp_{251}. In the TxtE pdb; however, also this Asp residue is missing and a proline residue takes its position. Therefore, the proton transfer machineries in P450 TxtE appear to have been mutated away with respect to typical monoxygenase structures and consequently, proton transfer into the active site for the conversion of the iron(III)-superoxo species into CpdI is hampered. This should give the iron(III)-superoxo species a relatively long lifetime until NO is delivered and can form a heme-peroxynitrite complex.

To find out if a bare indole group in the gas-phase would have a preference of nitration of a specific carbon site, we calculated the C–N bond formation energy by addition of NO_2 to methylindole, see Figure 4.6. As can be seen in all cases the formation of nitrated methylindole is endothermic by 10.5 – 15.3 kcal mol^{-1} in the gas-phase with a preference of activation of the C^4-position. As such, if all carbon atoms of L-Trp are accessible in the protein then a reaction with NO_2 should give dominant C^4-nitration. Indeed some studies have observed this. The fact that in the calculations reported in Table 4.1 above a mixture of products is predicted implies that our model has sufficient flexibility and freedom to access multiple sites.

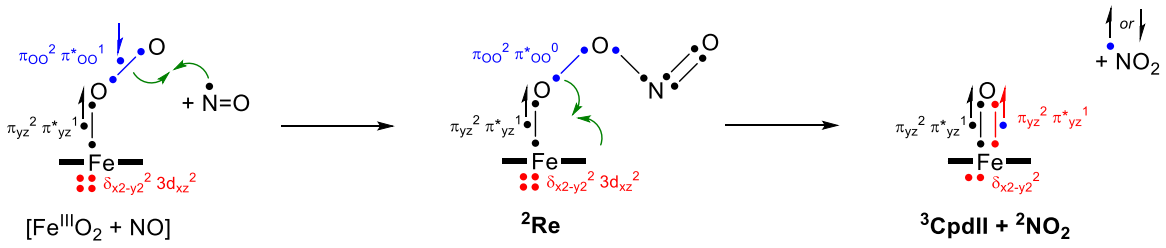

Figure 4.5. Valence bond scheme for the electron migrations during the conversion of the ferric-superoxo and NO into CpdII and NO_2 via a peroxynitrite intermediate.

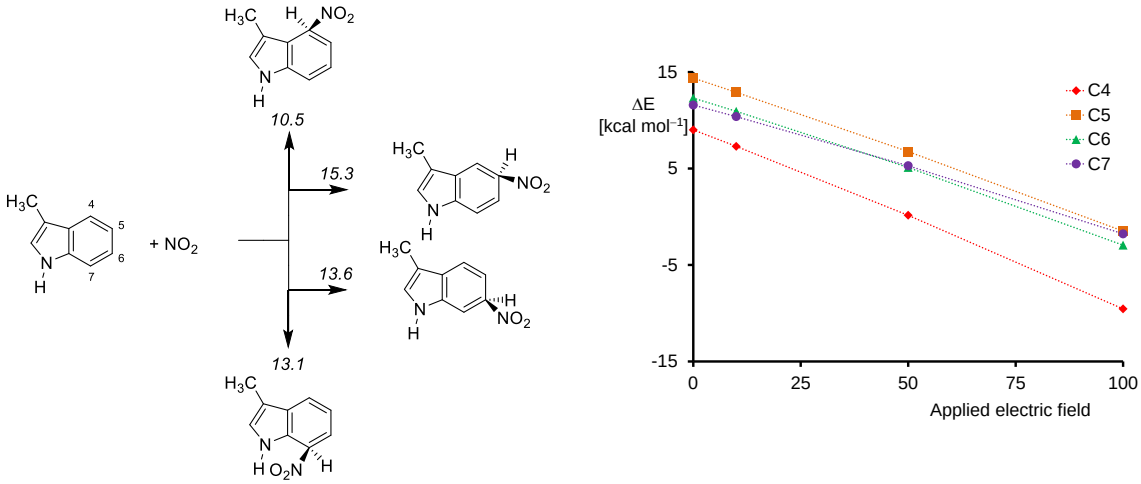

Figure 4.6. (a) UB3LYP/6-31G* calculated C–N bond formation energies in a bare methylindole molecule. Values are ΔE+ZPE data in kcal mol^{-1}. (b) Electric field effect on the relative energies of NO_2 addition to methylimidazole along the z-axis.

4.5 Conclusion

In this work a computational study is presented on the possible reaction mechanisms of aromatic nitration by a CYP450 isozyme. We set up several active site model complexes with bound L-Trp and investigate substrate activation pathways leading to nitration as well as oxidation of substrate. We find low-energy barriers for the homolytic cleavage of iron(III)-peroxynitrate into NO_2 and CpdII. Consequently, the reaction of NO and O_2 on an iron(III)-heme center is expected to generate free NO_2 radicals efficiently. We then explored NO_2 attack on L-Trp and find pathways for activation of the C^4, C^5, C^6 and C^7-position. Although NO_2 addition is generally a low-energy process, many pathways encounter relatively high energy proton transfer steps to form products. As such substrate positioning and binding will be essential in CYP450 TxtE to enable a selective reaction process.

Chapter 5

PROJECT 3

Second-coordination Sphere Effect on the Reactivity of Vanadium-Peroxo Complexes: A Computational Study

M. Qadri E. Mubarak,[‡] and Sam P. De Visser[‡]

[‡] The Manchester Institute of Biotechnology and Department of Chemical Engineering and Analytical Science, The University of Manchester, 131 Princess Street, Manchester M1 7DN, United Kingdom

Abstract

Vanadium-oxo and vanadium-peroxo complexes are common intermediates in biology and are, for instance, found in the catalytic cycle of vanadium haloperoxidases. In biomimetic chemistry synthetic models have been created that mimic the structural features of the coordination environment of these vanadium-oxo and vanadium-peroxo species. Recently two novel vanadium-oxo complexes were trapped and characterized with a trigonal bipyramidal ligand design with either a solvent exposed vanadium center or the vanadium inside a cage designated the "bowl"-shaped configuration and the "dome"-shaped structure, respectively. Density functional theory calculations are reported on these "bowl"- and "dome"-shaped structures and study the reaction with t-butylhydroperoxide to form the vanadium-peroxo species and its reaction with thioanisole. Although the structural features of the vanadate core are close for both structures; the calculations display a strong second-coordination sphere effect of the ligand architecture on the barrier heights of the reaction with a terminal oxidant even though the rate-determining transition states show little structural differences. A similar observation is seen for the reaction of the two vanadium-peroxo species with thioanisole. Overall, the calculations implicate that vanadium-peroxo is an efficient oxidant of sulfoxidation reactions although not as efficient as analogous iron(IV)-oxo heme and nonheme oxidants that react with substantially lower barriers. The reactivity differences are analyzed with thermochemical cycles and valence bond patterns that explain the differences in chemical properties and identify how the ligands affect the chemical reactivity with substrates.

Published Reference
Mubarak, M. Qadri E. and Sam P. De Visser. "Second-coordination Sphere Effect on the Reactivity of Vanadium-peroxo Complexes: A Computational Study" Inorganic Chemistry (2019).

5.1 Introduction

Metalloenzymes are commonly used in biological systems and have functions ranging from the metabolism of toxic compounds to electron transfer processes and substrate catalysis (Sono *et al.*, 1996; Solomon *et al.*, 2000; Costas *et al.*, 2004; Meunier, de Visser and Shaik, 2004; Abu-Omar, Loaiza and Hontzeas, 2005; Denisov *et al.*, 2005; Kryatov, Rybak-Akimova and Schindler, 2005; van Eldik, 2007; Bruijnincx, Van Koten and Gebbink, 2008; Ortiz De Montellano, 2010; SP de Visser, 2011; McDonald and Que, 2013; Nam, Lee and Fukuzumi, 2014; Huang and Groves, 2017). Despite its relatively large natural abundance, surprisingly there are very few vanadium-containing metalloenzymes in Nature. One of those is nitrogenase, which is a key enzyme in the biological nitrogen cycle. Nitrogenase has an active site cluster containing seven iron atoms and one vanadium or molybdenum atom that are bridged by nine sulfur atoms and a central carbide atom (Burgess and Lowe, 1996; Hu and Ribbe, 2011; Hoffman *et al.*, 2013; Eady, Antonyuk and Hasnain, 2016). This catalytic center is involved in the reduction of N2 to ammonia, although the exact function of the vanadium atom in the cluster remains unknown. Another vanadium-containing natural system is the vanadium-haloperoxidase enzyme that catalysis the biosynthesis of hypohalide from halide anions and hydrogenperoxide (Butler, 1999; Littlechild *et al.*, 2002; Winter and Moore, 2009; Wever and Van Der Horst, 2013; Leblanc *et al.*, 2015; Wever and Barnett, 2017; Craig C. McLauchlan *et al.*, 2018).

As these vanadium-containing enzymes react very fast, few short-lived catalytic cycle intermediates have been trapped and characterized. It is known that vanadium-haloperoxidases start from a vanadium(V)-oxo species that binds two hydroxo groups and is linked to the protein through a single covalently-linked histidine bridge. During the catalytic cycle the vanadium ion reacts with H_2O_2 to form a side-on vanadium-peroxo complex. The latter reacts with halides to form hypohalide that drifts

out of the active site and attacks a substrate usually through double bond activation to form halogenated substrate.

To gain insight into vanadium complexes in various coordination environments and oxidation states, biomimetic models have been synthesized and their reactivities studied (Colpas et al. 1996; Kravitz and Pecoraro 2005; Conte et al. 2011; Licini et al. 2011; Xia, Cormier, and Chen 2012; Egdal et al. 2005). For instance, these studies trapped and characterized vanadium(IV)-oxo (Smith, LoBrutto and Pecoraro, 2002; Fox *et al.*, 2004; Harada, Okawa and Kojima, 2005; Ghosh, Patra and Rath, 2008; Cordelle *et al.*, 2010; Mihaylov, Parac-Vogt and Pierloot, 2012; Hossain *et al.*, 2019), vanadium(V)-oxo (Bortolini and Conte, 2005; Hoppe, Limberg and Ziemer, 2006; Sessler, Tomat and Lynch, 2006; Zhang *et al.*, 2012), and vanadium-peroxo complexes using a range of spectroscopic and analytical techniques (Conte *et al.*, 2000; Kravitz and Pecoraro, 2005; Zampella *et al.*, 2005; Sun *et al.*, 2014; Schwendt *et al.*, 2016; Craig C. McLauchlan *et al.*, 2018). In particular, Pecorara et al reported the synthesis of vanadium(V)-oxo-peroxo complexes with trigonal bipyramidal configuration (Colpas *et al.*, 1996; Kravitz and Pecoraro, 2005). The complexes with peroxo bound were characterized spectroscopically with infrared (IR) spectroscopy and found to have peaks at around 920 cm^{-1} for the peroxo stretch vibration and 563 cm^{-1} for the V=O stretch vibration. Both bands had a very strong red-shift upon replacement of ^{16}O by ^{18}O in the molecular spectrum.

Some of these vanadium-oxo and vanadium-peroxo complexes have shown interesting reactivities, and, for instance, were found to react with olefins through epoxidation (Licini et al. 2011; Vandichel et al. 2012), but also were shown to activate C–H bonds leading to aliphatic hydroxylation (Dragancea *et al.*, 2016; J. Zhang *et al.*, 2017; Fomenko *et al.*, 2019; Ikbal *et al.*, 2019). Furthermore, several examples of substrate sulfoxidation has been observed (Conte and Floris, 2010; Sutradhar *et al.*, 2015; Salonen, Peuronen and Lehtonen, 2017). Recently, a series of trigonal bipyramidal vanadium-oxo structures were synthesized and characterized with binaphthol groups, namely structures **A** “bowl” and **B** “dome” as displayed in Scheme 5.1 (Zhang *et al.*, 2016; D. Zhang *et al.*, 2017). Thus, the

bowl-shaped structure has the vanadium-oxo group solvent exposed with the oxidant in a ligand structure at the bottom of a bowl. By contrast, structure **B** is a closed-conformation, where access is limited and restricted by the ligand periphery. These two systems were shown to give differences in reactivities with sulfides through second-coordination sphere effects.

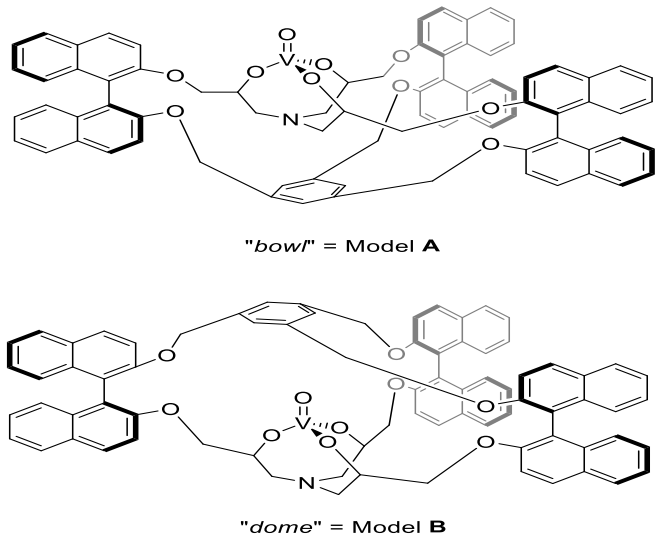

Scheme 5.1. Structures of complexes and reactions discussed in this work.

Despite the fact that quite some experimental results have been reported on the structure and reactivity of vanadium-oxo complexes; surprisingly, few computational studies have been published on these systems. Several computational studies were reported on the mechanism of haloperoxidase activity by vanadium-dependent haloperoxidases and biomimetic model complexes (Conte *et al.*, 2000; Fox *et al.*, 2004; Kravitz and Pecoraro, 2005; Zampella *et al.*, 2005; Sun *et al.*, 2014; Schwendt *et al.*, 2016). In addition, computational predictions of NMR parameters of intermediates in the catalytic cycle of vanadium-dependent haloperoxidases were reported (Waller *et al.*, 2007; Geethalakshmi *et al.*, 2009). In recent work, we explored the second-coordination sphere effect in iron-containing enzymes and biomimetic model complexes (Timmins, Saint-André and

De Visser, 2017; Timmins, Fowler, *et al.*, 2018; Mukherjee *et al.*, 2019). These studies gave insight into how the second-coordination sphere influences the positioning of the substrate and oxidant and enable efficient reactivity. Based on that we got intrigued by the bowl and dome shaped structures shown in Scheme 5.1 and decided to do a computational study into their chemical properties and reactivity. Our work shows that the accessibility of the vanadium center affects the rate constants for oxygen atom transfer dramatically and makes the oxidant more efficient.

5.2 Methods

We used the crystal structure coordinates of Ref (Zhang *et al.*, 2016; D. Zhang *et al.*, 2017) as starting points of the bowl- and dome-shaped vanadium-oxo complexes (Scheme 5.1) designated **A** and **B**. These structures have the ligand bound to a vanadate anion as shown in Scheme 5.1 and have overall charge 0. Our initial work focused on the mechanism for the conversion of vanadium(V)-oxo into vanadium-peroxo through a reaction with t-butylhydroperoxo (tBu-OOH). In a second set of calculations the reactivity of the vanadium-peroxo and vanadium-oxo complexes with thioanisole to form sulfoxide products was studied with DFT.

All calculations were performed in Gaussian-09 (Frisch, Hratchian and Nielsen, 2009), and utilized the unrestricted B3LYP hybrid density functional method (Lee, Yang and Parr, 1988; Becke, 1993). Geometry optimizations, frequencies and geometry scans were performed using the LANL2DZ basis set on vanadium with electron core potential and 6-31G* on the rest of the atoms: basis set BS1 (Francl *et al.*, 1982; Hay and Wadt, 1985). To correct the energies single point calculations on the optimized geometries were done with the LACV3P+ basis set on vanadium with electron core potential and 6-311+G* on the rest of the atoms: basis set BS2. Solvent was included in the BS2 calculations with the continuum polarized conductor model (CPCM) with a dielectric constant mimicking chlorobenzene (Tomasi, Mennucci and Cammi, 2005). Vibrational frequencies reported here are unscaled values. The methods described here have been extensively tested and

validated and were shown to reproduce experimental free energies of activation to within va few kcal mol^{-1} and correctly predicted chemo- and regioselectivities (Kumar *et al.*, 2014; Yang *et al.*, 2016; Pickl *et al.*, 2019).

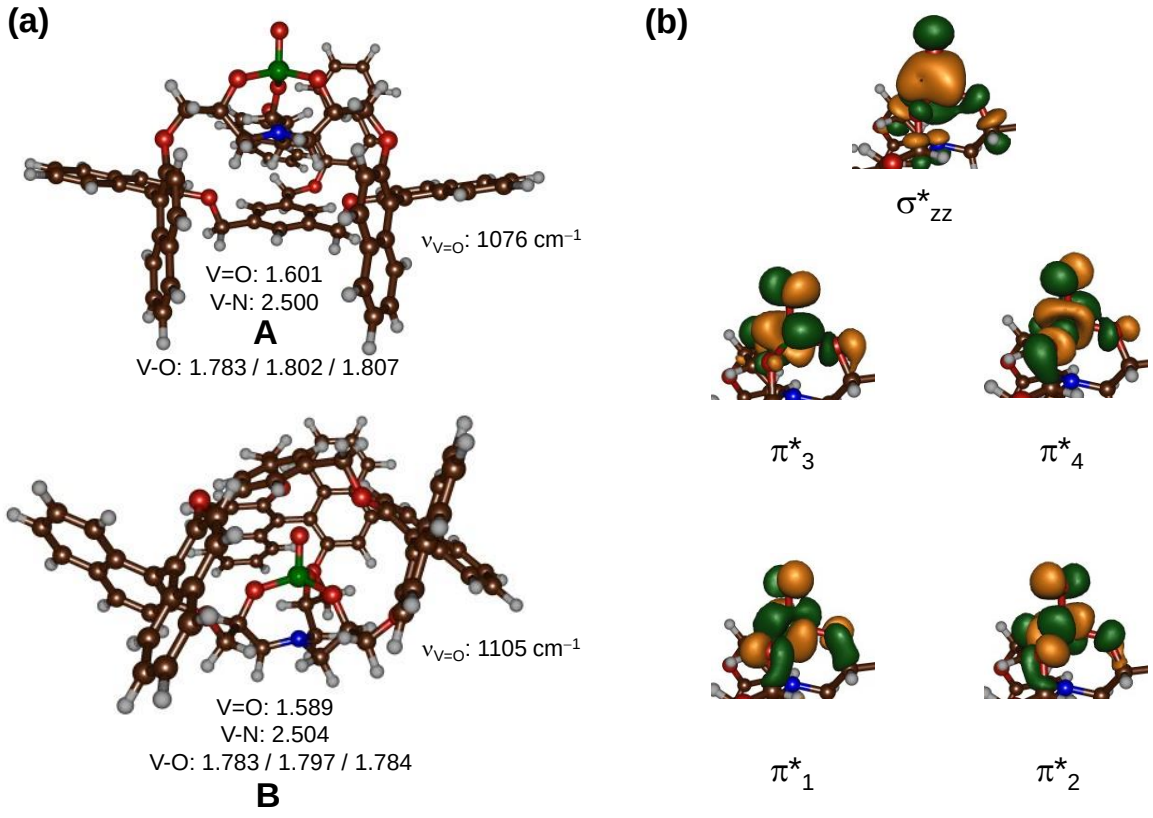

Figure 5.1. (a) UB3LYP/BS1 optimized geometries of A and B as obtained in Gaussian-09 with bond lengths in angstroms and the V=O stretch vibration in cm^{-1}. (b) Molecular orbitals of A.

Energies reported here are solvent corrected enthalpies ($\Delta E+ZPE+E_{solv}$) that contain electronic energies (at UB3LYP/BS2 level of theory) corrected with zero-point energy (ZPE) and solvent corrections (E_{solv}). In addition, free energies are reported at 298 K that take the solvent corrected enthalpies with added thermal and entropic corrections.

To test the effect of dispersion on the energetics of the reaction a series of single point calculations at UB3LYP-D3/BS2 level of theory were performed for the reaction mechanisms. In general, no dramatic changes are seen and the trends and conclusions remained the same, see Supporting Information for details.

5.3 Results and Discussion

We started the work with an electronic and structural comparison of the "bowl"- and "dome"-shaped vanadium(V)-oxo complexes A and B. Figure 5.1 displays the optimized geometries of A and B as well as relevant high-lying occupied and low-lying virtual molecular orbitals. The two coordination environments of structure A and B are very different, whereby in A the vanadate is solvent-exposed, while in B it is encapsulated by the ligand architecture. Nevertheless, little changes in the optimized geometries are seen. Thus, the three V-O interactions that link the metal to the ligand through ether bonds are 1.783 – 1.807Å for A, whereas they range from 1.783 – 1.797Å for B; and hence are of similar magnitude. Also the vanadium-amine interaction stays almost the same with values of 2.500 and 2.504Å for A and B, respectively. Therefore, the direct coordination environment of the vanadate center has not changed dramatically, whether it is solvent exposed or closed-in. Only a small change in the V=O bond length is seen, which drops by 0.012Å between A and B, although this may not be significant. Due to the small drop in V=O bond length, these complexes display slightly different V=O stretch vibrations ($\nu_{V=O}$) of 1076 and 1105 cm^{-1}, respectively. Our V=O stretch vibrations match experimental reports for pentacoordinated vanadium-oxo complexes from the literature well.[6e]

Specifically, Poli et al obtained values around 977 – 999 cm^{-1} for three vanadium(V)-oxo complexes. On the other hand, for an octahedral-bound vanadium(IV)-oxo corrolazine complex a V=O stretch vibration of 975 cm^{-1} was observed (Fox *et al.*, 2004), while Kojima et al (Harada, Okawa and Kojima, 2005) find a value of 998 cm^{-1} for a vanadium(IV)-oxo tetraphenylporphyrin system. However, the stretch vibrations are

considerably higher in value than those reported for iron(IV)-oxo complexes (typically these are in the 800 – 900 cm^{-1} range) (Borovik, 2005; Martinho *et al.*, 2005; de Visser *et al.*, 2013; Lee *et al.*, 2017) despite the fact that the mass of iron is only about 10% larger than that of vanadium. Our optimized geometries are also in good agreement with previous computational studies on vanadate complexes (Conte *et al.*, 2000; Fox *et al.*, 2004; Kravitz and Pecoraro, 2005; Zampella *et al.*, 2005; Sun *et al.*, 2014; Schwendt *et al.*, 2016).

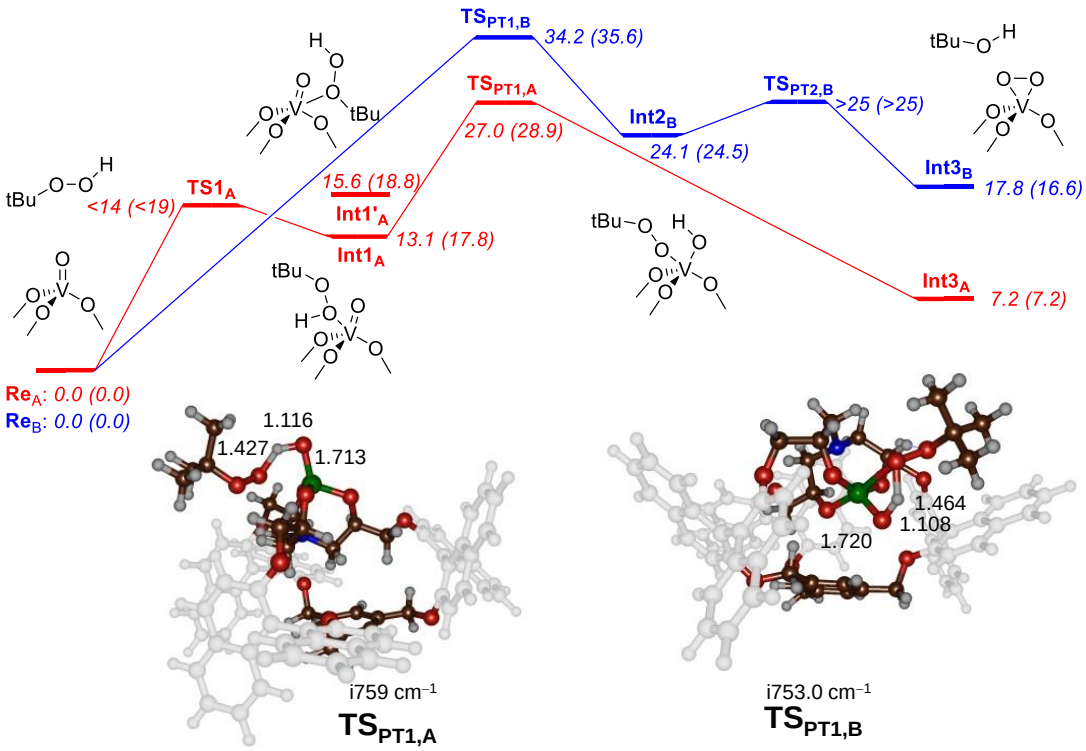

Figure 5.2. Potential energy landscape, $\Delta E+ZPE+E_{solv}$ and ΔG (in parenthesis) data in kcal mol^{-1}, for the reaction of vanadium-oxo complexes **A** and **B** with tBuOOH as calculated at UB3LYP in Gaussian-09. Optimized geometries of the rate-determining proton-transfer transition states are given with bond lengths in angstroms and the imaginary frequency in cm^{-1}. The landscape in red is for the bowl-structure **A**, while the landscape in blue is for the dome-structure **B**. Relative energies are with respect to **Re**

and obtained at UB3LYP/BS2, while ZPE, thermal corrections and entropies are taken from the UB3LYP/BS1 frequency files.

Relevant valence orbitals of **A** are shown on the right-hand-side of Figure 5.1. All high-lying occupied orbitals are ligand based. However, the two lowest virtual orbitals (LUMO and LUMO-1) are vanadate-based, i.e. π^*_1 and π^*_2. These orbitals reflect the antibonding interactions of the vanadium with its four oxygen ligands. Somewhat higher in energy are another pair of π^* antibonding interactions in that scaffold, namely π^*_3 and π^*_4. Well higher in energy is the interaction of the $3d_z2$ orbital on vanadium with a $2p_z$ orbital on the oxo group. Thus, electron abstraction by **A** will most likely result in occupation of one of these π^* orbitals with one electron and hence reduction of vanadium(V) to vanadium(IV). These set of orbitals are similar in size and shape for complex **A** and **B** and therefore, based on the electronic and structural features of the vanadate core no huge differences in reactivity and chemical properties are expected.

5.3.1 Conversion of Vanadium-Oxo Into Vanadium-Peroxo.

s the experimental studies of Ref 13 investigated the reaction in the presence of tBuOOH, we started with work on the vanadium(V)-oxo complexes with this oxidant. In particular, we investigated the pathways for conversion of the vanadium(V)-oxo species with t-butylhydroperoxide into a vanadium-peroxo complex and details of the lowest energy mechanisms are given in Figure 5.2. The overall reaction mechanism requires the heterolytic cleavage of the peroxo bond of tBuOOH in order to form the vanadium-peroxo species. The reaction starts from the reactant complexes of **A** and **B** with tBuOOH bound (**Re**$_A$ and **Re**$_B$), which have tBuOOH in the vicinity of complex **A** and **B**, respectively. These structures have the same electronic configuration and geometric features as the isolated complexes from Figure 5.1 (see Supporting Information Figures S2, S3 and S8).

Subsequently, the reaction proceeds with the hydroperoxo group binding to the vanadium center to form the hydroperoxo bound complex **Int1**. Two tBuOOH binding pathways were tested namely by binding through its distal and proximal oxygen atom to the

vanadium center. We did not manage to locate transition states for these steps and constraint geometry scans implicate the processes to be facile without a reaction barrier. For the open structure (**A**) two intermediates (**Int1$_A$** and **Int1'$_A$**) were located, which bind the tBuOOH either via the proximal or distal oxygen atom to the vanadium center. Complex **Int1$_A$** is 2.5 kcal mol^{-1} lower in energy than **Int1'$_A$** and hence the hydroperoxo group will bind the vanadate predominantly with the terminal oxygen atom.

In complex **Int1** a proton transfer from the hydroperoxo to the terminal oxo group takes place via transition state **TS$_{PT1}$** to form the vanadium-tBuOO-hydroxo complex **Int2**. A second proton transfer gives tBuOH and a side-on vanadium-peroxo species **Int3** via transition state **TS$_{PT2}$**. In the open structure, i.e. model **A**, the first proton transfer quickly relaxes the system to the vanadium-peroxo complex **Int3$_A$** and no stable intermediate **Int2$_A$** could be located. Thus, for the open form, the rate-determining reaction step is the first proton-transfer with a barrier of 27.0 kcal mol^{-1}. This is a relatively high barrier and implicates the reaction will be slow. Indeed, the proton-transfer transition state is late, with a long tBuOO-H bond of 1.427Å and a short H-OV distance of 1.116Å. Previous studies of hydrogen atom abstraction reaction by metal-oxo groups found structural relationships with barrier heights, whereby high barriers correlated with late transition states and low barriers with early transition states.[22]

An alternative pathway from **Int1'$_A$** and **Int1'$_B$** with tBu migration from the bound hydroperoxo to the oxo group was also tested, but found to be significantly higher in energy and therefore ruled out (see pathway 2 data in Tables S1 – S4 and Figure S15, Supporting Information). For the open structure this tBu-transfer mechanism encounters a barrier of $\Delta E+ZPE+E_{solv}$ = 37.4 kcal mol^{-1} (Supporting Information Table S2), and leads to a stable intermediate **Int$_{CT,A}$** that is only 7.1 kcal mol^{-1} in energy higher in energy than the reactant complex. Nevertheless, the barrier for reaching this particular intermediate is high and well above that of **TS$_{PT1}$** and hence unlikely to happen.

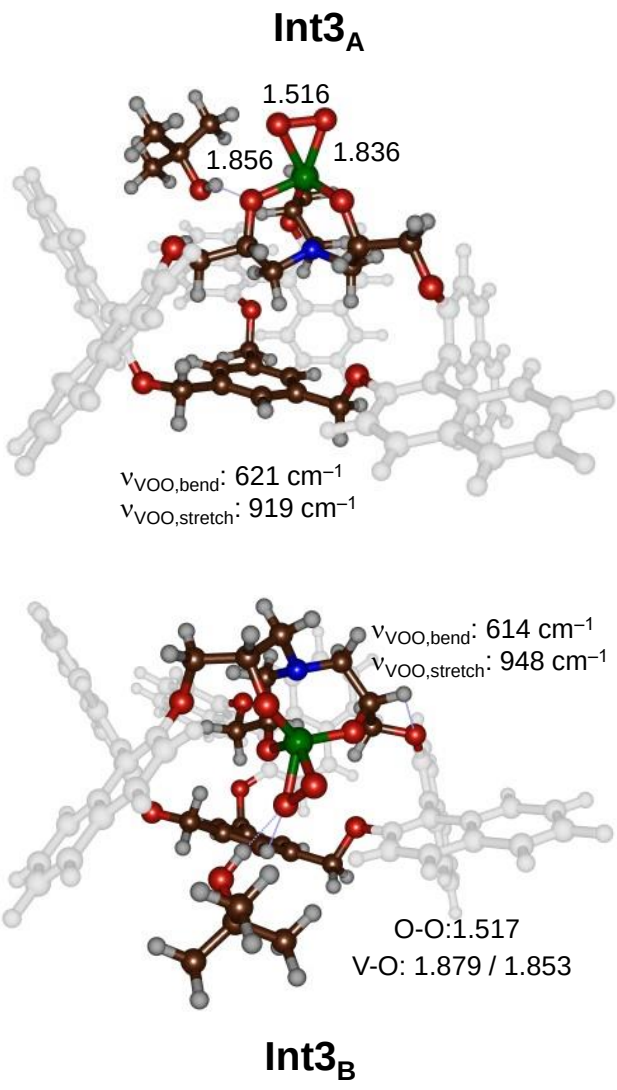

Figure 5.3. Optimized geometries of the vanadium-peroxo complexes (**Int3A**/**Int3B**) as calculated at UB3LYP/BS1 in Gaussian-09. Optimized geometries give bond lengths in angstroms and the imaginary frequency in cm^{-1}.

By contrast to the open structure **A**, the dome structure **B** gives major differences in energy and mechanism along the oxygen activation pathway for the reaction of vanadate with tBuOOH. In particular, the binding of the hydroperoxo group to the metal center is

highly endothermic (>46 kcal mol^{-1}) and probably will not happen at room temperature. Instead, the first proton-transfer from tBuOOH to vanadium-oxo will take place from a non-bound structure and proton-transfer proceeds simultaneously with peroxo binding to the vanadium via **$TS_{PT1,B}$**. This proton-transfer barrier is well higher in energy than that found for **$TS_{PT1,A}$** (by 7.2 kcal mol^{-1}) and probably is the result from the second coordination sphere effect that perturbs the approach of the tBuOOH onto the vanadium center and prevents it from direct binding to the metal center.

Interestingly, the geometry and imaginary frequency of **$TS_{PT1,B}$** is very much alike to that of **$TS_{PT1,A}$** (Figure 5.1) with imaginary frequencies of i759 and i753 cm^{-1}, respectively. Moreover, both structures are product-like with short H–OV distances. The proton-transfer via **$TS_{PT1,B}$** now results in the formation of a complex with tBuOO and hydroxo bound to the vanadium (**Int2**), which via a small barrier **$TS_{PT2,B}$** collapses to the side-on vanadium-peroxo intermediate **Int3**. Overall, the reaction endothermicity for the formation of **Int3** from **Re** is 7.2 kcal mol^{-1} for complex **A**, while it is 17.8 kcal mol^{-1} for complex **B**. Therefore, the second coordination sphere effect affects the thermodynamics of this reaction by almost 10 kcal mol^{-1}. Most probably this is due to the fact that the vanadium-peroxo group fits lesser good into the cavity of the ligand system than the analogous vanadium-oxo group and hence **$Int3_B$** is considerably higher in energy than **$Int3_A$**.

Optimized geometries of **$Int3_A$** and **$Int3_B$** are given in Figure 5.3 for comparison. Structurally there are no huge differences between the solvent-exposed and embedded vanadium-peroxo complexes with an O-O bond length of 1.52Å for both species. Additionally, the V-O distances are about 0.02Å longer for the dome structure than for the bowl structure. As a consequence of these small geometric differences there are spectroscopic differences expected. In particular, we find a peroxo bending vibration of 621 cm^{-1} for **$Int3_A$** and 614 cm^{-1} for **$Int3_B$**. An even larger vibrational shift is observed for the stretch vibration that is 919 cm^{-1} for **$Int3_A$** and 948 cm^{-1} in **$Int3_B$**. These values are in

good quantitative agreement with those reported on analogous vanadium-peroxo complexes.[5ab]

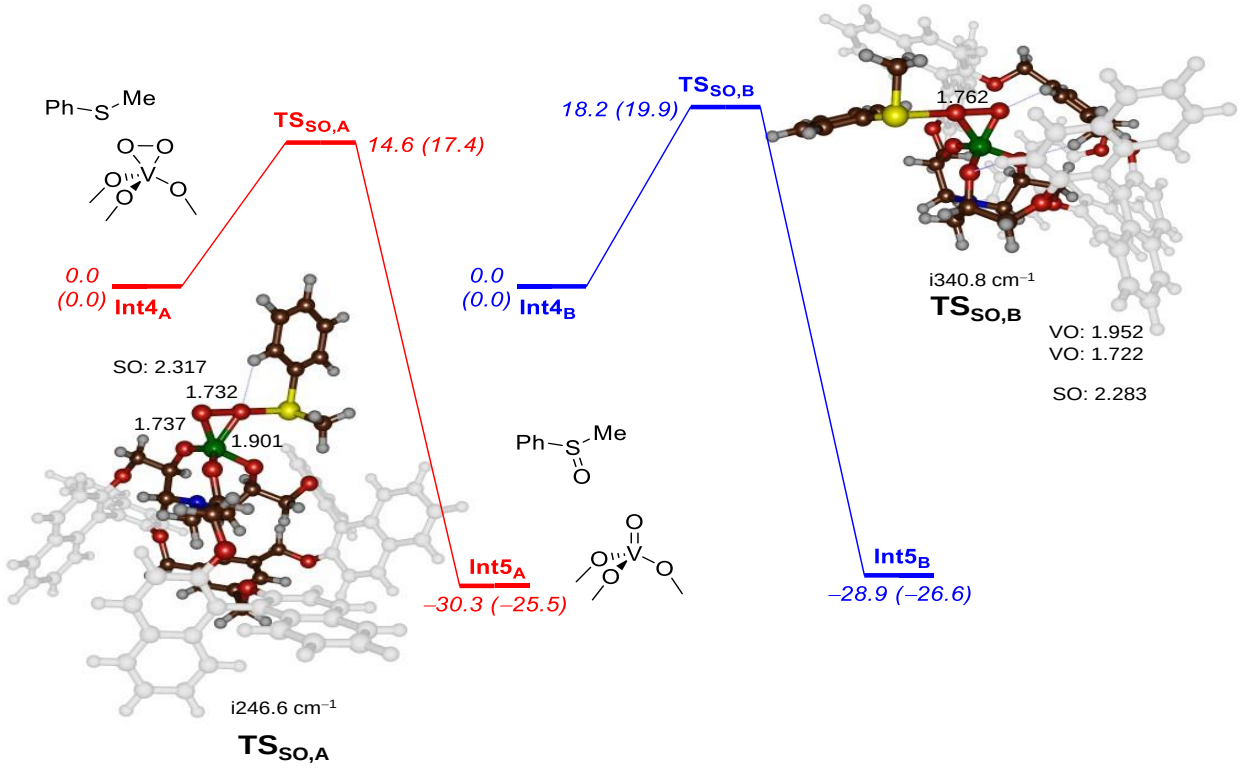

Figure 5.4. Potential energy landscape ($\Delta E+ZPE+E_{solv}$ and ΔG (in parenthesis) data in kcal mol^{-1}) for the sulfoxidation reaction of thioanisole by the vanadium-peroxo complexes as calculated at UB3LYP in *Gaussian*-09. Optimized geometries of the rate-determining proton-transfer transition states are given with bond lengths in angstroms and the imaginary frequency in cm^{-1}. Energies are obtained with basis set BS2, while ZPE, thermal corrections and entropies are taken from the UB3LYP/BS1 frequency files.

5.3.2 Sulfoxidation by the Vanadium-Peroxo Complex.

Subsequently, we calculated the thioanisole sulfoxidation by the vanadium-peroxo complexes with the bowl and dome-shaped ligand systems by replacing tBuOH in **Int3$_A$** and **Int3$_B$** by thioanisole to give structures **Int4$_A$** and **Int4$_B$**. Figure 5.4 displays the potential energy landscapes for the substrate sulfoxidation by the two complexes with key optimized geometries of the transition states. Similar to previous studies on substrate sulfoxidation by metal-oxo complexes (Kumar, Sastry and De Visser, 2011; Vardhaman, Barman, Kumar, C. V. Sastri, *et al.*, 2013), here the sulfoxidation reaction is concerted with a single transition state for S–O bond formation (**TS$_{SO}$**) leading to the sulfoxide product complex (**Int5**). For both the dome and bowl-shaped structures the same mechanism is seen. Not surprisingly, the open structure, i.e. the bowl, displays a significantly lower sulfoxidation barrier than the dome-shaped structure by 3.6 kcal mol^{-1}. As such the second coordination sphere has a major effect on the barrier height and the corresponding rate constant for substrate activation. Nevertheless, the free energies of activation of thioanisole of $\Delta G^{\ddagger}$ = 17.4 and 19.9 kcal mol^{-1} for models **A** and **B** are both well lower in energy than the activation of the vanadium(V)-oxo complex by tBuOOH, where free energies of activation of 28.9 and 35.6 kcal mol^{-1} are found for (Figure 5.2). Therefore, the synthesis of the vanadium-superoxo from the vanadium-oxo species will be rate-determining and affect the turnover frequencies.

Optimized geometries of **TS$_{SO,A}$** and **TS$_{SO,B}$** are shown in Figure 5.4. The imaginary frequency for the sulfoxidation barrier is low (i247 cm^{-1} for **TS$_{SO,A}$** and i341 cm^{-1} for **TS$_{SO,B}$**), which is typical for sulfoxidation transition states that often shows broad peaks with low imaginary frequencies.[23,24] The sulfoxidation transition states have the incoming S–O bond aligned with the peroxo bond and a simultaneous O–O bond cleavage with S–O bond formation takes place. As such, the peroxo bond changes from 1.520/1.519Å in **Int4$_A$**/**Int4$_B$** to 1.732/1.762Å in **TS$_{SO,A}$**/**TS$_{SO,B}$**. The S-O bond in the transition states are 2.317 and 2.283Å for **TS$_{SO,A}$** and **TS$_{SO,B}$**, respectively. Therefore, geometrically **TS$_{SO,A}$**

and $\mathbf{TS_{SO,B}}$ are alike and the structural changes do not explain the differences in energy for the barrier height. In addition, the electronic configuration of the two complexes is similar as well. Consequently, the changes in barrier height between model **A** and **B** is the result of second-coordination sphere effects that affect the approach of the substrate to the catalytic center and does not appear to have resulted from electronic differences.

Finally, we also calculated the direct sulfoxidation by the reactant vanadium(V)-oxo species and find a barrier $\mathbf{TS}_{SO,A2}$ of $\Delta E+ZPE+E_{solv}$ = 18.8 kcal mol^{-1} for model **A**. As such, the direct sulfoxidation by the vanadium(V)-oxo species has a considerably slower reaction rate. However, as the conversion from vanadium(V)-oxo to vanadium-peroxo encounters a high proton transfer step ($\mathbf{TS_{PT1}}$) of 27.0 kcal mol^{-1} the two processes may be competitive and happen in parallel. Therefore, the bowl-type structure reacts via parallel reaction pathways through either a vanadium(V)-oxo or vanadium-peroxo species alongside each other. The dominant pathway, therefore, will depend on the relative concentration of tBuOOH and substrate.

The optimized geometry of $\mathbf{TS}_{SO,A2}$ is given in Figure 5.5. As can be seen the imaginary frequency for the S-O stretch vibration is well higher than that seen for the analogous peroxo complexes and hence the potential energy surface is broader. The transition states have a short S-O distance of 2.049Å and hence the transition state is late on the potential energy surface. At the same time the V-O distance has elongated to 1.736Å.

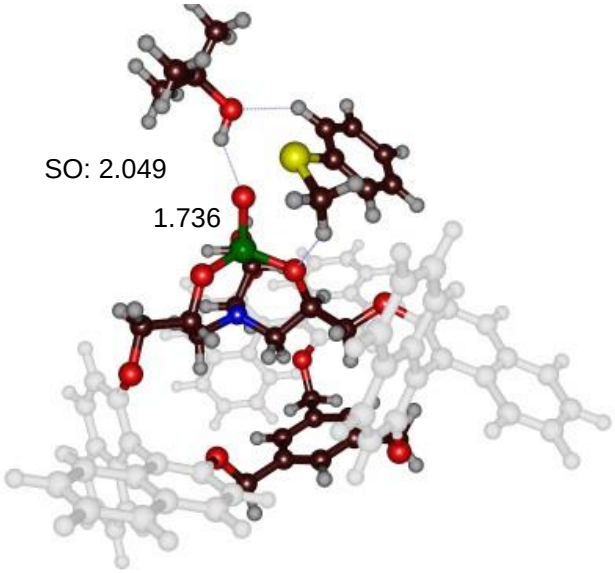

Figure 5.5. Optimized transition state geometry for the direct sulfoxidation reaction of thioanisole by the vanadium(V)- oxo complex of A as calculated at UB3LYP/BS1 in *Gaussian*-09. Bond lengths are in angstroms and the imaginary frequency in cm^{-1}.

5.3.3 Comparison of the Sulfoxidation Barriers with the Literature.

This work reports on the reactivity of two vanadium(V)-oxo complexes with tBuOOH and their formation of vanadium-peroxo intermediates. Subsequently, the sulfoxidation of these complexes by either vanadium-oxo or vanadium-peroxo are compared. It is shown that the second-coordination sphere of the oxidants affects the barrier heights dramatically and leads to an increase of the sulfoxidation barriers by 3.6 kcal mol^{-1}. Using transition state theory this change in barrier height would correspond to a rate enhancement of almost a factor of 200 at 298K. To understand these differences, we compare our obtained barriers with the literature for analogous reactions but also find thermochemical variables of the oxidants that may determine reactivity as well. Let us start with comparing our calculated sulfoxidation barriers with those reported before for iron(IV)-oxo and

manganese(V)-oxo complexes (Kumar, De Visser, *et al.*, 2005; Kumar, Sastry and Visser, 2011; Vardhaman, Barman, Kumar, C. V. Sastri, *et al.*, 2013; Cantú Reinhard, Faponle and de Visser, 2016; Faponle, Seebeck and De Visser, 2017; Mukherjee *et al.*, 2019).

Thus for a selection of sulfides the sulfoxidation reaction by a cytochrome P450 model complex, $[Fe^{IV}(O)(Por^{+\bullet})(SH)]$ with Por = protoporphyrin IX, was reported.[22a] These studies predicted efficient oxygen atom transfer to sulfides, such as methyl-ethyl sulfide, diethyl sulfide and ethyl-phenyl sulfide with activation barriers of around 7–8 $kcalmol^{-1}$. More recently several studies focused on thioanisole sulfoxidation by iron(IV)-oxo species. In particular, Mukherjee et al (Mukherjee *et al.*, 2019) investigated several iron(IV)-oxo oxidants with the N4Py scaffold as pentacoordinated ligand (N4Py = N,N-bis(2-pyridylmethyl)-N-bis(2-pyridyl)methylamine). Several of these complexes had substituents in the second-coordination sphere and affected substrate approach to the oxidant, i.e. the ligands ^{Me}N4Py and N4Py^{Me} contain two methyl groups in hydrogen bonding distance to the metal-oxo on either the front or back of the system. It was shown that these second-coordination sphere perturbations influenced the positioning of the oxidant with respect to substrate and actually enhanced the reactivity. In our work here, little electrochemical differences are seen between the bowl and dome shaped structures. In addition, the structural differences between the transition states is minor, hence the difference in barrier height is due to second-coordination sphere effects.

Table 5.1. Substrate sulfoxidation barriers calculated for metal-oxo oxidants.

Oxidant	$\Delta E^{\ddagger}+ZPE+E_{solv}$	Reference
VO_2 (bowl structure **A**)	14.6	This work
V=O (bowl structure **A**)	18.8	This work
VO_2 (dome structure **B**)	18.2	This work
$^3[Fe^{IV}(O)(N4Py)]^{2+}$	19.9	(Kumar, De Visser, *et al.*, 2005; Faponle, Seebeck and De Visser, 2017)
$^5[Fe^{IV}(O)(^{Me}N4Py)]^{2+}$	5.3	(Mukherjee *et al.*, 2019)
$^3[Fe^{IV}(O)(^{Me}N4Py)]^{2+}$	23.1	(Mukherjee *et al.*, 2019)
$^5[Fe^{IV}(O)(N4Py^{Me})]^{2+}$	1.5	(Mukherjee *et al.*, 2019)
$^3[Fe^{IV}(O)(N4Py^{Me})]^{2+}$	17.5	(Mukherjee *et al.*, 2019)

a. Barriers in kcal mol^{-1} relative to isolated reactants.

b. Energies are obtained with basis set BS2, while ZPE, thermal corrections and entropies are taken from the UB3LYP/BS1 frequency files.

Overall, low barrier heights were found on the quintet spin state surface for the reaction of $[Fe(O)(N4Py)]^{2+}$ with sulfides, but much higher ones were measured for the triplet spin state (Table 5.1). In general, the quintet spin barriers with N4Py and modified N4Py ligands are well lower in energy than the vanadium-peroxo complexes discussed in this work. Therefore, iron(IV)-oxo is a better oxidant for oxygen atom transfer reactions to sulfides than this vanadium-peroxo complex, although it can react with modest speed and efficiency.

5.3.4 Thermochemical Analysis of Reactivity Patterns.

To further understand the relative reactivity of vanadium-oxo and vanadium-peroxo complexes for oxygen atom transfer, we calculated a thermochemical cycle that includes electron transfer and hydrogen atom abstraction processes, see Figure 5.6. Thus, we calculate the bond dissociation energy (BDE_{OH}) from the sum of the three reactions displayed in Figure 5.6, Equation (Eq.) 5.1 – 5.5.

$$VO_2 + H^{\bullet} \rightarrow VOOH + BDE_{OH} \quad \textbf{(5.1)}$$

$$VO_2 + e^{-} \rightarrow VO_2^{-} + EA \quad \textbf{(5.2)}$$

$$H^{\bullet} \rightarrow H^{+} + e^{-} + IE_H \quad \textbf{(5.3)}$$

$$VOOH \rightarrow VO_2^{-} + H^{+} + \Delta G_{acid} \quad \textbf{(5.4)}$$

$$BDE_{OH} = EA + IE_H - \Delta G_{acid} \quad \textbf{(5.5)}$$

The BDE_{OH} for the vanadium-peroxo complexes is calculated from the sum of the electron affinity (EA) of the vanadium-peroxo complex, the gas-phase acidity (ΔG_{acid}) of the vanadium-hydroperoxo species and the ionization energy (IE_H) of a hydrogen atom. All individual structures in Figure 5.6 were geometry optimized with DFT and relative energies for the reactions in Eq. 1 – 4 were calculated. This enabled us to evaluate the reduction potential (electron affinity, EA) of the vanadium(V)-peroxo complex as well as the gas-phase acidity (ΔG_{acid}) of the vanadium(IV)-peroxo intermediate by converting it into the vanadium(IV)-hydroperoxo complex. Finally, to complete the thermochemical cycles in Figure 5.6, we used the ionization energy of a hydrogen atom (IE_H) as taken from the literature (Lias, 2005).

As can be seen from Figure 5.6 there are major effects resulting from the second-coordination sphere in vanadium(V)-peroxo complexes on the thermochemical properties of the complex. Thus, the electron affinity and the BDE_{OH} are enhanced by 7.6 and 14.7 kcal mol^{-1} between the bowl and dome shaped structures, respectively. As such the second-coordination sphere and the ligand binding is non-innocent and influences the electronic properties of the oxidant.

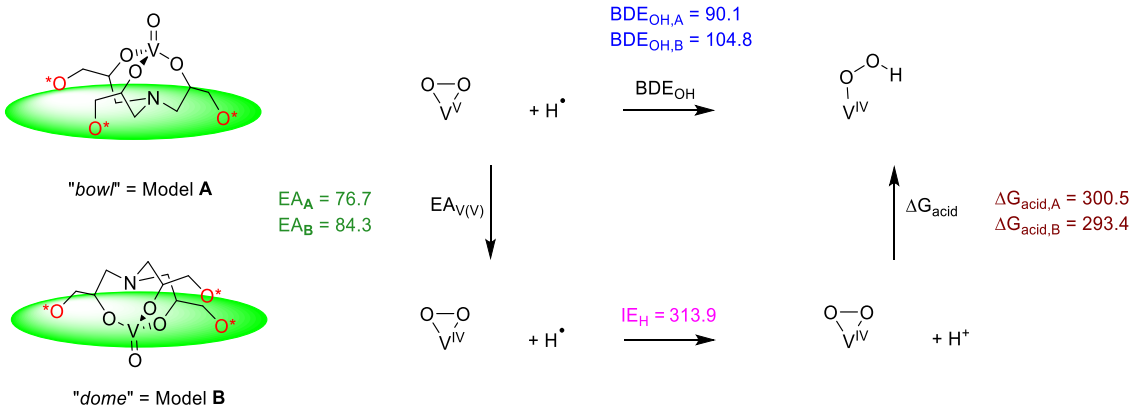

Figure 5.6. Thermochemical cycle for calculating intrinsic properties of the bowl and dome shaped vanadium-peroxo complexes. Energies calculated at $\Delta E+ZPE+E_{solv}$ level of theory with values in kcal mol^{-1}. Energies obtained at UB3LYP/BS2, while ZPE, thermal corrections and entropies are taken from the BS1 frequency files.

Thus, the enlarged value of the BDE_{OH} for the dome-type structure is partially the result of an enlarged redox potential (EA) and an enlarged gas-phase acidity difference of 7.1 kcal mol^{-1} in favor of the bowl-type structure. As such, based on the thermochemical properties, i.e. EA, BDE_{OH} and ΔG_{acid}, of the bowl and dome shaped structures, major differences in reactivity should be seen. Generally, a larger gas-phase acidity results in faster reactivity with substrates as is indeed seen from Table 5.1 where the relative sulfoxidation barriers are given.

5.3.5 Second-Coordination Sphere Effects.

As shown in this work, second-coordination sphere effects influence the reactivity as well as the mechanism of the reaction. Geometrically, the vanadium(V)-oxo complexes **A** and **B** are very similar and hence we predict both to have similar absorption and IR spectra. However, interaction with terminal oxidants and substrates is different. Thus, upon approach of tBuOOH (or H_2O_2) to the vanadium(V)-oxo group, it binds to vanadium in the open conformation prior to proton shuttle and oxygen atom transfer to form the side-on vanadium-peroxo complex.

By contrast, tBuOOH binding to vanadium is not possible in the dome conformation **B** and proton and oxygen atom transfer happen at larger distances. As a consequence of stereochemical interactions of the second-coordination sphere the mechanism and barriers for formation of the vanadium-peroxo species is different. In particular, the rate-determining proton transfer via $\mathbf{TS}_{PT1}$ is 27.0 kcal mol^{-1} for model **A**, while it is raised to 34.2 kcal mol^{-1} in model **B**. After the barrier, the oxygen atom transfer is spontaneous for model **A**, while it encounters another barrier ($\mathbf{TS}_{PT2}$) for the dome model **B**. As such the second-coordination sphere affects the formation of the active oxidant, i.e. the side-on vanadium-peroxo complex, as well as the reaction mechanisms.

In the next step substrate sulfoxidation was tested by the side-on vanadium-peroxo complexes $\mathbf{Int4}_A$ and $\mathbf{Int4}_B$. Also during the thioanisole sulfoxidation the substrate cannot access the oxidant well and the oxygen transfer barriers are raised in energy for model **B** with respect to model **A**. Thus, the sulfoxidation barrier is raised by 3.6 kcal mol^{-1} between models **A** and **B** as a result of the second-coordination sphere interactions that prevent ideal substrate approach. We then analyzed the thermochemical properties of **A** and **B** and see changes in electron affinity as well as acidity of the side-on vanadium-peroxo complexes. Even though, geometrically there are minor differences between the two complexes, actually the second-coordination sphere reduces the electron

affinity between the encapsulated ("dome") and open ("bowl") structures by 7.6 kcal mol^{-1}. At the same time, also the gas-phase acidity is raised by another 7 kcal mol^{-1}, which means the BDE_{OH} is changed by 14 kcal mol^{-1}. Consequently, a stronger O-H bond is formed through hydrogen atom abstraction by **B** than by **A**. Previously, it was shown that the stronger the BDE_{OH} is, the more exothermic a hydrogen atom abstraction is and also low oxygen atom transfer barriers are found (Visser, 2010; Li *et al.*, 2017). Interestingly, the sulfoxidation barriers in Figure 5.4 follow the opposite trend of the BDE_{OH} values. This implies that the second-coordination sphere effect is very large and reduces barriers by orders of magnitude.

5.4 Conclusions

In conclusion, we describe a DFT study on two vanadium(V)-oxo complexes with elaborate binaphthol ligand systems, whereby in model **A** the active site is solvent exposed, whereas in model **B** it is caged. We initially study the reaction of the vanadium(V)-oxo intermediates with t-BuOOH to form a side-on vanadium-peroxo complex. Not surprisingly, the caged system gives a higher rate-determining reaction step than the open structure by well over 7 kcal mol^{-1} in energy. This is not only the case for the conversion of the vanadium(V)-oxo into a vanadium-peroxo complex but also applies to the subsequent oxygen atom transfer to sulfide. Overall, these differences point to a second-coordination sphere effect on the reaction mechanism and kinetics. This was further analyzed by calculating a thermochemical cycle that shows there are differences in pK_a and redox potential expected for the two complexes.

Chapter 6

PROJECT 4

Reactivity Patterns of Vanadium(IV/V)-oxo Complexes with Olefins in the Presence of Peroxides: A Computational Study.

M. Qadri E. Mubarak[a] and Sam P. De Visser [a]

[a]The Manchester Institute of Biotechnology and Department of Chemical Engineering and Analytical Science, The University of Manchester, 131 Princess Street, Manchester M1 7DN, United Kingdom.

Abstract

Vanadium porphyrin complexes are naturally occuring substances found in crude oil and have been shown to have medicinal properties as well. Little is known on their activities with substrates; therefore, we decided to perform a detailed density functional theory study into the properties and reactivities of vanadium(IV)- and vanadium(V)-oxo complexes with a $TPPCl_8$ or 2,3,7,8,12,13,17,18-octachloro-meso-tetraphenylporphyrinato ligand system. In particular, we investigated the reactivity of $[V^{V}(O)(TPPCl_8)]^{+}$ and $[V^{IV}(O)(TPPCl_8)]$ with cyclohexene in the presence of H_2O_2 or HCO_4^{-}. The work shows that vanadium(IV)-oxo and vanadium(V)-oxo are sluggish oxidants by themselves and react with olefins slowly. However, in the presence of hydrogen peroxide these metal-oxo species can be transformed into a side-on vanadium-peroxo complex, which reacts with substrates more efficiently. Particularly with anionic axial ligands, the side-on vanadium-peroxo and vanadium-oxo complexes produced epoxides from cyclohexene with small barier heights. In addition to olefin epoxidation, we investigated aliphatic hydroxylation mechanisms of the same oxidants and some oxidants show efficient and viable cyclohexene hydroxylation mechanisms. The work implies that vanadium-oxo and vanadium-peroxo complexes can react with double bonds through epoxidation, and under certain conditions also give hydroxylation, but the overall reactivity is highly dependent on the equatorial ligand, the local environment and the presence of anionic axial ligands.

Published reference

Mubarak, M. Qadri E. and Sam P. De Visser. "Reactivity Patterns of Vanadium(IV/V)-oxo Complexes with Olefins in the Presence of Peroxides: A Computational Study" Dalton Transaction (2019): 48, 16899-16910.

6.1 Introduction

Vanadium-containing enzymes include vanadium-haloperoxidases and the vanadium-containing nitrogenase is one of the enzyme that can be found in nature. However, their actual mechanism remain a mystery as no one unable to reveal it yet (Plat, Krenn and Wever, 1987; Butler, 1999; Littlechild *et al.*, 2002; Winter and Moore, 2009; Wever and Van Der Horst, 2013; Leblanc *et al.*, 2015; Timmins and De Visser, 2015; Wever and Barnett, 2017; Craig C. McLauchlan *et al.*, 2018). In general, the vanadium-haloperoxidases bind H_2O_2 on a nonheme vanadium centre and through additional protons and binding of halide convert this to hypohalide products. In addition, vanadium-porphyrin complexes have been characterized in crude oils, although their function and origin remain unknown (Zhao *et al.*, 2014; Qian *et al.*, 2019). Moreover, the natural product amavidin is a vanadium(IV) containing compound found in fungi that showed catalase and peroxidase type activity (Da Silva, Fraústo da Silva and Pombeiro, 2013). Furthermore, evidence has emerged of useful pharmaceutical properties of vanadium containing compounds, whereby, for instance, vanadium-porphyrins are used as anti-HIV agents (Wong *et al.*, 2005), and diaminotris(phenolato) vanadium(V) complexes as anticancer drugs (Thompson, McNeill and Orvig, 1999). In biomimetic chemistry, many reports have appeared in the literature that discuss the coordination environment and reactivity of vanadium complexes (Licini et al. 2011; Sutradhar et al. 2015; Costa Pessoa et al. 2015; Langeslay et al. 2019; Smith, LoBrutto, and Pecoraro 2002; Fox et al. 2004; Harada, Okawa, and Kojima 2005; Hoppe, Limberg, and Ziemer 2006; Hossain et al. 2019; Egdal et al. 2005; Colpas et al. 1996; Kravitz and Pecoraro 2005). For instance, vanadium(IV) and vanadium(V) complexes have been shown to react with olefins through epoxidation (Cordelle *et al.*, 2010; Vandichel *et al.*, 2012; Salonen, Peuronen and Lehtonen, 2017; Sedighipoor *et al.*, 2017), but also react with aliphatic groups such as cyclohexane by hydroxylation and desaturation reactions (Mishra and Kumar, 2002; J. Zhang *et al.*, 2017; Steffensmeier, Swann and Nicholas, 2019). A recent report showed vanadium complexes to react with olefins through substitution of a C–H bond

with C–X (X = Cl, Br, I) (Trost and Tracy, 2017).Therefore, they are highly versatile as oxidation catalysts. However, it is not clear whether the reactivity is performed by an $V^{IV}(O)$, $V^{V}(O)$ or a vanadium-peroxo complex.

To gain insight into the properties and reactivity of vanadium complexes we decided to investigate the structure and reactivity of a set of vanadium(IV)-oxo and vanadium(V)-oxo porphyrins in the presence and absence of H_2O_2. Thus, vanadium-porphyrins are well studied and have been characterized with UV-Vis spectroscopy, ^{1}H NMR and EPR spectrometry and X-ray diffraction analysis methods (Doukkali *et al.*, 2006; Kandrashkin, Asano and Van Der Est, 2006; Sessler, Tomat and Lynch, 2006; Ghosh, Patra and Rath, 2008; Hopmann, Ghosh and Noodleman, 2009; Chen, Suenobu and Fukuzumi, 2011; Yamashita, Tazawa and Sugiura, 2016). These complexes were also found to react efficiently with olefins to form the corresponding epoxides (Kumar *et al.*, 2015; Dar *et al.*, 2019), although it is unclear whether the active species in a vanadium-oxo or vanadium-peroxo moiety (Simonova, Zaitseva and Koifman, 2016; Zechel *et al.*, 2019).

Over the years a number of density functional theory calculations have been reported on nonheme and heme vanadium-oxo complexes (Cundari, Saunders and Sisterhen, 1998; Salcedo, MartõÂnez and MartõÂnez-MagadaÂn, 2001; Schneider *et al.*, 2007; Li, Tian and Yang, 2008; Stoyanov *et al.*, 2010), but little is known on their activity, what the active oxidant is and how the reactivity compares to high-valent iron(IV)-oxo intermediates.

To find an answer to these questions we set up models of vanadium(IV)-oxo, vanadium(V)-oxo and vanadium-peroxo with porphyrin ligand system and studied substrate activation. Our model follows the system reported by previous study and considers a vanadium(IV/V)-oxo ion embedded into a 2,3,7,8,12,13,17,18-octachloro-*meso*-tetraphenylporphyrinato group ($TPPCl_8$), Scheme 6.1 (Kumar *et al.*, 2015). We studied a direct reaction of these complexes with cyclohexene to give either epoxide or enol products. In addition, we considered reaction mechanisms in the presence of H_2O_2 and/or peroxymonocarbonate (HCO_4^-).

The work shows that vanadium-oxo by itself is a sluggish oxidant, but in a reaction with hydrogen peroxide can be converted into a vanadium-peroxo group, which is considerably more reactive with substrates.

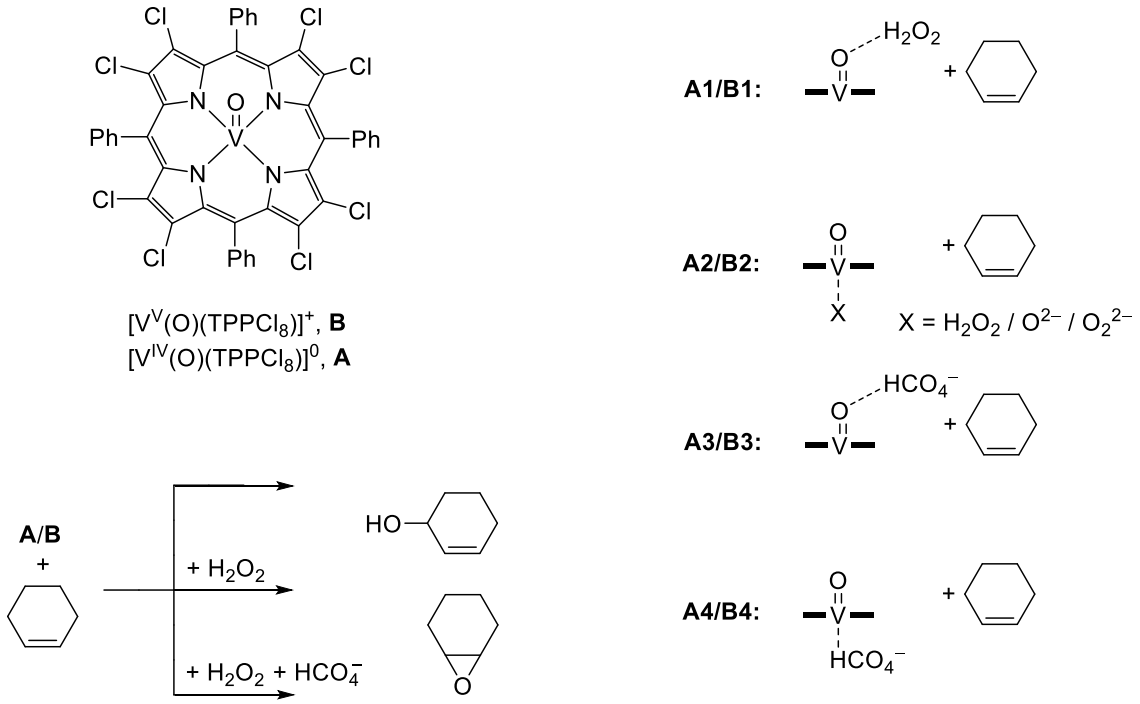

Scheme 6. 1. Model and reaction mechanism studied in this work.

6.2 Methods

Density functional theory (DFT) methods were applied as implemented in the Gaussian-09 software package. In general, the unrestricted B3LYP (Lee, Yang and Parr, 1988; Becke, 1993) hybrid density functional method was used for geometry optimizations, constraint geometry scans and frequency calculations. All structures were optimized without constraints with an LanL2DZ basis set on vanadium (with core potential) and 6-31G* on the rest of the atoms (H, C, Cl, N, O): basis set BS1 (Ditchfield, Hehre and Pople, 1971; Hay and Wadt, 1985). Single point energy calculations were performed to improve the energetics and used a triple-ζ quality basis

set on vanadium (with core potential), i.e. LACV3P+, and 6-311+G* on the rest of the atoms: basis set BS2. Solvent corrections were included during the geometry optimizations through the continuum polarized conductor model (CPCM) with a dielectric constant mimicking that of toluene. All local minima were characterized with real frequencies only and the transition states had a single imaginary mode for the correct transition. For a selection of structures and potential energy profiles we also did geometry optimizations using a modest 6-31G basis set on all atoms and LanL2DZ with core potential on vanadium: basis set BS3. These results gave almost identical structures and energetics to those obtained with the larger basis set, see Electronic Supporting Information for details.

The models contained the full $[V^{V}(O)(TPPCl_8)]^{+}$ (model **B**) and $[V^{IV}(O)(TPPCl_8)]^{0}$ (model **A**) complexes with peripheral substituents on the porphyrin unit included (Scheme 6.1). Subsequently, we added H_2O_2 to our system either on the distal side, i.e. on the vanadium-oxo side (models **A1** and **B1**), but also included a model without distal H_2O_2 and a ligand in the axial positions. Thus, models **A2** and **B2** have H_2O_2 in the axial position, models **A2'**/**B2'** have an axial oxo group and **A2"**/**B2"** an axial peroxo moiety. Cyclohexene was used as a model substrate and was located at the distal side of the vanadium-oxo complex and reaction mechanisms for its epoxidation and aliphatic hydroxylation pathways were studied. In addition to these models we investigated a system with HCO_4^{-} as terminal oxidant rather than H_2O_2 and repeated the calculated mechanisms: Models **A3**/**B3** with HCO_4^{-} on the distal side and models **A4**/**B4** with HCO_4^{-} on the axial side. Vibrational frequencies reported here are unscaled values.

6.3 Results and Discussion

Before discussing the reactivity patterns of the various vanadium-oxo and vanadium-peroxo complexes, we will start with a detailed analysis of the reactant complexes, namely $[V^{IV}(O)(TPPCl_8)]^{0}$ (**A**) and $[V^{V}(O)(TPPCl_8)]^{+}$ (**B**) with $TPPCl_8$ representing 2,3,7,8,12,13,17,18-octachloro-*meso*-tetraphenylporphyrinato. Thus, the vanadium(IV) complex is charge neutral and in a doublet spin ground state, while the

vanadium(V) has closed-shell singlet spin state and is singly charged (+1). These spin states match vanadium-oxo porphyrins experimentally characterized with electron paramagnetic resonance (EPR) spectroscopy (Doukkali *et al.*, 2006; Kandrashkin, Asano and Van Der Est, 2006; Sessler, Tomat and Lynch, 2006; Ghosh, Patra and Rath, 2008; Chen, Suenobu and Fukuzumi, 2011; Kumar *et al.*, 2015; Yamashita, Tazawa and Sugiura, 2016; Dar *et al.*, 2019). Optimized geometries and valence orbitals of the electronic ground states of **A** and **B** are given in Figure 6.1. The optimized geometries of the $V^{IV}(O)$ and $V^{V}(O)$ porphyrin complexes **A** and **B** are very similar with V–O distances of 1.568 and 1.583Å, respectively. As a consequence the V–O stretch vibration is similar too: 1120 (1094) cm^{-1} for **A** (**B**).

Our optimized geometries and vibrational frequencies are in good quantitative agreement with experimentally reported structures and vibrational frequencies of analogous complexes (Doukkali *et al.*, 2006; Kandrashkin, Asano and Van Der Est, 2006; Sessler, Tomat and Lynch, 2006; Ghosh, Patra and Rath, 2008; Chen, Suenobu and Fukuzumi, 2011; Yamashita, Tazawa and Sugiura, 2016). The V=O bond lengths are considerably shorter than those calculated for iron(IV)-oxo species but are close to the triple bond found for Mn^{V}-oxo (Kumar, Hirao, *et al.*, 2005; Visser, 2006; Bernasconi, Louwerse and Jan, 2007; Ye and Neese, 2010; Latifi *et al.*, 2013; Lundberg and Borowski, 2013; Neu *et al.*, 2014; Yang *et al.*, 2016). This is not surprising as iron(IV)-oxo has four metal 3d-type electrons and two of those form a triplet pair of antibonding interactions for the FeO π^* bond that elongate the Fe–O distance. As a result of this the vibrational frequency is also well higher than that typically found for iron(IV)-oxo complexes, where Fe–O frequencies in the order of 800 – 900 cm^{-1} were reported (Rohde *et al.*, 2003; Borovik, 2005; Martinho *et al.*, 2005; Andris *et al.*, 2018; Pattanayak *et al.*, 2019).

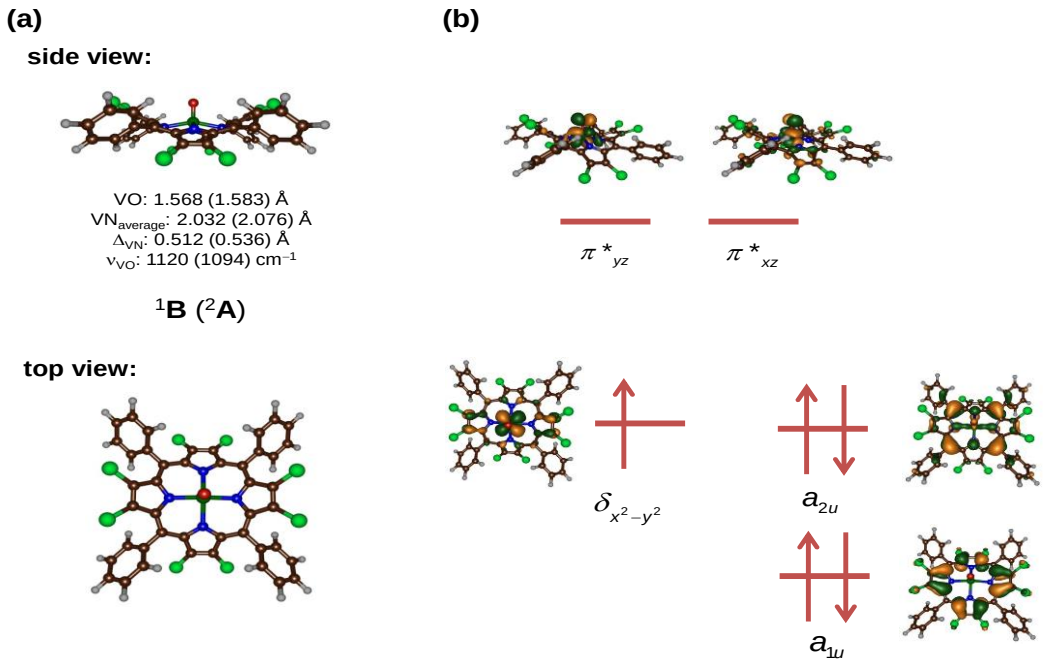

Figure 6.1. Optimized geometries of ^{2}**A** and ^{1}**B** as obtained at UB3LYP/BS1 in Gaussian-09. Bond lengths are in angstroms and the vibrational frequencies (ν_{VO}) in cm^{-1}. The right-hand-side gives relevant valence orbitals with orbital occupation of ^{2}**A**.

The origin of the short V–O distances in ^{2}**A** and ^{1}**B** is related to the orbital occupation (right-hand-side of Figure 6.1). Thus, the vanadium(V)-oxo species has valence orbitals that represent the metal-oxo and metal-ligand interactions. Lowest in energy is the δ_{x2-y2} orbital, which is a non-bonding orbital in the plane of the porphyrin ring. Higher in energy and virtual are two π* orbitals (π^*_{xz} and π^*_{yz}) for the antibonding interaction of the $3d_{xz}$ and $3d_{yz}$ on vanadium with the $2p_x$ and $2p_y$ on oxygen. In iron(IV)-oxo species these two orbitals are singly occupied and due to their antibonding character lead to elongation of the Fe–O bond to typically 1.65Å. With vanadium the two π* orbitals are virtual and consequently the V=O distances are much shorter as there is lesser antibonding character along those bonds. The vanadium-porphyrin system also has two high-lying π-orbitals on the ligand labelled as a_{1u} and a_{2u}. In cytochrome P450 Compound I, the a_{2u} orbital is singly occupied (Ghosh, 1998; Green, 1999; De Visser and Lee, 2008; Radoń, Broclawik and Pierloot,

2011) but in the vanadium systems this orbital is much lower in energy and doubly occupied and hence the valence orbitals are all metal-oxo based. The electronic ground state of ^{2}**A** and ^{1}**B**, therefore is: $\delta_{x2-y2}^1\ a_{1u}^2\ a_{2u}^2$ for ^{2}**A** and $a_{1u}^2\ a_{2u}^2$ for ^{1}**B** with all metal-type orbitals unoccupied.

The porphyrin is considerably distorted from planarity and is saddle-shaped with the metal 0.512 and 0.536Å above the plane through the four nitrogen atoms as defined as Δ_{VN}. This distortion of the planarity was also seen in crystal structures of vanadium-oxo porphyrin complexes (Ghosh, Patra and Rath, 2008), although in iron-porphyrin the calculations often converge to a planar structure. Overall, our optimized geometries match previous calculations on ^{2}**A** perfectly with similar bond distances, porphyrin saddling and the displacement of the metal from the plane through the four nitrogen atoms (Kumar *et al.*, 2015; Dar *et al.*, 2019).

6.3.1 Mechanism of Cyclohexene Epoxidation by A1/B1+H_2O_2

The vanadium(IV)-oxo complex **A** in the presence of H_2O_2 and cyclohexene was found to convert substrate into a mixture of epoxide, cyclohexenol and cyclohexanone products (Kumar *et al.*, 2015; Dar *et al.*, 2019). To understand these product distributions and the oxidant involved in these transformations, we investigated the mechanism of substrate epoxidation by vanadium(IV)-oxo and vanadium(V)-oxo complexes. We started with a model that includes H_2O_2 and cyclohexene as a substrate on the distal site of the vanadium-oxo group: models **A1** and **B1**, which we identify with a subscript after the label. Initially a reactant complex (**Re**) was calculated of the vanadium-oxo group in hydrogen bonding distance to H_2O_2 and cyclohexene in its vicinity. The mechanism starts with proton transfer from H_2O_2 to the oxo group and simultaneous binding of the hydroperoxo moiety to the vanadium centre to form intermediate **Int1** via a transition state **TS1**. Thereafter, a second proton transfer takes place via transition state **TS2** to form a side-on vanadium-peroxo with water ligand **Int2**, whereby the water is released from the metal centre via transition state **TS3** to

form the vanadium-peroxo-porphyrin complex **Int3**. Note that in the mechanism starting with the vanadium(IV)-oxo complex (**A1**) the water release happens simultaneously with **TS2** and no stable **Int2** and **TS3** structures could be characterized. Finally, the side-on peroxo species (**Int3**) reacts with olefin via a concerted oxygen atom transfer to form epoxide products (**P**) via a transition state **TS4**.

Figure 6.2 displays the potential energy landscape of cyclohexene activation by **A1**/**B1**+H_2O_2. In the case of the mechanism of **B1**+H_2O_2, we calculated the full reaction pathway with UB3LYP/BS1 and UB3LYP/BS3. As can be seen structure and energetics along the mechanism is virtually the same for both reactants and the effect of the basis set on optimized geometries and bond activation energies appears to be very small. Indeed most energies are well within 1 kcal mol^{-1}.

The rate determining reaction step is in all cases the initial proton transfer via **TS1** and is $\Delta E+ZPE+E_{solv}$ = 33.8 and 32.6 kcal mol^{-1} for the pathway starting with the vanadium(V)-oxo and vanadium(IV)-oxo, respectively. These proton-transfers from H_2O_2 to vanadium-oxo species lead to the end-on hydroperoxo-hydroxo-vanadium complexes as a local minimum. Complexes **Int1$_{A1}$**/**Int1$_{B1}$** are considerably less stable than the reactant vanadium-oxo complexes and have structures where the porphyrin is displaced from planarity further and, e.g. in **Int1$_{A1}$** the metal is above the porphyrin plane by 0.825Å. However, no major shift in spin density distributions (Table S13, Electronic Supporting Information) is seen during this proton transfer step. Therefore, **TS1** is a pure proton transfer and the activation of V(IV) or V(V) complexes requires the same amount of energy. This is not surprising as no electron transfer takes place here and the oxidation state of the metal stays the same. The barriers; however, for proton transfer are rather high in energy and the reaction will be very slow even at room temperature. The proton transfer transition states (Figure 6.2) have a large imaginary frequency typical for fast moving protons (Latifi, Bagherzadeh and Visser, 2009; Visser, 2010). Moreover, the proton transfer happens at short O–H distances.

In the next stage of the mechanism, the hydroperoxo loses a proton to the hydroxo group to form water and binds as a side-on vanadium-peroxo in **Int2** in a highly exothermic reaction step followed by a small barrier for water release. Indeed the imaginary frequency for this step is considerably lower than that for **TS1**. The structures are early on the potential energy landscape, i.e. with long O–H and short OO–H distances.

The final part of the mechanism involves the attack of the side-on vanadium-peroxo onto the substrate to form epoxide in a concerted reaction step, whereby one oxygen atom of the peroxo group approaches the middle of the double bond with approximately equal distance to each of the carbon atoms of that bond. Barriers of 16.6 and 24.4 kcal mol^{-1} are obtained for the epoxidation barriers from **Int3$_{A1}$** and **Int3$_{B1}$**, respectively. Typical reaction mechanisms observed for substrate epoxidation by metal-oxo oxidants usually give a stepwise reaction pathway via a radical intermediate with an initial C–O bond formation and followed by a ring-closure step (Visser, Harris and Shaik, 2001; Kumar *et al.*, 2013). Here, however, the radical intermediates appear less stable and product is formed in a single concerted epoxidation step. The imaginary frequency represents simultaneous O–O bond cleavage and C–O bond formation as expected for this transition state.

Overall, the two side-on peroxo complexes **Int3$_{A1}$** and **Int3$_{B1}$** are seen to react with cyclohexene with barriers that would be accessible at room temperature conditions; particularly the pathway from **Int3$_{A1}$**. As such the side-on peroxo complex **A1** should be a viable oxidant of oxygen atom transfer reactions. However, the barriers for the conversion of the vanadium-oxo complexes into the vanadium-peroxo through the use of H_2O_2 are of similar magnitude as the substrate activation barriers. Therefore the reaction is not expected to proceed through a clean first-order (or pseudo-first order) reaction mechanism and hence measuring rate constants may be misleading. Indeed, experimental work showed that HCO_4^- was needed as promotor to trigger a fast reaction process (Kumar *et al.*, 2015; Dar *et al.*, 2019). Consequently, we investigated some alternative pathways and structures to generate a vanadium-peroxo active

species particularly in the presence of promotors or through the binding of axial ligands to the vanadium centre. In addition, we also explored reaction pathways with cyclohexene to form alcohol products.

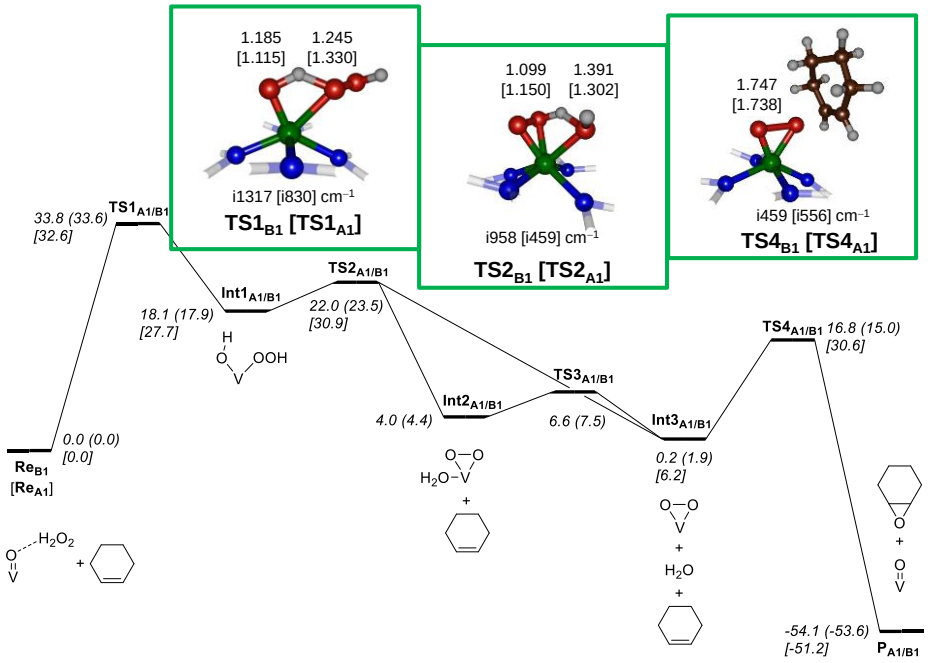

Figure 6.2. Potential energy (ΔE+ZPE) landscape with energies in kcal mol^{-1} for the reaction of ^{2}**A1** and ^{1}**B1** with H_2O_2 and cyclohexene (CH) as obtained with DFT methods in Gaussian-09. Geometry optimizations done at UB3LYP/BS1 or UB3LYP/BS3 (data in parenthesis). Extracts of the transition state structures are given with bond lengths are in angstroms and the imaginary frequencies in cm^{-1}.

6.3.2 Mechanism of Cyclohexene Hydroxylation by A1/B1+H_2O_2

Next, we investigated cyclohexene hydroxylation by models A1/B1. Of course, the mechanism proceeds like that shown in Figure 6.2 above with two proton transfer steps (via TS1 and TS2) and the formation of a side-on vanadium-peroxo complex and

a water molecule (Int2). Again release of the water molecule from the vanadium centre gives intermediate Int3. From this point onwards; however, the cyclohexene epoxidation and hydroxylation mechanisms diverge.

Thus, the peroxo group abstracts a hydrogen atom from substrate (via a transition state **TS5**) to form a vanadium-hydroperoxo complex (**Int5**), while an OH rebound barrier (**TS6**) then leads to the 1-hydroxocylohexene products (**P2**). The obtained potential energy profile of this process is given in Figure 6.3. The transition states **TS5$_{A1}$** and **TS5$_{B1}$** are relatively high in energy and values of 25.3 and 45.2 kcal mol^{-1} are obtained for the pathways starting from the V^{IV}(O) and V^{V}(O) complexes, respectively. An analysis of the group spin densities gives no radical character of the substrate for the V(V) process, while a spin of 1 is found in the V(IV) pathway. Therefore, the vanadium(V)-oxo will react via proton abstraction of substrate, while a hydrogen atom abstraction is found by the vanadium(IV)-oxo complex. Nevertheless, a barrier with a magnitude of 25.3 kcal mol^{-1} implicates a sluggish hydrogen atom abstraction process, whereas one of 45.2 kcal mol^{-1} is too high to be overcome under room temperature and pressure conditions. Consequently, the high reaction barriers found for the side-on peroxo complexes imply that these species will be not be able to react by aliphatic hydroxylation pathways, but can react through oxygen atom transfer to olefins.

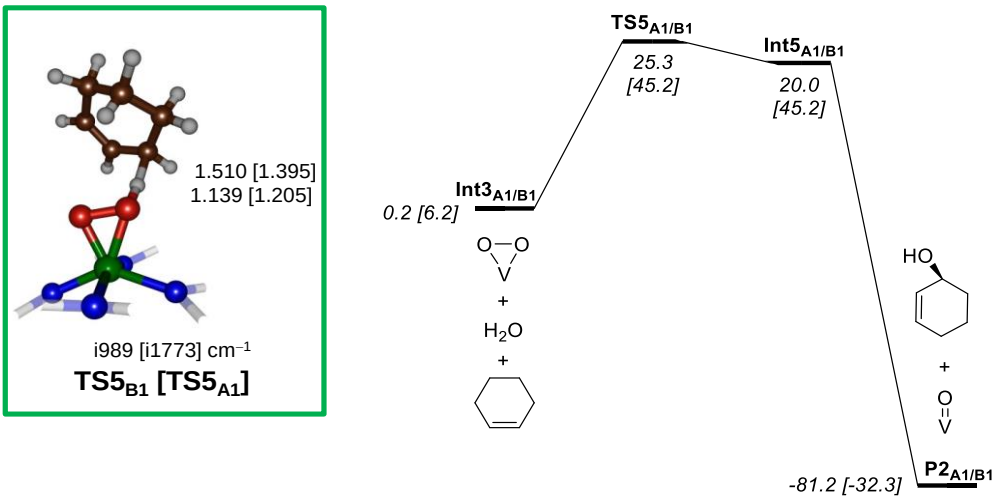

Figure 6.3. Potential energy landscape with energies in kcal mol^{-1} for the hydroxylation reaction of cyclohexene by ^{2}**A1** and ^{1}**B1** in the presence of H_2O_2 as obtained with DFT methods in Gaussian-09. Mechanism started from the vanadium-peroxo intermediate. Geometry optimizations done at UB3LYP/BS1. Bond lengths are in angstroms and the imaginary frequencies in cm^{-1}.

Optimized geometries of the hydrogen atom abstraction transition states are shown in Figure 6.3. The hydrogen atom abstraction transition state for the vanadium(V)-oxo reaction is late with a long C–H distance of 1.510Å and a relatively short O–H distance of 1.139Å. These types of product-type hydrogen atom abstraction barriers often correlate with high energy transition states (Shaik *et al.*, 2010; Kumar, Sastry and Visser, 2011). On the other hand, a more central transition state is seen for the vanadium(IV)-oxo pathway, although the energy is very high in energy. After the hydrogen atom/proton abstraction, both complexes relax to an intermediate prior to rebound to form the alcohol product complexes. The intermediates are short-lived and collapse to products with negligible rebound transition state (**TS6**).

Overall, the calculations show that vanadium-peroxo complexes will not react with aliphatic groups through substrate hydroxylation processes as high energy hydrogen atom abstraction or proton abstraction barriers are found. This matches experimental studies on these systems excellently that obtained >99% selectivity towards epoxide product formation (Kumar *et al.*, 2015; Dar *et al.*, 2019). Thus, the calculations give

favourable cyclohexene epoxidation over hydroxylation by a large margin and the chemoselectivity does not appear to be affected by the oxidation state of the vanadium centre in the reactant complex. In previous studies on iron(IV)-oxo reactivity with either propene or cyclohexadiene we investigated competitive epoxidation and hydrogen atom abstraction pathways (de Visser and Ogliaro, 2002; Visser, Sharma and Shaik, 2002; Kumar *et al.*, 2009). In these studies the two reaction channels were close in energy and small environmental perturbations affected the selectivity and product distributions. Clearly, here the energy gaps are wider apart. To understand the nature of the selectivity patterns, we calculated a number of alternative complexes with either H_2O_2, oxo or peroxo bound in the axial position.

6.3.3 Mechanism of Cyclohexene Epoxidation by A2/B2+H_2O_2

Subsequently, we investigated cyclohexene epoxidation from models **A2**/**B2**, which have the H_2O_2 molecule trans to the vanadium-oxo group and hence the oxygen atom transfer is from the oxo group rather than from H_2O_2. The optimized C–O bond activation transition states **TS4$_{A2}$** and **TS4$_{B2}$** are shown in Figure 6.4. By contrast to the concerted epoxidation transition states shown in Figure 6.2 for models **A1** and **B1**, the **TS4$_{A2}$** and **TS4$_{B2}$** structures are geometrically very different. Thus, in **TS4$_{A1}$** and **TS4$_{B1}$** the peroxo group attacks the midpoint of the C=C bond of the olefin and both C–O bond of the epoxide are simultaneously formed. By contrast, in **TS4$_{A2}$** and **TS4$_{B2}$** the oxo group attacks on specific carbon atom and single C–O. As such these transition states resemble those seen for stepwise epoxidation reactions (de Visser, Ogliaro and Shaik, 2001; Visser, Harris and Shaik, 2001; Kumar *et al.*, 2010, 2013), where one C–O bond at a time is formed. Usually these stepwise processes proceed through the formation of a radical intermediate. However, here no stable radical intermediates are found and the optimizations collapsed to epoxide products directly. Therefore, the radical intermediates for systems **A2** and **B2** are shoulders on the potential energy landscape en route to product formation. In previous work this type of pseudo-concerted reaction mechanisms were rationalized as resulting from a strong displacement of the metal from the porphyrin plane that enabled efficient oxygen atom

transfer to substrates and hence affected the ring-closure barriers.[30] Therefore, we decided to also explore alternative vanadium-oxo and vanadium-peroxo complexes with an electron-donating group in the axial position (see next section). Nevertheless, the barriers for oxygen atom transfer from vanadium(V)-oxo and vanadium(IV)-oxo are very high in energy, namely $\Delta E+ZPE+E_{solv}$ = 50.3 and 38.2 kcal mol^{-1}, respectively. Therefore, direct oxygen atom transfer by $[V^{V}(O)(TPPCl_8)]^{+}$ or $[V^{IV}(O)(TPPCl_8)]$ will be unlikely to happen at room temperature and these systems can be considered as sluggish oxidants for oxygen atom transfer reactions.

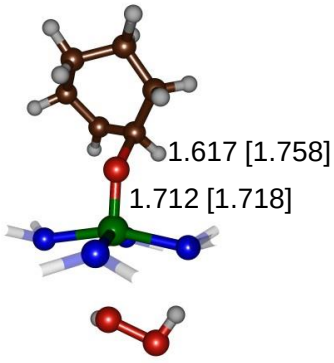

i537 [i702] cm^{-1}

$\Delta E+ZPE$ = 50.3 [38.2]

$TS5_{B2}$ [$TS5_{A2}$]

Figure 6.4. Optimized C–O bond formation transition states (**TS5**) for models **A2** and **B2**. Bond lengths are in angstroms, the imaginary frequency in cm^{-1} and relative energies in kcal mol^{-1}.

6.3.4 Mechanism of Cyclohexene Epoxidation and Hydroxylation by A2/B2 without H_2O_2

To test the effect of hydrogen peroxide and the binding of axial ligands to the vanadium-porphyrin on the reaction mechanism, we created models for a vanadium(IV/V)-dioxo complex without H_2O_2, namely models **A2'**/**B2'** and models of vanadium(IV/V)-peroxo(oxo) without H_2O_2: **A2"**/**B2"**. Note that all of these models have an oxo group in the trans (axial) position and substrate approaches on the distal site. The mechanism of models of vanadium(IV/V)-peroxo(oxo) namely as **A2"**/**B2"** was suggested by the Sankar and Maurya group where they were able to trap and characterize the structures using MALDI-TOF (Kumar *et al.*, 2015). Furthermore, substitutions on the ligand framework of the porphyrin group were made and the effects on catalysis and turnover studied (Dar *et al.*, 2019).

Figure 6.5 displays the potential energy landscape of cyclohexene activation by **A2',** **A2"**, **B2'** and **B2"**. In addition, we explored the vanadium-oxo and vanadium-peroxo complexes with different substituents to the porphyrin group. Thus, apart from the $TPPCl_8$ equatorial ligand, we investigated a porphyrin model with only hydrogen atoms as substituents on the meso-position (R) and β-position (X), designated ligands **A2-H**/**B2-H**. Furthermore, a porphyrin ligand with 3,5-dimethoxyphenyl on the meso-position and hydrogens on the β-positions was tested: ligands **A2-A**/**B2-A**. Finally, a porphyrin ligand with 2,4-dibromo-3,5-dimethoxyphenyl on the meso-position and bromide on the β-positions was studied: ligands **A2-B**/**B2-B**. Subsequently, the effect of the equatorial ligand on the reactivity was studied for the vanadium-oxo-peroxo and vanadium-dioxo complexes. Apart from the side-on peroxo, we also calculated an end-on conformation, but find it ΔE+ZPE = 9.1 and 13.0 kcal mol^{-1} higher in energy as compared to the side-on configuration of Re_{A2}" and $Re_{A2\text{-}B}$" respectively (See Electronic Supporting Information). We explored the direct cyclohexene epoxidation and hydroxylation by the vanadium(IV)-oxo, vanadium(V)-oxo complexes, vanadium(IV)-peroxo and vanadium(V)-peroxo complexes.

The potential energy landscape and optimized geometries of the electrophilic addition transition states for cyclohexene epoxidation are given in Figure 6.5. The optimized geometries shown in Figure 6.5 for the vanadium-dioxo and vanadium-oxo-peroxo complexes with $TPPCl_8$ ligand represent concerted epoxidation transition states for direct insertion of an oxygen atom into the C=C bond of the olefin. Indeed in most structures, the geometry is symmetric and almost equal C–O distances are observed. Structurally, therefore they look similar to those reported above with either H_2O_2 or water present.

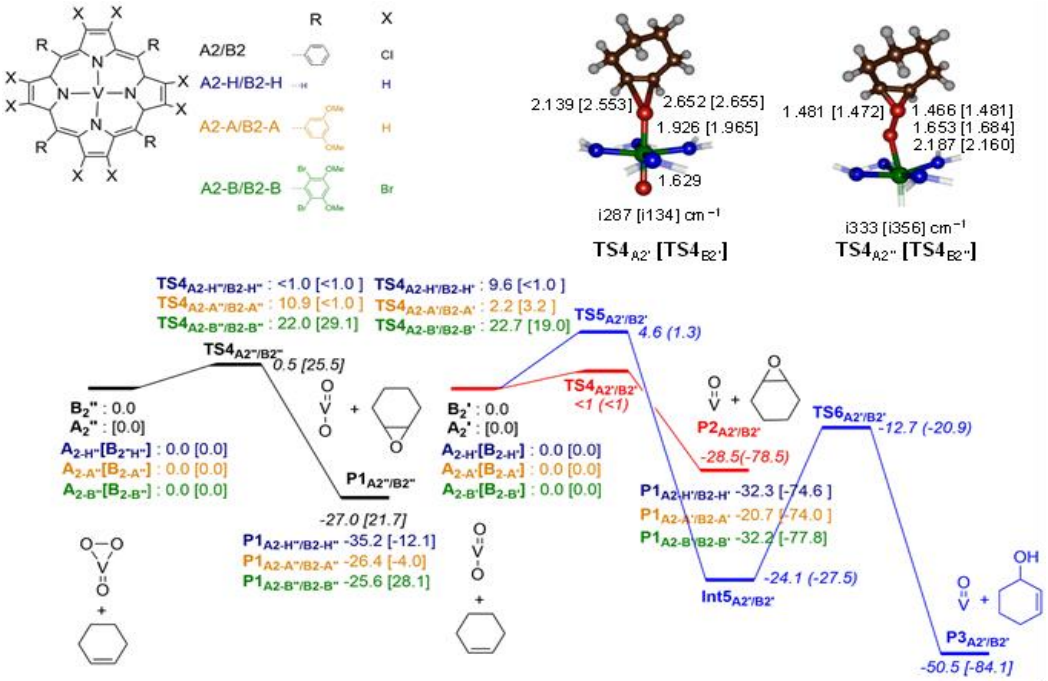

Figure 6.5. Potential energy landscape (ΔE+ZPE data) with energies in kcal mol^{-1} for the direct cyclohexene epoxidation and hydroxylation by the vanadium(IV)-oxo, vanadium(V)-oxo complexes, vanadium(IV)-peroxo and vanadium(V)-peroxo complexes with axial oxo group as obtained with DFT methods in Gaussian-09. Geometry optimizations done at UB3LYP/BS1 and energies use basis set BS2. Bond lengths are in angstroms and the imaginary frequencies in cm^{-1}.

Energetically, the barrier heights of the structures of the vanadium-dioxo in a reaction with cyclohexene are very low in energy; particularly those passing **TS4**$_{A2'}$, **TS4**$_{B2'}$ and **TS4**$_{A2"}$ where barriers of less than 1 kcal mol^{-1} are observed. Therefore, these reactions will be extremely fast and efficient and can be a good alternative for the oxidation of olefins to epoxides. The axial ligand is seen to pull the other oxygen atom more into the plane of the porphyrin, which should result in better orbital overlap and a more stable structure. As such the calculations predict that vanadium-dioxo porphyrin is a very efficient oxidant that reacts with substrates rapidly. These vanadium-dioxo

models are seen to activate a C=C double bond efficiently and react in a concerted pathway to epoxide products. The alternative cyclohexene hydroxylation was also tested. Although the initial hydrogen atom abstraction step is low in energy (barriers less than 5 kcal mol^{-1}) actually the OH rebound step to form products is 11.4 kcal mol^{-1} for **B2'** and 6.6 kcal mol^{-1} for **A2'**. Nevertheless, with barriers of less than 5 kcal mol^{-1} for the initial reaction step of epoxidation and hydroxylation, it is likely that these reactions happen in parallel and a mixture of products will be obtained. This result is in good agreement with experimental studies on cyclohexene activation by vanadium-porphyrins that give hydroxylation and epoxidation products.

To gain further insight into the chemical system, we replaced the substituents on the periphery of the porphyrin with alternative groups. As follows, seemingly small changes to the ligand system appear to have dramatic effects on the structure and reactivity of vanadium-oxo and vanadium-peroxo complexes. Thus, replacing all substituents with hydrogen atoms results in structures that have almost planar porphyrin rings, similar to previous cytochrome P450 model calculations.[31] Moreover, with 3,5-dimethoxyphenyl as meso-substituents most barriers go up in energy significantly due to stereochemical interactions of the approaching substrate to the oxidant and the ideal angles and structures cannot be reached. In particular, the addition of 2,5-dibromo to the meso-phenyl groups reduces the reactivity dramatically with rate determining barriers well over 19 kcal mol^{-1}. As such, vanadium-oxo and vanadium-peroxo complexes appear to be more sensitive to ligand substitution of the porphyrin macrocycle, which affect structure and reactivity. By contrast, in iron(IV)-oxo porphyrins and nonheme iron(V)-oxo tetraamidomacrocyclic ligand as the equatorial ligand, the effects were much smaller (Kumar, De Visser and Shaik, 2005; Kumar *et al.*, 2009; Pattanayak *et al.*, 2019).

To understand the axial ligand effect on the orbital shapes and energies we compared the structure and electronic configuration of the vanadium-peroxo complexes **Int3$_{B1}$** and **Int3$_{B2}$"** in Figure 6.6. Thus, without an axial ligand bound to the vanadium centre, as in **Int3$_{B1}$**, the vanadium-peroxo group is well displaced from the plane through the

four nitrogen atoms of the porphyrin by Δ = 0.595Å, while it is much closer to the plane in the vanadium-oxo-peroxo complex **Int3$_{B2}$"**: Δ = 0.127Å. As a consequence, the peroxo group enjoys better orbital overlap with orbitals on the porphyrin manifold and the V–O distances are shorter: 1.69Å in **Int3$_{B2}$"** and 1.79Å in **Int3$_{B1}$**.

As shown in Figure 6.6, a strong interaction between the δ_{x2-y2} and $\pi^*_{OO,xy}$ orbitals on the vanadium and peroxo groups, will widen the gap between the bonding and antibonding orbitals and stabilize the bonding orbitals in energy. A similar interaction, but then between a_{2u} and a lone-pair π-orbital on the axial ligand was seen in P450 Compound I and predicted to affect its electron affinity and reduction potential (Ogliaro *et al.*, 2001). A stronger push-effect of the axial ligand was shown to enhance to reactivity of Compound I (Visser *et al.*, 2003).

The molecular orbitals for the interaction of δ_{x2-y2} and $\pi^*_{OO,xy}$ for **Int3$_{B1}$ and Int3$_{B2}$"** are displayed in Figure 6.6. Without a group in the axial position the interaction is just between these two orbitals, but with the metal inside the plane of the porphyrin, as in **Int3$_{B2}$"**, further interactions with the a_{2u} orbital are seen, which raise this antibonding orbital further in energy and improve the oxidative power of the vanadium-peroxo moiety as seen from the reaction with cyclohexene. Therefore, vanadium-peroxo oxidants are more powerful oxidants when the vanadium-porphyrin complex has an anionic axial ligand that can pull the metal into the frame of the porphyrin and enable better and stronger orbital overlap.

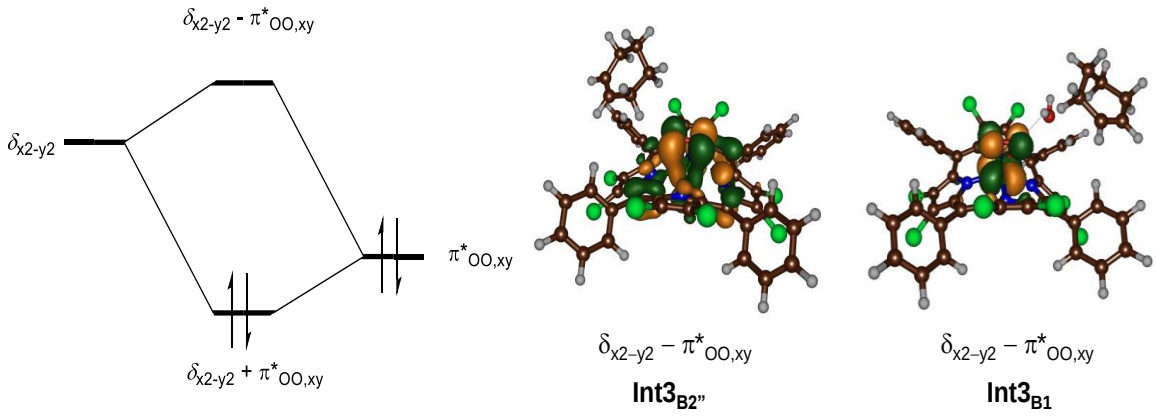

Figure 6.6. Molecular orbital splitting in vanadium-peroxo complexes for the interaction of the $\pi^*_{OO,xy}$ orbital on the peroxo group with the δ_{x2-y2} vanadium-orbital.

6.3.5 Mechanism of Cyclohexene Hydroxylation and Epoxidation by A/B+HCO_4^-

Finally, experimental work on the reaction of vanadium-oxo porphyrins in the presence of oxidant showed enhanced performance of substrate activation with HCO_4^- in the reaction mixture (Kumar *et al.*, 2015; Dar *et al.*, 2019). Therefore, we explored the potential energy profile of cyclohexene hydroxylation and epoxidation using a model that contains $[V^{IV/V}(O)(TPPCl_8)]^{0/+}$ + HCO_4^- and substrate: models **A3**/**B3**, see Figure 6.7.

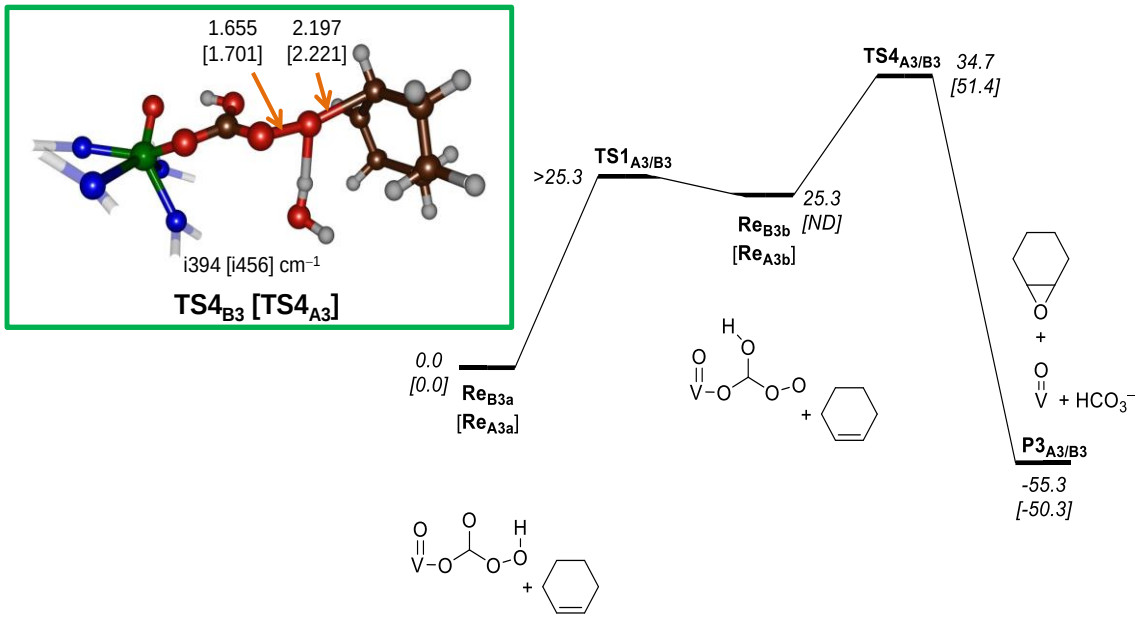

Figure 6. 7. Potential energy landscape with energies in kcal mol^{-1} for the epoxidation reaction of cyclohexene by ^{2}A3 and ^{1}B3 in the presence of HCO_4^- as obtained with DFT methods in Gaussian-09. Mechanism started from the vanadium-peroxo intermediate. Geometry optimizations done at UB3LYP/BS1. Bond lengths are in angstroms and the imaginary frequencies in cm^{-1}.

We tested two configurations of HCO_4^- for the reactant complexes, namely bound as either $HOOCO_2^-$ or $OOC(O)OH^-$, structures **Re$_{A3a/B3a}$** and **Re$_{A3b/B3b}$**, respectively. The former structure with a hydroperoxo group is found to be the most stable conformation by at least 25 kcal mol^{-1} for both **A** and **B** systems. The hydroperoxo proton forms an internal hydrogen bond with an oxo group of HCO_4^-, whereas the hydroxo group in the alternative

conformation formed a hydrogen bond with the vanadium-oxo group, see Electronic Supporting Information. Nevertheless, the reactant complexes of $[V^{IV/V}(O)(TPPCl_8]^{0/+}$ with HCO_4^-, a water molecule and cyclohexene have the HCO_4^- group bound to the vanadium centre.

We then tested direct oxygen atom activation of cyclohexene to form cyclohexene oxide using these models. The reaction starts from the reactant complexes **Re$_{A3a/B3a}$**, which are the $[V^{IV/V}(O)(TPPCl_8)]^{0/+}$ in complex with $HOOCO_2^-$, H_2O and cyclohexene. In the first stage of the reaction the $HOOCO_2^-$ species undergoes an internal proton transfer to form the $OOC(O)OH^-$ species (**Re$_{A3b/B3b}$**). We were not able to locate these transition states; therefore expect them to be close in energy to the **Re$_{A3b/B3b}$** structures.

In the next step of the reaction, the superoxo group of $OOC(O)OH^-$ then attacks the olefin bond via an epoxidation transition state **TS4$_{A3/B3}$** to form epoxide products (**P3$_{A3/B3}$**) in a concerted reaction step. We did not manage to locate transition states for direct activation of the olefin double bond from the hydroperoxo reactant complexes **Re$_{A3a/B3a}$**. All attempts for C–O bond formation through constraint geometry scans led to high-energy pathways without the formation of a local minimum.

The barriers for substrate activation of complexes **Re$_{A3b/B3b}$** are high in energy and are 34.7 kcal mol^{-1} for the pathway starting from the vanadium(V) complex and 51.4 kcal mol^{-1} for the one originating from the vanadium(IV) species. Optimized geometries of these transition states are shown in the inset in Figure 6.7. The imaginary frequency for the transition state shows attack of the peroxo group on one of the carbon atoms of the olefin only. However, no radical intermediate is formed, but en route to product the ring-closure step takes place. As such the pathway from models **A3**/**B3** has a much less symmetric transition state than that seen for the reaction with H_2O_2 as discussed above. The C–O bond in the transition state is very long, i.e. 2.197Å for **TS4$_{B3}$** and 2.221Å for **TS4$_{A3}$**. These distances are well longer than the distances of 1.747/1.738Å for the transition states in Figure 6. 2. Overall the calculations on models **A3** and **B3** show that

HCO_4^- is not the active oxidant in the reaction mechanism and is unlikely to be the oxygen transfer agent that generates cyclohexene epoxide products.

6.4 Conclusions

Density functional theory calculations on cyclohexene epoxidation and hydroxylation by vanadium porphyrin complexes are reported. We have conducted a detailed study of vanadium(IV) and vanadium(V) complexes with various models with oxo, peroxo or hydroperoxo groups as well as in the presence of either H_2O_2 or HCO_4^-. In addition, the axial and equatorial ligand effect on the reaction mechanism and reaction rates was investigated. Among all the models explored, we identify several vanadium complexes that are efficient oxidants of oxygen atom transfer reactions to olefins and particularly the vanadium-peroxo and vanadium-oxo complexes with an anionic axial ligand. These axial ligands pull the metal into the plane of the nitrogen porphyrin atoms and enable better orbital overlap; thereby affecting the electron affinity of these complexes and enhancing reaction rates. However, the reactivity, in contrast to iron-porphyrins, is highly sensitive to the equatorial ligand, whereby substituents to the meso-phenyl group – particularly methoxy groups – appear to reduce the catalytic performance dramatically. These changes are mostly the result of stereochemical interactions of the approaching substrate to the oxidant. The mechanisms of olefin epoxidation are concerted through a direct oxygen atom transfer rather than a stepwise reaction via a radical intermediate. This implies that we do not expect side reactions through isomerization and cis/trans scrambling of products. Overall, the work shows that olefin epoxidation by vanadium-oxo and vanadium-peroxo complexes should be highly efficient under the right conditions where a good oxidant is generated and this is in agreement with experimental work done previously. Moreover, these oxidants are expected to be highly specific and should produce limited amount of by-products in contrast to analogous iron-porphyrins.

Chapter 7

PROJECT 5

Selective Formation of an $Fe^{IV}O$ or an $Fe^{III}OOH$ Intermediate From Fe^{II}-H2O2 : Controlled Heterolytic vs Homolytic O-O Bond Cleavage by the Second Coordination Sphere

Khaled Cheaib,[a] M. Qadri E. Mubarak,[b] Katell Sénéchal-David,[a] Christian Herrero,[a] Régis Guillot,[a] Martin Clémancey,[c] Jean-Marc Latour,[c] Sam P. De Visser,*[b] Jean-Pierre Mahy,[a] Frédéric Banse,*[a] Frédéric Avenier*[a]

[a] Institut de Chimie Moléculaire et des matériaux d'Orsay (UMR 8182) Univ Paris Sud, Université Paris Saclay. 91405 Orsay cedex, France.
[b] Manchester Institute of Biotechnology and School of Chemical Engineering and Analytical Science, The University of Manchester 131 Princess Street, Manchester M1 7DN, United Kingdom.
[c] LCBM/PMB and CEA/BIG/CBM/ and CNRS UMR 5249, Université Grenoble Alpes, Grenoble 38054, France.

Abstract

Direct formation of Fe^{IV}-oxo species from nonheme Fe^{II} complexes and H_2O_2 is highly attractive for the development of selective oxidation reactions. Nonetheless, when using this oxidant, most of the Fe^{II} species known to date undergo a single electron oxidation generating Fe^{III} and hydroxyl radicals prone to engaging in uncontrolled radical chemistry. Here, we demonstrate that the devised incorporation of a dialkylamine group into the second coordination sphere of an Fe^{II} complex allows to switch the reactivity from the usual formation of Fe^{III} species towards the selective generation of an Fe^{IV}-oxo intermediate. We characterized the Fe^{IV}-oxo complex by UV-visible absorption and Mössbauer spectroscopy. Variable temperature kinetic analyses point towards a mechanism where the heterolytic cleavage of the O-O bond is triggered by a proton transfer from the proximal to the distal oxygen atom in the Fe^{II}-H_2O_2 complex with the assistance of the pendant amine. Density functional theory studies reveal that this heterolytic cleavage is actually initiated by an homolytic O–O bond cleavage immediately followed by a proton-coupled electron transfer that leads to the formation of the Fe^{IV}-oxo species and release of water through a concerted mechanism.

Published Reference
Cheaib, Khaled, M. Qadri E. Mubarak, Katell Sénéchal-David, Christian Herrero, Régis Guillot, Martin Clémancey, Jean-Marc Latour et al. "Selective Formation of an FeIVO or an FeIIIOOH Intermediate From Iron (II) and H_2O_2: Controlled Heterolytic versus Homolytic Oxygen–Oxygen Bond Cleavage by the Second Coordination Sphere." Angewandte Chemie 131, no. 3 (2019): 864-868.

7.1 Introduction

More than a century ago, Fenton discovered that the reaction of an Fe^{II} species with H_2O_2 led to the efficient oxidation of organic substrates in acidic aqueous media (Fenton, 1894). Ever since that discovery, debate continues on whether the active species of such systems is an OH radical (Haber and Weiss, 1932; Walling and Johnson, 1975; Walling, 1998) or an Fe^{IV}-oxo species (Bray and Gorin, 1932) resulting from either the homolytic or heterolytic cleavage of the O-O bond in its Fe-peroxide precursor. Beyond this historical controversy, understanding the key steps in the reactivity of Fe^{II} species with H_2O_2 is of great interest for the development of synthetic oxidation catalysts. Indeed, the production of high-valent Fe-oxo species capable of performing a priori selective 2-electron oxidation reactions, instead of hydroxyl radicals that would engage in uncontrolled oxidations has been a long term goal (Olivo *et al.*, 2017). Recent works suggest that changing the experimental conditions such as the pH may drive the reaction to a pathway or another (Goldstein and Meyerstein, 1999; Bataineh, Pestovsky and Bakac, 2012). Additionally, understanding the reaction between Fe^{II} and H_2O_2 is relevant to the comprehension of O_2 activation at the Fe^{II} centers of Fe enzymes (Kal and Que, 2017) such as tetrahydropterin-dependent monooxygenases (Fitzpatrick, 2003), or isopenicilin N synthase (Peck and van der Donk, 2017). It has been suggested that during the O_2 activation process by these enzymes, an Fe^{IV}-oxo species is formed via the heterolytic O-O cleavage of an $Fe^{II}OOR(H)$ intermediate. However, this reaction proved to be difficult to reproduce with synthetic catalysts and most of the Fe^{IV}-oxo species known to date have been obtained from the reaction of Fe^{II} complexes with oxygen donors such as iodosylbenzene (PhIO) or m-chloroperbenzoic acid (mCPBA) (Nam, 2007; McDonald and Que, 2013). The use of H_2O_2 with Fe^{II} complexes usually leads to the formation of the corresponding Fe^{III} complexes under stoichiometric conditions and yields $Fe^{III}OOH$ intermediates with excess H_2O_2 (Girerd, Banse and Simaan, 2000; Derat and Shaik, 2006b; Ségaud *et al.*, 2013; Padamati *et al.*, 2016). Only a few examples of nonheme Fe^{II} complexes have shown the direct formation of an Fe^{IV}-oxo species from their reaction

with H2O2 (Bautz *et al.*, 2006; Li, England and Que, 2010), or from the evolution of a putative $Fe^{II}OOH(R)$ intermediate (Bang *et al.*, 2014). Que et al. reported the nearly quantitative formation of $[Fe^{IV}O(TMC)]^{2+}$ from $[Fe^{II}(TMC)]^{2+}$ and H_2O_2 in the presence of 2,6-lutidine (Li, England and Que, 2010). DFT calculations showed that lutidine acted as a general base that promoted the proton transfer from the proximal to the distal O atom, thus facilitating the heterolytic O-O cleavage (Hirao *et al.*, 2011). The role played by lutidine was similar to that played by the distal His residue in horseradish peroxidase (HRP) (Derat and Shaik, 2006b), with the exception that it was added as a cofactor in solution and was not part of the catalyst scaffold. Thus, we reasoned that designing a ligand containing a non-coordinating base in the vicinity of the Fe^{II} ion would drastically influence its reactivity versus H_2O_2. Herein, we demonstrate that the incorporation of a secondary amine as a second coordination sphere group in the $[Fe^{II}(Bn\text{-}tpen)]^{2+}$ complex 2^{II} to give the new $[Fe^{II}(NHBn\text{-}tpen)]^{2+}$ 1^{II} (Figure 7.1) allows the direct formation of the $[FeIVO(NHBn\text{-}tpen)]^{2+}$ species 1^{IV}-O from the stoichiometric reaction between 1^{II} and H_2O_2. Interestingly, the reactivity of 1^{II} turns into the conventional reactivity of the original complex 2^{II} when the amine group is protonated, i.e. formation of an Fe^{III} species (Hazell *et al.*, 2002). Experimental and theoretical investigations of 1^{IV}-O formation converge towards a heterolytic O-O cleavage of the initial Fe^{II}-H_2O_2 complex promoted by a proton transfer assisted by the neighbouring amine. To the best of our knowledge, this is the first example of a nonheme Fe system where such a transformation is performed via an intra-molecular reaction.

7.2 Results and Discussion

The NHBn-tpen ligand was designed in such a way that the secondary amine fragment could not bind the metal through a stable 5- or 6-membered metallocycle. The X-ray structure of $[Fe^{II}(NHBn\text{-}tpen)(OH_2)]^{2+}$ (1^{II}) is displayed in Figure 7.1. It shows that the first coordination sphere of Fe^{II} is constituted of the typical N5 environment provided by Bn-tpen and related ligands(Mialane *et al.*, 1999; Hazell *et al.*, 2002; Taktak *et al.*, 2007) and confirms that the secondary amine (N6) is not coordinated to the metal center. The coordination sphere is completed by a water ligand, which is H-bonded to the secondary amine N-atom of the neighboring complex in the crystal. The mean Fe-N bond distance is 2.21 Å, which is typical of a high spin (S=2) Fe^{II}. Further characterizations indicate that the structure of 1^{II} is preserve in solution.

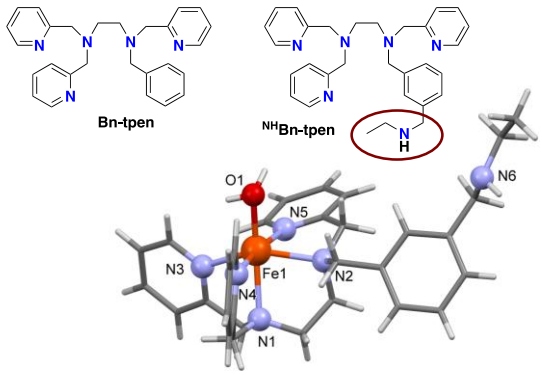

Figure 7.1. Structure of the ^{NH}Bn-tpen and Bn-tpen ligands and X-ray structure of the molecular cation, $\mathbf{1^{II}}$. Anions and disordered atoms were omitted for clarity. Bond distances (Å): Fe-N1 (2.24), Fe-N2 (2.24), Fe-N3 (2.15), Fe-N4 (2.18), Fe-N5 (2.23), Fe-O1 (1.92).

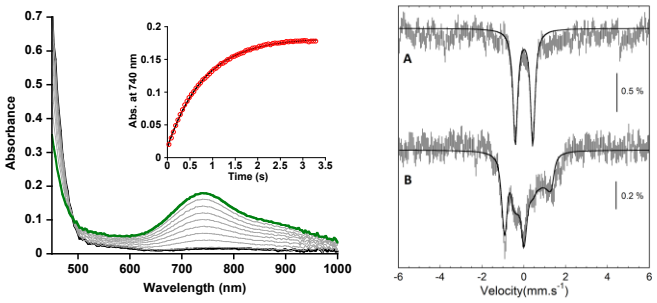

Figure 7.2. (Left) Time resolved UV-Vis spectra for the reaction of $\mathbf{1^{II}}$ (1mM) with 2.5 equiv. H^2O^2 in MeOH at 25°C. Black trace, spectrum recorded 12 ms after mixing the reactants. Green trace, spectrum recorded at the maximum of the formation of $\mathbf{1^{IV}}$**-O** (t = 3s). Insert: time trace monitored at 740 nm (red circles) and first order fitting of the curve (black trace). (Right) Mössbauer spectra of $\mathbf{1^{IV}}$**-O** (vertical bars) recorded at 4.5 K in absence (A) and presence (B) of a magnetic field of 6 T applied parallel to the γ ray. The black line is a spin-Hamiltonian simulation of both spectra with a unique set of parameters: δ = 0.015 mm/s, ΔE_Q = 0.83 mm/s, D = 21 cm−1 , E/D = 0, $g_x = g_y$ = 2.3, and g_z = 2.0, $A_{x,y,z}/g_N\beta N$ = (− 18, − 18, − 2) T, η = 0.26.

The reaction of $\mathbf{1^{II}}$ (1 mM) with 2.5 equiv. H_2O_2 in MeOH at 25°C monitored by stopped flow absorbance spectroscopy leads to the formation of a new species with an absorbance of 0.18 at 740 nm and a shoulder at 900 nm (Figure 7.2, green trace). Under these conditions, the maximum accumulation of this species occurred after 3s but decayed afterwards. Addition of PhIO (25 equiv. *vs* Fe) as oxidant instead of H_2O_2 yielded the same intermediate. Its spectroscopic signature is very similar to that observed for the $[Fe^{IV}O(Bn\text{-}tpen)]^{2+}$ species, $\mathbf{2^{IV}}$**-O** (λ_{max} = 739 nm with a shoulder at 900 nm, ε=400 M^{-1} cm^{-1} in acetonitrile) (Buron *et al.*, 2015). Hence, the intermediate observed in Figure 7.2 can be assigned as $[Fe^{IV}O(^{NH}Bn\text{-}tpen)]^{2+}$ $\mathbf{1^{IV}}$**-O**. The observation of an isosbestic point at

495 nm and the absence of any other intermediate in the course of the formation of **1^{IV}-O** suggests its direct formation from **1^{II}** and H_2O_2.

To further substantiate this assignment, the reaction product of **1^{II}** with H_2O_2 was studied by Mössbauer spectroscopy. Figure 7.2 shows the spectra obtained when a CD_3OD solution of ^{57}Fe-enriched **1^{II}** was reacted with 10 equiv. D_2O_2 for *ca.* 5 s and frozen. The spectra of the solution recorded at either 80 K (not shown) or 4.5 K (Figure 7.2A) in absence of magnetic field was dominated by a quadrupole doublet which can be simulated with a set of parameters $\delta = 0.015$ mm/s and $\Delta E_Q = 0.83$ mm/s. These values are very close to those reported for **2^{IV}-O** ($\delta = 0.01$ mm/s and $\Delta E_Q = 0.87$ mm/s) (Buron *et al.*, 2015) and in the usual range for $Fe^{IV}O$ species with S = 1 (McDonald and Que, 2013). This value of the spin was verified by performing an experiment under a field of 6 T applied parallel to the γ ray. The corresponding spectrum (Figure 7.2B) could be nicely simulated under this assumption with an axial zero field splitting value of 21 cm^{-1}. The quadrupole doublet accounts for ca 90 % of total Fe in the sample and the remaining Fe is probably present as ferric impurities as judged from the extra lines spread on both sides of the doublet in Figure 7.2A. Note that a sample obtained with 2.5 equiv. D_2O_2 *vs* **1^{II}** displayed identical spectroscopic characteristics.

Titration of **1^{II}** with H_2O_2 shows that the amount of **1^{IV}-O** formed was constant and maximum from 5 equiv. of added H_2O_2 up to 100 equiv. Considering that the reaction is quantitative under these conditions, an extinction coefficient of 190 $M^{-1}.cm^{-1}$ for the 740 nm chromophore is deduced (Bernal *et al.*, 1995). Additionally, the conversion in **1^{IV}-O** reached 80% and 93%, respectively, when 1 and 2.5 equiv. H_2O_2 were used. These results thus strongly suggest a 1:1 stoichiometry between **1^{II}** and H_2O_2 to yield **1^{IV}-O**. Consistently, further kinetic studies using different concentrations of H_2O_2 revealed that the reaction is first-order in both **1^{II}** and H_2O_2. At 25°C, a second-order rate constant of 0.316 $L.mmol^{-1}.s^{-1}$ was obtained from the plot of the pseudo first-order rate constant k_{obs} *vs* $[H_2O_2]$. The temperature dependence of k_{obs} was evaluated for samples containing 1 mM **1^{II}** and 10 equiv. H_2O_2. The resulting Eyring plot afforded an activation enthalpy $\Delta H^{\ddagger}$

of 3.75 kcal.mol^{-1} and an activation entropy $\Delta S^{\ddagger}$ of -43.3 cal.mol^{-1}.K^{-1}. These activation parameters compare well with those obtained for the formation of Fe^{IV}-oxo intermediates upon reaction of H_2O_2 with Fe^{II}(bispidine) ($\Delta H^{\ddagger}$ = 8.1 kcal.mol^{-1}, $\Delta S^{\ddagger}$ = -35.9 cal.mol^{-1}.K^{-1}) (Bautz *et al.*, 2006) or Fe^{II}(TMC) in the presence of 2,6-lutidine ($\Delta H^{\ddagger}$ = 6.9 kcal.mol^{-1}, $\Delta S^{\ddagger}$ = -34.4 kcal.mol^{-1}.K^{-1}) (Li, England and Que, 2010).

For the latter complex, the formation of the Fe^{IV}-oxo was explained as a global heterolytic O-O bond cleavage assisted by the external base which resulted from a combination of partial homolytic O-O cleavage and proton-coupled electron transfer as determined by DFT calculations (Hirao *et al.*, 2011).

The smaller activation enthalpy observed here suggests that, compared to an external base, the preorganization of the amine next to the metal center facilitates the formation of the Fe^{IV}-oxo intermediate. To support the crucial role played by the dialkylamine group in the formation of **1^{IV}-O**, similar experiments were performed under acidic conditions in the presence of 2 equiv. $HClO_4$ *vs* **1^{II}**. Under these conditions and even for a small amount of added H_2O_2 (2.5 equiv. *vs* Fe), formation of a low spin (S=½) Fe^{III}OOH intermediate was observed with typical UV-visible (λ_{max} = 539 nm) and EPR (g = 2.21, 2.14, 1.97) features (Hazell *et al.*, 2002; Horner *et al.*, 2002; Kaizer *et al.*, 2004) (Figure 7.3 and Scheme 1). In the presence of protons, the reactivity of **1^{II}** switches to the conventional Fe^{II}-to-Fe^{III} reactivity exhibited by most of nonheme Fe^{II} complexes supported by pentadentate ligands (Hazell *et al.*, 2002; Horner *et al.*, 2002; Balland *et al.*, 2003; Roelfes, Vrajmasu, Chen, Raymond Y N Ho, *et al.*, 2003; Kaizer *et al.*, 2004; Martinho *et al.*, 2008; Ségaud *et al.*, 2013).

Conversely, in its neutral form, the amine interacts specifically with the Fe^{II}-H_2O_2 adduct to promote the heterolytic O-O bond cleavage to yield **1^{IV}-O**, with the function of a springboard that relays protons between the proximal and distal oxygen atoms of H_2O_2. To substantiate our hypothesis, additional experiments were carried out using D_2O_2 in CD_3OD. Under these conditions, the formation of **1^{IV}-O** was observed as well, and a large

kinetic isotope effect (KIE, k_H/k_D) of 5.6 was measured. A similar value was reported by Li *et al.* for the formation of $[Fe^{IV}O(TMC)]^{2+}$ from the Fe^{II} complex and 2,6-lutidine as a base (Li, England and Que, 2010).

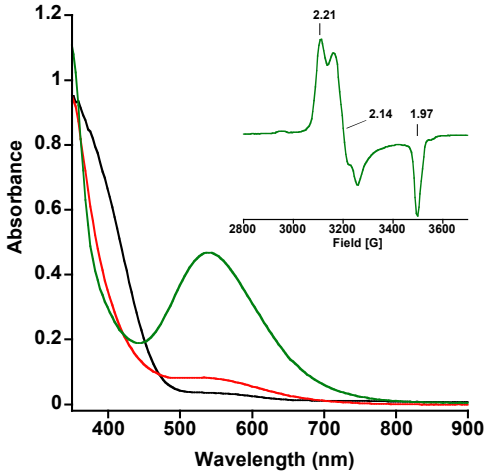

Figure 7.3. UV-Vis spectra of **1^{II}** in MeOH in the presence of $HClO_4$ (2 equiv.) before (black trace) and after addition of H_2O_2 (2.5 equiv., red trace or 100 equiv., green trace). Insert: X-band EPR spectrum at 100 K of the sample corresponding to the green UV-Vis. spectrum (Power 0.12 mW).

Given all the above observations, *i.e.*, (i) a direct conversion between **1^{II}** and **1^{IV}-O**, (ii) first-order kinetics in both Fe^{II} and H_2O_2, (iii) activation parameters consistent with O-O bond heterolysis and (iv) the implication of both protons and the amine in the second coordination sphere, one can suggest that the formation of **1^{IV}-O** is initiated by the heterolytic cleavage of an Fe^{II}-H_2O_2 intermediate promoted by the dialkylamine group acting as an acid-base relay. The role of this latter moiety being similar to the one assigned to distal histidine or glutamate residues in heme peroxidases (Roelfes, Vrajmasu, Chen, Raymond Y.N. Ho, *et al.*, 2003; Derat and Shaik, 2006b).

To gain more insight into the mechanism of the binding and activation of H_2O_2 on **1^{II}**, a series of DFT calculations were performed. We started from the $^{1,3,5}[Fe^{II}(H_2O_2)(^{NH}Bn\text{-}tpen)]^{2+}$(**$^{1,3,5}1^{II}$-$H_2O_2$**) complexes in either the singlet, triplet or quintet spin state. First, **1^{II}-H_2O_2** was optimized in various orientations of H_2O_2 with respect to the metal center and dialkylamine group. In particular, orientation (a) has the distal OH group of H_2O_2 in hydrogen bonding interaction with the pendant amine group (**1^{II}-H_2O_2-a**), whereas in the alternative structure the proximal OH group was hydrogen bonded to the amine (**1^{II}-H_2O_2-b**) (Figure 7.4). Test calculations with a range of density functional methods were performed including the full reaction mechanism with B3LYP and PBE1PBE DFT methods. Both density functional methods give virtually the same reaction mechanism and the only difference relates to the relative energies of the various complexes. Our results are consistent with a recent benchmark study that showed these methods to reproduce experimental free energies of activation for the reaction of nonheme Fe^{IV}-oxo with substrates to within 3 kcal mol^{-1} (Dunford, 1999; Cantú Reinhard, Faponle and de Visser, 2016) .

Finally, as the spin-state ordering of the Fe^{IV}-oxo species is sometimes sensitive to the choice of the density functional method, we calculated the Fe^{IV}-oxo species with several methods and procedures. With all methods, apart from BP86, the triplet spin **1^{IV}-O** is the ground state in agreement with the Mössbauer studies reported above. Despite these fluctuations in spin-state energies, previous studies of ours; however, showed that changing the density functional method generally does not change regio- and stereo-selectivities of a chemical reaction but only affects the relative energies (Cantú Reinhard *et al.*, 2016; Yang *et al.*, 2016).

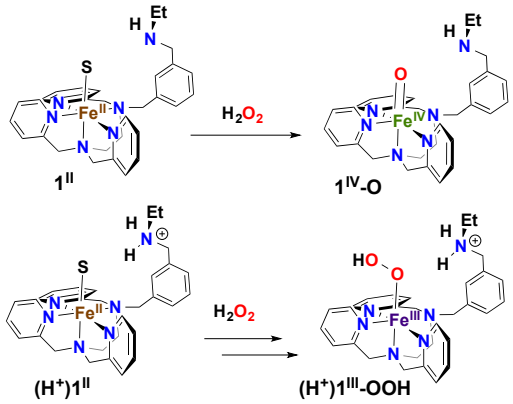

Scheme 7.1. Influence of the second coordination sphere on the formation of $Fe^{IV}O$ and $Fe^{III}OOH$ intermediates as observed in this work. (with S = H_2O or MeOH).

In the triplet and quintet spin states, the **1^{II}-H_2O_2-a** and **1^{II}-H_2O_2-b** structures are close in energy with a small preference of the latter at B3LYP level of theory. Well higher in energy than these quintet spin H_2O_2 complexes are the triplet spin states. Therefore, the triplet spin **^{3}1^{II}-H_2O_2** will not play a role in the reaction mechanism leading to the formation of the Fe^{IV}-oxo species. Subsequently, we investigated the proton transfer from H_2O_2 to the dialkylamine group to form an Fe^{II}-hydroperoxo intermediate, which is negligible from complex **1^{II}-H_2O_2-b** (Figure 7.4) at B3LYP and PBE1PBE level of theories.

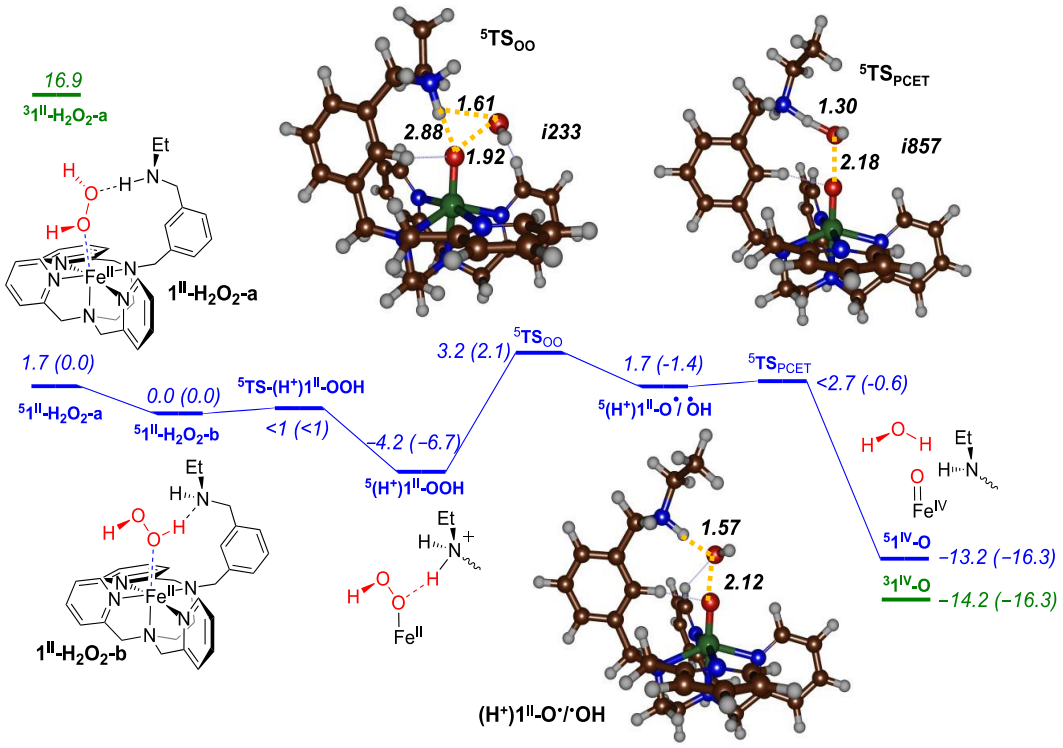

Figure 7. 4. Potential energy landscape for the formation of the $Fe^{IV}O$ species **1^{IV}-O** from the Fe^{II}-H_2O_2 adduct **1^{II}-H_2O_2** as calculated at UB3LYP/BS2//UB3LYP/BS1 level of theory. Energies are in kcal.mol^{-1} with ΔE_{BS2}+ZPE data outside parenthesis and ΔG_{BS2} data in parenthesis

However, in the case of **1^{II}-H_2O_2-a** no direct proton transfer from the terminal OH group could be located. Instead, an internal rotation occurs during the geometry scan and changes structure **1^{II}-H_2O_2-a** into **1^{II}-H_2O_2-b**.

The geometry scan converges to a proton transfer intermediate (H^+)1^{II}-OOH that shows a hydrogen bond between the nascent ammonium group and the proximal oxygen atom. The next step leads to the cleavage of the hydroperoxo bond in (H^+)1^{II}-OOH. Similarly to previous calculations on nonheme Fe complexes (Faponle *et al.*, 2015; Timmins, Saint-André and De Visser, 2017), we find a homolytic bond breaking to give a formal Fe^{II}-oxyl complex and an OH radical. In particular, we find an electronic configuration

with a spin density of 4.2 on the Fe-oxo unit and a down-spin electron (spin density of -0.6) on the leaving ˙OH in support of our characterization of $(H^+)1^{II}$-O˙/˙OH. The calculated reaction barrier for the homolytic cleavage of the O-O bond is $\Delta G^{\ddagger}$ = 8.8 (B3LYP) and 15.3 (PBE1PBE) kcal.mol^{-1} via $^5TS_{OO}$. The latter free energy of activation is in perfect agreement with the experimental Eyring values at 298 K of 16.7 kcal.mol^{-1} (Figure 7.4). Attempts to swap molecular orbitals to find an Fe^{IV}-oxo and an OH^- anion converged back to a radical situation in all cases and hence corresponds to a higher energy pathway.

In the final reaction step the Fe^{IV}-oxo or 1^{IV}-O is formed through a simultaneous electron and proton transfer process, namely proton transfer from the pendant ammonium group to the OH radical and electron transfer from the Fe^{II}-oxyl to ˙OH. This pathway has a small barrier of less than 1 kcal mol^{-1} above $(H^+)1^{II}$-O˙/˙OH. Interestingly, the energy surface from TS_{OO} to TS_{PCET} is almost flat (the Fe^{II}-oxyl ˙OH intermediate $(H^+)1^{II}$-O˙/˙OH is high in energy), which indicates that these steps will be seen as synchronous and the electron/proton transfer may be seen as coincidental with the initial homolytic O-O bond scission.

The structures of $^5TS_{OO}$, $(H^+)1^{II}$-O˙/˙OH and $^5TS_{PCET}$ are displayed in Figure 7.4 alongside the reaction profile. Clearly seen, particularly in $^5TS_{OO}$, are H-bond interactions of the ammonium group with the distal (1.61 Å) and proximal (2.88 Å) oxygen atoms. As such, O-O bond cleavage will be affected by H/D replacement and should lead to a KIE as observed experimentally. In conclusion, the computational modeling reveals that the activation of H_2O_2 indeed occurs *via* an overall heterolytic cleavage of the initial Fe^{II}-H_2O_2, as inferred from the experimental data. However, the heterolytic cleavage is initiated by a homolytic O-O bond cleavage immediately followed by a proton/electron-transfer from the ammonium/Fe^{II}-oxyl that forms the Fe^{IV}-oxo species and releases water.

Finally, we tested the same reaction mechanism under low pH conditions, *i.e.* starting from the H_2O_2 bound complex with protonated dialkylamine chain, (H^+)-1^{II}-H_2O_2-b. Thus, these calculations start from $^{5,3}(H^+)$-1^{II}-H_2O_2-b and a homolytic O-O bond cleavage barrier of $\Delta G^{\ddagger}$ = 8.2 kcal mol^{-1} splits H_2O_2 into two OH radicals directly in an exergonic step of 3.6 kcal mol^{-1} to form $^5(H^+)1^{III}(OH)/^{\bullet}OH$. The electronic configuration of the latter consists of an Fe^{III}-hydroxo with five unpaired electrons on the metal antiferromagnetically coupled to an OH radical. Subsequently, a proton-coupled electron-transfer barrier gives the Fe^{IV}-oxo species and a water molecule in a highly exergonic reaction step. These results are in line with the experimental work reported above. In the presence of acid, the substantial barrier for the PCET indicates that the nascent free $^{\bullet}OH$ may be easily scavenged by the MeOH solvent leading to the Fe^{III} species rather than yielding the Fe^{IV}-oxo directly. Our findings are consistent with those reported by Hirao et al. for the reaction of $[Fe^{II}(TMC)]^{2+}$ with H_2O_2 in the absence of base (Hirao *et al.*, 2011).

7.3 Conclusion

In summary, we demonstrate that the introduction of a pendant amine group in the second coordination sphere of a non heme Fe^{II} complex modifies its reactivity toward H_2O_2 and allows the direct formation of an Fe^{IV}-oxo intermediate instead of the $Fe^{III}OOH$ usually observed for related complexes lacking this second sphere moiety. To our knowledge, this is the first time that such an effect is demonstrated in an intra-molecular fashion. Activation parameters measured during the process correlate with the values previously associated to heterolytic O-O bond cleavage in the literature. The large (k_H/k_D) KIE is also in good agreement with the involvement of the amine group as an acid/base relay. Our mechanism is supported by density functional theory calculations, which shows that the mechanism involves a proton transfer from the proximal OH group of H_2O_2 towards the distal one, *via* the transient protonation of the pendant amine group. More precisely, the initial proton transfer to the alkylamine is followed by a homolytic O-O bond cleavage accompanied by proton-coupled electron transfer to form the Fe^{IV}-oxo species.

Acknowledgements

The authors thank the Labex CHARMMMAT as well as the Agence Nationale de la Recherche (ANR BIOXICAT; 12-JS07-0007-01) for financial support. M.Q.E.M. thanks the Ministry of Higher Education Malaysia for a studentship. J.-M. L. thanks the Labex ARCANE and CBH-EUR-GS (ANR-17-EURE-003) for partial funding. This work was also supported by the ECOSTBio Action CM1305.

Chapter 8

PROJECT 6

Hydrogen Atom Abstraction by High-Valent Fe(OH) versus Mn(OH) Porphyrinoid Complexes: Mechanistic Insights from Experimental and Computational Studies

Jan Paulo T. Zaragoza,[†] Daniel C. Cummins,[†] M. Qadri E. Mubarak,[§] Maxime A. Siegler,[†] Sam P. De Visser,[§] and David P. Goldberg[†]

[†]Department of Chemistry, The Johns Hopkins University, 3400 North Charles Street, Baltimore, Maryland 21218, United States.

[§]The Manchester Institute of Biotechnology and Department of Chemical Engineering and Analytical Science, The University of Manchester, 131 Princess Street, Manchester M1 7DN, United Kingdom.

Abstract

High-valent metal-hydroxide species have been implicated as key intermediates in hydroxylation chemistry catalyzed by heme monooxygenases such as the Cytochrome P450s. However, in some classes of P450s, a bifurcation from the typical oxygen rebound pathway is observed, wherein the reactive Fe^{IV}(OH)(porphyrin) (Cpd-II) species carries out a net hydrogen atom transfer reaction to form alkene metabolites. In this work, we examine the hydrogen atom transfer (HAT) reactivity of a Cpd-II model complex Fe^{IV}(OH)(ttppc) (1), tppcc = 5,10,15-tris(2,4,6-triphenyl)-phenyl corrole, towards substituted phenol derivatives. The iron hydroxide complex 1 reacts with a series of para-substituted 2,6-di-tert-butylphenol derivatives (4-X-2,6-DTBP; X = OMe, Me, Et, H, Ac), with second order rate constants k_2 = 3.6(2)–1.21(3) x 10^4 M^{-1} s^{-1}, and yielding linear Hammett and Marcus plot correlations. Based on mechanistic analyses, including a KIE = 2.9(1) and DFT calculations, a rate-determining O–H cleavage occurring through a concerted HAT mechanism is concluded. Comparison of the HAT reactivity of 1 to the analogous Mn complex, Mn^{IV}(OH)(ttppc), where only the central metal ion is different, indicates a faster HAT reaction and a steeper Hammett slope for 1. The O–H bond dissociation energy (BDE) of the M^{III}(HO-H) complexes were estimated from a kinetic analysis to be 85 and 89 kcal mol^{-1} for Mn and Fe, respectively. These estimated BDEs are closely reproduced by DFT calculations and are discussed in the context of how they influence the overall H-atom transfer reactivity.

Publish reference

Mubarak, M. Qadri E. and Sam P. De Visser. "Second-coordination Sphere Effect on the Reactivity of Vanadium-peroxo Complexes: A Computational Study" Inorganic Chemistry (2019).

8.1 Introduction

The design and development of well-defined, observable synthetic models of highly reactive metal–oxygen intermediates has helped elucidate the mechanisms of oxidation reactions catalyzed by metalloenzyme (Sahu and Goldberg, 2016; Zaragoza and Goldberg, 2018). For example, synthesis of biomimetic high-valent metal-oxo complexes and examination of their hydrogen atom transfer (HAT) reactivity has provided insights into the ground-state thermodynamics of related biological oxidations, as well as information for the design of synthetic catalysts (McDonald and Que, 2013; Nam, Lee and Fukuzumi, 2014; Engelmann, Monte-Pérez and Ray, 2016; Baglia, Zaragoza and Goldberg, 2017; Sacramento and Goldberg, 2018). Heme enzymes are biological catalysts that perform a large variety of oxidation reactions in nature. Cytochrome P450 (CYP), in particular, is a heme monooxygenase that activates inert C-H bonds *via* a high-valent iron-oxo intermediate, Compound I (Cpd-I) (Denisov *et al.*, 2005; Makris *et al.*, 2006; Ortiz De Montellano, 2010; Rittle and Green, 2010; Poulos, 2014; Huang and Groves, 2017). The rate determining step for this reaction is the HAT from the C-H substrate to Cpd-I to form Compound II (Cpd-II), an iron(IV)-hydroxide species (Scheme 8.1). The subsequent step, which is rapid, is the rebound of the $^{\bullet}$OH group to the incipient carbon radical to form the hydroxylated substrate. Indeed, many of the studies of HAT involving model systems have focused on the reactivity of metal-oxo complexes and the thermodynamic analysis of the O-H bond of the metal-hydroxide intermediate formed during the HAT reaction. However, CYP monooxygenases, and the related CYP peroxygenases, can perform desaturation and C-C bond cleaving reactions in addition to hydroxylation, where their pathways can bifurcate at the Cpd-II state between oxygen rebound and HAT mechanisms. Desaturation reactions result in the formation of toxic alkene metabolites (Scheme 8.1). Conversion of valproic acid to 4-ene valproic acid (Rettie *et al.*, 1987, 1988, 1995), ethyl carbamate to vinyl carbamate (Guengerich and Kim, 1991), testosterone to 17β-hydroxy-4,6-androstadiene-4-one (Nagata *et al.*, 1986),

lauric acid to 11-dodecenoic acid (Guan *et al.*, 1998), and decarboxylation of fatty acids to terminal alkenes (specifically by $OleT_{JE}$) (Rude *et al.*, 2011; Belcher *et al.*, 2014; Liu *et al.*, 2014; Amadio *et al.*, 2015; Faponle, Quesne and De Visser, 2016; Grant, Mitchell and Makris, 2016; Hsieh *et al.*, 2017) are just some of the examples of this CYP-mediated desaturation reactions.

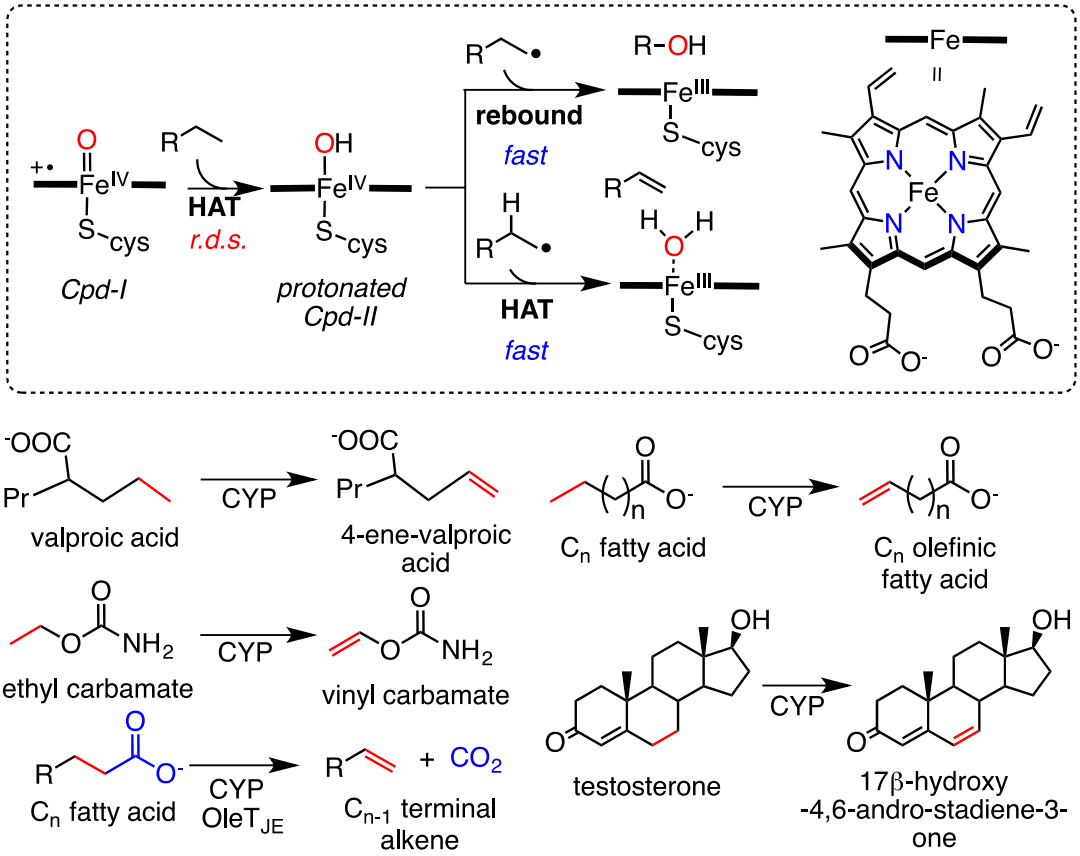

Scheme 8.1. Divergent Oxidation Pathways for CYP Cpd-II, and Examples of Desaturation Reactions Mediated by CYPs.

While substrate positioning in the active site binding pocket has been implicated to play a key role in selection of rebound hydroxylation versus HAT pathways for Cpd-II in CYPs (Faponle, Quesne and De Visser, 2016; Pickl *et al.*, 2019), the fundamental electronic and

structural factors that ultimately control these pathways remain poorly understood. Ground state thermodynamic properties are often invoked as key factors in controlling HAT by high-valent metal-oxo complexes. Along these lines, the ground state thermodynamics related to the HAT reactivity of Cpd-II can be assessed from the BDE(O-H) of the expected ferric-aquo product ($Fe^{III}(H_2O)$(porph)(cys)). Few such BDE values are available from experiment on heme enzymes, but a BDE(O-H) of 90 kcal mol^{-1} was recently reported in one case for the $Fe^{III}(H_2O)$ species in CYP158 (Mittra and Green, 2019).

In contrast, the $Fe^{III}(H_2O)$ form of the heme enzyme aromatic peroxygenase (APO) was characterized as having a much lower BDE of 81 kcal/mol, despite the similarity of this thiolate-ligated heme active site with that of Cys-bound CYP. The corresponding O-H bond strength in the ferric hydroxide form of horseradish peroxidase (HRP), which contains a neutral His axial ligand trans to the OH group, is 85 kcal/mol as derived from the $Fe^{IV}(O)/Fe^{III}(OH)$ redox potential(Hay and Wadt, 1985) (Hayashi and Yamazaki, 1979). Such a wide range in similar porphyrin ferric O-H bond strengths indicates that there are likely subtle, as yet unidentified factors regarding the metal ion active site that can affect this value and ultimately influence HAT reactivity. Given the challenges in characterizing these species in the native, enzymatic systems, we have set out to develop well-defined synthetic $Fe^{IV}(OH)/Fe^{III}(H_2O)$ porphyrinoid complexes that should allow for an examination of their reactivity and related thermodynamics. Such compounds, in heme or nonheme systems, are extremely rare. We previously reported the synthesis of Fe^{IV}(OH)(ttppc) (ttppc = 5,10,15-tris(2,4,6-triphenyl)-phenyl corrole) (**1**) and its reactivity towards *para*-X substituted trityl radical derivatives in efforts to model the radical rebound step leading to C-O bond formation (Zaragoza *et al.*, 2017). Kinetic studies indicated that the radical rebound step was a concerted, charge neutral process. It should be noted that with triarylcorrole ligands, the electronic ground state of formally Fe^{IV} and Mn^{IV} corroles has been described as varying between the two canonical valence

tautomers, $M^{III}(X)(corrole^{+\bullet})$ and $M^{IV}(X)(corrole)$, depending on the axial ligand X (Ganguly *et al.*, 2017, 2018).

Conclusive characterization of the ground electronic state of these compounds is challenging, and complex **1** and the analogous Mn(OH)(ttppc) will be described as metal(IV) hydroxide complexes throughout this work for simplicity. Since our original report, the complex $Fe^{IV}(OH_n)$(TAML) (TAML = tetra-amido macrocyclic ligand) was recently reported (Weitz *et al.*, 2019), as well as a non-heme Fe^{III}(OH) complex that demonstrated both radical rebound and hydrogen atom transfer reactivity (Drummond *et al.*, 2019).

Herein the H-atom transfer reactivity of Fe^{IV}(OH)(ttppc) (**1**) with a series of phenol derivatives is described, providing a mechanistic analysis of HAT reactivity. The synthesis and structural characterization of $Fe^{III}(H_2O)$(ttppc) (**2**), the corresponding HAT product, was also accomplished. Hammett and Marcus plot analyses, together with kinetic isotope effect (KIE) measurements, provide detailed insight into how the HAT reaction proceeds. A direct comparison with the reactivity of Mn^{IV}(OH)(ttppc), combined with computational analyses of the reaction trajectories of these two high-valent metal hydroxide complexes, enabled assessment of how the central metal ion (Mn vs Fe) tunes the H-atom transfer reactivity. The experimental and computational studies on **1**, along with work on the analogous Mn complex Mn^{IV}(OH)(ttppc), provide novel insights into the thermodynamic properties that govern the reactivity of metal hydroxide species towards H-atom donors.

8.2 Results and Discussion

8.2.1 Synthesis and Structural Characterization of an $Fe^{III}(H_2O)$ Complex.

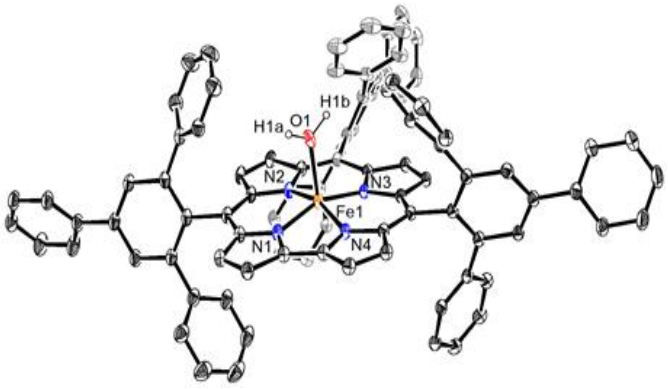

Figure 8.1. Displacement ellipsoid plot (35% probability level) for $Fe^{III}(H_2O)$(ttppc) (2) at 110(2) K. H atoms (except for those attached to O1) are omitted for clarity.

The synthesis of $Fe^{III}(H_2O)$(ttppc) (**2**), the expected H-atom abstraction product of Fe^{IV}(OH)(ttppc) (**1**), was prepared by ligand exchange of the previously synthesized $Fe^{III}(OEt_2)_2$(ttppc) (Zaragoza *et al.*, 2017) with H_2O, followed by fluorobenzene/*n*-pentane vapor diffusion to give single crystals for X-ray diffraction. The molecular structure of $Fe^{III}(H_2O)$(ttppc) (**2**) is shown in Figure 8.1. The structure of **2** shows an Fe–O bond distance of 2.126(2) Å, much longer as compared to that of **1** (Fe–O = 1.857(3) Å, Table S1). The Fe–O bond distance for **2** is similar to other well-characterized mononuclear $Fe^{III}(H_2O)$ units in porphyrin (2.012(2) – 2.084(4) Å) (Cheng *et al.*, 1994; Ohgo *et al.*, 2006; Xu, Powell and Richter-Addo, 2011) and tetra-amido macrocyclic ligand scaffolds (TAML) (2.097(2) – 2.1102(18) Å) (Ghosh *et al.*, 2003; Ellis *et al.*, 2010).

The X-ray structure of **2** is the first example of an H_2O-bound iron(III) corrole, which are typically isolated with NO, Et_2O, or pyridine axial ligands (Makris *et al.*, 2006; Rittle and Green, 2010; Huang and Groves, 2017). The frozen solution EPR spectrum of **2** shows an intense signal at g = 4.29 consistent with an intermediate spin (S = 3/2) Fe^{III} metal center, similar to $Fe^{III}(OEt_2)_2$(ttppc) in toluene (Figure S1) (Zaragoza *et al.*, 2017). An Evans method measurement of **2** gives μ_{eff} = 3.6(1) μ_B, (spin-only μ_{eff} = 3.87 μ_B for S = 3/2) further supporting the spin state assignment. It should be noted that we are not able to unambiguously determine the extent to which H_2O remains coordinated for the EPR and Evans method measurements in toluene. For comparison, the analogous $Mn^{III}(H_2O)$(ttppc) (Zaragoza, Siegler and Goldberg, 2018) has a much longer metal-oxygen bond distance of 2.2645(18) Å, likely due to Jahn-Teller distortion for the high-spin Mn^{III} ion (Blomberg and Siegbahn, 1997).

8.2.2 Reaction of Fe^{IV}(OH)(ttppc) (1) with H-atom Transfer Reagents

Initial studies on the HAT reactivity of **1** began with C-H substrates. Reaction of **1** with 9,10-dihydroanthracene (DHA), a common H-atom donor with a relatively weak C-H bond (BDE = 76.3 kcal mol^{-1}) was carried out (Stein and Brown, 1991). Preliminary UV-visible spectroscopy measurements showed that **1** reacts with DHA in toluene at 23 ˚C, although the reaction is very slow (<5% decay to $Fe^{III}(H_2O)$(ttppc) (**2**) over 5 h). In contrast, reaction of 1 with 2,4-di-*tert*-butylphenol (2,4-DTBP) (toluene, 23 ˚C) results in rapid formation of **2**, as observed by UV-vis spectroscopy. Product analysis of the reaction solution by gas chromatography (GC-FID) led to detection of the bis(phenol) dimer product 3,3′,5,5′-tetra-*tert*-butyl-(1,1′-biphenyl)-2,2′-diol in good yield (67(1) %), consistent with a 1:1 stoichiometry for oxidation of the phenol substrate by the iron complex **1**.

Having demonstrated the proficiency of **1** in cleaving the phenolic O-H bond in 2,4-DTBP, we employed a series of *para*-substituted 2,6-di-*tert*-butylphenol derivatives (4-X-2,6-di-*t*-Bu-C_6H_2OH; X = OMe, tBu, Et, Me, H) as H-atom transfer substrates.

Variation of the *para* substituents allowed us to measure the influence of the electronic and thermodynamic properties of the phenol derivatives on the H-atom transfer reactivity (Figure 8.2a). A direct comparison with the reactivity of Mn^{IV}(OH)(ttppc) can also be made, providing an opportunity to assess how the central metal ion (Mn vs Fe) affects the reactivity towards hydrogen atom donors. Reaction of **1** with a series of *para*-substituted phenols were carried out similarly to the reaction of **1** with 2,4-DTBP. A solution of **1** and excess 4-methoxy-2,6-di-*tert*-butylphenol (4-OMe-2,6- DTBP) (5.4 equiv) was analyzed by X -band electron paramagnetic resonance (EPR) spectroscopy (16 K), and gave EPR signals corresponding to $Fe^{III}(H_2O)$(ttppc) (**2**) (g = 4.29) and phenoxyl radical (g = 2.0) (Figure S2). These data showed **1** reacts with 4-OMe-2,6-DTBP in accordance to the scheme in Figure 8.2a. The reaction kinetics of **1** with 4-OMe-2,6-DTBP was monitored by stopped-flow UV-vis spectroscopy, showing isosbestic conversion of **1** to **2** within 1s (Figure 8.2b). Pseudo-first order conditions (>10-fold equiv substrate) were employed, and led to single exponential curves that were fit to up to five half-lives. The resulting observed rate constant (k_{obs}) varied linearly with phenol concentration, yielding a second order rate constant (k_2) of 1.21(3) x 10^4 M^{-1} s^{-1}. A kinetic isotope effect (KIE) was determined by reaction of **1** with the ArOD isotopologue of 4-OMe-2,6-DTBP. A significant KIE of 2.9(1) was measured, indicating that the rate-determining step involves O–H cleavage.

The second-order rate constants (k_2) for the other *para*-substituted 2,6-DTBP derivatives were obtained in a similar fashion (Figures S3-S8) and are listed in Table 1 together with their thermodynamic parameters (Hammett constants σ^+_p, re dox potentials, and BDEs). It should be noted that E_{ox} values listed in Table 1 where obtained in acetonitrile, however we obtain a good correlation between our measured k_2 values in toluene and the E_{ox} values from CH_3CN. In each case, isosbestic conversion of **1** to the $Fe^{III}(H_2O)$ product **2** was rapid and varied over two orders of magnitude (k_2 = 3.6(2) – 1.21(3) x 10^4 $M^{-1}s^{-1}$).

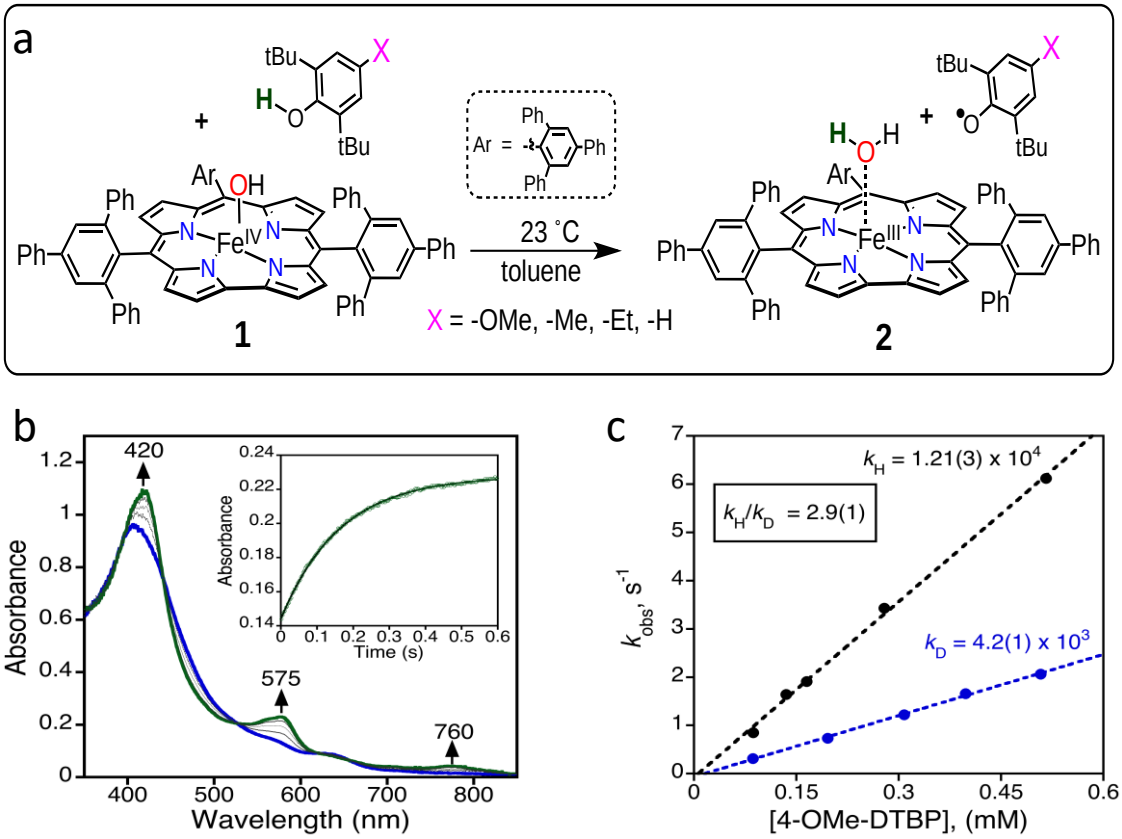

Figure 8.2. a) Reaction of Fe^{IV}(OH)(ttppc) with para-X-substituted 2,6-di-tert-butylphenol derivatives. b) Time-resolved UV−vis spectral changes observed in the reaction of **1** (15 μM) with 4-OMe-2,6-DTBP (0.52 mM) in toluene at 23 °C. Inset: changes in absorbance vs time for the growth of **2** (575 nm) (green circles) with the best fit line (black). c) Plot of pseudo-first order rate constants (k_{obs}) vs [4-OMe-2,6-DTBP] for the OH (black) and OD (blue) phenol isotopologues.

Table 8.1. Second order rate constants for the reaction between $Fe^{IV}(OH)$(ttppc) (1) and para-X-substituted phenol derivatives, Hammett σ^+ constants, redox potentials and BDEs of 4-X-2,6-DTBP.

	k_2 (M^{-1} s^{-1})	σ^+_p [a]	E_{ox} [b] (Vvs $Fc^{+/0}$)	BDE [c] (kcal mol^{-1})
-OMe	1.21(3) x 10^4	-0.78	0.53	78.3
-OMe (OD)	4.2(1) x 10^3	---	0.59	---
-Me	2.0(1) x 10^3	-0.31	0.81	81.0
-Et	3.2(3) x 10^3	-0.29	0.88	---
-H	83(3)	0.00	1.07	82.8
-Ac	3.6(2)	--	--	84.4

[a] Reference (Hansch, Leo and Taft, 1991).

[b] in CH_3CN (Lee *et al.*, 2014).

[c] in benzene (Lucarini *et al.*, 1996).

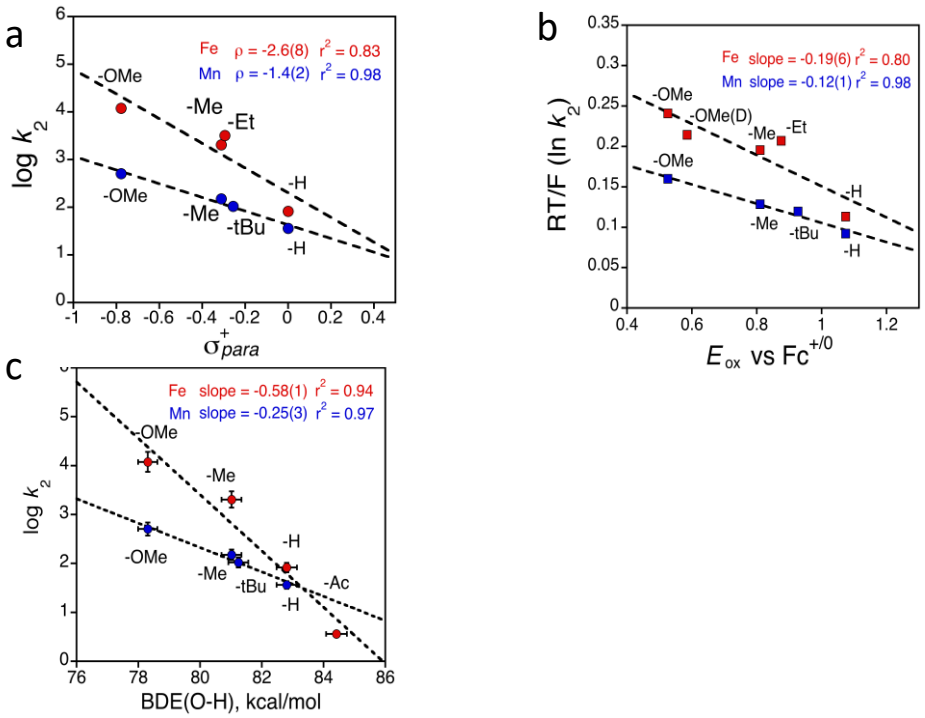

Figure 8.3. Comparison of a) Hammett, b) Marcus, and c) log k_2 vs BDE plots for the reaction of Fe^{IV}(OH)(ttppc) (1) (red circles/squares, in toluene) or Mn^{IV}(OH)(ttppc) (blue circles/squares, in benzene) with 4-X-2,6-DTBP. Kinetic data for Mn^{IV}(OH)(ttppc) from previous work (Zaragoza, Siegler and Goldberg, 2018)

8.2.2 Comparison of the Reactivity of $Fe^{IV}(OH)$(ttppc) (1) and $Mn^{IV}(OH)$(ttppc) with Phenol Derivatives.

Hammett analysis of the kinetic data for 1 (Figure 8.3a, red circles) showed a decrease in the rate constants with the more electron-deficient phenol, with a slope of ρ^+ = -2.6(8). This slope is higher as compared to that of Mn^{IV}(OH)(ttppc) (ρ^+ = - 1.4(2)) (Figure 8.3a, blue circles), implying a relatively greater charge separation in the HAT transition state for the Fe vs the Mn complex. A Marcus plot analysis, which provides information on the involvement of electron transfer on the rate-determining step of the reaction, was also performed. A slope of ~ -0.5 is predicted for the plot of (RT/F) ln k_2 vs E_{ox} (where k_2 is the second order rate constant and E_{ox} is the redox potential of the substrate being oxidized) for reactions with a rate-determining electron transfer step, provided that $\Delta G^{\circ}_{ET}/\lambda$ is close to zero (Marcus and Sutin, 1985).

A slope of -0.19(6) was obtained for **1** (Figure 8.3b, red squares), close to the values obtained for HAT reactions of a Cu-superoxo complex (slope = -0.29) (Lee *et al.*, 2014), and Mn^{IV}(OH)(ttppc) (slope = -0.12) (Figure 8.3b), in which a concerted H-atom transfer is invoked. Plotting the log k_2 for **1** vs the bond dissociation energy (BDEs) of O–H bond of the phenol substrate (Figure 8.3c) also show a good correlation, with a slope of -0.58(1). This slope is larger than that for Mn^{IV}(OH)(ttppc) (slope = -0.25(3)), showing that the Fe^{IV}(OH) complex is more sensitive to the changes in BDEs of the O-H bond being broken. However, it must be noted that the range of BDEs for the O-H substrates is small, and therefore caution must be used in the interpretation of these data. This difference in slope implies that Mn^{IV}(OH)(ttppc) will exhibit larger rate constants than **1** when reacting with O-H substrates having sufficiently high BDEs (> *ca.* 85 kcal mol^{-1}). A similar reversal in relative rate of HAT for a non-heme Mn^{IV}(O) versus an analogous Fe^{IV}(O) complex was recently described (Kaizer *et al.*, 2004; Wu *et al.*, 2011; Massie *et al.*, 2018). Taken together, the data suggest a rate-limiting H-atom transfer reaction for complex **1** with phenolic (O-H bond) substrates. It is reasonable to conclude that the HAT

reaction proceeds in a concerted manner but with a partial transfer of charge, rather than stepwise PT/ET or ET/PT pathways.

8.2.3 Comparison of HAT Reactivity with Other Oxidants, and Estimation of BDEs from the Kinetics Data

The rate constants for the oxidation of 4-X-2,6-DTBP (X = OMe, Me, H) by Fe^{IV}(OH)(ttppc) (1) and Mn^{IV}(OH)(ttppc) can be compared to the previously reported rate constants for substituted phenol oxidation by various metal-oxo and metal-hydroxo complexes, as well as a photolytically-generated *t*-BuO$^{\bullet}$ radical (Table 8.2) (Lansky and Goldberg, 2006; Sastri *et al.*, 2007; Wijeratne *et al.*, 2014). In general, the rate constants for **1** are orders of magnitude larger than those for Mn- and Fe-oxo and hydroxo complexes. Although the high-valent Fe^{IV}(oxo) complexes in Table 8.2 may be among the weaker Fe^{IV}(O) oxidants, it is still interesting to note that **1**, a terminal hydroxide complex, is a significantly more reactive oxidant for the electron-rich phenols.

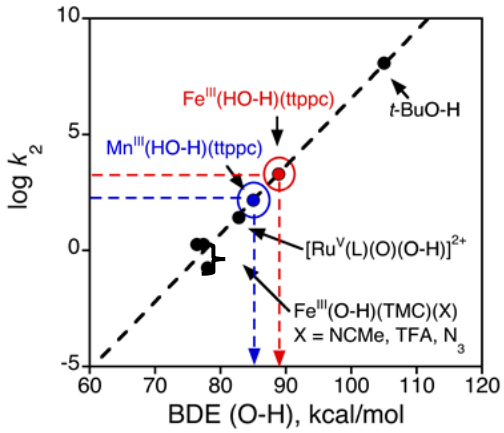

Figure 8.4. Plot of log k_2 for the reaction of metal-oxo/hydroxo complexes and tBuO$^{\bullet}$ with 4-Me-2,6-t-Bu-phenol (22-25 ˚C) vs BDE(O-H) of the O-H bond formed.

An Evans-Polanyi plot (Figure 8.4) shows good correlation of the 4-Me-2,6-DTBP reaction rates of these complexes with the BDE(O-H) of the HAT reaction product. To calibrate this relationship, a line was fit to the plot of rate constants (log k_2) of similar compounds whose BDE(O-H) values are determined experimentally or calculated by DFT methods. Based on this plot (Figure 8.4), BDEs of 85 and 89 kcal mol^{-1} are predicted for Mn^{III}(H**O-H**)(ttppc) and Fe^{III}(H**O-H**)(ttppc) (**2**) respectively. A similar linear correlation was obtained when the log k_2 vs BDE (Figure S9) for 4-H-2,6-DTBP was plotted.

8.2.4 Computational Studies on the HAT Mechanism.

Density functional theory (DFT) calculations were done using extensively tested and benchmarked methods, which have been shown to reproduce experimental BDEs within two kcal mol^{-1} (Kumar *et al.*, 2010; Visser, 2010; Cantú Reinhard, Faponle and de Visser, 2016).We began by calculating the reaction mechanism of Fe^{IV}(OH)(ttppc) (**1**) and Mn^{IV}(OH)(ttppc) with the 4-H-2,6-DTBP substrate. Starting with the reactants, both complexes are charge neutral and were studied with the complete ttppc ligand included with odd (for Fe) or even (for Mn) multiplicity. The [Fe^{IV}(OH)(ttppc)] complex is in a triplet spin ground state with the quintet and singlet spin states of ΔG = 3.7 and 15.4 kcal mol^{-1} higher in energy (Table S8). With manganese as the central metal ion, the ground state is the quartet spin state, while the doublet and sextet spin states are $\Delta E+ZPE$ = 21.3 and 8.0 kcal mol^{-1} higher (Table S10). The group spin densities of ^{3}[Fe(OH)(ttppc)] indicate approximately three unpaired electrons on the iron (ρ_{FeOH} = 2.79) antiferromagnetically coupled to one unpaired electron on the ttppc ligand (ρ_{tppcc} = –0.80) in an a_{2u} type orbital. These spin densities are more consistent with the ^{3}[Fe^{III}(OH)(ttppc$^{+\bullet}$)] valence tautomer. This is an unusual configuration as previous work on substrate oxidation by cytochrome P450s almost in all cases found an iron(IV)-hydroxo(heme) intermediate, i.e. ^{3}[Fe^{IV}(OH)(heme)] (Visser, Sharma and Shaik, 2002; Faponle, Quesne and De Visser, 2016).

We attempted to calculate the energy difference between the $Fe^{III}(OH)(ttppc^{+\bullet})$ and the $Fe^{IV}(OH)(ttppc)$ structures by swapping the molecular orbitals to obtain a structure with triplet spin configuration δ_{x2-y2}^2 $\pi^*_{xz}{}^1$ $\pi^*_{yz}{}^1$ $\sigma^*_{z2}{}^0$ $a_{1u}{}^2$ $a_{2u}{}^2$, designated as $^3[Fe^{IV}(OH)(ttppc)]$. Unfortunately, however, during the SCF convergence the state relaxed back to the $^3[Fe^{III}(OH)(ttppc^{+\bullet})]$ state. Previous studies on iron-hydroxo(corrole) complexes also found the $^3[Fe^{IV}(OH)(ttppc)]$ state to be inaccessible due to higher energy (Latifi et al. 2012). The ground state calculations for the manganese complex gives spin densities consistent with a similar description, i.e. $^4[Mn^{III}(OH)(ttppc^{+\bullet})]$. The bond distances from the DFT optimized structures for $^3[Fe^{III}(OH)(ttppc^{+\bullet})]$ (Figure S10, Table S2) and $^4[Mn^{III}(OH)(ttppc^{+\bullet})]$ (Figure S11, Table S3), as well as the reaction products $^4[Fe^{III}(H_2O)(ttppc)]$ (Figure S12, Table S4) and $^3[Mn^{III}(H_2O)(ttppc)]$ (Figure S13, Table S5), are all in good agreement with the experimentally obtained bond distances from the X-ray crystal structures of these complexes. While the DFT-optimized structures for **1** and the Mn analog suggest a metal(III)(corrole$^{+\bullet}$) structure, a definitive electronic structure assignment cannot be made from the available structural and spectroscopic data.

Geometrically, the transition states are relatively central with almost equal FeO–H vs H–OPh and MnO–H vs H–OPh distances. In particular, short FeO–H/MnO–H distances of 1.158/1.183 Å are found, while the H–O distance with the phenol is 1.267/1.242 Å. Consequently, the iron and manganese structures are very similar. The transition states are early and have an electronic structure close to the reactants, with only about 20% charge-transfer (ρ_{Sub} = -0.18/-0.20 in $^3\mathbf{TS}_{HA,Fe}/^4\mathbf{TS}_{HA,Mn}$). These results match the Hammett and Marcus plots reported above that excluded a separation of proton and electron transfer through either ET/PT or PT/ET pathways. Indeed, the electron transfer is simultaneous with proton transfer and indicates an HAT mechanism for the reaction. These spin and charge distributions in the transition states match those calculated previously for desaturation reactions by CYPs (Li *et al.*, 2017; Pickl *et al.*, 2019). To calculate the contribution of the secondary coordination sphere effect of the sterically hindered ligand ttppc (5,10,15-tris(2,4,6-triphenyl)phenyl corrole) to the HAT reaction,

we also ran transition state calculations with a hypothetical bare corrole, with the substituents on the 5,10,15- positions replaced with hydrogen atoms. Based on the potential energy landscape for the HAT reaction, the barrier drops considerably by 3.6 kcal mol^{-1} for ^{3}[Fe(OH)(corrole)] and by 5.3 kcal mol^{-1} for ^{4}[Mn(OH)(corrole)]. The second-coordination sphere effect of the bulky phenyl groups appears to increase the HAT barrier and facilitate the direct observation of these kinetically transient chemical steps. The larger increase in barrier for the Mn(OH) species upon incorporation of steric bulk around the metal-hydroxo unit is intriguing, given that the transition state structures for the two species are similar.

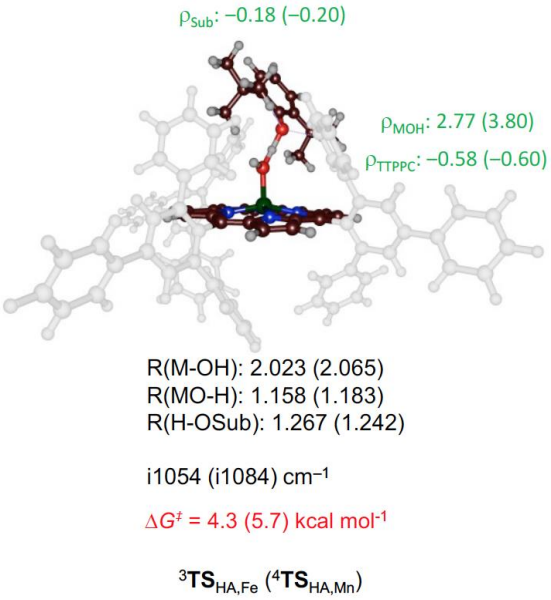

Figure 8.5. UB3LYP/BS2 optimized transition state geometries in solvent for the hydrogen atom abstraction from para-H-2,6-DTBP by Fe^{IV}(OH)(ttppc) and Mn^{IV}(OH)(ttppc). Bond lengths are in angstroms, energies contain zero-point energy and solvent corrections and are in kcal mol^{-1}.

8.2.5 Calculation of Bond Dissociation Energies (BDEs) from Density Functional Theory (DFT)

Bond dissociation energies (BDE_{OH}) were calculated from the following reaction: $M^{III}(H_2O)(L) \rightarrow M^{IV}(OH)(L) + H^{\bullet} + BDE_{OH}$, and taken as the energy difference of the electron affinity (EA) of the metal(IV)-hydroxide complex, the experimental ionization energy of a hydrogen atom (IE_H) (Lias, 2005) and the acidity (ΔG_{acid}) of the metal(III)-aquo complex (Figure S15) in their respective solvents (toluene for Fe and benzene for Mn). Our calculated BDE_{OH} values (with ZPE included) match the predicted values well, with BDE_{OH} ($Mn^{III}(H_2O)$(ttppc)) = 83.7 kcal mol^{-1} (in benzene), and BDE_{OH} ($Fe^{III}(H_2O)$(ttppc)) = 88.5 kcal mol^{-1} (in toluene) (Table S19-20). The difference between these two values comes from a larger electron affinity of the iron(IV)-hydroxo complex (by 12.1 kcal mol^{-1}), which is partially cancelled by a larger acidity (by 7.3 kcal mol^{-1}) of the iron(III)-aquo complex. This relative reactivity for directly analogous Fe vs Mn complexes has been similarly observed in comparisons of Fe^{IV}(O) vs Mn^{IV}(O) non-heme complexes, where Fe^{IV}(O) species are much more reactive towards HAT substrates, due to their larger redox potential (Chen *et al.*, 2015; Denler *et al.*, 2019). Similarly, for porphyrin and porphyrin-type complexes, Fe^{IV}(O)(porphyrin$^{\bullet+}$) species have been shown to be much reactive towards HAT reactions vs the analogous Mn^{V}(O) species in the same ligand environment (Baglia, Zaragoza and Goldberg, 2017) .In contrast, previous thermodynamic analysis of H-atom transfer reactions of Mn^{V}(O) vs Cr^{V}(O) corrolazines revealed that the basicity of the M^{IV}(O) (M = Mn, Cr) intermediate controls the H-atom transfer reactivity for these reactions (Baglia *et al.*, 2015). In the case of H-atom transfer reactions of M^{IV}(OH)(ttppc) (M = Fe, Mn) studied here, the larger redox potential of the Fe^{IV}(OH) complex seem to have a larger effect on its faster H-atom transfer reactivity in comparison to Mn^{IV}(OH)(ttppc).

8.3 Summary and Conclusions

The hydrogen atom transfer reactivity of Fe^{IV}(OH)(ttppc) (**1**), a Cpd-II analog, was described. It is capable of the rapid oxidation of phenol derivatives by H-atom abstraction of the O-H bond, and is more reactive than the other high-valent metal-hydroxo oxidants and the weakly oxidizing Fe^{IV}(O)(TMC) complexes given in Table 8.2 as tested against the same substrates. It also reacts more rapidly than the analogous Mn^{IV}(OH)(ttppc) complex, providing a direct comparison of the oxidizing power of Fe(OH) versus Mn(OH) species at the same oxidation level and in identical ligand environments. The final HAT product, $Fe^{III}(H_2O)$(ttppc), was also definitively characterized by XRD.

The kinetic analyses and computational studies provide strong support for a mechanism of phenol oxidation by **1,** and its Mn analog, that involves a concerted, rate-determining HAT step. The calculations suggest a modest amount of charge transfer in the transition state, and this finding is in line with the weak Hammett and Marcus plot slopes. A plot of BDE(O-H) values for M(O(H)) complexes versus log k_2 for the oxidation of 4-Me-2,6-di-*tert*-butyl phenol is linear, and provides a means to estimate the BDE(O-H) values for the $Fe^{III}(H_2O)$ and $Mn^{III}(H_2O)$ ttppc complexes from kinetics data. These estimated values are BDE(Fe^{III}(H**O-H**)) = ~89 kcal mol^{-1} and BDE(Mn^{III}(H**O-H**)) = ~85 kcal mol^{-1}, and DFT calculations fully support these values. The estimated BDE(O-H) for $Fe^{III}(H_2O)$(ttppc) is strikingly similar to the BDE(O-H) recently reported for the $Fe^{III}(H_2O)$ form of CYP158 (90 kcal mol^{-1}) (Mittra and Green, 2019). However, it should be noted that the BDE(O-H) calculations here are ± 2 kcal mol^{-1} at best from the error in DFT calculations and kinetic measurements. Taken together, these data suggest that **1** is a viable model for Cpd-II in CYP.

The BDE(O-H) values for the $Fe^{III}(H_2O)$ and $Mn^{III}(H_2O)$ complexes align with the relative HAT reactivity exhibited by **1** and the Mn analog, and suggest that it is the overall thermodynamic driving force for these reactions, determined by the BDE(O-H) values,

that is a key factor in controlling the reaction rates of phenol oxidation. However, examination of the log k_2 versus the phenol BDE(O-H) plots for **1** and the Mn analog show that **1** is much more reactive toward the electron-rich phenols, but is only modestly more reactive toward the stronger O-H bond substrates. In fact, the relative reactivities for Fe versus Mn should invert with substrates that have O-H bonds much stronger than the 83 kcal mol^{-1} reported for the *para*-H derivative. This hypothetical switch in relative reactivities, as expressed in the different slopes of log k_2 versus BDE(OH) for Fe and Mn, suggest that the BDE(O-H) of the metal-bound water ligand, and hence the thermodynamics of the overall HAT reaction, are not the only predictors of efficient H-atom transfer reactivity for a high-valent metal-oxo/hydroxo species.

The Fe^{IV}(OH) complex **1** is capable of H-atom abstraction, as shown with the phenols in this study, and is also capable of hydroxyl radical transfer to carbon radicals to give hydroxylated product as seen in the model "rebound" reactions described previously (Zaragoza *et al.*, 2017). These findings may give some insight regarding the selection of iron, as opposed to other redox-active, earth-abundant metals such as manganese, as the metal of choice in heme monoooxygenases. The iron center appears to be an efficient and versatile oxidant in a variety of oxidation and protonation states.

8.4 Experimental Section

8.4.1 Materials

All chemicals were purchased from commercial sources and used without further purification unless otherwise stated. Reactions involving inert atmosphere were performed under Ar using standard Schlenk techniques or in an N_2-filled dry box. Toluene, dichloromethane, acetonitrile, and diethyl ether were purified via a Pure-Solv solvent purification system from Innovative Technologies, Inc. Benzene, ethyl acetate, and fluorobenzene were obtained from commercial sources. Deuterated solvents for NMR were purchased from Cambridge Isotope Laboratories, Inc (Tewksbury, MA). The 4-X-2,6-di-*tert*-butyl-phenol derivatives were recrystallized twice in ethanol (X = OMe, Me), acetonitrile (X = Et) or *n*-pentane (X = H), and dried under vacuum. The mono-deuterated 4-OMe-2,6-di-*tert*-butylphenol was synthesized using a previously published procedure (Kundu *et al.*, 2014). Fe^{IV}(OH)(ttppc) was synthesized and purified as previously reported (Zaragoza *et al.*, 2017). The dark-red complex $Fe^{III}(OEt_2)_2$(ttppc) was synthesized by reduction of Fe^{IV}(Cl)(ttppc), following a previously published report (Zaragoza *et al.*, 2017).

8.4.2 Instrumentation

Kinetics and other UV-vis measurements were performed on a Hewlett-Packard Agilent 8453 diode-array spectrophotometer with a 3.5 mL quartz cuvette (path length = 1 cm). For reactions with total reaction time of <10 seconds, stopped-flow experiments were carried out using a HiTech SHU-61SX2 (TgK scientific Ltd.) stopped-flow spectrophotometer with a Xenon light source and Kinetic Studio software. ^{1}H NMR spectra were recorded on a Bruker Avance 400 MHz NMR spectrometer at 298 K, and referenced against residual solvent proton signals. Electron paramagnetic resonance (EPR) spectra were recorded with a Bruker EMX spectrometer equipped with a Bruker ER 041 X G microwave bridge and a continuous-flow liquid helium cryostat (ESR900)

coupled to an Oxford Instruments TC503 temperature controller for low temperature data collection. Laser desorption ionization mass spectrometry (LDI-MS) was conducted on a Bruker Autoflex III MALDI ToF/ToF instrument (Billerica, MA) equipped with a nitrogen laser at 335 nm using an MTP 384 ground steel target plate. The instrument was calibrated using peptide standards of known molecular weights. Gas chromatography (GC-FID) was carried out on an Agilent 6890N gas chromatograph fitted with a DB−5 5% phenylmethyl siloxane capillary column (30 m × 0.32 mm × 0.25 μm) and equipped with a flame-ionization detector. Elemental analysis was performed at Atlantic Microlab, Inc., Norcross, GA. Cyclic voltammetry was performed on an EG&G Princeton Applied Research potentiostat/galvanostat model 263A with a three-electrode system consisting of a glassy carbon working electrode, a $Ag/AgNO_3$ non-aqueous reference electrode (0.01 M $AgNO_3$ with 0.1 M Bu_4NPF_6 in CH_3CN), and a platinum wire counter electrode. Potentials were referenced using an external ferrocene standard. Scans were run under an Ar or N_2 atmosphere at 23 °C using Bu_4NPF_6 (0.1 M) as the supporting electrolyte.

8.4.3 $Fe^{III}(H_2O)$(ttppc) (2)

Distilled H_2O (0.5 mL) was added to a solution of $Fe^{III}(OEt_2)_2$(ttppc) in fluorobenzene (2 mL). Vapor diffusion of pentane to this biphasic solution led to the slow formation of dark red blocks (55 mg, 56% yield) after one week. UV-vis (C_6H_6): λ_{max}, nm (ε x 10^4 M^{-1} cm^{-1}): 344 (3.29), 429 (7.27), 578 (1.35), 764 (0.24); ^{1}H-NMR (400 MHz, benzene-d_6): 35.1 (s, br), 12.4 (s, br), 12.3 (s, br), 10.8 (s, br), 8.3 (s, br), 6.0 (s, br), 4.98 (s, br), 4.66 (s, br), -19.0 (s, br), -35.1 (s, br), -61.6 (s, br), -69.0 (s, br) δ (ppm); IR (KBr): 3580 (w, O-H), 3512 (vw, O-H), 3055 (m), 3028 (m), 1593 (s), 1556 (w), 1491 (s), 1443 (m), 1424 (w), 1394 (w), 1362 (w), 1332 (m), 1296 (m), 1214 (s), 1180 (w), 1154 (m), 1075 (m), 1045 (sh), 1020 (s), 984 (s), 916 (w), 885 (s), 851 (w), 821 (w), 794 (m), 750 (vs), 695 (vs), 637 (m), 609 (w), 574 (m), 537 (m), 499 (m), 443 (w); LDI-MS (m/z): isotopic cluster centered at 1264.6 ($[M - H_2O]^+$). Anal. Calcd. for $C_{91}H_{59}N_4Fe•H_2O•2C_6H_5F$: C, 81.33; H, 5.07; N, 3.91. Found: C, 81.53; H, 4.80; N, 4.05.; μ_{eff} = 3.6(1) μ_B (Evan's Method). EPR: g = 4.29 (16 K).

8.4.4 Reaction of $Fe^{IV}(OH)$(ttppc) with 2,4-di-*tert*-butylphenol

8.4.4.1 Product Analysis

Under an inert atmosphere, a solution of $Fe^{IV}(OH)$(ttppc) in benzene (2.1 mM, 500 µL) was combined with 2,4-di-*tert*-butylphenol (0.132 mmol, 126 equiv), and 3.4 mg of eicosane (6 mM) as an internal standard. The reaction mixture was stirred and monitored by UV-vis spectroscopy, which showed complete, instantaneous conversion of $Fe^{IV}(OH)$(ttppc)(**1**) to $Fe^{III}(H_2O)$(ttppc) (**2**). An aliquot of the reaction mixture was injected directly onto the GC for analysis. The phenol oxidation product 3,3′,5,5′-tetra-tert-butyl-(1,1′-biphenyl)-2,2′-diol was identified by GC in comparison with an authentic sample, and quantified by integration of the peak and comparison with a calibration curve constructed with eicosane. The analysis was performed in triplicate. Average yield = 67(1)% based on the reaction stoichiometry of 0.5 equiv of phenol oxidation product per 1.0 equiv of $Fe^{IV}(OH)$(ttppc).

8.4.4.2 Kinetics

To a solution of $Fe^{IV}(OH)$(ttppc) (15 µM) in toluene, varying amounts of 4-X-2,6-di-*tert*-butylphenol (X = OMe, Me, Et, H) (0.1 – 0.6 mM) in toluene were added to start the reaction. The spectral changes showed isosbestic conversion of $Fe^{IV}(OH)$(ttppc) to $Fe^{III}(H_2O)$(ttppc). The pseudo-first-order rate constants, k_{obs}, for these reactions were obtained through non-linear least-squares fitting of the plots of absorbance at 575 nm (Abs_t) versus time (t) over 5 half-lives according to the equation $Abs_t = Abs_f + (Abs_0 - Abs_f) \exp(-k_{obs}t)$, where Abs_0 and Abs_f are the initial and final absorbance, respectively. Second order rate constants (k_2) were obtained from the slope of the best-fit line from a plot of k_{obs} versus phenol concentration.

8.4.5 X-ray Crystallography

All reflection intensities for **2** were measured at 110(2) K using a SuperNova diffractometer (equipped with Atlas detector) Cu Kα radiation (λ = 1.54178 Å) under the

program CrysAlisPro (Version 1.171.39.29c, Rigaku OD, 2017). The same program was used to refine the cell dimensions and for data reduction. The structure was solved with the program SHELXS-2014/7 and refined on F^2 with SHELXL-2014/7 (Sheldrick, 2015). The temperature of the data collection was controlled using the system Cryojet (manufactured by Oxford Instruments). An analytical numeric absorption correction method was used involving a multifaceted crystal model based on expressions derived elsewhere (Clark and Reid, 1995). The H atoms were placed at calculated positions using the instructions AFIX 43 with isotropic displacement parameters having values 1.2 Ueq of the attached C atoms. The crystal lattice contains disordered and/or partially occupied lattice solvent molecules (C_6H_5F and C_5H_{12}). Their contributions were removed from the final refinement using the SQUEEZE program. The crystallographic data for $Fe^{III}(H_2O)$(ttppc) are summarized in Table S6.

8.4.6 Computational Modeling

Calculations on the complexes Fe^{IV}(OH)(ttppc) and Mn^{IV}(OH)(ttppc) and their reactions with *para*-H-2,6-DTBP included all atoms for both metal complex and phenol. Geometry optimizations, constraint geometry scans and vibrational frequencies were calculated with DFT in the *Gaussian*-09 software package (Frisch, Hratchian and Nielsen, 2009). We utilized the unrestricted B3LYP hybrid density functional method (Lee, Yang and Parr, 1988; Becke, 1993) in combination with an LANL2DZ basis set (Hay and Wadt, 1985) on iron/manganese (with core potential) and 6-31G on the rest of the atoms (H, C, N, O): basis set BS1. Single points using the LACV3P+ (with core potential) on Fe/Mn, and 6-311+G* on the rest of the atoms were done to correct the energies: basis set BS2. The continuum polarized conductor model with a dielectric constant mimicking toluene was applied to the system during the geometry optimizations and frequencies (Tomasi, Mennucci and Cammi, 2005). Single point energy calculations were done in benzene for the BDE determination of $Mn^{III}(H_2O)$(ttppc) to match the experimental conditions (Table S20). We initially optimized a reactant complex of substrate and metal(IV)-hydroxo species in close proximity and followed the pathway for OH transfer through a constraint

geometry scan. Subsequently, the maximum of these scans was subjected to a full transition state search and the obtained transition state was characterized with a frequency calculation that gave an imaginary frequency for the correct mode. These transition states were shown to be connected to reactants and products through an intrinsic reaction coordinate (IRC) scan. As in some cases, the transition states energies were lower than those of the original reactant complexes, the latter were reoptimized from the final points of the IRCs, which gave slightly more stable isomers. These methods were used in previous studies and showed to predict the correct spin-state orderings and barrier heights of reaction mechanisms (Kumar *et al.*, 2014; Yang *et al.*, 2016; Pickl *et al.*, 2019). The calculations of the BDE(O-H) values are described in the Supporting Information (Tables S19-S20).

Acknowledgements

The authors would like to thank the NIH (GM101153) (D.P.G.) for the financial support of this research. M.Q.E.M. thanks the Government of Malaysia and Islamic Science University of Malaysia for a studentship.

Chapter 9

Project 7

Properties and Reactivity of μ-Nitrido Bridged Dimetal Porphyrin Complexes. How Does Ruthenium Compare to Iron?

M. Qadri E. Mubarak[§], Alexander B. Sorokin[†], and Sam P. De Visser[§]

[§]The Manchester Institute of Biotechnology and Department of Chemical Engineering and Analytical Science, The University of Manchester, 131 Princess Street, Manchester M1 7DN, United Kingdom.

[†]Institut de Recherches sur la Catalyse et l'Environnement de Lyon (IRCELYON), UMR 5256, CNRS-Université Lyon 1, 2, av. A. Einstein, 69626 Villeurbanne Cedex (France).

Abstract

Methane hydroxylation by metal-oxo oxidants is one of the Holy Grails in biomimetic and biotechnological chemistry. The only enzymes known to perform this reaction in Nature are iron-containing soluble methane monooxygenase and copper-containing particulate methane monooxygenase. Furthermore, few biomimetic iron-containing oxidants have been designed that can hydroxylate methane efficiently. Recent studies reported that μ-nitrido bridged diiron(IV)-oxo porphyrin and phthalocyanine complexes hydroxylate methane to methanol efficiently. To find out whether the reaction rates are enhanced by replacing iron by ruthenium we performed a detailed computational study. Our work shows that the μ-nitrido bridged diruthenium(IV)-oxo reacts with methane via hydrogen atom abstraction barriers that are considerably lower in energy (by about 5 kcal mol^{-1}) as compared to the analogous diiron(IV)-oxo complex. An analysis of the electronic structure implicates similar spin and charge distributions for the diiron(IV)-oxo and diruthenium(IV)-oxo complexes, but the strength of the O–H bond formed during the reaction is much stronger for the latter. As such a larger hydrogen atom abstraction driving force for the Ru complex than for the Fe complex is found, which should result in higher reactivity in the oxidation of methane.

Published Reference
Mubarak, M. Qadri E., Alexander B. Sorokin, and Sam P. De Visser. "Properties and reactivity of μ-nitrido-bridged dimetal porphyrinoid complexes: how does ruthenium compare to iron?." JBIC Journal of Biological Inorganic Chemistry (2019): 1-8.

9.1 Introduction

Heme monoxygenases are common enzymes in biology with a variety of functions related to biosynthesis and biodegradation. In general, they react through oxygen atom transfer to substrates on an iron(III)-heme co-factor that binds molecular oxygen, but uses two reduction and two protonation equivalents in the catalytic cycle. The most extensively studied heme monoxygenases are the cytochromes P450, which initiate the biodegradation of drug molecules in the liver as well as the biosynthesis of hormones (Sono *et al.*, 1996; Girerd, Banse and Simaan, 2000; Groves, 2003; Meunier, de Visser and Shaik, 2004; De Montellano, 2005; Denisov *et al.*, 2005; Ortiz De Montellano, 2010; Grogan, 2011; Kadish, Smith and Guilard, 2013; Poulos, 2014; Huang and Groves, 2018) . During their catalytic cycle the iron(III)-heme reacts with molecular oxygen and using two external electrons and protons a high-valent iron(IV)-oxo heme cation radical species called Compound I (Cpd I) is formed (Ogliaro *et al.*, 2000; Shaik *et al.*, 2005; Rittle and Green, 2010). Although Cpd I is able to hydroxylate a large range of aliphatic and aromatic C–H bonds, it is not known to hydroxylate methane, which has the strongest C–H bond in nature. However, work of Sorokin and co-workers on biomimetic porphyrin and phthalocyanine complexes (Scheme 9.1) found evidence of methane hydroxylation by □-nitrido bridged diiron(oxo) porphyrin and phthalocyanine (Sorokin, Kudrik and Bouchu, 2008; Sorokin *et al.*, 2010; Sorokin, 2013) and as such these complexes are unique and highly reactive including the supramolecular diiron phthalocyanine-porphyrin conjugates (Mihara *et al.*, 2019; Yamada *et al.*, 2019). In previous work the synthesis of several μ-nitrido bridged diiron(III) phthalocyanine and porphyrin complexes was reported and using terminal oxidants such as hydrogen peroxide or *m*-chloroperbenzoic acid they were converted to a μ-nitrido bridged diiron(IV)-oxo species (Afanasiev and Sorokin, 2016). These short-living intermediates were efficient in a reaction with aliphatic substrates (cyclohexane, adamantane and ethylbenzene) leading to substrate hydroxylation (Afanasiev and Sorokin, 2016). Furthermore, methane hydroxylation to methanol was observed with several complexes, which implicates that these oxidants are more powerful than cytochrome P450 Cpd I (Kudrik *et al.*, 2012; Colomban *et al.*, 2014).

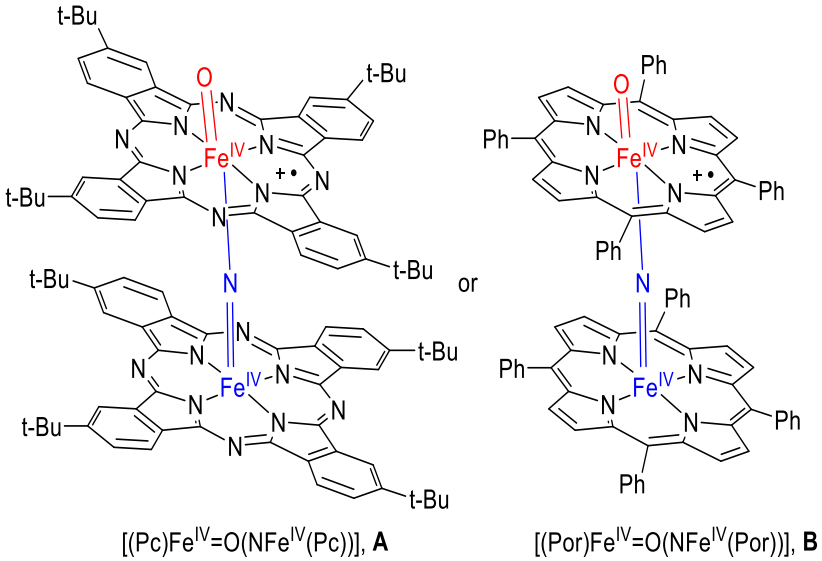

Figure 9.1. Examples of μ-nitrido bridged diiron(IV)-oxo phthalocyanine (Pc, left) and porphyrin (Por, right) complexes.

Unprecedented reactivity of μ-nitrido diiron tetrapyrrolic complexes has initiated synthetic development of this platform involving different metals supported by various macrocyclic ligands (Stuzhin *et al.*, 2012; Işci *et al.*, 2014; Cheung *et al.*, 2017, 2018; Colomban, Kudrik and Sorokin, 2017; Mihara *et al.*, 2019; So *et al.*, 2019; Yamada *et al.*, 2019). In parallel, several detailed computational studies on μ-nitrido bridged diiron(IV)-oxo phthalocyanine and porphyrin complexes have been reported by us and others(Silaghi-Dumitrescu *et al.*, 2011; Ansari *et al.*, 2015; Işci *et al.*, 2015; Quesne *et al.*, 2016; Phung and Pierloot, 2019). In general, these studies showed that the electron-donating ability of the μ-nitrido group lowers the acidity of the corresponding iron-hydroxo species, and consequently, the strength of the O–H bond of the iron(III)-hydroxo group is large. As the driving force for a hydrogen atom abstraction reaction is larger when a stronger O–H bond is formed (Mayer, 2004; Visser, 2010; Kumar, Sastry and Visser, 2011), this implies that a significant enhancement of the rate constant for hydrogen atom abstraction will be observed. In this context, it is of great interest to probe how the nature of metal sites might influence on the catalytic properties of μ-nitrido binuclear construction. To gain further insight into the properties and reactivities of μ-nitrido bridged dimetal-oxo porphyrins and phthalocyanines we decided

to create the analogous diruthenium complexes and compare the structure, electronic properties and catalysis with the diiron complexes. We predict that these diruthenium(IV)-oxo phthalocyanine complexes if they can be formed will react with methane even more efficiently than their corresponding iron complexes.

9.2 Methods

The work presented here uses computational methods and procedures as reported and discussed previously on biomimetic model complexes that reproduced experimental data well (de Visser *et al.*, 2014; Kumar *et al.*, 2014). Overall, density functional theory (DFT) approaches were used as implemented in the *Gaussian*-09 program package (Frisch, Hratchian and Nielsen, 2009). The full potential energy profile was calculated with two unrestricted DFT methods, namely the hybrid density functional method UB3LYP (Lee, Yang and Parr, 1988; Becke, 1993) and the pure density functional UBP86 (Perdew, 1986; Becke, 1988), for all geometry optimizations, geometry scans and frequencies. Geometry optimizations and potential energy scans were performed with a double-ζ quality LACVP basis set (with core potential) on ruthenium and 6-31G on the rest of the atoms, basis set BS1 (Ditchfield, Hehre and Pople, 1971; Hay and Wadt, 1985). All local minima and transition states were optimized without constraints and characterized with an analytical frequency that confirmed the status of the structures with all transition states having a single imaginary frequency for the correct mode. Calculations include a polarized continuum model (CPCM) as implemented in Gaussian using a dielectric constant of $\varepsilon = 35.688$ mimicking acetonitrile. Energies were improved through a single point calculation with an LACV3P+ (with core potential) basis set on ruthenium and 6-311+G* on the rest of the atoms: basis set BS2. These methods were used previously and reproduced experimentally determined free energies of activation and kinetic isotope effects well (Cantú Reinhard, Faponle and de Visser, 2016; Cantú Reinhard *et al.*, 2017). In the past, we validated our computational methods and showed that these procedures can reproduce experimental free energies of activation to within 3 kcal mol^{-1}. Moreover, changing the basis set for geometry optimizations from BS1 to BS2 gave little changes to the optimized geometries, relative energies, and chemoselectivities of the reaction (Vardhaman *et al.*, 2011; Barman *et al.*, 2019; Khaled Cheaib *et al.*, 2019).

Finally, the effect of dispersion on the optimized geometries of μ-nitrido-bridged diiron(IV)-oxo porphyrins was tested for the defluorination reaction of C_6F_6 and found to give little changes in geometry and energetics, and hence, dispersion was not used in this work (Colomban *et al.*, 2019).

9.3 Results and Discussion

In this work, we focus on the chemical properties of the μ-nitrido bound diruthenium(IV)-oxo porphyrazine (Pz) complex $^{2,4,6}[O=Ru^{IV}(Pz^{+\bullet})NFe^{IV}(Pz)]^0$ (or $^{2,4,6}[O=Ru^{V}(Pz)NFe^{IV}(Pz)]^0$), **1**, whereby all side chains of the macrocycle are abbreviated to hydrogen atoms. The complex is charge neutral and was calculated in all low lying doublet, quartet and sextet spin states using two density functional theory methods (UB3LYP and UBP86). In addition, the reactivity patterns of the complexes with methane was compared with the analogous diiron(IV)-oxo complex ^{2,4,6}**2** reported previously (Silaghi-Dumitrescu *et al.*, 2011; Ansari *et al.*, 2015; Quesne *et al.*, 2016).

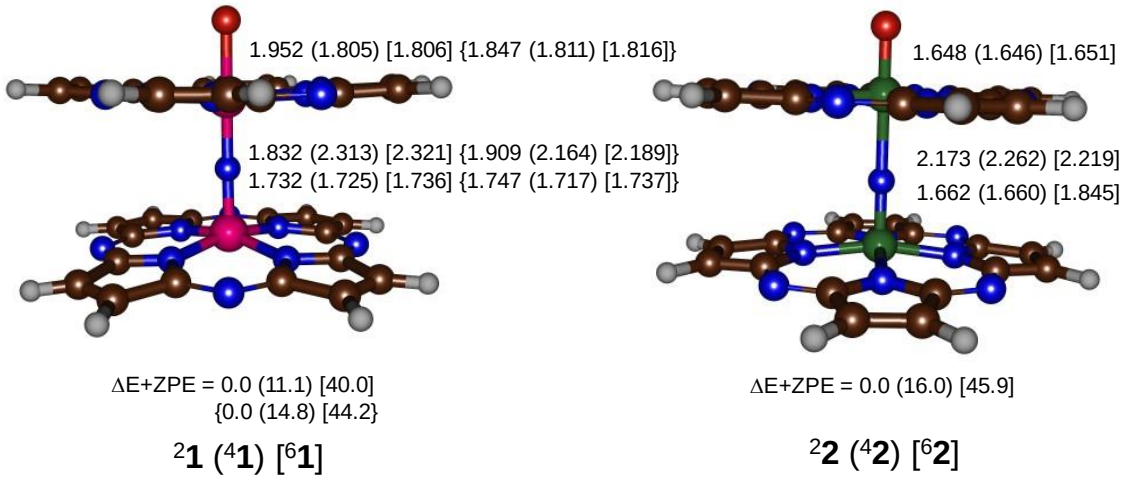

Figure 9.2. Optimized geometries of ^{2,4,6}**1** (left-hand-side) and ^{2,4,6}**2** (right-hand-side) as obtained in Gaussian-09. Bond lengths are in angstroms and relative energies in kcalmol^{-1}. Data for ^{2,4,6}2 taken from our previous work (Quesne *et al.*, 2016)

Before we show the results on the catalytic properties of oxidant ^{2,4,6}**1**, let us investigate the electronic and structural properties of the reactant species in more detail. Figure 9.2 displays the optimized geometries and relative energies of ^{2,4,6}**1**. In both complexes the doublet spin state is the ground state and well separated from the quartet and sextet spin states by at least 10 kcal mol^{-1}. This is independent on the density functional method chosen and implicates that the quartet and sextet spin states will play no role in catalysis. As such the reactivity with substrates is expected to take place on the doublet spin state only and the oxidants will react through single-state-reactivity (Hirao *et al.*, 2006; Visser, 2006) selectively. Mononuclear iron(IV)-oxo oxidants often have close-lying spin state surfaces, where reactivity patterns appear on multiple accessible electronic and spin states. It is not surprising that the ruthenium complexes react through single-state-reactivity patterns as Ru^{IV}=O complexes tend to have well separated metal 4d orbitals and hence usually stabilize low-spin states (Sharma *et al.*, 2003; Guo *et al.*, 2013; Man *et al.*, 2013).

Indeed, previous studies on mononuclear Ru^{IV}=O complexes showed the high-spin states to be considerably higher in energy than the lower spin states (Dhuri *et al.*, 2008) in agreement with what is seen here.

In structures ^{2,4}**2** the Fe_1–O and Fe_2-μ-N distances were found to be about 1.65Å in length, which indicates that both bonds will be formally a double bond. In the ruthenium complexes both of these bonds have significantly elongated as expected for a heavier element. However, the Ru_1–O distances are significantly longer than the Ru_2–□-N distances, which implicates that they have different bonding character. Furthermore, the ruthenium atom of the Ru_1–O group is located below the plane through the four nitrogen atoms of the equatorial ligand, while in the iron complexes the Fe_1 atom remains above the plane. Finally, particularly in the low-spin state the bridging nitrogen atom is close to the center of the Ru_1–Ru_2 interaction, whereas in the corresponding diiron(IV)-oxo species it is closer to Fe_2 than to Fe_1.

To understand the differences in geometry between the diiron and diruthenium complexes we analyzed the molecular orbitals, which are displayed in Figure 9.3. The orbitals are dominated by the π-interactions in the xz and yz molecular planes, where we take the z-axis along the Ru-O bond. Thus, the $4d_{xz}$ and $4d_{yz}$ atomic orbitals on both Ru atoms interact with the $2p_x$ and $2p_y$ atomic orbitals on the oxo and bridging nitrogen atoms to form four sets of orbitals: $\pi_{1,x}/\pi_{1,y}$ $\pi 2_{,x}/\pi_{2,y}$ $\pi^*_{3,x}/$ $\pi^*_{3,y}$ $\pi^*_{4,x}/$ $\pi^*_{4,y}$. The lowest two sets of orbitals represent the bonding interactions for the Ru–O and Ru–N interaction. The $\pi^*_{3,x}$ and $\pi^*_{3,y}$ orbitals have a bonding interaction between the top Ru atom and the axial ligand but are antibonding for the Ru–O and Ru–N interactions. The doublet spin state for both ^{2}**1** and ^{2}**2** has orbital occupation $\pi_{1,x}^2$ $\pi_{1,y}^2$ $\pi_{2,x}^2$ $\pi 2_{,y}^2$ $\pi^{*2}_{3,x}$ π $^*{}^1_{3,y}$ $\pi^{*0}_{4,x0}$ $\pi^{*0}_{4,y}$. These orbital occupations are quite different from typical mononuclear heme complexes, i.e. Fe^{IV}=O(heme$^{+\bullet}$) or P450 Cpd I, that have a heme radical with singly occupied a_{2u} orbital. In the μ-nitrido bridged complexes, by contrast, the a_{2u} orbitals are lower in energy and are doubly occupied.

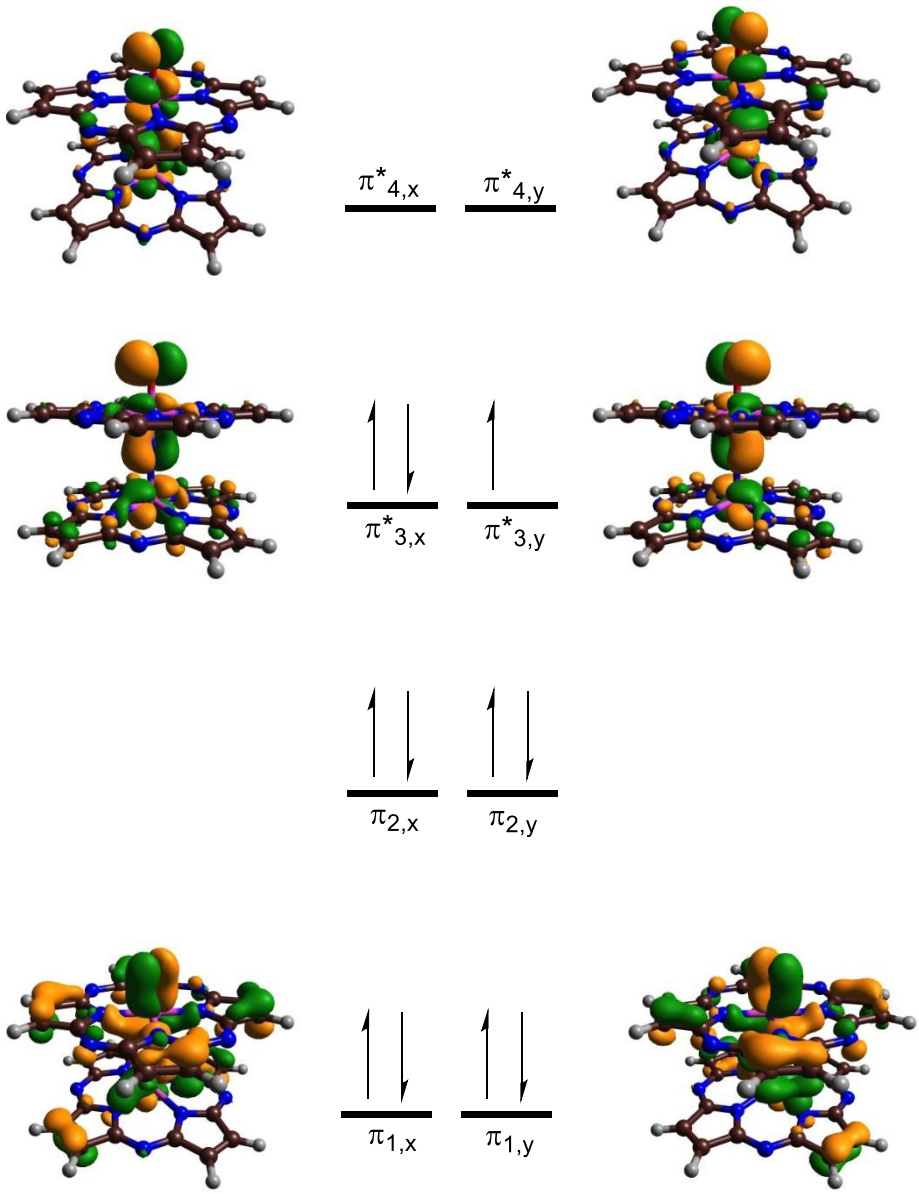

Figure 9. 3. High-lying occupied and virtual orbitals of ^{2}**1**.

Group spin densities of the doublet spin state reactants give dominant oxo radical character (ρ_O = 0.90 at UB3LYP and 0.56 for the UBP86 calculation). Nevertheless, in both cases the radical refers to a singly occupied $\pi^*_{3,y}$ molecular orbital. These two results give S^2 values of 0.792 and 0.775 and hence include very little multiconfiguration perturbations.

Subsequently, we investigated methane hydroxylation by ^{2,4,6}**1** and ^{2,4,6}**2** and the results are depicted in Figure 9.4. Similar to methane hydroxylation by iron(IV)-oxo complexes (Ogliaro *et al.*, 2000; De Visser *et al.*, 2004; Meunier, de Visser and Shaik, 2004; Yoshizawa, 2006; Dhuri *et al.*, 2008; Shaik, Kumar and De Visser, 2008; Tang *et al.*, 2012; Singh, Kumar and de Visser, 2016) the reaction is stepwise with an initial hydrogen atom abstraction (via transition state $\mathbf{TS}_{HA}$) to form a radical intermediate ($\mathbf{I}_{HA}$). Thereafter, an OH rebound barrier (via transition state $\mathbf{TS}_{reb}$) gives alcohol product complexes ($\mathbf{P}_{HA}$). The free energies obtained with B3LYP and BP86 are very similar particularly for the transition states and also analogous structures are found. Therefore, the density functional method appears to have little effect on the structure and energies of the reaction mechanism. This contrast the spin-state ordering and relative energies of mononuclear iron and manganese-oxo complexes that often give strong variations depending on the density functional method chosen and particularly the amount of Hartree-Fock Exchange that is included in the method (Sainna, Sil, *et al.*, 2015; Cantú Reinhard, Faponle and de Visser, 2016; Yang *et al.*, 2016). In all cases the doublet spin state is well below the quartet and sextet spin state and hence the reaction takes place via single-state-reactivity on the doublet spin state surface and no spin crossing to another spin state is expected. Therefore, we focus on the doublet spin results in Figure 9.4 only, whereas the results on the quartet and sextet spin states are relegated to the Supporting Information.

Optimized geometries of the rate determining doublet spin transition states ($^{2}\mathbf{TS}_{HA}$) are given in Figure 9.4. The transition states are late with long C–H distances (1.375 and 1.471 Å at B3LYP and BP86 level of theory) and short O–H distances (1.157 and 1.117 Å at B3LYP and BP86 level of theory). Late transition states often related to high energy barriers. Thus, for a series of hydrogen atom abstraction barriers by the same metal(IV)-oxo oxidant it was shown that the barrier height correlated with the strength of the C–H bond that was broken (De Visser et al. 2004; Shaik, Kumar, and De Visser 2008; Latifi, Bagherzadeh, and Visser 2009; Latifi et al. 2012). It was found that reactions with substrates with strong C–H bonds gave more product-like transition states, whereas with substrates with weak C–H bonds more reactant-like transition states were found. As methane has a strong C–H bond strength with bond dissociation energy ($BDE_{CH,methane}$ =

101.6 kcal mol^{-1} at UB3LYP level of theory) it is not surprising that the hydrogen atom abstraction barriers are high.

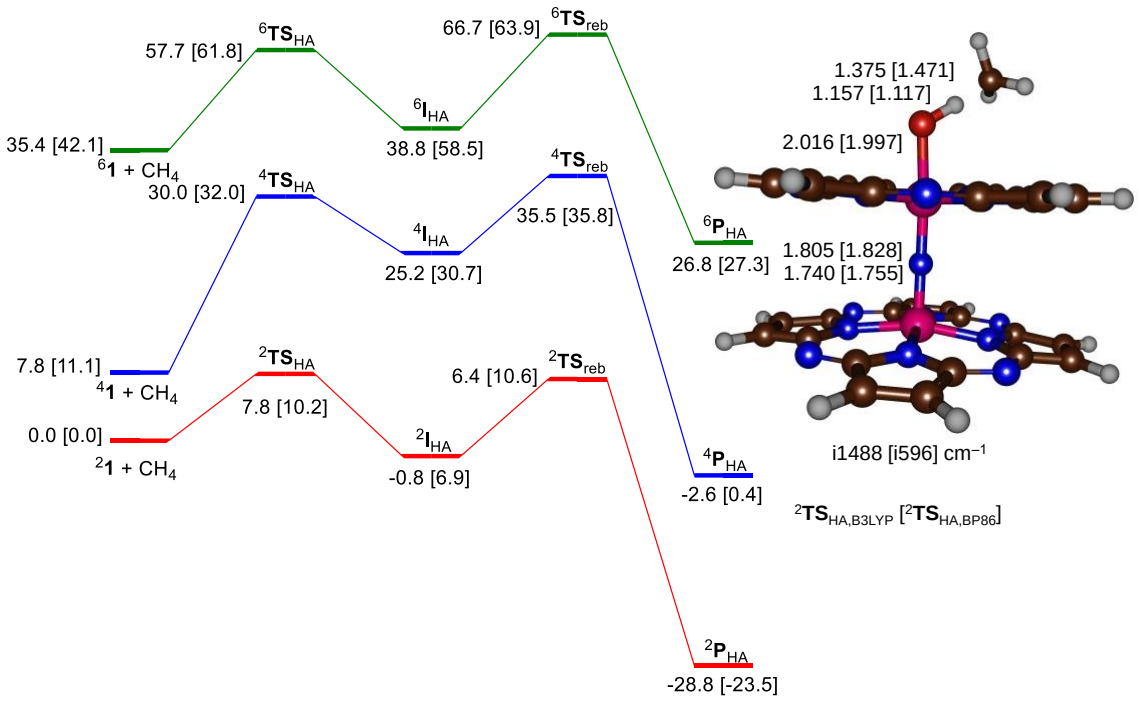

Figure 9. 4. Potential energy landscape of methane hydroxylation by ^{2,4,6}1 as obtained with DFT. Data obtained through full geometry optimization with UB3LYP [UBP86] level of theory. Free energies (at BS2 level of theory) are in kcal mol^{-1} with solvent, thermal, entropic and ZPE corrections included. Optimized geometries give bond lengths in angstroms and the imaginary frequency in cm^{-1}.

The rate-determining step in the reaction mechanism is hydrogen atom abstraction with a free energy of activation of 7.8 kcal mol^{-1}, which is well lower in free energy here than that found for the analogous μ-nitrido bridged diiron(IV)-oxo phthalocyanine complexes reported before (Quesne *et al.*, 2016), where a value of 15.7 kcal mol^{-1} was found. Therefore, the diruthenium complex is expected to react with hydrogen atom abstraction barriers that are almost 8 kcal mol^{-1} lower in free energy, which would correspond to a rate enhancement of over 10^6. Clearly, the diruthenium(IV)-oxo species is a considerably better oxidant that the corresponding diiron(IV)-oxo species. We will analyze the differences in structure and reactivity in detail in the following. Note that the rebound barrier is 7.2 (3.7) kcal mol^{-1} in energy above the radical intermediate $^2\mathbf{I}_{HA}$ as calculated at UB3LYP (UPB86) level of theory. These barriers are considerable and may implicate a finite lifetime of the radical intermediates, which in the case of ethene activation by iron(IV)-oxo complexes was shown to lead to by-products (de Visser, Ogliaro and Shaik, 2001; Timmins, Quesne, *et al.*, 2018). Furthermore, the radical could be released from the intermediate complex as dissipate into solution as suggested for nonheme iron reactivities (Cho *et al.*, 2016).

Figure 9.5 gives the orbital energy changes during the methane hydroxylation reaction on the doublet spin state in a valence bond description. Thus, we describe electrons as a dot and a line bordered by two dots in a bonding orbital occupied by two electrons. These schemes were used previously to rationalize regioselectivities as electronic configurations of oxidants (Visser, 2010; Sainna, Sil, *et al.*, 2015; Cantú Reinhard *et al.*, 2016; Kaczmarek *et al.*, 2018).

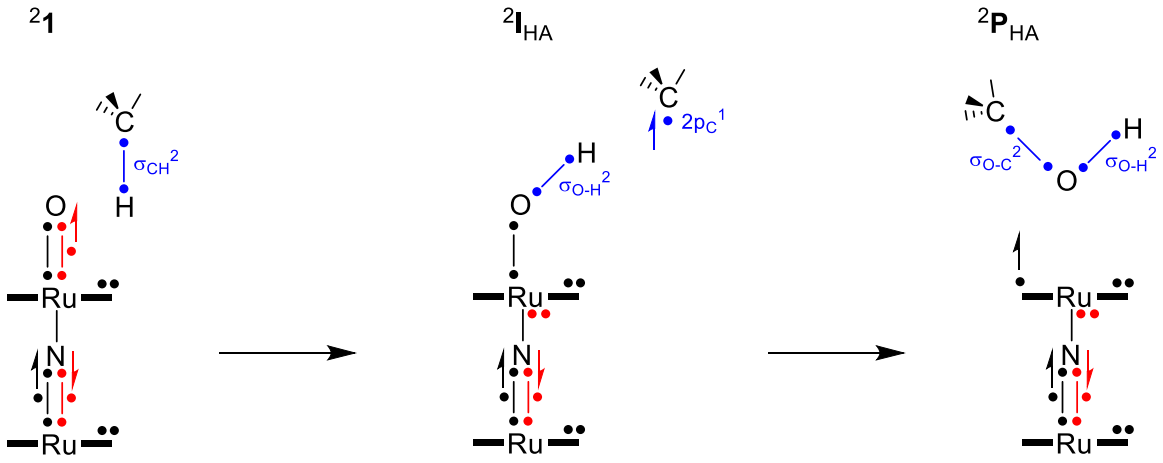

Figure 9.5. Orbital occupation changes along the doublet spin reaction mechanism in Valence Bond description.

As mentioned above in Figure 9.3 the μ-nitrido bridged diruthenium(IV)-oxo complex has electronic configuration of $\pi^*_{3,x}{}^2$ $\pi^*_{3,y}{}^1$. Upon abstraction of a hydrogen atom from substrate, a σ_{CH} bond of methane is broken and splits into atomic orbitals: $2p_C$ and $1s_H$. The hydrogen atom pairs up with one electron from the $\pi^*_{3,y}$ molecular orbital to form the σ_{O-H} orbital with two electrons, while the π_y set of orbitals splits into a new set of three orbitals ($\pi'_{1,y}$ $\pi'_{2,y}$ $\pi^{*\prime}_{3,y}$) that only spread over the Ru, N and Ru atoms and contain four electrons. During the OH rebound process also the π orbitals along the x-axis lose the oxygen contribution and split into a new set of orbitals $\pi'_{1,x}$ $\pi'_{2,x}$ $\pi^{*\prime}_{3,x}$ with four electrons. One electron from the Ru–O interaction pairs up with the radical on the CH_3 group to form the new σ_{O-C} orbital, whereas the second one is promoted to a virtual □ orbital on the porphyrazine group. As a consequence the product has spin density on the ligand but not on the metals.

We also did a thermochemical analysis on the hydrogen atom and electron abstraction ability of the μ-nitrido-bridged diiron and diruthenium-oxo complexes, see Figure 9.6. First we calculated the bond dissociation energy of the O–H bond (BDE_{OH}) in the M^{IV}(OH) complex (M = Fe, Ru) as defined in Eq 1, where we compare the energy of the M^{IV}(OH) complex relative to that of the M^{IV}=O complex and a separate hydrogen atom. For the iron complex a value of 86.7 kcal mol^{-1} was reported for the structure without

axial ligand and 82.3 kcal mol^{-1} when an axial acetate was present (Quesne *et al.*, 2016). Interestingly, using the same methods and techniques a value of 134.9 kcal mol^{-1} is found for the $Ru^{IV}(OH)$ system. Therefore, based on the relative BDE values, the μ-nitrido bridged diruthenium-oxo complex is expected to be a considerably better oxidant than the corresponding iron complex and should react with methane even faster. The relative energies of the hydrogen atom abstraction transition states discussed above indeed confirm this.

$$M^{IV}(OH) \rightarrow M^{IV}{=}O + H^{\bullet} + BDE_{OH} \quad (1)$$

Technically, a hydrogen atom abstraction is the sum of a proton transfer and an electron transfer; therefore, we split the BDE_{OH} further into the sum of the acidity of the reduced oxidant (ΔG_{acid}), the electron affinity (EA) of the starting complex and the ionization energy of a hydrogen atom (IE_H). The latter was taken from the literature (Lias, 2005). Interestingly, the acidity of the iron and ruthenium-oxo complexes are alike and the differences in electron affinity compensates for stronger O–H bond formation. As a particularly strong O–H bond is formed after hydrogen atom abstraction this results in a large driving force for hydrogen atom abstraction and consequently low energy hydrogen atom abstraction barriers.

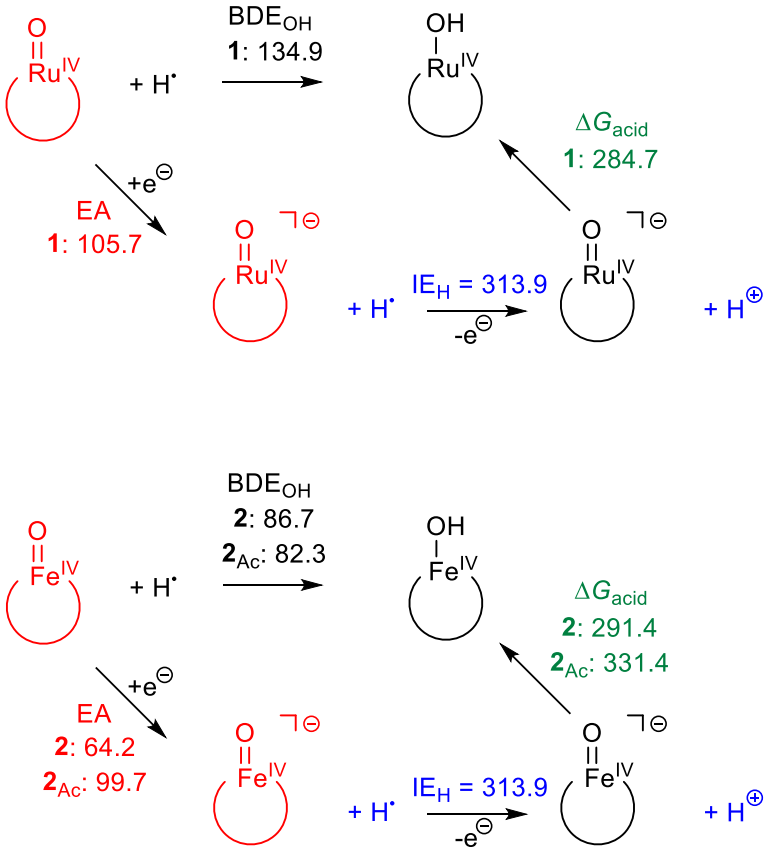

Figure 9.6. Thermochemical analysis of hydrogen atom abstraction, proton transfer and electron transfer ability of the iron(IV)-oxo versus ruthenium(IV)-oxo complexes. Values are in kcal mol^{-1}.

9.4 Conclusions

Computational studies on a μ-nitrido bridged diruthenium(IV)-oxo porphyrazine complex were performed and its reactivity with methane investigated. Our studies show that the complex is in a doublet spin ground state that is well separated from other spin states and with significant radical character on the oxo group. The electronic configuration of the μ-nitrido bridged diruthenium(IV)-oxo complex is analogous to the corresponding diiron complex; however, it reacts with substrate with considerably lower barriers due to a more favorable hydrogen atom abstraction reaction. These differences are rationalized with thermochemical cycles and valence bond schemes.

Acknowledgements
MQEM thanks the Government of Malaysia for a studentship. The EU-COST Network for Bioinorganic Reaction Mechanisms (CM1003) is acknowledged for support. ABS is grateful to ANR, France for support (grant ANR-16-CE29-0018-01).

10.0 Concluding Remarks

Enzyme is one of amazing component existing in nature, where it able to convert their respective substrate to specific product. By observing nature, human try to recreate the favourable reaction by synthesizing biomimetic complexes analogous to natural enzyme. We presented here an extensive computational study on the mechanism of reaction of peroxidase and haloperoxidase activity in enzymes and biomimetic model complexes as well as some reaches and limitations of the currently used models and QM methods. Throughout the results, some key aspects relevant to all the enzymes are discussed and shown. We have shown that small cluster model of active site of enzyme consist less than 100 atoms is sufficicent for exploratory work in DFT study. However, it is recommended to use larger model by expanding the selection of protein structure around the active site of enzymes. From our study, the energy of reaction is improve significantly where we believe the amino acid residues surrounding the enzyme play vital role in stabilizing the enzyme. Even most of heme enzymes have identical framework on heme structure, however the type of reaction of each heme enzyme is closely related with the amino acid arrangement in their active site. Besides, the amino acid surrounded at the heme center believe to be responsible in proton relay in the enzyme centre. Furthermore, one of key aspect that need to be consider to reveal the mechanistic cycle of enzymes is the protonation state of enzyme where it will lead to favourable pathway. The combination of different models and computational methods used in this study has enabled us to deepen our understanding and make predictions as to how the regioselectivity, stereoselectivity and reactivity of these systems may be altered for the benefit of future application in various field.

In chapter 3, we were used different density functional theory methods on the catalytic cycle of the heme chloroperoxidase enzymes as well as different protonation states were explored. In heme system, the density functional theory method has little effect on the mechanism and optimized geometries and has only a small effect on the calculated kinetics. However, by introducing additional proton into the active site might lead to alternative pathway of the conversion of chloride ion to hypochloric acid by Cpd I. Futhermore, chloroperoxidase contains manganese ion nearby the active site, however

their function remain unclear. Further study can be conducted to reveal the properties and function of the manganese ion in the active site centre.

In Chapter 4, we presented detailed computational study on the possible reaction mechanisms of aromatic nitration by a CYP450 isozyme. We set up several active site model complexes with bound L-Trp and investigate substrate activation pathways leading to nitration as well as oxidation of substrate. The reaction of NO and O_2 on an iron(III)-heme center will generate free NO_2 radicals followed by NO_2 attack on L-Trp at the C^4, C^5, C^6 and C^7-position then proton transfer take place to form products. Although NO_2 addition on L-Trp is involved low energy at various positon of carbon however latter step were vary in energy. Therefore, it is likely that this enzyme would result in a mixture of products. In addition, substrate positioning and binding will be essential factor in CYP450 TxtE to enable a selective reaction process.

In Chapter 5 and Chapter 6, we did DFT study of biomimetic complexes containing vanadium. Both studies indicated that the conversion of vanadium-oxo to vanadium-peroxo intermediate is vital step to improve the sulfoxidation and epoxidation reaction of their respective system. Interestingly in Chapter 6, we observed the vanadium-porphyrin structure distorted from planarity and is saddle-shaped compare to iron-porphyrin by introducing different ligand framework. Thus, we recommend that further study should been extensively explore in future to improvise the reaction rate of conversion of vanadium-oxo to vanadium-peroxo complexes.

In Chapter 7, we did a collaboration work with experimentalist group to show that second coordination effects can form novel Fe^{IV}-oxo intermediate which is unusual reaction by introduce pendant amine group in framework structure of a non heme Fe^{II} complex. Both studies highly agree to whole mechanism proposed where the first step of mechanism involves a proton transfer from the proximal OH group of H_2O_2 via the transient protonation of the pendant amine group, followed by a homolytic O-O bond cleavage accompanied by proton-coupled electron transfer. Therefore, modifiying the ligand architecture will be one of the key factors towards the development of new intermediate which can be used for future modification of any biomemitic model complexes enabling realistic industrial applications.

In Chapter 8 and Chapter 9, we did work to identify whether the reaction rates of biomemitic complexes containing iron are enhanced by replacing by different metal elements. We did replaced iron by ruthenium and manganese, and performed a detailed computational study into their respective systems. Our work shows that, the differences in reactivity ranging from 5 to 10 $kcalmol^{-1}$ as compared to their analogous system. In addition, the thermochemical cycles and valence bond patterns reveal the chemical properties leads to this differences for both systems.

In conclusion, the results of this thesis paint an interesting picture of the factors influencing peroxidase and haloperodisase activity in various systems using computational approach. We have shown that computation analysis can be one of alternative tool able to give qualitative results when carefully applied to gain insight into various enzymes as well as able to support experimental findings. These results form a platform to gain better understanding of peroxidase and haloperoxidsase activity in various systems which will further our understanding into the future development.

11.0 References

1. Abu-Omar, M.M., Loaiza, A. and Hontzeas, N., 2005. “Reaction Mechanisms of Mononuclear Non-Heme Iron Oxygenases.” *Chemical reviews*, 105(6), pp.2227-2252. https://doi.org/10.1021/cr040653o.

2. Adamo, C. and Barone, V., 1999. “Toward Reliable Density Functional Methods without Adjustable Parameters: The PBE0 Model.” *The Journal of chemical physics*, 110(13), pp.6158-6170. https://doi.org/10.1063/1.478522.

3. Afanasiev, P. and Sorokin, A.B., 2016. “μ-Nitrido Diiron Macrocyclic Platform: Particular Structure for Particular Catalysis.” *Accounts of chemical research*, 49(4), pp.583-593. https://doi.org/10.1021/acs.accounts.5b00458.

4. Alkhalaf, L.M., Barry, S.M., Rea, D., Gallo, A., Griffiths, D., Lewandowski, J.R., Fulop, V. and Challis, G.L., 2018. “Binding of Distinct Substrate Conformations Enables Hydroxylation of Remote Sites in Thaxtomin D by Cytochrome P450 TxtC.” *Journal of the American Chemical Society*, 141(1), pp.216-222. https://doi.org/10.1021/jacs.8b08864

5. Amadio, E., Di Lorenzo, R., Zonta, C. and Licini, G., 2015. "Vanadium catalyzed aerobic carbon–carbon cleavage." *Coordination Chemistry Reviews* 301–302 (11): pp.147-162. https://doi.org/10.1016/j.ccr.2015.02.013.

6. Andris, E., Navratil, R., Jasik, J., Puri, M., Costas, M., Que Jr, L. and Roithova, J., 2018. “Trapping Iron(III)-Oxo Species at the Boundary of the ‘Oxo Wall’: Insights into the Nature of the Fe(III)-O Bond.” *Journal of the American Chemical Society*, *140*(43), pp.14391-14400. https://doi.org/10.1021/jacs.8b08950.

7. Ansari, M., Vyas, N., Ansari, A. and Rajaraman, G., 2015. “Oxidation of Methane by an N-Bridged High-Valent Diiron-Oxo Species: Electronic Structure Implications on the Reactivity.” *Dalton Transactions*, 44(34), pp.15232-15243. https://doi.org/10.1039/c5dt01060h.

8. Arber, J.M., De Boer, E., Garner, C.D., Hasnain, S.S. and Wever, R., 1989. “Vanadium K-Edge X-Ray Absorption Spectroscopy of Bromoperoxidase from Ascophyllum Nodosum.”*Biochemistry*, 28(19), pp.7968-7973.

9. Atkins, P.W. and Friedman, R.S., 2011. *Molecular quantum mechanics*. Oxford university press.

10. Baglia, R.A., Prokop-Prigge, K.A., Neu, H.M., Siegler, M.A. and Goldberg, D.P., 2015. “Mn(V)(O) versus Cr(V)(O) Porphyrinoid Complexes: Structural Characterization and Implications for Basicity Controlling H-Atom Abstraction.

”*Journal of the American Chemical Society*, 137(34), pp.10874-10877. https://doi.org/10.1021/jacs.5b05142.

11. Baglia, R.A., Zaragoza, J.P.T. and Goldberg, D.P., 2017. “Biomimetic Reactivity of Oxygen-Derived Manganese and Iron Porphyrinoid Complexes.” *Chemical reviews*, 117(21), pp.13320-13352.

12. Balding, P.R., Porro, C.S., McLean, K.J., Sutcliffe, M.J., Maréchal, J.D., Munro, A.W. and Visser, S.P.D., 2008. “How Do Azoles Inhibit Cytochrome P450 Enzymes? A Density Functional Study.” *The Journal of Physical Chemistry A*, 112(50), pp.12911-12918.

13. Balland, V., Banse, F., Anxolabéhère-Mallart, E., Nierlich, M. and Girerd, J.J., 2003."Iron Complexes Containing the Ligand N, N′-Bis (6-methyl-2-pyridylmethyl)-N, N′-bis (2-pyridylmethyl) ethane-1, 2-diamine: Structural, Spectroscopic, and Electrochemical Studies, Reactivity with Hydrogen Peroxide and the Formation of a Low-Spin Fe− OOH Complex." *European Journal of Inorganic Chemistry* 13: 2529-2535.

14. Bang, S., Park, S., Lee, Y.M., Hong, S., Cho, K.B. and Nam, W., 2014. “Demonstration of the Heterolytic O-O Bond Cleavage of Putative Nonheme Iron(II)-OOH(R) Complexes for Fenton and Enzymatic Reactions.” *Angewandte Chemie - International Edition* 53(30): 7843–47. https://doi.org/10.1002/anie.201404556.

15. Barman, P., Cantu Reinhard, F., Bagha, U.K., Kumar, D., Sastri, C. and de Visser, S., 2019. “Hydrogen by Deuterium Substitution in an Aldehyde Tunes the Regioselectivity by a Nonheme Manganese(III)-Peroxo Complex.” *Angewandte Chemie - International Edition* 58(31): 10639-43.

16. Barman, P., Faponle, A.S., Vardhaman, A.K., Angelone, D., Löhr, A.M., Browne, W.R., Comba, P., Sastri, C.V. and de Visser, S.P., 2016. “Influence of Ligand Architecture in Tuning Reaction Bifurcation Pathways for Chlorite Oxidation by Non-Heme Iron Complexes.” *Inorganic Chemistry* 55 (20): 10170–81. https://doi.org/10.1021/acs.inorgchem.6b01384.

17. Barry, S.M., Kers, J.A., Johnson, E.G., Song, L., Aston, P.R., Patel, B., Krasnoff, S.B., Crane, B.R., Gibson, D.M., Loria, R. and Challis, G.L., 2012. “Cytochrome P450-Catalyzed L-Tryptophan Nitration in Thaxtomin Phytotoxin Biosynthesis.” *Nature Chemical Biology* 810: 814-16.

18. Bataineh, H., Pestovsky, O. and Bakac, A., 2012 “PH-Induced Mechanistic Changeover from Hydroxyl Radicals to Iron(IV) in the Fenton Reaction.” *Chemical Science* 3(5): 1594–99. https://doi.org/10.1039/c2sc20099f.

19. Bathelt, C.M., Mulholland, A.J. and Harvey, J.N., 2005. “QM/MM Studies of the Electronic Structure of the Compound I Intermediate in Cytochrome c Peroxidase and Ascorbate Peroxidase.” *Dalton transactions*, (21): 3470-3476.

20. Bathelt, C.M., Zurek, J., Mulholland, A.J. and Harvey, J.N., 2005. “Electronic Structure of Compound I in Human Isoforms of Cytochrome P450 from QM/MM Modeling.” *ournal of the American Chemical Society*, 127(37):12900-12908.

21. Bautz, J., Bukowski, M.R., Kerscher, M., Stubna, A., Comba, P., Lienke, A., Münck, E. and Que Jr, L., 2006. “Formation of an Aqueous Oxoiron(IV) Complex at PH 2-6 from a Nonheme Iron(II) Complex and H_2O_2.” *Angewandte Chemie International Edition*, 45(34): 5681-5684. https://doi.org/10.1002/anie.200601134.

22. Becke, A. D., 1988. “Density-Functional Exchange-Energy Approximation with Correct Asymptotic Behavior.” *Physical Review A* 38 (6): 3098–3100. https://doi.org/10.1103/PhysRevA.38.3098.

23. Becke, A. D., 1993. “Density-functional Thermochemistry. III. The Role of Exact Exchange.” *The Journal of Chemical Physics* 98 (7): 5648–52. https://doi.org/10.1063/1.464913.

24. Beitlich, T., Kühnel, K., Schulze-Briese, C., Shoeman, R.L. and Schlichting, I., 2007. “Cryoradiolytic Reduction of Crystalline Heme Proteins: Analysis by UV-Vis Spectroscopy and X-Ray Crystallography.” *Journal of Synchrotron Radiation* 14 (1): 11–23. https://doi.org/10.1107/S0909049506049806.

25. Belcher, J., McLean, K.J., Matthews, S., Woodward, L.S., Fisher, K., Rigby, S.E., Nelson, D.R., Potts, D., Baynham, M.T., Parker, D.A. and Leys, D., 2014. “Structure and Biochemical Properties of the Alkene Producing Cytochrome P450 OleTJE (CYP152l1) from the Jeotgalicoccus Sp. 8456 Bacterium.” *Journal of Biological Chemistry 289*(10): 6535-6550. https://doi.org/10.1074/jbc.M113.527325.

26. Berman, H.M., Westbrook, J., Feng, Z., Gilliland, G.B., Bhat, T.N. and Wessig, H., H., Shindyalov, IN and Bourne, P.E., 2000. “The Protein Data Bank.” *Nucleic Acids Research*, 28: 235-242.

27. Bernal, I., Jensen, I.M., Jensen, K.B., McKenzie, C.J., Toftlund, H. and Tuchagues, J.P., 1995. “Iron(II) Complexes of Polydentate Aminopyridyl Ligands and an Exchangeable Sixth Ligand; Reactions with Peroxides. Crystal Structure of [FeL1(H_2O)][PF_6]2·H_2O[L1=N,N′-Bis-(6-Methyl-2-Pyridylmethyl)-N,N′-Bis(2-Py ridylmethyl)Ethane-1,2-Diamine].” *Journal of the Chemical Society, Dalton Transactions* 22: 3667–75. https://doi.org/10.1039/DT9950003667.

28. Bernasconi, L., Louwerse, M.J. and Baerends, E.J., 2007. “The Role of Equatorial and Axial Ligands in Promoting the Activity of Non-Heme Oxidoiron (IV) Catalysts in Alkane Hydroxylation.” *European Journal of Inorganic Chemistry* 19: 3023-3033. https://doi.org/10.1002/ejic.200601238.

29. Blomberg, M.R. and Siegbahn, P.E., 1997. “A Comparative Study of High-Spin Manganese and Iron Complexes.” *Theoretical Chemistry Accounts* 97(1-4): 72-80. https://doi.org/10.1007/s002140050239.

30. Blunt, J.W., Copp, B.R., Munro, M.H., Northcote, P.T. and Prinsep, M.R., 2011. “Marine Natural Products.” *Natural product reports*, 28(2): 196-268.

31. Borchardt, S. A., E. J. Allain, J. J. Michels, G. W. Stearns, R. F. Kelly, and W. F. McCoy. 2001. “Reaction of Acylated Homoserine Lactone Bacterial Signaling Molecules with Oxidized Halogen Antimicrobials.” *Applied and Environmental Microbiology* 67 (7): 3174–79. https://doi.org/10.1128/AEM.67.7.3174-3179.2001 PM - 11425738 M4 - Citavi.

32. Born, M. and Oppenheimer, R., 1927. “On the Quantum Theory of Molecules.” Annals of Physics. 84: 458.

33. Born, M. and Oppenheimer, R., 2000. “On the Quantum Theory of Molecules.” In *Quantum Chemistry: Classic Scientific Papers* (pp. 1-24).

34. Borovik, A.S., 2005. “Bioinspired Hydrogen Bond Motifs in Ligand Design: the Role of Noncovalent Interactions in Metal Ion Mediated Activation of Dioxygen.” *Accounts of chemical research*, 38(1): 54-61. https://doi.org/10.1021/ar030160q.

35. Bortolini, O. and Conte, V., 2005. “Vanadium (V) peroxocomplexes: Structure, Chemistry and Biological Implications.” *Journal of inorganic biochemistry*, 99(8): 1549-1557. https://doi.org/10.1016/j.jinorgbio.2005.04.003.

36. Bourassa, J.L., Ives, E.P., Marqueling, A.L., Shimanovich, R. and Groves, J.T., 2001. “Myoglobin catalyzes its own nitration.” *Journal of the American Chemical Society*, 123(21): 5142-5143. https://doi.org/10.1021/ja015621m.

37. Boys, S.F., 1950. “Electronic Wave Functions-I. A General Method of Calculation for the Stationary States of Any Molecular System.” *Proceedings of the Royal Society of London. Series A. Mathematical and Physical Sciences*, *200*(1063): 542-554.

38. Bray, W.C. and Gorin, M.H., 1932. “Ferryl Ion, a Compound of Tetravalent Iron.” *Journal of the American Chemical Society* 54 (5): 2124–25. https://doi.org/10.1021/ja01344a505.

39. Bruijnincx, P.C., van Koten, G. and Gebbink, R.J.K., 2008. “Mononuclear Non-Heme Iron Enzymes with the 2-His-1-Carboxylate Facial Triad: Recent Developments in Enzymology and Modeling Studies.” *Chemical Society Reviews* 37 (12): 2716–44. https://doi.org/10.1039/b707179p.

40. Burgess, B.K. and Lowe, D.J., 1996. “Mechanism of Molybdenum Nitrogenase.” *Chemical Reviews* 96 (7): 2983–3011. https://doi.org/10.1021/cr950055x.

41. Burns, R.C., W.H. Fuchsman, and R.W.F. Hardy. 1971. “Nitrogenase from Vanadium-Grown : Isolation, Characteristics, and Mechanistic Implications.” *Biochemical and Biophysical Research Communications* 42 (3): 353–58. https://doi.org/10.1016/0006-291X(71)90377-9.

42. Buron, C., Sénéchal-David, K., Ricoux, R., Le Caër, J.P., Guérineau, V., Méjanelle, P., Guillot, R., Herrero, C., Mahy, J.P. and Banse, F., 2015. “An Artificial Enzyme Made by Covalent Grafting of an FeII Complex into β-Lactoglobulin: Molecular Chemistry, Oxidation Catalysis, and Reaction-Intermediate Monitoring in a Protein.” *Chemistry - A European Journal* 21 (34): 12188–93. https://doi.org/10.1002/chem.201501755.

43. Butler, A. and Sandy, M., 2009. “Mechanistic Considerations of Halogenating Enzymes.” *Nature* 460 (7257): 848–54.

44. Butler, A., 1999. “Mechanistic Considerations of the Vanadium Haloperoxidases.” *Coordination Chemistry Reviews* 187 (1): 17–35. https://doi.org/10.1016/S0010-8545(99)00033-8.

45. Cantú Reinhard, F.G. and de Visser, S.P., 2017. “Oxygen Atom Transfer Using an Iron(IV)-Oxo Embedded in a Tetracyclic N-Heterocyclic Carbene System: How Does the Reactivity Compare to Cytochrome P450 Compound I?” *Chemistry - A European Journal* 23 (12): 2935–44. https://doi.org/10.1002/chem.201605505.

46. Cantú Reinhard, F.G., Barman, P., Mukherjee, G., Kumar, J., Kumar, D., Kumar, D., Sastri, C.V. and de Visser, S.P., 2017. “Keto-Enol Tautomerization Triggers an Electrophilic Aldehyde Deformylation Reaction by a Nonheme Manganese(III)-Peroxo Complex.” *Journal of the American Chemical Society* 139 (50): 18328–38. https://doi.org/10.1021/jacs.7b10033.

47. Cantú Reinhard, F.G., Faponle, A.S. and de Visser, S.P., 2016. “Substrate Sulfoxidation by an Iron(IV)-Oxo Complex: Benchmarking Computationally Calculated Barrier Heights to Experiment.” *The Journal of Physical Chemistry A* 120 (49): 9805–14. https://doi.org/10.1021/acs.jpca.6b09765.

48. Cantú Reinhard, F.G., Sainna, M.A., Upadhyay, P., Balan, G.A., Kumar, D., Fornarini, S., Crestoni, M.E. and de Visser, S.P., 2016. "A Systematic Account on Aromatic Hydroxylation by a Cytochrome P450 Model Compound I: A Low-Pressure Mass Spectrometry and Computational Study." *Chemistry - A European Journal* 22 (51): 18608–19. https://doi.org/10.1002/chem.201604361.

49. Carter-Franklin, J.N. and Butler, A., 2004. "Vanadium Bromoperoxidase-Catalyzed Biosynthesis of Halogenated Marine Natural Products." *Journal of the American Chemical Society* 126 (46): 15060–66. https://doi.org/10.1021/ja047925p.

50. Casny, M. and Rehder, D., 2001. "Towards Hydroperoxovanadium Complexes: The X-Ray Crystal Structure of a Peroxovanadium(v) Complex Containing a V(O2)(RCO2H)(H2O)2 Cluster with Hydrogen Bond Inter-Linkages." *Chemical Communications*, no. 10: 921–22. https://doi.org/10.1039/b101010g.

51. Chaki, M., Valderrama, R., Fernández-Ocaña, A.M., Carreras, A., López-Jaramillo, J., Luque, F., Palma, J.M., Pedrajas, J.R., Begara-Morales, J.C., Sánchez-Calvo, B. and Gómez-Rodríguez, M.V., 2009. "Protein Targets of Tyrosine Nitration in Sunflower (Helianthus Annuus L.) Hypocotyls." *Journal of Experimental Botany* 60 (15): 4221–34. https://doi.org/10.1093/jxb/erp263.

52. Chatfield, D.C. and Morozov, A.N., 2018. "Proximal Pocket Controls Alkene Oxidation Selectivity of Cytochrome P450 and Chloroperoxidase toward Small, Nonpolar Substrates." *Journal of Physical Chemistry B* 122 (32): 7828–38. https://doi.org/10.1021/acs.jpcb.8b04279.

53. Cheaib, K., Mubarak, M.Q.E., Sénéchal-David, K., Herrero, C., Guillot, R., Clémancey, M., Latour, J.M., de Visser, S.P., Mahy, J.P., Banse, F. and Avenier, F., 2019. "Selective Formation of an Fe IV O or an Fe III OOH Intermediate From Iron(II) and H_2O_2 : Controlled Heterolytic versus Homolytic Oxygen-Oxygen Bond Cleavage by the Second Coordination Sphere." *Angewandte Chemie International Edition* 58 (3): 854–58. https://doi.org/10.1002/anie.201812724.

54. Chen, H., Song, J., Lai, W., Wu, W. and Shaik, S., 2010. "Multiple Low-Lying States for Compound i of P450cam and Chloroperoxidase Revealed from Multireference Ab Initio QM/MM Calculations." *Journal of Chemical Theory and Computation* 6 (3): 940–53. https://doi.org/10.1021/ct9006234.

55. Chen, J., Cho, K.B., Lee, Y.M., Kwon, Y.H. and Nam, W., 2015. "Mononuclear Nonheme Iron (IV)–Oxo and Manganese (IV)–Oxo Complexes in Oxidation Reactions: Experimental Results Prove Theoretical Prediction." *Chemical Communications* 51 (66): 13094–97.

56. Chen, W., Suenobu, T. and Fukuzumi, S., 2011. "A Vanadium Porphyrin with Temperature-Dependent Phase Transformation: Synthesis, Crystal Structures, Supramolecular Motifs and Properties." *Chemistry - An Asian Journal* 6 (6): 1416–22. https://doi.org/10.1002/asia.201000822.

57. Cheng, B., Safo, M.K., Orosz, R.D., Reed, C.A., Debrunner, P.G. and Scheidt, W.R., 1994. "Synthesis, Structure, and Characterization of Five-Coordinate Aquo(Octaethylporphinato)Iron(III) Perchlorate." *Inorganic Chemistry* 33 (7): 1319–24. https://doi.org/10.1021/ic00085a018.

58. Cheung, W.M., Chiu, W.H., de Vere-Tucker, M., Sung, H.H.Y., Williams, I.D. and Leung, W.H., 2017. "Heterobimetallic Nitrido Complexes of Group 8 Metalloporphyrins." *Inorganic Chemistry* 56 (10): 5680–87. https://doi.org/10.1021/acs.inorgchem.7b00281.

59. Cheung, W.M., Ng, W.M., Wong, W.H., Lee, H.K., Sung, H.H.Y., Williams, I.D. and Leung, W.H., 2018. "A Nitrido-Bridged Heterometallic Ruthenium(IV)/Iron(IV) Phthalocyanine Complex Supported by A Tripodal Oxygen Ligand, [Co(H5-C5H5){P(O)(OEt)2}3]-: Synthesis, Structure, and Its Oxidation to Give Phthalocyanine Cation Radical and Hydroxyphthalocyanine Complexes" *Inorganic Chemistry* 57 (15): 9215–22. https://doi.org/10.1021/acs.inorgchem.8b01229.

60. Cho, K.B., Hirao, H., Shaik, S. and Nam, W., 2016. "To Rebound or Dissociate? This Is the Mechanistic Question in C–H Hydroxylation by Heme and Nonheme Metal–Oxo Complexes." *Chemical Society Reviews* 45 (5): 1197–1210.

61. Clark, R.C. and Reid, J.S., 1995. "The Analytical Calculation of Absorption in Multifaceted Crystals." *Acta Crystallographica Section A: Foundations of Crystallography* 51 (6): 887–97.

62. Colomban, C., Kudrik, E.V., Afanasiev, P. and Sorokin, A.B., 2014. "Catalytic Defluorination of Perfluorinated Aromatics under Oxidative Conditions Using N-Bridged Diiron Phthalocyanine." *Journal of the American Chemical Society* 136 (32): 11321–30. https://doi.org/10.1021/ja505437h.

63. Colomban, C., Kudrik, E.V., Afanasiev, P. and Sorokin, A.B., 2017. "Heteroleptic μ-Nitrido Diiron Complex Supported by Phthalocyanine and Octapropylporphyrazine Ligands: Formation of Oxo Species and Their Reactivity with Fluorinated Compounds." *Journal of Porphyrins and Phthalocyanines* 21 (04–06): 345–53.

64. Colomban, C., Tobing, A.H., Mukherjee, G., Sastri, C.V., Sorokin, A.B. and de Visser, S.P., 2019. "Mechanism of Oxidative Activation of Fluorinated Aromatic

Compounds by N-Bridged Diiron-Phthalocyanine: What Determines the Reactivity?" *Chemistry–A European Journal*.

65. Colpas, G.J., Hamstra, B.J., Kampf, J.W. and Pecoraro, V.L., 1996. "Functional Models for Vanadium Haloperoxidase: Reactivity and Mechanism of Halide Oxidation." *Journal of the American Chemical Society* 118 (14): 3469–78. https://doi.org/10.1021/ja953791r.

66. Conte, V. and Floris, B., 2010. "Vanadium Catalyzed Oxidation with Hydrogen Peroxide." *Inorganica Chimica Acta* 363 (9): 1935–46. https://doi.org/10.1016/j.ica.2009.06.056.

67. Conte, V., Bortolini, O., Carraro, M. and Moro, S., 2000. "Models for the Active Site of Vanadium-Dependent Haloperoxidases: Insight into the Solution Structure of Peroxo Vanadium Compounds." *Journal of Inorganic Biochemistry* 80 (1–2): 41–49. https://doi.org/10.1016/S0162-0134(00)00038-6.

68. Conte, V., Coletti, A., Floris, B., Licini, G. and Zonta, C., 2011. "Mechanistic Aspects of Vanadium Catalysed Oxidations with Peroxides." *Coordination Chemistry Reviews* 255 (19–20): 2165–77. https://doi.org/10.1016/j.ccr.2011.03.006.

69. Cordelle, C., Agustin, D., Daran, J.C. and Poli, R., 2010. "Oxo-Bridged Bis Oxo-Vanadium(V) Complexes with Tridentate Schiff Base Ligands (VOL)2O (L = SAE, SAMP, SAP): Synthesis, Structure and Epoxidation Catalysis under Solvent-Free Conditions." *Inorganica Chimica Acta* 364 (1): 144–49. https://doi.org/10.1016/j.ica.2010.09.021. 223

70. Costas, M., Mehn, M.P., Jensen, M.P. and Que, L., 2004. "Dioxygen Activation at Mononuclear Nonheme Iron Active Sites: Enzymes, Models, and Intermediates." *Chemical Reviews* 104 (2): 939–86. https://doi.org/10.1021/cr020628n.

71. Coupe, E.E., Smyth, M.G., Fosberry, A.P., Hall, R.M. and Littlechild, J.A., 2007. "The Dodecameric Vanadium-Dependent Haloperoxidase from the Marine Algae Corallina Officinalis: Cloning, Expression, and Refolding of the Recombinant Enzyme." *Protein Expression and Purification* 52 (2): 265–72.

72. Crans, D.C., Smee, J.J., Gaidamauskas, E. and Yang, L., 2004. "The Chemistry and Biochemistry of Vanadium and the Biological Activities Exerted by Vanadium Compounds." *Chemical Reviews* 104 (2): 849–902. https://doi.org/10.1021/cr020607t.

73. Cundari, T.R., Saunders, L. and Sisterhen, L.L., 1998. "Molecular Modeling of Vanadium-Oxo Complexes. A Comparison of Quantum and Classical Methods."

Journal of Physical Chemistry A 102 (6): 997–1004. https://doi.org/10.1021/jp972827u.

74. da Silva, J.A., da Silva, J.J.F. and Pombeiro, A.J., 2013. "Amavadin, a Vanadium Natural Complex: Its Role and Applications." *Coordination Chemistry Reviews* 257 (15–16): 2388–2400. https://doi.org/10.1016/j.ccr.2013.03.010.

75. Dairi, T., Nakano, T., Aisaka, K., Katsumata, R. and Hasegawa, M., 1995. "Cloning and Nucleotide Sequence of the Gene Responsible for Chlorination of Tetracycline." *Bioscience, Biotechnology, and Biochemistry* 59 (6): 1099–1106. https://doi.org/10.1271/bbb.59.1099.

76. Dar, T.A., Uprety, B., Sankar, M. and Maurya, M.R., 2019. "Robust and Electron Deficient Oxidovanadium(Iv) Porphyrin Catalysts for Selective Epoxidation and Oxidative Bromination Reactions in Aqueous Media." *Green Chemistry* 21 (7): 1757–68. https://doi.org/10.1039/c8gc03909g.

77. Das, A., Grinkova, Y.V. and Sligar, S.G., 2007. "Redox Potential Control by Drug Binding to Cytochrome P450 3A4." *Journal of the American Chemical Society* 129 (45): 13778–79. https://doi.org/10.1021/ja074864x.

78. Davydov, R., Makris, T.M., Kofman, V., Werst, D.E., Sligar, S.G. and Hoffman, B.M., 2001. "Hydroxylation of Camphor by Reduced Oxy-Cytochrome P450cam: Mechanistic Implications of EPR and ENDOR Studies of Catalytic Intermediates in Native and Mutant Enzymes." *Journal of the American Chemical Society* 123 (7): 1403–15. https://doi.org/10.1021/ja003583l.

79. Davydov, R., Osborne, R.L., Kim, S.H., Dawson, J.H. and Hoffman, B.M., 2008. "EPR and ENDOR Studies of Cryoreduced Compounds II of Peroxidases and Myoglobin. Proton-Coupled Electron Transfer and Protonation Status of Ferryl Hemes." *Biochemistry* 47 (18): 5147–55. https://doi.org/10.1021/bi702514d.

80. Dawson, J.H. and Sono, M., 1987. "Cytochrome P-450 and Chloroperoxidase: Thiolate-Ligated Heme Enzymes. Spectroscopic Determination of Their Active Site Structures and Mechanistic Implications of Thiolate Ligation." *Chemical Reviews* 87 (5): 1255–76. https://doi.org/10.1021/cr00081a015.

81. Dawson, J.H., Holm, R.H., Trudell, J.R., Barth, G., Linder, R.E., Bunnenberg, E., Djerassi, C. and Tang, S.C., 1976. "Oxidized Cytochrome P-450. Magnetic Circular Dichroism Evidence for Thiolate Ligation in the Substrate-Bound Form. Implications for the Catalytic Mechanism." *Journal of the American Chemical Society* 98 (12): 3707–9. https://doi.org/10.1021/ja00428a054.

82. De Boer, E., Boon, K. and Wever, R., 1988. “Electron Paramagnetic Resonance Studies on Conformation States and Metal Ion Exchange Properties of Vanadium Bromoperoxidase.” *Biochemistry*, 27(5):1629-1635.

83. De Boer, E., Van Kooyk, Y., Tromp, M.G.M., Plat, H. and Wever, R., 1986. “Bromoperoxidase from Ascophyllum Nodosum: A Novel Class of Enzymes Containing Vanadium as a Prosthetic Group?” *Biochimica et Biophysica Acta (BBA)-Protein Structure and Molecular Enzymology* 869(1): 48-53. https://doi.org/10.1016/0167-4838(86)90308-0.

84. De Broglie, L., 1923. “Waves and Quanta.” *Nature* 112 (2815): 540.

85. De Montellano, P.R.O. ed., 2005. *Cytochrome P450: structure, mechanism, and biochemistry*. Springer Science & Business Media.

86. De Visser, S.P., and Kumar D., 2011. “Iron-Containing Enzymes: Versatile Catalysts of Hydroxylation Reaction in Nature.” Royal Society of Chemistry Publishing: Cambridge, UK, 2011.

87. De Visser, S.P., Timmins, A., Fowler, N., Warwicker, J. and Straganz, G., 2018. “Does Substrate Positioning Affect the Selectivity and Reactivity in the Hectochlorin Biosynthesis Halogenase?” *Frontiers in Chemistry* 6: 513. https://doi.org/10.3389/fchem.2018.00513.

88. Denisov, I.G., Makris, T.M., Sligar, S.G. and Schlichting, I., 2005. “Structure and Chemistry of Cytochrome P450.” *Chemical Reviews* 105 (6): 2253–77. https://doi.org/10.1021/cr0307143.

89. Denler, M.C., Massie, A.A., Singh, R., Stewart-Jones, E., Sinha, A., Day, V.W., Nordlander, E. and Jackson, T.A., 2019. “Mn IV-Oxo Complex of a Bis (Benzimidazolyl)-Containing N5 Ligand Reveals Different Reactivity Trends for Mn IV-Oxo than Fe IV-Oxo Species.” *Dalton Transactions* 48 (15): 5007–21.

90. Derat, E. and Shaik, S., 2006a. “An Efficient Proton-Coupled Electron-Transfer Process during Oxidation of Ferulic Acid by Horseradish Peroxidase: Coming Full Cycle.” *Journal of the American Chemical Society* 128 (42): 13940–49. https://doi.org/10.1021/ja065058d.

91. Derat, E. and Shaik, S., 2006b. “The Poulos−Kraut Mechanism of Compound I Formation in Horseradish Peroxidase: A QM/MM Study.” *The Journal of Physical Chemistry B* 110 (21): 10526–33. https://doi.org/10.1021/jp055412e.

92. Derat, E., Cohen, S., Shaik, S., Altun, A. and Thiel, W., 2005. “Principal Active Species of Horseradish Peroxidase, Compound I: A Hybrid Quantum Mechanical/Molecular Mechanical Study.” *Journal of the American Chemical Society* 127 (39): 13611–21. https://doi.org/10.1021/ja0534046.

93. Dhuri, S.N., Seo, M.S., Lee, Y.M., Hirao, H., Wang, Y., Nam, W. and Shaik, S., 2008. "Experiment and Theory Reveal the Fundamental Difference between Two-State and Single-State Reactivity Patterns in Nonheme FeIV=O versus Ru IV=O Oxidants." *Angewandte Chemie - International Edition* 47 (18): 3356–59. https://doi.org/10.1002/anie.200705880.

94. Ditchfield, R.H.W.J., Hehre, W.J. and Pople, J.A., 1971."Self-Consistent Molecular-Orbital Methods. IX. An Extended Gaussian-Type Basis for Molecular-Orbital Studies of Organic Molecules." *The Journal of Chemical Physics* 54 (2): 724–28. https://doi.org/10.1063/1.1674902.

95. Dodani, S.C., Cahn, J.K., Heinisch, T., Brinkmann-Chen, S., McIntosh, J.A. and Arnold, F.H., 2014. "Structural, Functional, and Spectroscopic Characterization of the Substrate Scope of the Novel Nitrating Cytochrome P450 TxtE." *Chembiochem : A European Journal of Chemical Biology* 15 (15): 2259–67. https://doi.org/10.1002/cbic.201402241.

96. Dodani, S.C., Kiss, G., Cahn, J.K., Su, Y., Pande, V.S. and Arnold, F.H., 2016. "Discovery of a Regioselectivity Switch in Nitrating P450s Guided by Molecular Dynamics Simulations and Markov Models." *Nature Chemistry* 8 (5): 419–25. https://doi.org/10.1038/nchem.2474.

97. Doukkali, A., Saoiabi, A., Ferhat, M., Mugnier, Y., Vallat, A. and Guilard, R., 2006. "Thermodynamic and Kinetic Control over the Oxidation Mechanism of the Natural Vanadyl Porphyrin Series (DPEP)VO in Methylene Chloride: Electrogeneration of an Unusual Dicationic Species $[(DPEP)VO]_2^{2+}$." *New Journal of Chemistry* 30 (7): 997–1003. https://doi.org/10.1039/b512360g.

98. Dragancea, D., Talmaci, N., Shova, S., Novitchi, G., Darvasiova, D., Rapta, P., Breza, M., Galanski, M., Kožíšek, J., Martins, N.M. and Martins, L.M., 2016. "Vanadium(V) Complexes with Substituted 1,5-Bis(2-Hydroxybenzaldehyde)Carbohydrazones and Their Use as Catalyst Precursors in Oxidation of Cyclohexane." *Inorganic Chemistry* 55 (18): 9187–9203. https://doi.org/10.1021/acs.inorgchem.6b01011.

99. Draksharapu, A., Angelone, D., Quesne, M.G., Padamati, S.K., Gómez, L., Hage, R., Costas, M., Browne, W.R. and De Visser, S.P., 2015. "Identification and Spectroscopic Characterization of Nonheme Iron(III) Hypochlorite Intermediates." *Angewandte Chemie - International Edition* 54 (14): 4357–61. https://doi.org/10.1002/anie.201411995.

100. Drummond, M.J., Ford, C.L., Gray, D.L., Popescu, C.V. and Fout, A.R., 2019. "Radical Rebound Hydroxylation Versus H-Atom Transfer in Non-Heme Iron(III)-Hydroxo Complexes: Reactivity and Structural Differentiation."

Research-article. *Journal of the American Chemical Society* 141 (16): 6639–50. https://doi.org/10.1021/jacs.9b01516.

101. Duck, I., Pauli, W. and Sudarshan, E.C.G., 1997. *Pauli and the Spin-Statistics Theorem*. World Scientific.

102. Dunford, H.B., 1999. *Heme Peroxidases*. Wiley-vch.

103. Eady, R.R., Antonyuk, S.V. and Hasnain, S.S., 2016. "Fresh Insight to Functioning of Selected Enzymes of the Nitrogen Cycle." *Current Opinion in Chemical Biology* 31 (1): 103–12. https://doi.org/10.1016/j.cbpa.2016.02.009.

104. Egawa, T., Proshlyakov, D.A., Miki, H., Makino, R., Ogura, T., Kitagawa, T. and Ishimura, Y., 2001. "Effects of a Thiolate Axial Ligand on the $\pi \rightarrow \pi^*$ Electronic States of Oxoferryl Porphyrins: A Study of the Optical and Resonance Raman Spectra of Compounds I and II of Chloroperoxidase." *Journal of Biological Inorganic Chemistry* 6 (1): 46–54. https://doi.org/10.1007/s007750000181.

105. Egdal, R.K., Larsen, F.B., Bond, A.D. and McKenzie, C.J., 2005. "A Vanadium-Promoted C-N Bond Cleavage." *Inorganica Chimica Acta* 358 (2): 376–82. https://doi.org/10.1016/j.ica.2004.09.004.

106. Ellis, W.C., Tran, C.T., Roy, R., Rusten, M., Fischer, A., Ryabov, A.D., Blumberg, B. and Collins, T.J., 2010. . "Designing Green Oxidation Catalysts for Purifying Environmental Waters." *Journal of the American Chemical Society* 132 (28): 9774–81. https://doi.org/10.1021/ja102524v.

107. Engelmann, X., Monte-Pérez, I. and Ray, K., 2016. "Oxidation Reactions with Bioinspired Mononuclear Non-Heme Metal–Oxo Complexes." *Angewandte Chemie - International Edition* 55 (27): 7632–49. https://doi.org/10.1002/anie.201600507.

108. Esteves, P.M., de M. Carneiro, J.W., Cardoso, S.P., Barbosa, A.G., Laali, K.K., Rasul, G., Prakash, G.S. and Olah, G.A., 2003 "Unified Mechanistic Concept of Electrophilic Aromatic Nitration: Convergence of Computational Results and Experimental Data." *Journal of the American Chemical Society* 125 (16): 4836–49. https://doi.org/10.1021/ja021307w.

109. Everett, R.R., Soedjak, H.S. and Butler, A., 1990. "Mechanism of Dioxygen Formation Catalyzed by Vanadium Bromoperoxidase." *Journal of Biological Chemistry* 265 (26): 15671–79.

110. Faponle, A.S., Quesne, M.G. and de Visser, S.P., 2016. "Origin of the Regioselective Fatty-Acid Hydroxylation versus Decarboxylation by a Cytochrome P450 Peroxygenase: What Drives the Reaction to Biofuel

Production?" *Chemistry - A European Journal* 22 (16): 5478–83. https://doi.org/10.1002/chem.201600739.

111. Faponle, A.S., Quesne, M.G., Sastri, C.V., Banse, F. and de Visser, S.P., 2015. "Differences and Comparisons of the Properties and Reactivities of Iron(III)-Hydroperoxo Complexes with Saturated Coordination Sphere." *Chemistry - A European Journal* 21 (3): 1221–36. https://doi.org/10.1002/chem.201404918.

112. Faponle, A.S., Seebeck, F.P. and de Visser, S.P., 2017. "Sulfoxide Synthase versus Cysteine Dioxygenase Reactivity in a Nonheme Iron Enzyme." *Journal of the American Chemical Society* 139 (27): 9259–70. https://doi.org/10.1021/jacs.7b04251.

113. Fenton, H.J.H., 1894. "LXXIII.—Oxidation of Tartaric Acid in Presence of Iron." *Journal of the Chemical Society, Transactions* 65: 899–910. https://doi.org/10.1039/CT8946500899.

114. Fitzpatrick, P.F., 2003. . "Mechanism of Aromatic Amino Acid Hydroxylation." *Biochemistry* 42 (48): 14083–91. https://doi.org/10.1021/bi035656u.

115. Fomenko, I.S., Gushchin, A.L., Abramov, P.A., Sokolov, M.N., Shul'pina, L.S., Ikonnikov, N.S., Kuznetsov, M.L., Pombeiro, A.J., Kozlov, Y.N. and Shul'pin, G.B., 2019. "New Oxidovanadium(IV) Complexes with 2,2′-Bipyridine and 1,10-Phenathroline Ligands: Synthesis, Structure and High Catalytic Activity in Oxidations of Alkanes and Alcohols with Peroxides." *Catalysts* 9 (3): 217-237. https://doi.org/10.3390/catal9030217.

116. Foresman, J.B. and Frisch, A., 1996."Exploring Chemistry with Electronic Structure Methods: A Guide to Using Gaussian."

117. Fox, J.P., Ramdhanie, B., Zareba, A.A., Czernuszewicz, R.S. and Goldberg, D.P., 2004. "Copper(III) and Vanadium(IV)-Oxo Corrolazines." *Inorganic Chemistry* 43 (21): 6600–6608. https://doi.org/10.1021/ic049384a.

118. Francl, M.M., Pietro, W.J., Hehre, W.J., Binkley, J.S., Gordon, M.S., DeFrees, D.J. and Pople, J.A., 1982. "Self - Consistent Molecular Orbital Methods . XXIII . A Polarization - Type Basis Set for Second - Row Elements."

119. Frisch, M.J., Hratchian, H.P. and Nielsen, A.B., 2009. *Gaussian 09: Programmer's Reference*. gaussian.

120. Ganguly, S., Giles, L.J., Thomas, K.E., Sarangi, R. and Ghosh, A., 2017. "Ligand Noninnocence in Iron Corroles: Insights from Optical and X-Ray Absorption Spectroscopies and Electrochemical Redox Potentials." *Chemistry - A European Journal* 23 (60): 15098–106. https://doi.org/10.1002/chem.201702621.

121. Ganguly, S., Giles, L.J., Thomas, K.E., Sarangi, R. and Ghosh, A., 2018. "Electronic Structure of Manganese Corroles Revisited: X-Ray Structures, Optical and X-Ray Absorption Spectroscopies, and Electrochemistry as Probes of Ligand Noninnocence." *Inorganic Chemistry* 57 (16): 9656–69. https://doi.org/10.1021/acs.inorgchem.8b00537.

122. Geethalakshmi, K.R., Waller, M.P., Thiel, W. and Bühl, M., 2009. "^{51}V NMR Chemical Shifts Calculated from Qm/Mm Models of Peroxo Forms of Vanadium Haloperoxidases." *Journal of Physical Chemistry B* 113 (13): 4456–65. https://doi.org/10.1021/jp8109308.

123. Geigert, J., Lee, T.D., Dalietos, D.J., Hirano, D.S. and Neidleman, S.L., 1986. "Epoxidation of Alkenes by Chloroperoxidase Catalysis." *Biochemical and Biophysical Research Communications* 136 (2): 778–82. https://doi.org/10.1016/0006-291X(86)90507-3.

124. Ghosh, A., 1998. "First-Principles Quantum Chemical Studies of Porphyrins." *Accounts of Chemical Research* 31 (4): 189–98. https://doi.org/10.1021/ar950033x.

125. Ghosh, A., Ryabov, A.D., Mayer, S.M., Horner, D.C., Prasuhn, D.E., Sen Gupta, S., Vuocolo, L., Culver, C., Hendrich, M.P., Rickard, C.E. and Norman, R.E., 2003. "Understanding the Mechanism of H+-Induced Demetalation as a Design Strategy for Robust Iron(III) Peroxide-Activating Catalysts." *Journal of the American Chemical Society* 125 (41): 12378–79. https://doi.org/10.1021/ja0367344.

126. Ghosh, S.K., Patra, R. and Rath, S.P., 2008. "Axial Ligand Coordination in Sterically Strained Vanadyl Porphyrins: Synthesis, Structure, and Properties." *Inorganic Chemistry* 47 (21): 9848–56. https://doi.org/10.1021/ic800714w.

127. Girerd, J.J., Banse, F. and Simaan, A.J., 2000. "Characterization and Properties of Non-Heme Iron Peroxo Complexes." In *Metal-Oxo and Metal-Peroxo Species in Catalytic Oxidations*, edited by Bernard Meunier, 145–77. Berlin, Heidelberg: Springer Berlin Heidelberg. https://doi.org/10.1007/3-540-46592-8_6.

128. Girvan, H.M. and Munro, A.W., 2016. "Applications of Microbial Cytochrome P450 Enzymes in Biotechnology and Synthetic Biology." *Current Opinion in Chemical Biology* 31: 136–45. https://doi.org/10.1016/j.cbpa.2016.02.018.

129. Goldstein, S. and Meyerstein, D., 1999. "Comments on the Mechanism of the 'Fenton-Like' Reaction." *Accounts of Chemical Research* 32 (7): 547–50. https://doi.org/10.1021/ar9800789.

130. Grant, J.L., Mitchell, M.E. and Makris, T.M., 2016. "Catalytic Strategy for Carbon-Carbon Bond Scission by the Cytochrome P450 OleT." *Proceedings of the National Academy of Sciences of the United States of America* 113 (36): 10049–54. https://doi.org/10.1073/pnas.1606294113.

131. Green, M.T., 1999. "Evidence for Sulfur-Based Radicals in Thiolate Compound I Intermediates." *Journal of the American Chemical Society* 121 (34): 7939–40. https://doi.org/10.1021/ja991541v.

132. Green, M.T., 2000. "Imidazole-Ligated Compound I Intermediates: The Effects of Hydrogen Bonding." *Journal of the American Chemical Society* 122 (39): 9495–99. https://doi.org/10.1021/ja994377k.

133. Green, M.T., Dawson, J.H. and Gray, H.B., 2004. "Oxoiron(IV) in Chloroperoxidase Compound II Is Basic: Implications for P450 Chemistry." *Science* 304 (5677): 1653–56. https://doi.org/10.1126/science.1096897.

134. Greule, A., Stok, J.E., De Voss, J.J. and Cryle, M.J., 2018. "Unrivalled Diversity: The Many Roles and Reactions of Bacterial Cytochromes P450 in Secondary Metabolism." *Natural Product Reports* 35 (8): 757–91. https://doi.org/10.1039/c7np00063d.

135. Grimme, S., 2011. "Density Functional Theory with London Dispersion Corrections." *Wiley Interdisciplinary Reviews: Computational Molecular Science* 1 (2): 211–28. https://doi.org/10.1002/wcms.30.

136. Grimme, S., Antony, J., Ehrlich, S. and Krieg, H., 2010. "A Consistent and Accurate Ab Initio Parametrization of Density Functional Dispersion Correction (DFT-D) for the 94 Elements H-Pu." *The Journal of Chemical Physics* 132 (15): 154104. https://doi.org/10.1063/1.3382344.

137. Grimme, S., Hansen, A., Brandenburg, J.G. and Bannwarth, C., 2016. "Dispersion-Corrected Mean-Field Electronic Structure Methods." *Chemical Reviews* 116 (9): 5105–54. https://doi.org/10.1021/acs.chemrev.5b00533.

138. Groenhof, A.R., Swart, M., Ehlers, A.W. and Lammertsma, K., 2005. "Electronic Ground States of Iron Porphyrin and of the First Species in the Catalytic Reaction Cycle of Cytochrome P450s." *Journal of Physical Chemistry A* 109 (15): 3411–17. https://doi.org/10.1021/jp0441442.

139. Grogan, G., 2011. "Cytochromes P450: Exploiting Diversity and Enabling Application as Biocatalysts." *Current Opinion in Chemical Biology* 15 (2): 241–48. https://doi.org/10.1016/j.cbpa.2010.11.014.

140. Gross, E.K. and Dreizler, R.M. eds., 2013. *Density functional theory* (Vol. 337). Springer Science & Business Media.

141. Groves, J.T., 2003. "The Bioinorganic Chemistry of Iron in Oxygenases and Supramolecular Assemblies." *Proceedings of the National Academy of Sciences of the United States of America* 100 (7): 3569–74. https://doi.org/10.1073/pnas.0830019100.

142. Guan, X., Fisher, M.B., Lang, D.H., Zheng, Y.M., Koop, D.R. and Rettie, A.E., 1998. "Cytochrome P450-dependent desaturation of lauric acid: isoform selectivity and mechanism of formation of 11-dodecenoic acid." *Chemico-biological interactions*, 110(1-2), 103-121

143. Guengerich, F. P., 2017. "Intersection of the Roles of Cytochrome P450 Enzymes with Xenobiotic and Endogenous Substrates: Relevance to Toxicity and Drug Interactions." *Chemical Research in Toxicology* 30 (1): 2–12. https://doi.org/10.1021/acs.chemrestox.6b00226.

144. Guengerich, F.P. and Kim, D.H., 1991. "Enzymic Oxidation of Ethyl Carbamate to Vinyl Carbamate and Its Role as an Intermediate in the Formation of 1,N6-Ethenoadenosine." *Chemical Research in Toxicology* 4 (4): 413–21. https://doi.org/10.1021/tx00022a003.

145. Guengerich, F.P. and Yoshimoto, F.K., 2018. "Formation and Cleavage of C-C Bonds by Enzymatic Oxidation-Reduction Reactions." Review-article. *Chemical Reviews* 118 (14): 6573–6655. https://doi.org/10.1021/acs.chemrev.8b00031.

146. Guo, Z., Guan, X., Huang, J.S., Tsui, W.M., Lin, Z. and Che, C.M., 2013 "Bis (Sulfonylimide) Ruthenium (VI) Porphyrins: X-ray Crystal Structure and Mechanism of C H Bond Amination by Density Functional Theory Calculations." *Chemistry–A European Journal* 19 (34): 11320–31.

147. Gupta, R., Hou, G., Renirie, R., Wever, R. and Polenova, T., 2015. "^{51}V NMR Crystallography of Vanadium Chloroperoxidase and Its Directed Evolution P395D/L241V/T343A Mutant: Protonation Environments of the Active Site." *Journal of the American Chemical Society* 137 (16): 5618–28. https://doi.org/10.1021/jacs.5b02635.

148. Haber, F. and Weiss, J., 1934. "The Catalytic Decomposition of Hydrogen Peroxide by Iron Salts." *Proceedings of the Royal Society of London. Series A-Mathematical and Physical Sciences*, *147*(861), pp.332-351.

149. Hager, L.P., Morris, D.R., Brown, F.S. and Eberwein, H., 1966. "Chloroperoxidase II. Utilization of Halogen Anions." *Journal of Biological Chemistry* 241 (8): 1769–77.

150. Hansch, C., Leo, A. and Taft, R.W., 1991. “A Survey of Hammett Substituent Constants and Resonance and Field Parameters.” *Chemical Reviews* 91 (2): 165–95. https://doi.org/10.1021/cr00002a004.

151. Harada, R., Ōkawa, H. and Kojima, T., 2005. “Synthesis, Characterization, and Distortion Properties of Vanadyl Complexes of Octaphenylporphyrin and Dodecaphenylporphyrin.” *Inorganica Chimica Acta* 358 (3): 489–96. https://doi.org/10.1016/j.ica.2004.08.009.

152. Hartree, D.R., 1928, “The Wave Mechanics of an Atom with a Non-Coulomb Central Field. Part I. Theory and Methods.” In *Mathematical Proceedings of the Cambridge Philosophical Society*, 24:89–110. Cambridge University Press.

153. Harvey, J.N., Bathelt, C.M. and Mulholland, A.J., 2006. “QM/MM Modeling of Compound I Active Species in Cytochrome P450, Cytochrome C Peroxidase, and Ascorbate Peroxidase.” *Journal of Computational Chemistry* 27 (12): 1352–62. https://doi.org/10.1002/jcc.20446.

154. Hay, P.J. and Wadt, W.R., 1985. “Ab Initio Effective Core Potentials for Molecular Calculations. Potentials for the Transition Metal Atoms Sc to Hg.” *The Journal of Chemical Physics* 82 (1): 270–83. https://doi.org/10.1063/1.448799.

155. Hayashi, Y. and Yamazaki, I., 1979. “The Oxidation-Reduction Potentials of Compound I/Compound II and Compound II/Ferric Couples of Horseradish Peroxidases A2 and C.” *Journal of Biological Chemistry* 254 (18): 9101–6.

156. Hazell, A., McKenzie, C.J., Nielsen, L.P., Schindler, S. and Weitzer, M., 2002. “Mononuclear Non-Heme Iron(III) Peroxide Complexes: Syntheses, Characterisation, Mass Spectrometric and Kinetic Studies.” *Journal of the Chemical Society, Dalton Transactions*, no. 3: 310–17. https://doi.org/10.1039/b103844n.

157. Hemrika, W., Renirie, R., Dekker, H.L., Barnett, P. and Wever, R., 1997. “From Phosphatases to Vanadium Peroxidases: A Similar Architecture of the Active Site.” *Pnas* 94 (6): 2145–49. https://doi.org/10.1073/pnas.94.6.2145.

158. Hemrika, W., Renirie, R., Macedo-Ribeiro, S., Messerschmidt, A. and Wever, R., 1999. “Heterologous Expression of the from Curvularia Inaequalis in Saccharomyces Cerevisiae and Site-Directed Mutagenesis of the Active Site Residues His Heterologous Expression of the Vanadium-Containing Chloroperoxidase from Curvularia Inaequalis.” *The Journal of Biological*

159. Hersleth, H. P., Ryde, U., Rydberg, P., Görbitz, C. H., and Andersson, K. K. 2006. “Structures of the High-Valent Metal-Ion Haem-Oxygen Intermediates in

Peroxidases, Oxygenases and Catalases." *Journal of Inorganic Biochemistry* 100 (4): 460–76. https://doi.org/10.1016/j.jinorgbio.2006.01.018.

160. Hirao, H., Kumar, D. and Shaik, S., 2006. "On the Identity and Reactivity Patterns of the 'Second Oxidant' of the T252A Mutant of Cytochrome P450cam in the Oxidation of 5-Methylenenylcamphor." *Journal of Inorganic Biochemistry* 100 (12): 2054–68. https://doi.org/10.1016/j.jinorgbio.2006.09.001. 231

161. Hirao, H., Kumar, D., Que Jr, L. and Shaik, S., 2006. "Two-State Reactivity in Alkane Hydroxylation by Non-Heme Iron-Oxo Complexes." *Journal of the American Chemical Society* 128 (26): 8590–8606. https://doi.org/10.1021/ja061609o.

162. Hirao, H., Li, F., Que Jr, L. and Morokuma, K., 2011. "Theoretical Study of the Mechanism of Oxoiron (IV) Formation from H_2O_2 and a Nonheme Iron (II) Complex : O-O Cleavage Involving Proton-Coupled Electron Transfer." *Inorganic Chemistry* 50 (14): 6637–48.

163. Hoffman, B.M., 2003. "Electron-nuclear double resonance spectroscopy (and electron spin-echo envelope modulation spectroscopy) in bioinorganic chemistry." *Proceedings of the National Academy of Sciences, 100*(7): pp.3575-3578.

164. Hoffman, B.M., Lukoyanov, D., Dean, D.R. and Seefeldt, L.C., 2013. "Nitrogenase: A Draft Mechanism." *Accounts of Chemical Research* 46 (2): 587–95. https://doi.org/10.1021/ar300267m.

165. Hohenberg, P. and Kohn, W., 1964. "Inhomogeneous Electron Gas." *Physical Review* 136 (3B): B864–71. https://doi.org/10.1103/PhysRev.136.B864.

166. Hopmann, K.H., Ghosh, A. and Noodleman, L., 2009. "Density Functional Theory Calculations on Mössbauer Parameters of Nonheme Iron Nitrosyls." 48(19): 9155–65. https://doi.org/10.1021/ic9008784.

167. Hoppe, E., Limberg, C. and Ziemer, B., 2006. "Mono- and Dinuclear Oxovanadium(V)Calixarene Complexes and Their Activity as Oxidation Catalysts." *Inorganic Chemistry* 45 (20): 8308–17. https://doi.org/10.1021/ic061106j.

168. Horner, O., Jeandey, C., Oddou, J.L., Bonville, P., McKenzie, C.J. and Latour, J.M., 2002. "Hydrogenperoxo-[(bztpen)Fe(OOH)]$^{2+}$ and Its Deprotonation Product Peroxo-[(bztpen) Fe (O2)]$^{+}$, Studied by EPR and Mössbauer Spectroscopy− Implications for the Electronic Structures of Peroxo Model Complexes." *European Journal of Inorganic Chemistry*, 12: 3278-3283.

169. Hossain, M.K., Haukka, M., Lisensky, G.C., Lehtonen, A. and Nordlander, E., 2019. "Oxovanadium(V) Complexes with Tripodal Bisphenolate and Monophenolate Ligands: Syntheses, Structures and Catalytic Activities." *Inorganica Chimica Acta* 487: pp. 112–19. https://doi.org/10.1016/j.ica.2018.11.049.

170. Hsieh, C.H., Huang, X., Amaya, J.A., Rutland, C.D., Keys, C.L., Groves, J.T., Austin, R.N. and Makris, T.M., 2017. "The Enigmatic P450 Decarboxylase OleT Is Capable of, but Evolved to Frustrate, Oxygen Rebound Chemistry." *Biochemistry* 56 (26): 3347–57. https://doi.org/10.1021/acs.biochem.7b00338.

171. Hu, Y. and Ribbe, M.W., 2011. Historic overview of nitrogenase research. In *Nitrogen Fixation* (pp. 3-7). Humana Press.

172. Huang, X. and Groves, J.T., 2017. "Beyond Ferryl-Mediated Hydroxylation: 40 Years of the Rebound Mechanism and C–H Activation." *Journal of Biological Inorganic Chemistry* 22 (2–3): 185–207. https://doi.org/10.1007/s00775-016-1414-3.

173. Huang, X. and Groves, J.T., 2018. "Oxygen Activation and Radical Transformations in Heme Proteins and Metalloporphyrins." *Chemical Reviews* 118 (5): 2491–2553. https://doi.org/10.1021/acs.chemrev.7b00373.

174. Ikbal, S.A., Colomban, C., Zhang, D., Delecluse, M., Brotin, T., Dufaud, V., Dutasta, J.P., Sorokin, A.B. and Martinez, A., 2019. "Bioinspired Oxidation of Methane in the Confined Spaces of Molecular Cages." *Inorganic Chemistry* 58, (11): 7220-7228 .https://doi.org/10.1021/acs.inorgchem.9b00199.

175. Işci, Ü., Dumoulin, F., Sorokin, A.B. and Ahsen, V., 2014. "N-Bridged Dimers of Tetrapyrroles Complexed by Transition Metals: Syntheses, Characterization Methods, and Uses as Oxidation Catalysts." *Turkish Journal of Chemistry* 38 (6): 923–49. https://doi.org/10.3906/kim-1407-47.

176. Işci, Ü., Faponle, A.S., Afanasiev, P., Albrieux, F., Briois, V., Ahsen, V., Dumoulin, F., Sorokin, A.B. and de Visser, S.P., 2015. "Site-Selective Formation of an Iron(Iv)-Oxo Species at the More Electron-Rich Iron Atom of Heteroleptic μ-Nitrido Diiron Phthalocyanines." *Chemical Science* 6 (8): 5063–75. https://doi.org/10.1039/c5sc01811k.

177. Isupov, M.N., Dalby, A.R., Brindley, A.A., Izumi, Y., Tanabe, T., Murshudov, G.N. and Littlechild, J.A., 2000 "Crystal Structure of Dodecameric Vanadium-Dependent Bromoperoxidase from the Red Algae Corallina Officinalis." *Journal of Molecular Biology* 299 (4): 1035–49.

178. Jensen, F., 2007. Introduction to Computational Chemistry, Willey. *Chichester, UK*.

179. Jeschke, P., 2010. "The Unique Role of Halogen Substituents in the Design of Modern Agrochemicals." *Pest Management Science* 66 (1): 10–27. https://doi.org/10.1002/ps.1829.

180. Ji, L., Faponle, A.S., Quesne, M.G., Sainna, M.A., Zhang, J., Franke, A., Kumar, D., van Eldik, R., Liu, W. and de Visser, S.P., 2015. "Drug Metabolism by Cytochrome P450 Enzymes: What Distinguishes the Pathways Leading to Substrate Hydroxylation over Desaturation?" *Chemistry - A European Journal* 21 (25): 9083–92. https://doi.org/10.1002/chem.201500329.

181. Jiang, G., Zuo, R., Zhang, Y., Powell, M.M., Zhang, P., Hylton, S.M., Loria, R. and Ding, Y., 2018. "One-Pot Biocombinatorial Synthesis of Herbicidal Thaxtomins." *ACS Catalysis* 8 (11): 10761–68. https://doi.org/10.1021/acscatal.8b03317.

182. Kaczmarek, M.A., Malhotra, A., Balan, G.A., Timmins, A. and de Visser, S.P., 2018. "Nitrogen Reduction to Ammonia on a Biomimetic Mononuclear Iron Centre: Insights into the Nitrogenase Enzyme." *Chemistry–A European Journal* 24 (20): 5293–5302.

183. Kadish, K.M., Smith, K.M. and Guilard, R., 2013. Handbook of Porphyrin Science (Volumes 26–30): With Applications To Chemistry, Physics, Materials Science, Engineering, Biology And Medicine (Vol. 6). World Scientific.

184. Kaizer, J., Klinker, E.J., Oh, N.Y., Rohde, J.U., Song, W.J., Stubna, A., Kim, J., Münck, E., Nam, W. and Que, L., 2004. "Nonheme $Fe^{IV}O$ Complexes That Can Oxidize the C-H Bonds of Cyclohexane at Room Temperature." *Journal of the American Chemical Society* 126 (2): 472–73. https://doi.org/10.1021/ja037288n.

185. Kal, S. and Que, L., 2017. "Dioxygen Activation by Nonheme Iron Enzymes with the 2-His-1-Carboxylate Facial Triad That Generate High-Valent Oxoiron Oxidants." *Journal of Biological Inorganic Chemistry* 22 (2–3): 339–65. https://doi.org/10.1007/s00775-016-1431-2.

186. Kamachi, T. and Yoshizawa, K., 2003. "A Theoretical Study on the Mechanism of Camphor Hydroxylation by Compound I of Cytochrome P450." *Journal of the American Chemical Society* 125 (15): 4652–61. https://doi.org/10.1021/ja0208862.

187. Kamachi, T., Shiota, Y., Ohta, T. and Yoshizawa, K., 2003. "Does the Hydroperoxo Species of Cytochrome P450 Participate in Olefin Epoxidation with the Main Oxidant, Compound I? Criticism from Density Functional Theory Calculations." *Bulletin of the Chemical Society of Japan* 76 (4): 721–32.

188. Kandrashkin, Y.E., Asano, M.S. and van der Est, A., 2006. “Light-Induced Electron Spin Polarization in Vanadyl Octaethylporphyrin: II. Dynamics of the Excited States.” *Journal of Physical Chemistry A* 110 (31): 9617–26. https://doi.org/10.1021/jp062037x.

189. Kim, S.H., Perera, R., Hager, L.P., Dawson, J.H. and Hoffman, B.M., 2006. “Rapid Freeze-Quench ENDOR Study of Chloroperoxidase Compound I: The Site of the Radical.” *Journal of the American Chemical Society* 128 (17): 5598–99. https://doi.org/10.1021/ja060776l.

190. Kobayashi, K., Tamura, M., Hayashi, K., Hori, H. and Morimoto, H., 1980. “Electron Paramagnetic Resonance and Optical Absorption Spectrum of the Pentacoordinated Ferrihemoproteins.” *Journal of Biological Chemistry* 255 (6): 2239–42.

191. Kochi, J.K., 1992. “Inner-Sphere Electron Transfer in Organic Chemistry. Relevance to Electrophilic Aromatic Nitration.” *Accounts of Chemical Research* 25 (1): 39–47. https://doi.org/10.1021/ar00013a006.

192. Kohn, W. and Sham, L.J., 1965. “Self-Consistent Equations Including Exchange and Correlation Effects.” *Physical Review* 140(4A): A1133. https://doi.org/10.1103/PhysRev.140.A1133.

193. Kong, M., Wang, K., Dong, R. and Gao, H., 2015. “Enzyme Catalytic Nitration of Aromatic Compounds.” *Enzyme and Microbial Technology* 73–74: 34–43. https://doi.org/10.1016/j.enzmictec.2015.03.008.

194. Kramos, B. and Olah, J., 2014. “Enolization as an Alternative Proton Delivery Pathway in Human Aromatase (P450 19A1).” *Journal of Physical Chemistry B* 118 (2): 390–405. https://doi.org/10.1021/jp407365x.

195. Kravitz, J.Y. and Pecoraro, V.L., 2005. “Synthetic and Computational Modeling of the Vanadium-Dependent Haloperoxidases.” *Pure and Applied Chemistry* 77 (9): 1595–1605. https://doi.org/10.1351/pac200577091595. 234

196. Kryatov, S.V., Rybak-Akimova, E.V. and Schindler, S., 2005. “Kinetics and Mechanisms of Formation and Reactivity of Non-Heme Iron Oxygen Intermediates.” *Chemical Reviews* 105 (6): 2175–2226. https://doi.org/10.1021/cr030709z.

197. Kudrik, E.V., Afanasiev, P., Alvarez, L.X., Dubourdeaux, P., Clémancey, M., Latour, J.M., Blondin, G., Bouchu, D., Albrieux, F., Nefedov, S.E. and Sorokin, A.B., 2012. “An N-Bridged High-Valent Diiron-Oxo Species on a Porphyrin Platform That Can Oxidize Methane.” *Nature Chemistry* 4 (12): 1024–29. https://doi.org/10.1038/nchem.1471.

198. Kumar, D., de Visser, S.P. and Shaik, S., 2005. "Multistate Reactivity in Styrene Epoxidation by Compound I of Cytochrome P450: Mechanisms of Products and Side Products Formation." *Chemistry - A European Journal* 11 (9): 2825–35. https://doi.org/10.1002/chem.200401044.

199. Kumar, D., De Visser, S.P., Sharma, P.K., Hirao, H. and Shaik, S., 2005. "Sulfoxidation Mechanisms Catalyzed by Cytochrome P450 and Horseradish Peroxidase Models: Spin Selection Induced by the Ligand." *Biochemistry* 44 (22): 8148–58. https://doi.org/10.1021/bi050348c.

200. Kumar, D., Hirao, H., Que, L. and Shaik, S., 2005. "Theoretical Investigation of C-H Hydroxylation by (N4Py) $Fe^{IV}O^{2+}$: An Oxidant More Powerful than P450 ?" 127(22): 8026–27. https://doi.org/10.1021/ja0512428.

201. Kumar, D., Karamzadeh, B., Sastry, G.N. and de Visser, S.P., 2010. "What Factors Influence the Rate Constant of Substrate Epoxidation by Compound I of Cytochrome P450 and Analogous Iron(IV)-Oxo Oxidants?" *Journal of the American Chemical Society* 132 (22): 7656–67. https://doi.org/10.1021/ja9106176.

202. Kumar, D., Latifi, R., Kumar, S., Rybak-Akimova, E.V., Sainna, M.A. and de Visser, S.P., 2013. "Rationalization of the Barrier Height for p-Z-Styrene Epoxidation by Iron(IV)-Oxo Porphyrin Cation Radicals with Variable Axial Ligands" 52(14): 7968-7979. https://doi.org/10.1021/ic4005104.

203. Kumar, D., Sastry, G.N. and De Visser, S.P., 2011. "Effect of the Axial Ligand on Substrate Sulfoxidation Mediated by Iron (IV)–Oxo Porphyrin Cation Radical Oxidants." *Chemistry–A European Journal* 17 (22): 6196–6205. https://doi.org/10.1002/chem.201003187.

204. Kumar, D., Tahsini, L., de Visser, S.P., Kang, H.Y., Kim, S.J. and Nam, W., 2009. "Effect of Porphyrin Ligands on the Regioselective Dehydrogenation versus Epoxidation of Olefins by Oxoiron (IV) Mimics of Cytochrome P450 " *The Journal of Physical Chemistry A* 113(43):11713–22.

205. Kumar, R., Chaudhary, N., Sankar, M. and Maurya, M.R., 2015. "Electron Deficient Nonplanar β-Octachlorovanadylporphyrin as a Highly Efficient and Selective Epoxidation Catalyst for Olefins." *Dalton Transactions* 44 (40): 17720–29. https://doi.org/10.1039/c5dt02349a. 235

206. Kumar, S., Faponle, A.S., Barman, P., Vardhaman, A.K., Sastri, C.V., Kumar, D. and de Visser, S.P., 2014. "Long-Range Electron Transfer Triggers Mechanistic Differences between Iron(IV)-Oxo and Iron(IV)-Imido Oxidants." *Journal of the American Chemical Society* 136 (49): 17102–15. https://doi.org/10.1021/ja508403w.

207. Kundu, S., Miceli, E., Farquhar, E.R. and Ray, K., 2014. “Mechanism of Phenol Oxidation by Heterodinuclear Ni Cu Bis (μ-Oxo) Complexes Involving Nucleophilic Oxo Groups.” *Dalton Transactions* 43 (11): 4264–67.

208. Lai, W., Chen, H. and Shaik, S., 2009. “What Kinds of Ferryl Species Exist for Compound II of Chloroperoxidase? A Dialog of Theory with Experiment.” *Journal of Physical Chemistry B* 113 (22): 7912–17. https://doi.org/10.1021/jp902288q.

209. Lai, W., Chen, H., Cho, K.B. and Shaik, S., 2009. “Effects of Substrate, Protein Environment, and Proximal Ligand Mutation on Compound I and Compound 0 of Chloroperoxidase.” *Journal of Physical Chemistry A* 113 (43): 11763–71. https://doi.org/10.1021/jp902898s.

210. Lang, J., Maréchal, A., Couture, M. and Santolini, J., 2016. “Reaction Intermediates and Molecular Mechanism of Peroxynitrite Activation by NO Synthases.” *Biophysical Journal* 111 (10): 2099–2109. https://doi.org/10.1016/j.bpj.2016.05.056.

211. Langeslay, R.R., Kaphan, D.M., Marshall, C.L., Stair, P.C., Sattelberger, A.P. and Delferro, M., 2018. “Catalytic Applications of Vanadium: A Mechanistic Perspective.” Review-article. *Chemical Reviews* 119 (4): 2128–91. https://doi.org/10.1021/acs.chemrev.8b00245.

212. Lansky, D.E. and Goldberg, D.P., 2006. “Hydrogen Atom Abstraction by a High-Valent Manganese(V)-Oxo Corrolazine.” *Inorganic Chemistry* 45 (13): 5119–25. https://doi.org/10.1021/ic060491+.

213. Latham, J., Brandenburger, E., Shepherd, S.A., Menon, B.R. and Micklefield, J., 2018. “Development of Halogenase Enzymes for Use in Synthesis.” *Chemical Reviews* 118 (1): 232–69. https://doi.org/10.1021/acs.chemrev.7b00032.

214. Latifi, R., Bagherzadeh, M. and de Visser, S.P., 2009. “Origin of the Correlation of the Rate Constant of Substrate Hydroxylation by Nonheme Iron(IV)–Oxo Complexes with the Bond-Dissociation Energy of the C-H Bond of the Substrate,” 15(27) 6651–62. https://doi.org/10.1002/chem.200900211.

215. Latifi, R., Sainna, M.A., Rybak-Akimova, E.V. and de Visser, S.P., 2013. “Does Hydrogen-Bonding Donation to Manganese(IV)-Oxo and Iron(IV)-Oxo Oxidants Affect the Oxygen-Atom Transfer Ability? A Computational Study.” *Chemistry - A European Journal* 19 (12): 4058–68. https://doi.org/10.1002/chem.201202811.

216. Latifi, R., Valentine, J.S., Nam, W. and de Visser, S.P., 2012. “Predictive Studies of H-Atom Abstraction Reactions by an Iron(IV)-Oxo Corrole Cation Radical

Oxidant." *Chemical Communications* 48 (29): 3491–93. https://doi.org/10.1039/c2cc30365e.

217. Leach, A.R., 2001. *Molecular Modelling: Principles and Applications*. Pearson education.

218. Leblanc, C., Vilter, H., Fournier, J.B., Delage, L., Potin, P., Rebuffet, E., Michel, G., Solari, P.L., Feiters, M.C. and Czjzek, M., 2015. "Vanadium Haloperoxidases: From the Discovery 30 Years Ago to X-Ray Crystallographic and V K-Edge Absorption Spectroscopic Studies." *Coordination Chemistry Reviews* 301–302: 134–46. https://doi.org/10.1016/j.ccr.2015.02.013.

219. Lee, C., Yang, W. and Parr, R.G., 1988. "Development of the Colle-Salvetti Correlation-Energy Formula into a Functional of the Electron Density." *Physical Review B* 37 (2): 785–89. https://doi.org/10.1103/PhysRevB.37.785.

220. Lee, J.Y., Peterson, R.L., Ohkubo, K., Garcia-Bosch, I., Himes, R.A., Woertink, J., Moore, C.D., Solomon, E.I., Fukuzumi, S. and Karlin, K.D., 2014.. "Mechanistic Insights into the Oxidation of Substituted Phenols via Hydrogen Atom Abstraction by a Cupric-Superoxo Complex." *Journal of the American Chemical Society* 136 (28): 9925–37. https://doi.org/10.1021/ja503105b.

221. Lee, N.Y., Mandal, D., Bae, S.H., Seo, M.S., Lee, Y.M., Shaik, S., Cho, K.B. and Nam, W., 2017. "Structure and Spin State of Nonheme FeIVO Complexes Depending on Temperature: Predictive Insights from DFT Calculations and Experiments." *Chemical Science* 8 (8): 5460–67. https://doi.org/10.1039/c7sc01738c.

222. Lewars, E.G., 2016. "An Outline of What Computational Chemistry Is All About." Springer.

223. Li, F., England, J. and Que Jr, L., 2010. "Near-Stoichiometric Conversion of H_2O_2 to $Fe^{IV}O$ at a Nonheme Iron(II) Center . Insights into the O-O Bond Cleavage Step." *Biochemistry*, no. 132(7) 2134–35. https://doi.org/10.1021/bi901772w.

224. Li, H.B., Tian, S.X. and Yang, J., 2008. "Theoretical Study of the Stepwise Protonation of the Dioxo Manganese(V) Porphyrin." *Journal of Physical Chemistry B* 112 (49): 15807–12. https://doi.org/10.1021/jp808443n.

225. Li, X.X., Postils, V., Sun, W., Faponle, A.S., Solà, M., Wang, Y., Nam, W. and de Visser, S.P., 2017. "Reactivity Patterns of (Protonated) Compound II and Compound I of Cytochrome P450: Which Is the Better Oxidant?" *Chemistry - A European Journal* 23 (26): 6406–18. https://doi.org/10.1002/chem.201700363.

226. Lias, S.G., 2005. "Ionization Energy Evaluation. NIST Chemistry WebBook, NIST Standard Reference Database 69. online: http. webbok. nist. gov.

227. Licini, G., Conte, V., Coletti, A., Mba, M. and Zonta, C., 2011. 2011. “Recent Advances in Vanadium Catalyzed Oxygen Transfer Reactions.” *Coordination Chemistry Reviews* 255 (19–20): 2345–57. https://doi.org/10.1016/j.ccr.2011.05.004.

228. Ligtenbarg, A.G., Hage, R. and Feringa, B.L., 2003. “Catalytic Oxidations by Vanadium Complexes.” *Coordination Chemistry Reviews* 237 (1–2): 89–101. https://doi.org/10.1016/S0010-8545(02)00308-9.

229. Lin, H.L., Kenaan, C., Zhang, H. and Hollenberg, P.F., 2012.. “Reaction of Human Cytochrome P450 3A4 with Peroxynitrite: Nitrotyrosine Formation on the Proximal Side Impairs Its Interaction with NADPH-Cytochrome P450 Reductase.” *Chemical Research in Toxicology* 25 (12): 2642–53. https://doi.org/10.1021/tx3002753.

230. Littlechild, J., Garcia-Rodriguez, E., Dalby, A. and Isupov, M., 2002. “Structural and Functional Comparisons between Vanadium Haloperoxidase and Acid Phosphatase Enzymes.” *Journal of Molecular Recognition* 15 (5): 291–96. https://doi.org/10.1002/jmr.590.

231. Liu, T.N.E., M'Timkulu, T., Geigert, J., Wolf, B., Neidleman, S.L., Silva, D. and Hunter-Cevera, J.C., 1987. “Isolation and Characterization of a Novel Nonhepe Chloroperoxidase” *Biochemical and biophysical Research Communications* 142(2): 329-333.

232. Liu, Y., Wang, C., Yan, J., Zhang, W., Guan, W., Lu, X. and Li, S., 2014. “Hydrogen Peroxide-Independent Production of α-Alkenes by $OleT_{JE}$ P450 Fatty Acid Decarboxylase.” *Biotechnology for Biofuels* 7 (1): 1–12. https://doi.org/10.1186/1754-6834-7-28.

233. Lucarini, M., Pedrielli, P., Pedulli, G.F., Cabiddu, S. and Fattuoni, C., 1996. “Bond Dissociation Energies of O-H Bonds in Substituted Phenols from Equilibration Studies.” *Journal of Organic Chemistry* 61 (26): 9259–63. https://doi.org/10.1021/jo961039i.

234. Lundberg, M. and Borowski, T., 2013. “Oxoferryl Species in Mononuclear Non-Heme Iron Enzymes : Biosynthesis , Properties and Reactivity from a Theoretical Perspective.” *Coordination Chemistry Reviews* 257 (1): 277–89. https://doi.org/10.1016/j.ccr.2012.03.047.

235. Macedo-Ribeiro, S., Hemrika, W., Renirie, R., Wever, R. and Messerschmidt, A., 1999 “X-Ray Crystal Structures of Active Site Mutants of the Vanadium-Containing Chloroperoxidase from the Fungus Curvularia Inaequalis.” *Journal of Biological Inorganic Chemistry* 4 (2): 209–19.

236. Makris, T.M., von Koenig, K., Schlichting, I. and Sligar, S.G., 2006. "The Status of High-Valent Metal Oxo Complexes in the P450 Cytochromes." *Journal of Inorganic Biochemistry* 100 (4): 507–18. https://doi.org/10.1016/j.jinorgbio.2006.01.025. 238

237. Man, W.L., Xie, J., Pan, Y., Lam, W.W., Kwong, H.K., Ip, K.W., Yiu, S.M., Lau, K.C. and Lau, T.C., 2013 "C-N Bond Cleavage of Anilines by a (Salen)Ruthenium(VI) Nitrido Complex." *Journal of the American Chemical Society* 135 (15): 5533–36. https://doi.org/10.1021/ja401553d.

238. Manna, P. R., D. Molehin, and A. U. Ahmed. 2016. Dysregulation of Aromatase in Breast, Endometrial, and Ovarian Cancers: An Overview of Therapeutic Strategies. *Progress in Molecular Biology and Translational Science*. 144: 487-537. https://doi.org/10.1016/bs.pmbts.2016.10.002.

239. Manoj, K.M. and Hager, L.P., 2008. "Chloroperoxidase, a Janus Enzyme." *Biochemistry* 47 (9): 2997–3003. https://doi.org/10.1021/bi7022656.

240. Marcus, R.A. and Sutin, N., 1985. "Electron Transfers in Chemistry and Biology." *Biochimica et Biophysica Acta (BBA)-Reviews on Bioenergetics* 811 (3): 265–322.

241. Martinez, J.S., Carroll, G.L., Tschirret-Guth, R.A., Altenhoff, G., Little, R.D. and Butler, A., 2001. "On the Regiospecificity of Vanadium Bromoperoxidase." *Journal of the American Chemical Society* 123 (14): 3289–94. https://doi.org/10.1021/ja004176c.

242. Martinho, M., Banse, F., Bartoli, J.F., Mattioli, T.A., Battioni, P., Horner, O., Bourcier, S. and Girerd, J.J., 2005. "New Example of a Non-Heme Mononuclear Iron(IV) Oxo Complex. Spectroscopic Data and Oxidation Activity." *Inorganic Chemistry* 44 (25): 9592–96. https://doi.org/10.1021/ic051213y.

243. Martinho, M., Dorlet, P., Rivière, E., Thibon, A., Ribal, C., Banse, F. and Girerd, J.J., 2008. "Preparation and Characterization of a Microcrystalline Non-Heme Fe^{III}(OOH) Complex Powder: EPR Reinvestigation of Fe^{III}(OOH) Complexes-Improvement of the Perturbation Equations for the g Tensor of Low-Spin Fe^{III}." *Chemistry - A European Journal* 14 (10): 3182–88. https://doi.org/10.1002/chem.200701592.

244. Massie, A.A., Sinha, A., Parham, J.D., Nordlander, E. and Jackson, T.A., 2018. "Relationship between Hydrogen-Atom Transfer Driving Force and Reaction Rates for an Oxomanganese(IV) Adduct." Research-article. *Inorganic Chemistry* 57 (14): 8253–63. https://doi.org/10.1021/acs.inorgchem.8b00852.

245. Matthews, M.L., Chang, W.C., Layne, A.P., Miles, L.A., Krebs, C. and Bollinger Jr, J.M., 2014. "Direct Nitration and Azidation of Aliphatic Carbons by an

Iron-Dependent Halogenase." *Nature Chemical Biology* 10 (3): 209–15. https://doi.org/10.1038/nchembio.1438.

246. Mayer, J.M., 2004. "Proton-Coupled Electron Transfer: A Reaction Chemist's View." *Annual Review of Physical Chemistry* 55: 363–90.

247. McDonald, A.R. and Que Jr, L., 2013. "High-Valent Nonheme Iron-Oxo Complexes: Synthesis, Structure, and Spectroscopy." *Coordination Chemistry Reviews* 257 (2): 414–28. https://doi.org/10.1016/j.ccr.2012.08.002. 239

248. McKenna, C.E., Benemann, J.R. and Traylor, T.G., 1970. "A Vanadium Containing Nitrogenase Preparation: Implications for the Role of Molybdenum in Nitrogen Fixation." *Biochemical and Biophysical Research Communications* 41 (6): 1501–8. https://doi.org/10.1016/0006-291X(70)90557-7.

249. McLauchlan, C.C., Murakami, H.A., Wallace, C.A. and Crans, D.C., 2018. "Coordination Environment Changes of the Vanadium in Vanadium-Dependent Haloperoxidase Enzymes." *Journal of Inorganic Biochemistry* 186 (June): 267–79. https://doi.org/10.1016/j.jinorgbio.2018.06.011.

250. Messerschmidt, A. and Wever, R., 1996. "X-Ray Structure of a Vanadium-Containing Enzyme: Chloroperoxidase from the Fungus Curvularia Inaequalis." *Proceedings of the National Academy of Sciences* 93 (1): 392–96.

251. Messerschmidt, A., Prade, L. and Wever, R., 1997. "Implications for the Catalytic Mechanism of the Vanadium-Containing Enzyme Chloroperoxidase from the Fungus Curvularia Inaequalis by X-Ray Structures of the Native and Peroxide Form." *Biological Chemistry* 378 (3–4): 309–15. https://doi.org/10.1515/bchm.1997.378.3-4.309.

252. Meunier, B., de Visser, S.P. and Shaik, S., 2004. "Mechanism of Oxidation Reactions Catalyzed by Cytochrome P450 Enzymes." *Chemical Reviews* 104 (9): 3947–80. https://doi.org/10.1021/cr020443g.

253. Mialane, P., Nivorojkine, A., Pratviel, G., Azema, L., Slany, M., Godde, F., Simaan, A., Banse, F., Kargar-Grisel, T., Bouchoux, G. and Sainton, J., 1999. "Structures of Fe(II) Complexes with N,N,N′-Tris(2-Pyridylmethyl)Ethane-1,2-Diamine Type Ligands. Bleomycin-like DNA Cleavage and Enhancement by an Alkylammonium Substituent on the N′ Atom of the Ligand." *Inorganic Chemistry* 38 (6): 1085–92. https://doi.org/10.1021/ic971059i.

254. Mihara, N., Yamada, Y., Takaya, H., Kitagawa, Y., Igawa, K., Tomooka, K., Fujii, H. and Tanaka, K., 2019. "Site-Selective Supramolecular Complexation Activates Catalytic Ethane Oxidation by a Nitrido-Bridged Iron Porphyrinoid Dimer."

Chemistry - A European Journal 25 (13): 3369–75. https://doi.org/10.1002/chem.201805580.

255. Mihaylov, T., Parac-Vogt, T. and Pierloot, K., 2012. "Unraveling the Mechanisms of Carboxyl Ester Bond Hydrolysis Catalyzed by a Vanadate Anion." *Inorganic Chemistry* 51 (18): 9619–28. https://doi.org/10.1021/ic300620b.

256. Minenkov, Y., Occhipinti, G. and Jensen, V.R., 2009. "Metal-Phosphine Bond Strengths of the Transition Metals: A Challenge for DFT." *The Journal of Physical Chemistry A*, 11833–44. https://doi.org/10.1021/jp902940c.

257. Mishra, G.S. and Kumar, A., 2002. "Preparation of Heterogeneous Vanadium (VO^{2+}) Catalyst for Selective Hydroxylation of Cyclohexane by Molecular Oxygen." *Catalysis Letters* 81 (1–2): 113–17. https://doi.org/10.1023/A:1016076526549.

258. Mittra, K. and Green, M.T., 2019. "Reduction Potentials of P450 Compounds I and II: Insight into the Thermodynamics of C-H Bond Activation." Research-article. *Journal of the American Chemical Society* 141 (13): 5504–10. https://doi.org/10.1021/jacs.9b00242.

259. Morozov, A. and Chatfield, D., 2016. "How the Proximal Pocket May Influence the Enantiospecificities of Chloroperoxidase-Catalyzed Epoxidations of Olefins." *International Journal of Molecular Sciences* 17 (8). https://doi.org/10.3390/ijms17081297.

260. Morris, D.R. and Hager, L.P., 1966. "Chloroperoxidase I. Isolation and Properties of the Crystalline Glycoprotein." *Journal of Biological Chemistry* 241 (8): 1763–68.

261. Mubarak, M.Q.E. and de Visser, S.P., 2019a. "Reactivity Patterns of Vanadium(IV/V)-Oxo Complexes with Olefins in the Presence of Peroxides: A Computational Study." *Dalton Transactions* 48 (45): 16899–910. https://doi.org/10.1039/c9dt03048d.

262. Mubarak, M.Q.E. and de Visser, S.P., 2019b. "Second-Coordination Sphere Effect on the Reactivity of Vanadium-Peroxo Complexes: A Computational Study." Research-article. *Inorganic Chemistry* 58: 15741–50. https://doi.org/10.1021/acs.inorgchem.9b01778.

263. Mueller, M.P., 2007. *Fundamentals of quantum chemistry: molecular spectroscopy and modern electronic structure computations*. Springer Science & Business Media.

264. Mukherjee, G., Alili, A., Barman, P., Kumar, D., Sastri, C.V. and de Visser, S.P., 2019. "Interplay Between Steric and Electronic Effects: A Joint Spectroscopy and

Computational Study of Nonheme Iron(IV)-Oxo Complexes." *Chemistry - A European Journal* 25 (19): 5086–98. https://doi.org/10.1002/chem.201806430.

265. Nagata, K., Liberato, D.J., Gillette, J.R. and Sasame, H.A., 1986. "An Unusual Metabolite of Testosterone. 17 Beta-Hydroxy-4, 6-Androstadiene-3-One." *Drug Metabolism and Disposition* 14 (5): 559–65.

266. Nam, W., 2007. "High-Valent Iron(IV)-Oxo Complexes of Heme and Non-Heme Ligands in Oxygenation Reactions." *Accounts of Chemical Research* 40 (7): 522–31. https://doi.org/10.1021/ar700027f.

267. Nam, W., Lee, Y.M. and Fukuzumi, S., 2014. "Tuning Reactivity and Mechanism in Oxidation Reactions by Mononuclear Nonheme Iron(IV)-Oxo Complexes." *Accounts of Chemical Research* 47 (4): 1146–54. https://doi.org/10.1021/ar400258p.

268. Neu, H.M., Yang, T., Baglia, R.A., Yosca, T.H., Green, M.T., Quesne, M.G., de Visser, S.P. and Goldberg, D.P., 2014. "Oxygen-Atom Transfer Reactivity of Axially Ligated Mn(V)-Oxo Complexes: Evidence for Enhanced Electrophilic and Nucleophilic Pathways." *Journal of the American Chemical Society* 136 (39): 13845–52. https://doi.org/10.1021/ja507177h.

269. Nicholls, P., Fita, I. and Loewen, P.C., 2000. Enzymology and structure of catalases.

270. Njuma, O.J., Ndontsa, E.N. and Goodwin, D.C., 2014. "Catalase in Peroxidase Clothing: Interdependent Cooperation of Two Cofactors in the Catalytic Versatility of KatG." *Archives of Biochemistry and Biophysics* 544: 27–39. https://doi.org/10.1016/j.abb.2013.11.007.

271. Ogliaro, F., Cohen, S., de Visser, S.P. and Shaik, S., 2000. "Medium Polarization and Hydrogen Bonding Effects on Compound I of Cytochrome P450: What Kind of a Radical Is It Really?" *Journal of the American Chemical Society* 122 (51): 12892–93. https://doi.org/10.1021/ja005619f.

272. Ogliaro, F., Cohen, S., de Visser, S.P. and Shaik, S.. 2002. "The 'Push'Effect of the Thiolate Ligand in Cytochrome P450: A Theoretical Gauging." *Journal of Inorganic Biochemistry* 91 (4): 554–67.

273. Ogliaro, F., de Visser, S.P., Cohen, S., Kaneti, J. and Shaik, S., 2001. "The Experimentally Elusive Oxidant of Cytochrome P450 : A Theoretical 'Trapping' Defining More Closely the 'Real' Species," C*hemBioChem*, 2(11):848-851. https://doi.org/10.1002/1439-7633(20011105)2:11<848::AID-CBIC848>3.0.CO;2-0.

274. Ogliaro, F., de Visser, S.P., Cohen, S., Sharma, P.K. and Shaik, S., 2002. "Searching for the Second Oxidant in the Catalytic Cycle of Cytochrome P450: A Theoretical Investigation of the Iron(III)-Hydroperoxo Species and Its Epoxidation Pathways." *Journal of the American Chemical Society* 124 (11): 2806–17. https://doi.org/10.1021/ja0171963.

275. Ohgo, Y., Chiba, Y., Hashizume, D., Uekusa, H., Ozeki, T. and Nakamura, M., 2006. "Novel Spin Transition between S= 5/2 and S= 3/2 in Highly Saddled Iron (III) Porphyrin Complexes at Extremely Low Temperatures." *Chemical Communications*, no. 18: 1935–37.

276. Olivo, G., Cussó, O., Borrell, M. and Costas, M., 2017. "Oxidation of Alkane and Alkene Moieties with Biologically Inspired Nonheme Iron Catalysts and Hydrogen Peroxide: From Free Radicals to Stereoselective Transformations." *Journal of Biological Inorganic Chemistry* 22 (2–3): 425–52. https://doi.org/10.1007/s00775-016-1434-z.

277. Ortiz de Montellano, P.R., 2009. "Hydrocarbon Hydroxylation by Cytochrome P450 Enzymes." *Chemical Reviews* 110 (2): 932–48. https://doi.org/10.1021/cr9002193.

278. Pacios, L.F. and Gálvez, O., 2010. "Active Site, Catalytic Cycle, and Iodination Reactions of Vanadium Iodoperoxidase: A Computational Study." *Journal of Chemical Theory and Computation* 6 (5): 1738–52. https://doi.org/10.1021/ct100041x.

279. Padamati, S.K., Draksharapu, A., Unjaroen, D. and Browne, W.R., 2016. "Conflicting Role of Water in the Activation of H_2O_2 and the Formation and Reactivity of Non-Heme Fe^{III}-OOH and Fe^{III}-O-Fe^{III} Complexes at Room Temperature." *Inorganic Chemistry* 55 (9): 4211–22. https://doi.org/10.1021/acs.inorgchem.5b02976.

280. Palcic, M.M., Rutter, R., Araiso, T., Hager, L.P. and Dunford, H.B., 1980. "Spectrum of Chloroperoxidase Compound I." *Biochemical and Biophysical Research Communications* 94 (4): 1123–27. https://doi.org/10.1016/0006-291X(80)90535-5.

281. Pan, Z., Zhang, R., Fung, L.W.M. and Newcomb, M., 2007. 2007. "Photochemical Production of a Highly Reactive Porphyrin-Iron-Oxo Species." *Inorganic Chemistry* 46 (5): 1517–19. https://doi.org/10.1021/ic061972w.

282. Pattanayak, S., Cantú, F.R., Rana, A. and Gupta, S.S., 2019. "The Equatorial Ligand Effect on the Properties and Reactivity of Iron(V) Oxo Intermediates." *Chemistry - A European Journal* 25 (34): 8092–8104. https://doi.org/10.1002/chem.201900708.

283. Peck, S.C. and van der Donk, W.A., 2017. "Go It Alone: Four-Electron Oxidations by Mononuclear Non-Heme Iron Enzymes." *Journal of Biological Inorganic Chemistry* 22 (2–3): 381–94. https://doi.org/10.1007/s00775-016-1399-y.

284. Perdew, J.P., 1986. "Density-Functional Approximation for the Correlation Energy of the Inhomogeneous Electron Gas." *Physical Review B* 33 (12): 8822.

285. Perdew, J.P., Burke, K. and Ernzerhof, M., 1996. "Generalized Gradient Approximation Made Simple." *Physical Review Letters* 77 (18): 3865–68. https://doi.org/10.1103/PhysRevLett.77.3865.

286. Perdew, J.P., Ruzsinszky, A., Tao, J., Staroverov, V.N., Scuseria, G.E. and Csonka, G.I., 2005. "Prescription for the Design and Selection of Density Functional Approximations: More Constraint Satisfaction with Fewer Fits." *Journal of Chemical Physics* 123 (6). https://doi.org/10.1063/1.1904565.

287. Pessoa, J.C., Garribba, E., Santos, M.F. and Santos-Silva, T., 2015. "Vanadium and Proteins: Uptake, Transport, Structure, Activity and Function." *Coordination Chemistry Reviews* 301–302: 49–86. https://doi.org/10.1016/j.ccr.2015.03.016.

288. Phung, Q.M. and Pierloot, K., 2019. "Electronic Structure of N-Bridged High-Valent Diiron-Oxo." *Chemistry–A European Journal* 25(54) :12491-96.

289. Pickl, M., Kurakin, S., Cantú Reinhard, F.G., Schmid, P., Pöcheim, A., Winkler, C.K., Kroutil, W., de Visser, S.P. and Faber, K., 2018. "Mechanistic Studies of Fatty Acid Activation by CYP152 Peroxygenases Reveal Unexpected Desaturase Activity." *ACS Catalysis* 9 (1): 565–77. https://doi.org/10.1021/acscatal.8b03733.

290. Plat, H., Krenn, B.E. and Wever, R., 1987. "The Bromoperoxidase from the Lichen Xanthoria Parietina Is a Novel Vanadium Enzyme." *Biochemical Journal* 248 (1): 277–79.

291. Porro, C.S., Sutcliffe, M.J. and de Visser, S.P., 2009. "Quantum Mechanics/Molecular Mechanics Studies on the Sulfoxidation of Dimethyl Sulfide by Compound I and Compound 0 of Cytochrome P450: Which Is the Better Oxidant." *Journal of Physical Chemistry A* 113 (43): 11635–42. https://doi.org/10.1021/jp9023926.

292. Postils, V., Saint-André, M., Timmins, A., Li, X.X., Wang, Y., Luis, J., Solà, M. and de Visser, S., 2018. "Quantum Mechanics/Molecular Mechanics Studies on the Relative Reactivities of Compound I and II in Cytochrome P450 Enzymes." *International Journal of Molecular Sciences* 19 (7): 1–20. https://doi.org/10.3390/ijms19071974.

293. Poulos, T.L., 1996. “The Role of the Proximal Ligand in Heme Enzymes.” *Journal of Biological Inorganic Chemistry* 1 (4): 356–59.

294. Poulos, T.L., 2014. “Heme Enzyme Structure and Function.” *Chemical Reviews* 114 (7): 3919–62. https://doi.org/10.1021/cr400415k.

295. Qian, K., Fredriksen, T.R., Mennito, A.S., Zhang, Y., Harper, M.R., Merchant, S., Kushnerick, J.D., Rytting, B.M. and Kilpatrick, P.K., 2019. “Evidence of Naturally-Occurring Vanadyl Porphyrins Containing Multiple S and O Atoms.” *Fuel* 239 (November 2018): 1258–64. https://doi.org/10.1016/j.fuel.2018.09.115.

296. Quesne, M.G., Borowski, T. and de Visser, S.P., 2016. “Quantum Mechanics/Molecular Mechanics Modeling of Enzymatic Processes: Caveats and Breakthroughs.” *Chemistry - A European Journal* 22 (8): 2562–81. https://doi.org/10.1002/chem.201503802.

297. Quesne, M.G., Senthilnathan, D., Singh, D., Kumar, D., Maldivi, P., Sorokin, A.B. and de Visser, S.P., 2016. “Origin of the Enhanced Reactivity of ??-Nitrido-Bridged Diiron(IV)-Oxo Porphyrinoid Complexes over Cytochrome P450 Compound I.” *ACS Catalysis* 6 (4): 2230–43. https://doi.org/10.1021/acscatal.5b02720.

298. Radon, M., Broclawik, E. and Pierloot, K., 2011. “DFT and Ab Initio Study of Iron-Oxo Porphyrins: May They Have a Low-Lying Iron(V)-Oxo Electromer?” *Journal of Chemical Theory and Computation* 7 (4): 898–908. https://doi.org/10.1021/ct1006168.

299. Ramezanian, M.S., Padmaja, S. and Koppenol, W.H., 1996. “Nitration and Hydroxylation of Phenolic Compounds by Peroxynitrite.” *Chemical Research in Toxicology* 9 (1): 232–40. https://doi.org/10.1021/tx950135w. 244

300. Raven, E.L., 2003. “Understanding Functional Diversity and Substrate Specificity in Haem Peroxidases: What Can We Learn from Ascorbate Peroxidase?” *Natural Product Reports* 20 (4): 367–81.

301. Rehder, D., 1999. “The Coordination Chemistry of Vanadium as Related to Its Biological Functions.” *Coordination Chemistry Reviews* 182: 297–322. https://doi.org/10.1016/S0010-8545(98)00194-5.

302. Rehder, D., 2013. “Vanadium. Its Role for Humans.” In *Metal Ions in Life Sciences*, edited by Astrid Sigel, Helmut Sigel, and Roland K.O. Sigel, 13:139–69. Metal Ions in Life Sciences. Dordrecht: Springer Netherlands. https://doi.org/10.1007/978-94-007-7500-8_5.

303. Rehder, D., 2015. “The Role of Vanadium in Biology.” *Metallomics* 7: 730–42. https://doi.org/10.1039/C4MT00304G.

304. Rettie, A.E., Boberg, M., Rettenmeier, A.W. and Baillie, T.A., 1988. “Cytochrome P-450-Catalyzed Desaturation of Valproic Acid in Vitro. Species Differences, Induction Effects, and Mechanistic Studies.” *Journal of Biological Chemistry* 263 (27): 13733–38.

305. Rettie, A.E., Rettenmeier, A.W., Howald, W.N. and Baillie, T.A., 1987. “Cytochrome P-450--Catalyzed Formation of Delta 4-VPA, a Toxic Metabolite of Valproic Acid.” *Science* 235 (4791): 890–93.

306. Rettie, A.E., Sheffels, P.R., Korzekwa, K.R., Gonzalez, F.J., Philpot, R.M. and Baillie, T.A., 1995. “CYP4 Isoenzyme Specificity and the Relationship between. Omega.-Hydroxylation and Terminal Desaturation of Valproic Acid.” *Biochemistry* 34 (24): 7889–95.

307. Rittle, J. and Green, M.T., 2010. “Cytochrome P450 Compound I: Capture, Characterization, and C-H Bond Activation Kinetics.” *Science* 330 (6006): 933–37. https://doi.org/10.1126/science.1193478.

308. Roelfes, G., Vrajmasu, V., Chen, K., Ho, R.Y., Rohde, J.U., Zondervan, C., la Crois, R.M., Schudde, E.P., Lutz, M., Spek, A.L. and Hage, R., 2003. “End-on and Side-on Peroxo Derivatives of Non-Heme Iron Complexes with Pentadentate Ligands: Models for Putative Intermediates in Biological Iron/Dioxygen Chemistry.” *Inorganic Chemistry* 42 (8): 2639–53. https://doi.org/10.1021/ic034065p.

309. Rohde, J.U., In, J.H., Lim, M.H., Brennessel, W.W., Bukowski, M.R., Stubna, A., Münck, E., Nam, W. and Que, L., 2003. “Crystallographic and Spectroscopic Characterization of a Nonheme Fe(IV)=O Complex.” *Science* 299 (5609): 1037–39. https://doi.org/10.1126/science.299.5609.1037. 245

310. Rude, M.A., Baron, T.S., Brubaker, S., Alibhai, M., Del Cardayre, S.B. and Schirmer, A., 2011. “Terminal Olefin (1-Alkene) Biosynthesis by a Novel P450 Fatty Acid Decarboxylase from Jeotgalicoccus Species.” *Applied and Environmental Microbiology* 77 (5): 1718–27. https://doi.org/10.1128/AEM.02580-10.

311. Rydberg, P., Sigfridsson, E. and Ryde, U., 2004. “On the Role of the Axial Ligand in Heme Proteins: A Theoretical Study.” *Journal of Biological Inorganic Chemistry* 9 (2): 203–23. https://doi.org/10.1007/s00775-003-0515-y.

312. Sacramento, J.J.D. and Goldberg, D.P., 2018. “Factors Affecting Hydrogen Atom Transfer Reactivity of Metal-Oxo Porphyrinoid Complexes.” Research-article. *Accounts of Chemical Research* 51 (11): 2641–52. https://doi.org/10.1021/acs.accounts.8b00414.

313. Sahu, S. and Goldberg, D.P., 2016. “Activation of Dioxygen by Iron and Manganese Complexes: A Heme and Nonheme Perspective.” *Journal of the American Chemical Society* 138 (36): 11410–28.

314. Sainna, M.A., Kumar, S., Kumar, D., Fornarini, S., Crestoni, M.E. and de Visser, S.P., 2015 “A Comprehensive Test Set of Epoxidation Rate Constants for Iron(IV)-Oxo Porphyrin Cation Radical Complexes.” *Chemical Science* 6 (2): 1516–29. https://doi.org/10.1039/c4sc02717e.

315. Sainna, M.A., Sil, D., Sahoo, D., Martin, B., Rath, S.P., Comba, P. and de Visser, S.P., 2015. “Spin-State Ordering in Hydroxo-Bridged Diiron(III)Bisporphyrin Complexes.” *Inorganic Chemistry* 54 (4): 1919–30. https://doi.org/10.1021/ic502803b.

316. Salcedo, R., Martínez, L.M.R. and Martınez-Magadán, J.M., 2001. “Theoretical Study of High-Valent Vanadium Oxo-Porphyrins as a Dopant of Crude Oil.” *Journal of Molecular Structure: THEOCHEM* 542 (1–3): 115–21. https://doi.org/10.1016/S0166-1280(00)00825-3.

317. Salonen, P., Peuronen, A. and Lehtonen, A., 2017. “Oxidovanadium(V) Amine Bisphenolates as Epoxidation, Sulfoxidation and Catechol Oxidation Catalysts.” *Inorganic Chemistry Communications* 86: 165–67. https://doi.org/10.1016/j.inoche.2017.10.017.

318. Sanna, D., Pecoraro, V.L., Micera, G. and Garribba, E., 2012. “Application of DFT Methods to the Study of the Coordination Environment of the VO^{2+} Ion in V Proteins.” *Journal of Biological Inorganic Chemistry* 17 (5): 773–90. https://doi.org/10.1007/s00775-012-0895-y.

319. Santoro, S., Kalek, M., Huang, G. and Himo, F., 2016. “Elucidation of Mechanisms and Selectivities of Metal-Catalyzed Reactions Using Quantum Chemical Methodology.” *Accounts of Chemical Research* 49 (5): 1006–18. https://doi.org/10.1021/acs.accounts.6b00050.

320. Sastri, C.V., Lee, J., Oh, K., Lee, Y.J., Lee, J., Jackson, T.A., Ray, K., Hirao, H., Shin, W., Halfen, J.A. and Kim, J., 2007. “Axial Ligand Tuning of a Nonheme Iron(IV)-Oxo Unit for Hydrogen Atom Abstraction.” *Proceedings of the National Academy of Sciences of the United States of America* 104 (49): 19181–86. https://doi.org/10.1073/pnas.0709471104.

321. Schneider, C.J., Zampella, G., Greco, C., Pecoraro, V.L. and De Gioia, L., 2007. “Mechanistic Analysis of Nucleophilic Substrates Oxidation by Functional Models of Vanadium-Dependent Haloperoxidases: A Density Functional Theory Study.” *European Journal of Inorganic Chemistry*, no. 4: 515–23. https://doi.org/10.1002/ejic.200600739.

322. Schöneboom, J.C., Lin, H., Reuter, N., Thiel, W., Cohen, S., Ogliaro, F. and Shaik, S., 2002. "The Elusive Oxidant Species of Cytochrome P450 Enzymes: Characterization by Combined Quantum Mechanical/Molecular Mechanical (QM/MM) Calculations." *Journal of the American Chemical Society* 124 (27): 8142–51. https://doi.org/10.1021/ja026279w.

323. Schopfer, F.J., Baker, P.R. and Freeman, B.A., 2003. "NO-Dependent Protein Nitration: A Cell Signaling Event or an Oxidative Inflammatory Response?" *Trends in Biochemical Sciences* 28 (12): 646–54. https://doi.org/10.1016/j.tibs.2003.10.006.

324. Schrödinger, E., 1926. "An Undulatory Theory of the Mechanics of Atoms and Molecules." *Physical Review* 28 (6): 1049.

325. Schulz, C.E., Rutter, R., Sage, J.T., Debrunner, P.G. and Hager, L.P., 1984. "Mössbauer and Electron Paramagnetic Resonance Studies of Horseradish Peroxidase and Its Catalytic Intermediates." *Biochemistry* 23 (20): 4743–54.

326. Schweitzer, A., Gutmann, T., Wächtler, M., Breitzke, H., Buchholz, A., Plass, W. and Buntkowsky, G., 2008. "^{51}V Solid-State NMR Investigations and DFT Studies of Model Compounds for Vanadium Haloperoxidases." *Solid State Nuclear Magnetic Resonance* 34 (1–2): 52–67. https://doi.org/10.1016/j.ssnmr.2008.02.003.

327. Schwendt, P., Tatiersky, J., Krivosudský, L. and Šimuneková, M., 2016. "Peroxido Complexes of Vanadium." *Coordination Chemistry Reviews* 318: 135–57. https://doi.org/10.1016/j.ccr.2016.03.011.

328. Sedighipoor, M., Kianfar, A.H., Mahmood, W.A.K. and Azarian, M.H., 2017. "Epoxidation of Alkenes by an Oxidovanadium(IV) Tetradentate Schiff Base Complex as an Efficient Catalyst with Tert-Butyl Hydroperoxide." *Inorganica Chimica Acta* 457: 116–21. https://doi.org/10.1016/j.ica.2016.12.018.

329. Ségaud, N., Rebilly, J.N., Sénéchal-David, K., Guillot, R., Billon, L., Baltaze, J.P., Farjon, J., Reinaud, O. and Banse, F., 2013. "Iron Coordination Chemistry with New Ligands Containing Triazole and Pyridine Moieties. Comparison of the Coordination Ability of the N-Donors." *Inorganic Chemistry* 52 (2): 691–700. https://doi.org/10.1021/ic301834x.

330. Sessler, J.L., Tomat, E. and Lynch, V.M., 2006. "Coordination of Oxovanadium(V) in an Expanded Porphyrin Macrocycle." *Chemical Communications*, no. 43: 4486–88. https://doi.org/10.1039/b608143f.

331. Sevrioukova, I.F. and Poulos, T.L., 2013. “Understanding the Mechanism of Cytochrome P450 3A4: Recent Advances and Remaining Problems.” *Dalton Transactions* 42 (9): 3116–26. https://doi.org/10.1039/c2dt31833d.

332. Shaik, S., de Visser, S.P., Ogliaro, F., Schwarz, H. and Schröder, D., 2002. “Two-State Reactivity Mechanisms of Hydroxylation and Epoxidation by Cytochrome P-450 Revealed by Theory.” *Current Opinion in Chemical Biology* 6 (5): 556–67. https://doi.org/10.1016/S1367-5931(02)00363-0.

333. Shaik, S., Kumar, D. and de Visser, S.P., 2008. “A Valence Bond Modeling of Trends in Hydrogen Abstraction Barriers and Transition States of Hydroxylation Reactions Catalyzed by Cytochrome P450 Enzymes.” *Journal of the American Chemical Society* 130 (42): 14016. https://doi.org/10.1021/ja806917f.

334. Shaik, S., Kumar, D., de Visser, S.P., Altun, A. and Thiel, W., 2005. “Theoretical Perspective on the Structure and Mechanism of Cytochrome P450 Enzymes.” *Chemical Reviews* 105(6): 2279-2328. https://doi.org/10.1021/cr030722j.

335. Shaik, S., Milko, P., Schyman, P., Usharani, D. and Chen, H., 2011. “Trends in Aromatic Oxidation Reactions Catalyzed by Cytochrome P450 Enzymes: A Valence Bond Modeling.” *Journal of Chemical Theory and Computation* 7 (2): 327–39. https://doi.org/10.1021/ct100554g.

336. Shaik, Sason, Wenzhen Lai, H U I Chen, and Yong Wang. 2010. “The Valence Bond Way : Reactivity Patterns of Cytochrome P450 Enzymes and Synthetic Analogs.” *Accounts of Chemical Research* 43(8): 1154-1165.

337. Sharma, P.K., de Visser, S.P., Ogliaro, F. and Shaik, S., 2003. “Is the Ruthenium Analogue of Compound I of Cytochrome P450 an Efficient Oxidant? A Theoretical Investigation of the Methane Hydroxylation Reaction.” *Journal of the American Chemical Society* 125 (8): 2291–2300. https://doi.org/10.1021/ja0282487.

338. Sheldrick, G. M., 2015. “Crystal Structure Refinement with SHELXL.” *Acta Crystallographica Section C: Structural Chemistry* 71 (1): 3–8.

339. Shepherd, S.A., Karthikeyan, C., Latham, J., Struck, A.W., Thompson, M.L., Menon, B.R., Styles, M.Q., Levy, C., Leys, D. and Micklefield, J., 2015. “Extending the Biocatalytic Scope of Regiocomplementary Flavin-Dependent Halogenase Enzymes.” *Chemical Science* 6 (6): 3454–60.

340. Sholl, David, and Janice A Steckel. 2011. “Density Functional Theory: A Practical Introduction.” John Wiley & Sons.

341. Siegbahn, P.E. and Himo, F., 2009. “Recent Developments of the Quantum Chemical Cluster Approach for Modeling Enzyme Reactions.” *Journal of Biological Inorganic Chemistry* 14 (5): 643–51.

342. Silaghi-Dumitrescu, R., 2008. “Halide Activation by Heme Peroxidases: Theoretical Predictions on Putative Adducts of Halides with Compound I.” *European Journal of Inorganic Chemistry*, no. 34: 5404–7. https://doi.org/10.1002/ejic.200800732.

343. Silaghi-Dumitrescu, R., Makarov, S.V., Uta, M.M., Dereven'kov, I.A. and Stuzhin, P.A., 2011. “Redox Non-Innocence of a Nitrido Bridge in a Methane-Activating Dimer of Iron Phthalocyanine.” *New Journal of Chemistry* 35 (5): 1140–45.

344. Simonova, O.R., Zaitseva, S.V. and Koifman, O.I., 2016. “Influence of the Macrocycle Nature on the Redox Properties of Vanadium Porphyrinates in Their Reaction with an Organic Peroxide.” *Russian Journal of General Chemistry* 86 (6): 1322–29. https://doi.org/10.1134/S1070363216060177.

345. Singh, D., Kumar, D. and de Visser, S.P., 2016. “Methane Hydroxylation by Axially Ligated Iron (IV)-Oxo Porphyrin Cation Radical Models.” *International Journal of Science, Technology & Society* 1 (2).

346. Slater, J. C., 1930. “Atomic Shielding Constants.” *Physical Review* 36 (1): 57.

347. Smith II, T.S., LoBrutto, R. and Pecoraro, V.L., 2002. “Paramagnetic Spectroscopy of Vanadyl Complexes and Its Applications to Biological Systems.” *Coordination Chemistry Reviews* 228 (1): 1–18. https://doi.org/10.1016/S0010-8545(01)00437-4.

348. Smulevich, G., Feis, A. and Howes, B.D., 2005. “Fifteen Years of Raman Spectroscopy of Engineered Heme Containing Peroxidases: What Have We Learned?” *Accounts of Chemical Research* 38 (5): 433–40. https://doi.org/10.1021/ar020112q.

349. So, S.C., Cheung, W.M., Chiu, W.H., de Vere-Tucker, M., Sung, H.H., Williams, I.D. and Leung, W.H., 2019. “Iridium Porphyrin Complexes with μ-Nitrido, Hydroxo, Hydrosulfido and Alkynyl Ligands.” *Dalton Transactions*. 48: 8340-8349

350. Solomon, E.I., Brunold, T.C., Davis, M.I., Kemsley, J.N., Lee, S.K., Lehnert, N., Neese, F., Skulan, A.J., Yang, Y.S. and Zhou, J., 2000. “Geometric and Electronic Structure/Function Correlations in Non-Heme Iron Enzymes.” *Chemical Reviews* 100 (1): 235–349. https://doi.org/10.1021/cr9900275.

351. Sono, M., Roach, M.P., Coulter, E.D. and Dawson, J.H., 1996. “Heme-Containing Oxygenases.” *Chemical Reviews* 96 (7): 2841–87. https://doi.org/10.1021/cr9500500.

352. Sorokin, A. B., 2013. “Phthalocyanine Metal Complexes in Catalysis.” *Chemical Reviews* 113 (10): 8152–91. https://doi.org/10.1021/cr4000072.

353. Sorokin, A.B., Kudrik, E.V. and Bouchu, D., 2008. “Bio-Inspired Oxidation of Methane in Water Catalyzed by N-Bridged Diiron Phthalocyanine Complex.” *Chemical Communications* 22: 2562–64.

354. Sorokin, A.B., Kudrik, E.V., Alvarez, L.X., Afanasiev, P., Millet, J.M.M. and Bouchu, D., 2010. “Oxidation of Methane and Ethylene in Water at Ambient Conditions.” *Catalysis Today* 157 (1–4): 149–54. https://doi.org/10.1016/j.cattod.2010.02.007.

355. Steffensmeier, E., Swann, M.T. and Nicholas, K.M., 2018. “Mechanistic Features of the Oxidation-Reductive Coupling of Alcohols Catalyzed by Oxo-Vanadium Complexes.” *Inorganic Chemistry* 58 (1): 844–54. https://doi.org/10.1021/acs.inorgchem.8b02968.

356. Stein, S. E., and Brown R. L., 1991. “Prediction of Carbon-Hydrogen Bond Dissociation Energies for Polycyclic Aromatic Hydrocarbons of Arbitrary Size.” *Journal of the American Chemical Society* 113 (3): 787–93. https://doi.org/10.1021/ja00003a009.

357. Stephens, P.J., Devlin, F.J., Chabalowski, C.F.N. and Frisch, M.J., 1994. “Ab Initio Calculation of Vibrational Absorption and Circular Dichroism Spectra Using Density Functional Force Fields.” *The Journal of Physical Chemistry* 98 (45): 11623–27. https://doi.org/10.1021/j100096a001.

358. Stone, K.L., Behan, R.K. and Green, M.T., 2005. “X-Ray Absorption Spectroscopy of Chloroperoxidase Compound I: Insight into the Reactive Intermediate of P450 Chemistry.” *Proceedings of the National Academy of Sciences of the United States of America* 102 (46): 16563–65. https://doi.org/10.1073/pnas.0507069102.

359. Stone, K.L., Behan, R.K. and Green, M.T., 2006. “Resonance Raman Spectroscopy of Chloroperoxidase Compound II Provides Direct Evidence for the Existence of an Iron(IV)-Hydroxide.” *Proceedings of the National Academy of Sciences of the United States of America* 103 (33): 12307–10. https://doi.org/10.1073/pnas.0603159103.

360. Stone, K.L., Hoffart, L.M., Behan, R.K., Krebs, C. and Green, M.T., 2006. “Evidence for Two Ferryl Species in Chloroperoxidase Compound II.” *Journal of*

the American Chemical Society 128 (18): 6147–53. https://doi.org/10.1021/ja057876w. 250

361. Stoyanov, S.R., Yin, C.X., Gray, M.R., Stryker, J.M., Gusarov, S. and Kovalenko, A., 2010. "Computational and Experimental Study of the Structure Preferences Binding Preferences, and Spectroscopy of Nickel(II) and Petroleum Vanadyl Porphyrins in Petroleum." *Journal of Physical Chemistry B* 114 (6): 2180–88. https://doi.org/10.1021/jp908641t.

362. Stuzhin, P.A., Ivanova, S.S., Dereven'kov, I., Makarov, S.V., Silaghi-Dumitrescu, R. and Homborgc, H., 2012. "First Water-Soluble μ-Nitrido Dimer of Iron Phthalocyanine." *Macroheterocycles* 5 (2): 175–77. https://doi.org/10.6060/mhc2012.120360s.

363. Su, J. and Groves, J.T., 2009. "Direct Detection of the Oxygen Rebound Intermediates, Ferryl Mb and NO 2, in the Reaction of Metmyoglobin with Peroxynitrite." *Journal of the American Chemical Society* 131 (36): 12979–88. https://doi.org/10.1021/ja902473r.

364. Sun, L.L., Hermann, K.E., Noack, J., Timpe, O., Teschner, D., Hävecker, M., Trunschke, A. and Schlögl, R., 2014. "DFT Studies and Experiments on Biocatalytic Centers: Structure, Vibrations, and Core Excitations of the K[VO(O_2)Hheida] Complex." *Journal of Physical Chemistry C* 118 (42): 24611–22. https://doi.org/10.1021/jp5081719.

365. Sun, X., 2014. "Recent Advances in Mechanistic Studies of the Aromatic CH Bond Substitution and Related Chemistry-A Mini-Review." *Current Organic Chemistry* 18 (24): 3066–77.

366. Sutradhar, M., Martins, L.M., da Silva, M.F.C.G. and Pombeiro, A.J., 2015. "Vanadium Complexes: Recent Progress in Oxidation Catalysis." *Coordination Chemistry Reviews* 301–302: 200–239. https://doi.org/10.1016/j.ccr.2015.01.020.

367. Taktak, S., Ye, W., Herrera, A.M. and Rybak-Akimova, E.V., 2007. "Synthesis and Catalytic Properties in Olefin Epoxidation of Novel Iron(II) Complexes with Pyridine-Containing Macrocycles Bearing an Aminopropyl Pendant Arm." *Inorganic Chemistry* 46 (7): 2929–42. https://doi.org/10.1021/ic070094e.

368. Tang, H., Guan, J., Zhang, L., Liu, H. and Huang, X., 2012. "The Effect of the Axial Ligand on Distinct Reaction Tunneling for Methane Hydroxylation by Nonheme Iron (Iv)–Oxo Complexes." *Physical Chemistry Chemical Physics* 14 (37): 12863–74.

369. ten Brink, H.B., Dekker, H.L., Schoemaker, H.E. and Wever, R., 2000. "Oxidation Reactions Catalyzed by Vanadium Chloroperoxidase from Curvularia Inaequalis."

Journal of Inorganic Biochemistry 80 (1–2): 91–98. https://doi.org/10.1016/S0162-0134(00)00044-1.

370. Thompson, K., 2001. "Coordination Chemistry of Vanadium in Metallopharmaceutical Candidate Compounds." *Coordination Chemistry Reviews* 219: 1033–53. https://doi.org/10.1016/S0010-8545(01)00395-2.

371. Thompson, K.H., McNeill, J.H. and Orvig, C., 1999. "Vanadium Compounds as Insulin Mimics." *Chemical Reviews* 99 (9): 2561–72. https://doi.org/10.1021/cr980427c.

372. Timmins, A. and de Visser, S.P., 2015. "Enzymatic Halogenases and Haloperoxidases: Computational Studies on Mechanism and Function." *Advances in Protein Chemistry and Structural Biology* 100: 113-151. https://doi.org/10.1016/bs.apcsb.2015.06.001.

373. Timmins, A. and de Visser, S.P., 2018. "A Comparative Review on the Catalytic Mechanism of Nonheme Iron Hydroxylases and Halogenases." *Catalysts* 8 (8). https://doi.org/10.3390/catal8080314.

374. Timmins, A., Quesne, M.G., Borowski, T. and de Visser, S.P., 2018. "Group Transfer to an Aliphatic Bond: A Biomimetic Study Inspired by Nonheme Iron Halogenases." *ACS Catalysis* 8 (9): 8685–98.

375. Timmins, A., Saint-André, M. and de Visser, S.P., 2017. "Understanding How Prolyl-4-Hydroxylase Structure Steers a Ferryl Oxidant toward Scission of a Strong C-H Bond." *Journal of the American Chemical Society* 139 (29): 9855–66. https://doi.org/10.1021/jacs.7b02839.

376. Toader, V., Xu, X., Nicolescu, A., Yu, L., Bolton, J.L. and Thatcher, G.R., 2003. "Nitrosation, Nitration, and Autoxidation of the Selective Estrogen Receptor Modulator Raloxifene by Nitric Oxide, Peroxynitrite, and Reactive Nitrogen/Oxygen Species." *Chemical Research in Toxicology* 16 (10): 1264–76. https://doi.org/10.1021/tx025641h.

377. Tomasi, J., Mennucci, B. and Cammi, R., 2005. "Quantum Mechanical Continuum Solvation Models." *Chemical Reviews* 105 (8): 2999–3094.

378. Tomita, H., Katsuyama, Y., Minami, H. and Ohnishi, Y., 2017. "Identification and Characterization of a Bacterial Cytochrome P450 Monooxygenase Catalyzing the 3-Nitration of Tyrosine in Rufomycin Biosynthesis." *Journal of Biological Chemistry* 292 (38): 15859–69. https://doi.org/10.1074/jbc.M117.791269.

379. Tromp, M., Van, T.T. and Wever, R., 1991. "Reactivation of Vanadium Bromoperoxidase; Inhibition by Metallofluoric Compounds." *Biochimica et*

Biophysica Acta (BBA) - Protein Structure and Molecular Enzymology 1079 (1): 53–56. https://doi.org/10.1016/0167-4838(91)90023-S.

380. Trost, B.M. and Tracy, J.S., 2017. "Carbon-Nitrogen Bond Formation via the Vanadium Oxo Catalyzed Sigmatropic Functionalization of Allenols." *Organic Letters* 19 (10): 2630–33. https://doi.org/10.1021/acs.orglett.7b00961.

381. Vaillancourt, F.H., Yeh, E., Vosburg, D.A., Garneau-Tsodikova, S. and Walsh, C.T., 2006. "Nature's Inventory of Halogenation Catalysts: Oxidative Strategies Predominate." *Chemical Reviews* 106 (8): 3364–78. https://doi.org/10.1021/cr050313i.

382. van Eldik, R., 2007. "Fascinating Inorganic/Bioinorganic Reaction Mechanisms." *Coordination Chemistry Reviews* 251 (13-14): 1649–62. https://doi.org/10.1016/j.ccr.2007.02.004.

383. van Pe, K.H., Dong, C., Flecks, S., Naismith, J., Patallo, E.P. and Wage, T., 2006.. "Biological Halogenation Has Moved Far beyond Haloperoxidases." *Advances in Applied Microbiology* 59: 127–57.

384. Van Schijndel, J.W., Barnett, P., Roelse, J., Vollenbroek, E.G. and Wever, R., 1994. "The Stability and Steady-state Kinetics of Vanadium Chloroperoxidase from the Fungus Curvularia Inaequalis." *European Journal of Biochemistry* 225 (1): 151–57.

385. Vandichel, M., Leus, K., Van Der Voort, P., Waroquier, M. and Van Speybroeck, V., 2012. "Mechanistic Insight into the Cyclohexene Epoxidation with $VO(Acac)_2$ and Tert-Butyl Hydroperoxide." *Journal of Catalysis* 294: 1–18. https://doi.org/10.1016/j.jcat.2012.06.002.

386. Vardhaman, A.K., Barman, P., Kumar, S., Sastri, C.V., Kumar, D. and de Visser, S.P., 2013. "Comparison of the Reactivity of Nonheme Iron(IV)-Oxo versus Iron(IV)-Imido Complexes: Which Is the Better Oxidant?" *Angewandte Chemie - International Edition* 52 (47): 12288–92. https://doi.org/10.1002/anie.201305370.

387. Vardhaman, A.K., Barman, P., Kumar, S., Sastri, C.V., Kumar, D. and de Visser, S.P., 2013. "Mechanistic Insight into Halide Oxidation by Non-Heme Iron Complexes. Haloperoxidase versus Halogenase Activity." *Chemical Communications* 49 (93): 10926–28.

388. Vardhaman, A.K., Sastri, C.V., Kumar, D. and de Visser, S.P., 2011. "Nonheme Ferric Hydroperoxo Intermediates Are Efficient Oxidants of Bromide Oxidation." *Chemical Communications* 47 (39): 11044–46.

389. Veitch, N.C. and Smith, A.T., 2000. "Horseradish Peroxidase." *Advances in Inorganic Chemistry* 51: 107-162.

390. Vidossich, P., Alfonso-Prieto, M. and Rovira, C., 2012. “Catalases versus Peroxidases: DFT Investigation of H_2O_2 Oxidation in Models Systems and Implications for Heme Protein Engineering.” *Journal of Inorganic Biochemistry* 117: 292–97. https://doi.org/10.1016/j.jinorgbio.2012.07.002.

391. Vidossich, P., Fiorin, G., Alfonso-Prieto, M., Derat, E., Shaik, S. and Rovira, C., 2010. “On the Role of Water in Peroxidase Catalysis: A Theoretical Investigation of HRP Compound I Formation.” *Journal of Physical Chemistry B* 114 (15): 5161–69. https://doi.org/10.1021/jp911170b.

392. Vilter, H., 1984. “Peroxidases from Phaeophyceae: A Vanadium(V)-Dependent Peroxidase from Ascophyllum Nodosum.” *Phytochemistry* 23 (7): 1387–90. https://doi.org/10.1016/S0031-9422(00)80471-9.

393. Visser, S. P. D.,. 2006. “Substitution of Hydrogen by Deuterium Changes the Regioselectivity of Ethylbenzene Hydroxylation by an Oxo-Iron-Porphyrin Catalyst.” *Chemistry - A European Journal* 12 (31): 8168–77. https://doi.org/10.1002/chem.200600376.

394. Visser, S.P.D., 2006. “Propene Activation by the Oxo-Iron Active Species of Taurine / r -Ketoglutarate Dioxygenase (TauD) Enzyme . How Does the Catalysis Compare to Heme-Enzymes ?,” no. 6: 9813–24. https://doi.org/10.1021/ja061581g.

395. Visser, S.P.D., 2010. “Trends in Substrate Hydroxylation Reactions by Heme and Nonheme Iron(IV)-Oxo Oxidants Give Correlations between Intrinsic Properties of the Oxidant with Barrier Height,” *Journal of the American Chemical Society*, *132*(3): 1087-1097.

396. Visser, S.P.D., and Sason S., 2003. “A Proton-Shuttle Mechanism Mediated by the Porphyrin in Benzene Hydroxylation by Cytochrome P450 Enzymes.” *Journal of the American Chemical Society* 125 (24): 7413–24. https://doi.org/10.1021/ja034142f.

397. Visser, S.P.D., and Tan, L.S., 2008. “Is the Bound Substrate in Nitric Oxide Synthase Protonated or Neutral and What Is the Active Oxidant That Performs Substrate Hydroxylation?” *Journal of the American Chemical Society* 130 (39): 12961–74. https://doi.org/10.1021/ja8010995.

398. Visser, S.P.D., Kumar, D., Cohen, S., Shacham, R. and Shaik, S., 2004 “A Predictive Pattern of Computed Barriers for C-H Hydroxylation by Compound I of Cytochrome P450.” *Journal of the American Chemical Society* 126 (27): 8362–63. https://doi.org/10.1021/ja048528h.

399. Visser, S.P.D., Ogliaro, F. and Shaik, S., 2001. “How Does Ethene Inactivate Cytochrome P450 En Route to Its Epoxidation? A Density Functional Study.” *Angewandte Chemie International Edition* 40 (15): 2871–74.

400. Visser, S.P.D., Ogliaro, F., Harris, N. and Shaik, S., 2001. “Multi-State Epoxidation of Ethene by Cytochrome P450 : A Quantum Chemical Study,” *Journal of the American Chemical Society*, *123*(13): 3037–47.

401. Visser, S.P.D., Ogliaro, F., Sharma, P.K. and Shaik, S., 2002. “What Factors Affect the Regioselectivity of Oxidation by Cytochrome P450 ? A DFT Study of Allylic Hydroxylation and Double Bond Epoxidation in a Model Reaction.” *Journal of the American Chemical Society*, 124(39): 11809–26. https://doi.org/10.1021/ja026872d.

402. Visser, S.P.D., Ogliaro, F., Sharma, P.K. and Shaik, S., 2002.. “Hydrogen Bonding Modulates the Selectivity of Enzymatic Oxidation by P450 : Chameleon Oxidant Behavior by Compound I.” *Angewandte Chemie International Edition* 41(11): 1947-51. https://doi.org/https://doi.org/10.1002/1521-3773(20020603)41:11<1947::AID-ANIE1947>3.0.CO;2-W.

403. Visser, S.P.D., Quesne, M.G., Martin, B., Comba, P. and Ryde, U., 2014 “Computational Modelling of Oxygenation Processes in Enzymes and Biomimetic Model Complexes.” *Chemical Communications* 50 (3): 262–82. https://doi.org/10.1039/c3cc47148a.

404. Visser, S.P.D., Rohde, J.U., Lee, Y.M., Cho, J. and Nam, W., 2013. “Intrinsic Properties and Reactivities of Mononuclear Nonheme Iron-Oxygen Complexes Bearing the Tetramethylcyclam Ligand.” *Coordination Chemistry Reviews* 257 (2): 381–93. https://doi.org/10.1016/j.ccr.2012.06.002.

405. Visser, S.P.D., Shaik, S., Sharma, P.K., Kumar, D. and Thiel, W., 2003. “Active Species of Horseradish Peroxidase (HRP) and Cytochrome P450 : Two Electronic Chameleons,” *Journal of the American Chemical Society125*(51): 15779–88. https://doi.org/10.1021/ja0380906.

406. Vollenbroek, E.G.M., Simons, L.H., Van Schijndel, J.W.P.M., Barnett, P., Balzar, M., Dekker, H., Van der Linden, C. and Wever, R., 1995. “Vanadium Chloroperoxidases Occur Widely in Nature.” *Biochemical Society Transactions* 23 (2): 267–71. https://doi.org/10.1042/bst0230267.

407. Vosko, S.H., Wilk, L. and Nusair, M., 1980. “Accurate Spin-Dependent Electron Liquid Correlation Energies for Local Spin Density Calculations: A Critical Analysis.” *Canadian Journal of Physics* 58 (8): 1200–1211. https://doi.org/10.1139/p80-159.

408. Wagenknecht, H.A. and Woggon, W.D., 1997. "Identification of Intermediates in the Catalytic Cycle of Chloroperoxidase." *Chemistry & Biology* 4 (5): 367–72. https://doi.org/10.1016/s1074-5521(97)90127-7.

409. Waller, M.P., Bühl, M., Geethalakshmi, K.E., Wang, D. and Thiel, W., 2007. "^{51}V NMR Chemical Shifts Calculated from QM/MM Models of Vanadium Chloroperoxidase." *Chemistry (Weinheim an Der Bergstrasse, Germany)* 13 (17): 4723–32. https://doi.org/10.1002/chem.200700295.

410. Walling, C. and Johnson, R.A., 1975. "Fenton's Reagent. V. Hydroxylation and Side-Chain Cleavage of Aromatics." *Journal of the American Chemical Society* 97 (2): 363–67. https://doi.org/10.1021/ja00835a024.

411. Walling, C., 1998. "Intermediates in the Reactions of Fenton Type Reagents." *Accounts of Chemical Research* 31 (4): 155–57. https://doi.org/10.1021/ar9700567.

412. Wang, J., Li, R., Dong, Z., Liu, P. and Dong, G., 2018. "Complementary Site-Selectivity in Arene Functionalization Enabled by Overcoming the Ortho Constraint in Palladium/Norbornene Catalysis." *Nature Chemistry* 10 (8): 866–72. https://doi.org/10.1038/s41557-018-0074-z.

413. Warshel, A., 1998. "Electrostatic Origin of the Catalytic Power of Enzymes and the Role of Preorganized Active Sites." *Journal of Biological Chemistry* 273 (42): 27035–38. https://doi.org/10.1074/jbc.273.42.27035.

414. Watanabe, Y., Nakajima, H. and Ueno, T., 2007. "Reactivities of Oxo and Peroxo Intermediates Studied by Hemoprotein Mutants." *Accounts of Chemical Research* 40 (7): 554–62. https://doi.org/10.1021/ar600046a.

415. Weichold, V., Milbredt, D. and van Pée, K.H., 2016. "Specific Enzymatic Halogenation-From the Discovery of Halogenated Enzymes to Their Applications In Vitro and In Vivo." *Angewandte Chemie International Edition* 55 (22): 6374–89. https://doi.org/10.1002/anie.201509573.

416. Weitz, A.C., Mills, M.R., Ryabov, A.D., Collins, T.J., Guo, Y., Bominaar, E.L. and Hendrich, M.P., 2019. "A Synthetically Generated $LFe^{IV}OH_n$ Complex." *Inorganic Chemistry* 58 (3): 2099–2108. https://doi.org/10.1021/acs.inorgchem.8b03200.

417. Wever, R. and Barnett, P., 2017. "Vanadium Chloroperoxidases: The Missing Link in the Formation of Chlorinated Compounds and Chloroform in the Terrestrial Environment?" *Chemistry - An Asian Journal* 12 (16): 1997–2007. https://doi.org/10.1002/asia.201700420.

418. Wever, R. and van der Horst, M.A., 2013. "The Role of Vanadium Haloperoxidases in the Formation of Volatile Brominated Compounds and Their Impact on the Environment." *Dalton Transactions* 42 (33): 11778–86. https://doi.org/10.1039/c3dt50525a.

419. Wever, R., 2012. "Structure and Function of Vanadium Haloperoxidases." In: Michibata H. (eds) Vanadium. Springer, Dordrecht. https://doi.org/10.1007/978-94-007-0913-3.

420. Wever, R., and Wieger Hemrika W., 2006. "Vanadium Haloperoxidases." *Handbook of Metalloproteins*, 276:3008–19. Chichester: John Wiley & Sons, Ltd. https://doi.org/10.1002/0470028637.met204.

421. Weyand, M., Hecht, H.J., Kiess, M., Liaud, M.F., Vilter, H. and Schomburg, D., 1999. "X-Ray Structure Determination of a Vanadium-Dependent Haloperoxidase from Ascophyllum Nodosum at 2.0 Å Resolution." *Journal of Molecular Biology* 293 (3): 595–611. https://doi.org/10.1006/jmbi.1999.3179.

422. Wijeratne, G.B., Corzine, B., Day, V.W. and Jackson, T.A., 2014. "Saturation Kinetics in Phenolic O-H Bond Oxidation by a Mononuclear Mn(III)-OH Complex Derived from Dioxygen." *Inorganic Chemistry* 53 (14): 7622–34. https://doi.org/10.1021/ic500943k.

423. Winter, J.M. and Moore, B.S., 2009. "Exploring the Chemistry and Biology of Vanadium-Dependent Haloperoxidases." *Journal of Biological Chemistry* 284 (28): 18577–81. https://doi.org/10.1074/jbc.R109.001602.

424. Wong, S.Y., Sun, R.W.Y., Chung, N.P.Y., Lin, C.L. and Che, C.M., 2005. "Physiologically Stable Vanadium(IV) Porphyrins as a New Class of Anti-HIV Agents." *Chemical Communications*, no. 28: 3544–46. https://doi.org/10.1039/b503535j.

425. Wu, X., Seo, M.S., Davis, K.M., Lee, Y.M., Chen, J., Cho, K.B., Pushkar, Y.N. and Nam, W., 2011. "A Highly Reactive Mononuclear Non-Heme Manganese(IV)-Oxo Complex That Can Activate the Strong C-H Bonds of Alkanes." *Journal of the American Chemical Society* 133 (50): 20088–91. https://doi.org/10.1021/ja208523u.

426. Xia, J.B., Cormier, K.W. and Chen, C., 2012. "A Highly Selective Vanadium Catalyst for Benzylic C–H Oxidation." *Chemical Science* 3 (7): 2240-45. https://doi.org/10.1039/c2sc20178j.

427. Xu, N., Powell, D.R. and Richter-Addo, G.B., 2011. "Nitrosylation in a Crystal: Remarkable Movements of Iron Porphyrins upon Binding of Nitric Oxide."

Angewandte Chemie - International Edition 50 (41): 9694–96. https://doi.org/10.1002/anie.201103329.

428. Yamada, Y., Morita, K., Mihara, N., Igawa, K., Tomooka, K. and Tanaka, K., 2019. "Catalytic Methane Oxidation by Supramolecular Conjugate Based on μ-Nitrido-Bridged Iron Porphyrinoid Dimer." *New Journal of Chemistry*. 43: 11477-11482.

429. Yamashita, K.I., Tazawa, S. and Sugiura, K.I., 2016. "Oxo(Porphyrinato)Vanadium(IV) as a Standard for Geoporphyrins." *Inorganica Chimica Acta* 439: 173–77. https://doi.org/10.1016/j.ica.2015.10.019.

430. Yan, G. and Yang, M., 2013. "Recent Advances in the Synthesis of Aromatic Nitro Compounds." *Organic and Biomolecular Chemistry* 11 (16): 2554–66. https://doi.org/10.1039/c3ob27354g.

431. Yang, T., Quesne, M.G., Neu, H.M., Cantú Reinhard, F.G., Goldberg, D.P. and de Visser, S.P., 2016. "Singlet versus Triplet Reactivity in an Mn(V)-Oxo Species: Testing Theoretical Predictions Against Experimental Evidence." *Journal of the American Chemical Society* 138 (38): 12375–86. https://doi.org/10.1021/jacs.6b05027.

432. Ye, S. and Neese, F., 2011. "Nonheme Oxo-Iron(IV) Intermediates Form an Oxyl Radical upon Approaching the C – H Bond Activation Transition State," *Proceedings of the National Academy of Sciences*, 108(4):1228-33. https://doi.org/10.1073/pnas.1008411108/

433. Yoshizawa, K., 2006. "Nonradical Mechanism for Methane Hydroxylation by Iron-Oxo Complexes." *Accounts of Chemical Research* 39 (6): 375–82. https://doi.org/10.1021/ar050194t.

434. Yu, F., Li, M., Xu, C., Wang, Z., Zhou, H., Yang, M., Chen, Y., Tang, L. and He, J., 2013. "Structural Insights into the Mechanism for Recognizing Substrate of the Cytochrome P450 Enzyme TxtE." *PLoS ONE* 8 (11): 1–11. https://doi.org/10.1371/journal.pone.0081526.

435. Zampella, G., Fantucci, P., Pecoraro, V.L. and De Gioia, L., 2005. "Reactivity of Peroxo Forms of the Vanadium Haloperoxidase Cofactor. A DFT Investigation." *Journal of the American Chemical Society* 127 (3): 953–60. https://doi.org/10.1021/ja046016x.

436. Zampella, G., Fantucci, P., Pecoraro, V.L. and De Gioia, L., 2006. "Insight into the Catalytic Mechanism of Vanadium Haloperoxidases. DFT Investigation of Vanadium Cofactor Reactivity." *Inorganic Chemistry* 45 (18): 7133–43. https://doi.org/10.1021/ic060555g.

437. Zaragoza, J.P.T. and Goldberg, D.P., 2018. “Dioxygen Binding and Activation Mediated by Transition Metal Porphyrinoid Complexes.” *Dioxygen-Dependent Heme Enzymes*, 1–36.

438. Zaragoza, J.P.T., Siegler, M.A. and Goldberg, D.P., 2018 “A Reactive Manganese(IV)-Hydroxide Complex: A Missing Intermediate in Hydrogen Atom Transfer by High-Valent Metal-Oxo Porphyrinoid Compounds.” *Journal of the American Chemical Society* 140 (12): 4380–90. https://doi.org/10.1021/jacs.8b00350.

439. Zaragoza, J.P.T., Yosca, T.H., Siegler, M.A., Moënne-Loccoz, P., Green, M.T. and Goldberg, D.P., 2017. “Direct Observation of Oxygen Rebound with an Iron-Hydroxide Complex.” *Journal of the American Chemical Society* 139 (39): 13640–43. https://doi.org/10.1021/jacs.7b07979.

440. Zeb, N., Rashid, M.H., Mubarak, M.Q.E., Ghafoor, S. and de Visser, S.P., 2019. “Flavonol Biosynthesis by Nonheme Iron Dioxygenases: A Computational Study into the Structure and Mechanism.” *Journal of Inorganic Biochemistry* 198:110728-35. https://doi.org/10.1016/j.jinorgbio.2019.110728.

441. Zechel, F., Schwendt, P., Gyepes, R., Šimunek, J., Tatiersky, J. and Krivosudský, L., 2019. “ Vanadium(V) Complexes of Mandelic Acid .” *New Journal of Chemistry*. 43(45): 17696-702. https://doi.org/10.1039/c9nj02275a.

442. Zederbauer, M., Furtmüller, P.G., Brogioni, S., Jakopitsch, C., Smulevich, G. and Obinger, C., 2007. “Heme to Protein Linkages in Mammalian Peroxidases: Impact on Spectroscopic, Redox and Catalytic Properties.” *Natural Product Reports* 24 (3): 571–84.

443. Zhang, D., Dutasta, J.P., Dufaud, V., Guy, L. and Martinez, A., 2017. “Sulfoxidation inside a C3-Vanadium(V) Bowl-Shaped Catalyst.” *ACS Catalysis*, 7(10): 7340–45. https://doi.org/10.1021/acscatal.7b01886.

444. Zhang, D., Jamieson, K., Guy, L., Gao, G., Dutasta, J.P. and Martinez, A., 2016. “Tailored Oxido-Vanadium(V) Cage Complexes for Selective Sulfoxidation in Confined Spaces.” *Chemical Science* 8 (1): 789–94. https://doi.org/10.1039/c6sc03045a.

445. Zhang, G., Scott, B.L., Wu, R., Silks, L.P. and Hanson, S.K., 2012. “Aerobic Oxidation Reactions Catalyzed by Vanadium Complexes of Bis(Phenolate) Ligands.” *Inorganic Chemistry* 51 (13): 7354–61. https://doi.org/10.1021/ic3007525.

446. Zhang, J., Yang, H., Sun, T., Chen, Z. and Yin, G., 2017. “Nonredox Metal-Ions-Enhanced Dioxygen Activation by Oxidovanadium (IV) Complexes

toward Hydrogen Atom Abstraction." *Inorganic Chemistry* 56 (2): 834–44. https://doi.org/10.1021/acs.inorgchem.6b02277.

447. Zhao, X., Shi, Q., Gray, M.R. and Xu, C., 2014. "New Vanadium Compounds in Venezuela Heavy Crude Oil Detected by Positive-Ion Electrospray Ionization Fourier Transform Ion Cyclotron Resonance Mass Spectrometry." *Scientific Reports* 4: 1–6. https://doi.org/10.1038/srep05373.

448. Zuo, R. and Ding, Y., 2019. "Direct Aromatic Nitration System for Synthesis of Nitrotryptophans in *Escherichia Coli*." *ACS Synthetic Biology* 8 (4): 857–65. https://doi.org/10.1021/acssynbio.8b00534.

449. Zuo, R., Zhang, Y., Jiang, C., Hackett, J.C., Loria, R., Bruner, S.D. and Ding, Y., 2017. "Engineered P450 Biocatalysts Show Improved Activity and Regio-Promiscuity in Aromatic Nitration." *Scientific Reports* 7(1): 1–9. https://doi.org/10.1038/s41598-017-00897-z.